Mechanical design and dynamic performance characterisation for non-contact form measurement systems



University of Nottingham
UK | CHINA | MALAYSIA

Patrick Bointon

Faculty of Engineering

University of Nottingham

Thesis submitted to the University of Nottingham for the degree of

Doctor of Philosophy

April 2020

I would like to dedicate this thesis to my loving family, who have always supported and loved me unconditionally. Especially my parents, who I am sure would have had a lovely holiday home in the south of France, had they not had me and indulged all of my many hobbies ...

Declaration

I hereby declare that except where specific reference is made to the work of others, the contents of this thesis are original and have not been submitted in whole or in part for consideration for any other degree or qualification in this, or any other university. This thesis is my own work and contains nothing which is the outcome of work done in collaboration with others, except as specified in the text and Acknowledgements. This dissertation contains fewer than 65,000 words including appendices, bibliography, footnotes, tables and equations and has fewer than 150 figures.

This work has been carried out with the support of the engineering and Physical Sciences Research Council and the Centre for Doctoral Training in Ultra Precision Engineering.

Patrick Bointon

April 2020

Acknowledgements

I would like to acknowledge Richard Leach and Adam Clare for their valuable supervision and guidance throughout my PhD. I would also like to thank them for prrof reding my work, without which, I am sure the work would not read half as well.

I would also like to thank my friends and colleagues in the MMT for their friendship and help throughout the past four years. This includes and is not limited to, Shaun Harris, Suhin Thawani, Matt Blenkinsop, Connor Jones, Danny-Sims Waterhouse, Adam Thompson, Alex Gasper, Lars Korner, Lewis Newton and Sofia Catalucci. With a special thanks to Luke Todhunter for only working part-time, so that I could get some work done in the morning before distracting me for the rest of day, and to Kevin Bersch for all the free beers and always picking the Titans.

And last but not least, a massive thank you to Savannah Worne, for everything you have done for me throughout the PhD, and for always keeping a smile on my face, especially when the times were tough.

Abstract

This thesis presents work in the fields of optical metrology, mechanical design and condition monitoring, with a focus on developing the mechanical design for a novel multi-view fringe projection system, enhancing the understanding of the effects of mechanical noise on fringe projection measurements and demonstrating the benefits of multi-point condition monitoring for measurement system applications. The work given in this thesis provides a number of key methodologies that are used to establish a detailed mechanical design process and facilitate the investigation of the effects of vibration on fringe projection measurements. In addition, a flexible multi-point condition monitoring system is presented which allows for the live appraisal of the dynamic performance of measurement systems in multiple locations around the mechanical structure.

A state-of-the-art review was performed that identifies a number of key knowledge gaps in the field. The first section of review investigated different available form measurement techniques and identified fringe projection as an appropriate technique for the proposed measurement system. A discussion of the potential error sources in fringe projection measurements was carried out, with a focus on the mechanical error sources. The mechanical design of current commercial and laboratory fringe projection systems was then critically assessed in order to identify areas for improvement for the design of the multi-view fringe projection system. Finally, the methodology and benefits of effective condition monitoring were reviewed, in an attempt to utilise these principles to develop a new system for measurement system applications.

The thesis provides a complete design history of the development of the mechanical frame, which was designed for the multi-view fringe projection prototype system. The development of the design included a number of experimental investigations which were carried out in order to better define mechanical performance metrics in the statement of requirements for the design. In order to define the stability performance metric required, a methodology was developed and presented which allowed the effects of vibration on fringe projection measurements to be studied in both a theoretical simulation and experimental study. A systematic description of the design processes and techniques used to progress from the initial design concepts to the final design stage were included in the design history, along with a breakdown of the finite element analysis (FEA) simulations that were used to prove the design met the required performance specifications. The detailed design process provides a clear and structured methodology, which can be utilised in order to design and develop future measurement frames.

A methodology was developed which allowed for the experimental characterisation of the multi-view fringe projection mechanical system. In order to characterise the multi-view frame, a detailed review was carried out of several available vibration sensors, such as laser vibrometers and proximity sensors, with piezoelectric accelerometers identified as the most appropriate solution for this application. An investigation into the different acceleration/velocity/displacement conversion methods was presented, which showed the unreliability of the widely used double integration method and highlighted the advantages of the omega arithmetic method. Finally, using the developed characterisation method, the multi-view frame was fully characterised in both a non-excited and camera shutter-excited state in a number of identified key positions around the system. The characterisation results were then used to verify the results of the FEA simulations.

A novel live multi-point vibration monitoring setup that combined multiple triaxial accelerometers was developed utilising a bespoke LabVIEW software framework that provides

the capability to live-monitor the dynamic performance of any system in three axes at multiple locations simultaneously, collecting large amounts of data in real time. The software framework was designed with flexibility in mind to enable compatibility with a wide variety of applications. An investigation into the effects of tool wear and cutting depth on a CNC lathe was carried out in order to demonstrate the functionality of the system and highlight the advantages of structure health monitoring.

The live multi-point condition monitoring system was used to perform two experimental case studies to demonstrate the effectiveness of condition monitoring in measurement system applications and investigate the sensitivity of fringe projection measurements to vibration. The two measurement systems used were a commercial fringe projection system and an in-house multi-view fringe projection prototype system. The results of the case study experiments showed new information about the mechanical error sources in fringe projection measurements, and highlighted regions of the measurement that were more susceptible to particular vibration directions. The relationships between the measured vibrations and point-cloud deviation errors were established for each case study and allowed the sensitivity to vibrations for each system to be established. The vibration-error relationships were used alongside multi-point vibration measurements to estimate the variation in errors for each of the camera-projector pairs at different locations on the multi-view fringe projection frame, which clearly demonstrated the importance of multi-point condition monitoring in measurement system applications.

Table of contents

List of figures **xix**

List of tables **xxxiii**

Nomenclature **xxxv**

1 Introduction **1**

1.1 Background and motivation 1

1.2 Aims and objectives 9

1.3 Structure of the thesis 10

2 State-of-the-art review **13**

2.1 Introduction 13

2.2 Measurement techniques 14

2.2.1 Contact form measurement techniques 14

2.2.2 Non-contact measurement systems 15

2.2.2.1 Laser scanning 16

2.2.2.2 Photogrammetry 17

2.2.2.3 Interferometry 18

2.2.2.4 Moiré fringes 19

2.2.2.5 Fringe projection 20

2.3 Uncertainty and error sources in fringe projection 23
2.3.1 Camera and lens properties 23
2.3.2 Sampling 27
2.3.3 Phase error 28
2.3.4 Projection errors 29
2.3.5 Noise 29
2.3.6 Mechanical noise 32
2.4 Fringe projection frame design 35
2.4.1 Condition monitoring 39
2.5 Chapter summary 42

3 Research methodology 45
3.1 Software methodology 46
3.1.1 Computer aided design 46
3.1.2 ANSYS 47
3.1.3 MATLAB 47
3.1.4 LabVIEW 48
3.2 Hardware methodology 49
3.2.1 Additive manufacturing 49
3.2.2 Piezoelectric accelerometers 50
3.2.3 Laser vibrometer 52
3.2.4 Smart shaker 53
3.3 Analysis methods 53
3.3.1 Vibration analysis 54
3.4 Chapter summary 56

4 Design specification and system design 59

4.1 Introduction . . . 59
4.2 The effects of vibration on fringe projection measurements . . . 61
4.2.1 Simulation of vibration in fringe projection . . . 61
4.2.2 Experimental investigation . . . 64
4.3 Statement of requirements for multi-view mechanical design . . . 69
4.4 Multi-view fringe projection frame design . . . 70
4.4.1 Design concepts . . . 71
4.4.2 Design development and final design . . . 83
4.4.3 Proof of concept . . . 85
4.5 Camera and projector mount design . . . 91
4.6 Chapter summary . . . 92

5 Design characterisation and results 97

5.1 Introduction . . . 97
5.2 Vibration sensor comparison . . . 98
5.2.1 Available sensors . . . 98
5.2.2 Choice of sensor . . . 101
5.3 Displacement results . . . 105
5.3.1 Double integration . . . 105
5.3.2 Omega Arithmetic . . . 106
5.3.3 Comparison of conversion methods . . . 108
5.4 Multi-point full frame characterisation . . . 119
5.5 Chapter summary . . . 130

6 Development of live multi-point vibration monitoring setup 131

6.1 Introduction . . . 131
6.2 System overview . . . 132

6.2.1 Software 132
6.2.2 Hardware 133
6.3 Software framework 134
6.3.1 Establishing parameter set 135
6.3.2 Filtering 137
6.3.3 Windowing options 137
6.3.4 Signal conversion 138
6.4 Analysis techniques 138
6.4.1 Peak-to-peak 139
6.4.2 Frequency spectrum analysis 140
6.4.3 Power spectral density 140
6.4.4 Event analysis 140
6.4.5 User interface 142
6.4.5.1 Results - Live data VI 142
6.4.5.2 Results – Post-measurement analysis VI 143
6.4.6 System properties and errors section 145
6.4.7 Data handling 146
6.5 Lathe condition monitoring investigation 146
6.6 Chapter summary 152

7 Live vibration monitoring of fringe projection systems 155

7.1 Introduction 155
7.2 Case study one – Commercial fringe projection system 156
7.3 Case study two – multi-view fringe projection 171
7.3.1 Multi-point condition monitoring demonstration 182
7.4 Chapter summary 184

8 Conclusions and future work **187**

8.1 Contributions to the field 188

8.2 Areas for future work 190

8.3 Summary 193

References **195**

List of figures

1.1 The traceability pyramid. In order to ensure traceability is transferred between each level by calibration, and creates a traceable unbroken chain from the measured part to the definition of the SI unit. 3

1.2 Practical example of the traceability chain applied to a length measurement of the width of a ball bearing part. 4

2.1 Example of an (a) large-scale CMM from Leitz and (b) a small-scale CMM from Zeiss 15

2.2 The experimental configuration for laser scanning, which uses a laser and camera, and the principle of triangulation to measure the height of each point on the objects surface. 17

2.3 The experimental configuration for photogrammetry, which uses two cameras to measures the form of an object by finding correspondence between the two captured images and triangulation to find the height of each point. . . . 18

2.4 The experimental configuration for interferometry, which reconstructs the object's surface by analysing the interference pattern created when the reference beam and measurement beam are superimposed. 19

2.5 The experimental configuration for Moiré fringe techniques, which uses two gratings to create the fringe patterns, and a camera to capture the pattern, which can be analysed to reconstruct the object's form. 21

2.6 Fringe projection system setup with one projector and one camera, the angles and baseline used for triangulation based fringe projection have also been illustrated 22
2.7 Point spread function produced by a point source passing through a simple optical system consisting of a lens and circular aperture. 24
2.8 Effects of changing distances between two point spread functions. (a) Easily distinguishable, (b) Only just, but still distinguishable and (c) no longer distinguish the two sources. 25
2.9 Illustration of the principle behind the circle of confusion. 26
2.10 Illustration of the projection errors caused by the uncertainty in the projection angles in both the camera and projector for both (a) wider baseline and (b) narrow baseline. 30
2.11 Effect of noise on a point spread function. A noise level of $0\%, 5\%, 10\%$ and 20% are shown. 31
2.12 Simple sinusoidal vibration wave with the key characteristics (amplitude, period, frequency and peak-to-peak) used to define the vibration identified. 32
2.13 Example of a commercially available fringe projection system mounted on a robot arm. 37
2.14 Example of a commercially available fringe projection system mounted on a tripod. 38

3.1 Schematic diagram depicting the process used for additive manufacturing powder bed fusion technologies. 51
3.2 Schematic diagram depicting the key elements of a piezoelectric accelerometer. 52
3.3 The Modal Shop smart shaker K2007E01 [1] that was used to excite the different structures in each vibration experiment 54

3.4 An exemplar vibration dataset collected using an accelerometer mounted on a lathe during the cutting process. 55

4.1 An example dataset created using the simulation method of combining the ideal sinusoidal phase shifting pattern with a normalised pseudo-random noise signal to create simulated noisy fringe projection images. 63

4.2 Simulated results for the effects of vibration on fringe projection measurements, which shows increasing the amplitude of vibration causes an increase in the measured phase error, with a sharp increase in error seen when the amplitude exceeds the size of the phase shifts between patterns leading to phase unwrapping errors illustrated by the dashed line. 63

4.3 Schema and picture of the camera vibrating isolated experimental setup using an (a) iCODIS G1 pico projector (b) Raspberry Pi 2 with an 8 MP camera module, and (c) Smart Shaker K2007E01 which provides the vibration to the setup 64

4.4 Schema and picture of the projector vibrating isolated experimental setup using an (a) iCODIS G1 pico projector (b) Raspberry Pi 2 with an 8 MP camera module, and (c) Smart Shaker K2007E01 which provides the vibration to the setup 65

4.5 Schema and picture of the combined vibrating experimental setup using an (a) iCODIS G1 pico projector (b) Raspberry Pi 2 with an 8 MP camera module, and (c) Smart Shaker K2007E01 which provides the vibration to the setup 65

4.6 Frequency response of both the isolated configuration and the combined configuration to varying vibration frequencies applied to the system, used to identify the natural frequency of the experimental setups. 67

4.7 Experimental results showing, increasing the amplitude of vibration on three experimental fringe projection setups causes an increase in mean measurement error. 68
4.8 Breakdown of the individual steps used in the design process to produce the multi-view fringe projection mechanical system. 70
4.9 CAD representation of the first concept ('individual posts') proposed as a design solution for the multi-view fringe projection system. 72
4.10 CAD representation of the second concept ('rectangular item cage') proposed as a design solution for the multi-view fringe projection system. 74
4.11 CAD representation of the third concept ('one-piece frame') proposed as a design solution for the multi-view fringe projection system. 76
4.12 CAD representation of the fourth concept ('circular arcs frame') proposed as a design solution for the multi-view fringe projection system. 78
4.13 CAD representation of the fifth concept ('linkage cage') proposed as a design solution for the multi-view fringe projection system. 80
4.14 Heat map of the maximum deformation on a 60 mm $\times$ 60 mm aluminium extrusion profile showing how the excitation force applied to the middle of the strut propagates around the part. 84
4.15 CAD model of the final multi-view frame design, using 60 mm $\times$ 60 mm aluminium profile for the vertical posts, and 60 mm $\times$ 30 mm aluminium extrusion for the horizontal beams, based on the results of the FEA simulations. 86
4.16 Experimental setup to characterise the excitation that the DSLR camera inputs into the metrology frame, using a triaxial accelerometer to measure the acceleration when capturing images. 87

4.17 Camera excitation characterisation results, the averaged peak-to-peak response in each of the x, y and z axes, is plotted against log of changing exposure time, and shows that the response of the camera is increased at smaller exposure times but the exposure time negligible effect at the longer exposure times. 88

4.18 Heat map results, (a) isometric view and (b) side view, of the maximum deformation on the complete frame assembly with the camera excitation applied to the frame in the z-axis, showing how the camera excitation in the middle of the horizontal strut would propagate around the structure. 89

4.19 ANSYS simulation results for the frequency response of the full frame assembly, which shows the largest response and natural frequency of the system is at 360 Hz. 90

4.20 CAD scehmatic of the camera mount design that was used in the multi-view fringe projection system. 92

4.21 Multi-view fringe projection camera mount, designed to provide adjustability in the pitch and yaw axes of rotation. (a) Side on view and (b) front on view. 93

4.22 CAD scehmatic of the projector mount design that was used in the multi-view fringe projection system. 93

4.23 Multi-view fringe projection projector mount, designed to provide adjustability in the pitch and yaw axes of rotation. (a) Side on view and (b) front on view. 94

4.24 Final design of the multi-view fringe projection frame, mounted on an optical breadboard and vibration isolation support frame, with two sets of cameras and projectors. 94

5.1 Schematic diagram depicting the key elements of a proximity sensor. 99

5.2 Schematic diagram depicting the key elements of a velocity transducer. . . 100

5.3 Schematic diagram depicting the key elements of a laser vibrometer. 101

5.4 The experimental setup used to investigate the proposed acceleration to velocity/displacement conversion methods, using a piezoelectric accelerometer, digital oscilloscope and surface transducer. A laser vibrometer was used to verify the behaviour of the surface transducer and the measured accelerometer data. 109

5.5 Discrete sample dataset of the raw z-axis acceleration data measured using the piezoelectric accelerometer mounted on the surface transducer generating a 200 Hz sinusoidal signal. 110

5.6 The velocity dataset obtained using the raw measured z-axis acceleration data of a 200 Hz sinusoidal signal and the integration method to convert to velocity. 111

5.7 The displacement dataset obtained using the raw measured z-axis acceleration data of a 200 Hz sinusoidal signal and the double integration method to convert to displacement. 112

5.8 The measured acceleration data after the bias (red line) has been removed and a Butterworth passband filter of 30 Hz to 1600 Hz has been applied to the measured accelerometer z-axis data. 114

5.9 The velocity data obtained using the integration method and the acceleration data with the bias removed and the Butterworth filter applied. 115

5.10 The displacement data obtained using the double integration method and the acceleration data with the bias removed and the Butterworth filter applied. . 116

5.11 The velocity data obtained using the omega arithmetic method to convert the acceleration data with a Butterworth filter applied. 117

5.12 The displacement data obtained using the omega arithmetic method to convert the acceleration data with a Butterworth filter applied. 118

5.13 Frequency response experiment on the full frame, applying an excitation in the z-axis with the frequency varied from 20 Hz to 700 Hz, in steps of 20 Hz to study the natural frequency of the frame, which is at $\sim$320 Hz. 120
5.14 Key locations identified around the multi-view frame to study the vibrational response of the system in both a non-excited and camera excited state. . . . 121
5.15 Full frame three axis characterisation results in 5 key positions with no excitation applied to the frame. 122
5.16 Full frame three axis characterisation results in 5 key positions with the frame excited by a DSLR camera. 123
5.17 The frequency response of the background vibration used to identify the different components of the signal, such as excitation from motorised equipment, machinery and road traffic. 125
5.18 The experimental setup using the Polytec portable digital laser vibrometer (PDV-100) to characterise the multi-view fringe projection mechanical system in order to verify the measured accelerometer results. 126
5.19 Average characterisation results using a triaxial accelerometer to compare the excitation of the different camera and projector mounts used in the multi-view fringe projection setup, as well as assess the ability of the characterisation method to identify a mechanical fault in the system I.E. the mounts not being fastened properly. 129

6.1 The developed multi-accelerometer live monitoring system, which includes six triaxial IEPE accelereometers, a CompactRIO-9022 controller, with an eight module slot chassis attached and six NI-9230 vibration and sound modules integrated. 133

6.2 Top-level programme function flowchart of the designed target VI, which is compiled onboard the cRIO, to collect and stream the accelerometer data to the host VI. 135

6.3 Top-level programme function flowchart of the designed host VI which is executed on the main computer and communicates and reads the accelerometer data from the target VI on the cRIO. The Host VI uses the producer-consumer architecture to read and process data efficiently. 136

6.4 The event analysis plot to investigate the dynamic behaviour around the area of interest, which is identified by the peak above the user defined threshold (dashed line), with the peak-to-peak analysis also illustrated. 141

6.5 Front panel LabVIEW display of the multi-accelerometer host VI, which allows the user to control the system and view the measurement results. . . 142

6.6 Live acceleration results for the z-axis for each of the six accelerometers allowing the user to immediately see any changes to the dynamics of the system. 143

6.7 Displacement results for the three channels that have been identified to have the largest average responses in the system within the time window analysed, which was 5 seconds in the example shown. 144

6.8 Frequency responses of the three channels identified to have the largest average responses in the system within the time window analysed, which was 5 seconds in the example and shows a dominant excitation input with a frequency of 400 Hz. 144

6.9 3D stacked ribbon plot of the displacement envelope results for all 18 measurement signals (x, y and z axes for each accelerometer) with the key events that are identified to be of interest and so further analysed. 145

6.10 Schema of the experimental configuration showing the key components of a lathe, and the accelerometer mounting positions for the condition monitoring investigation into the effects of the depth of cut and tool wear. 147

6.11 Example measured vibration dataset in the z-axis, collected whilst performing a 2.0 mm depth of cut on a CNC lathe using a new cutting tip. 148

6.12 Example frequency response analysis plot of the measured vibration dataset collected whilst performing a 2.0 mm depth of cut on a CNC lathe using a new cutting tip, showing the largest response at 10 Hz, which matches the frequency of the spindle. 149

6.13 Vibration results in the x-axis for the effect of increasing depth of cut and tool wear, showing the vibration increases that can be measured as the cutting tip progressively wears to predict tool failure. 149

6.14 Vibration results in the y-axis for the effect of increasing depth of cut and tool wear, showing the vibration increases that can be measured as the cutting tip progressively wears to predict tool failure. 150

6.15 Vibration results in the z-axis for the effect of increasing depth of cut and tool wear, showing the vibration increases that can be measured as the cutting tip progressively wears to predict tool failure. 151

6.16 Example of an 'event' identified by the event analysis tool, as the measured signal exceeds the user defined thresholds (dashed lines). In this example, the 'event' is as a result of the brake being applied to stop the spindle after the cutting process has finished. 152

7.1 Schema of the experimental setup using the GOM ATOS Core 300, a triaxial accelerometer and a Smart Shaker K2007E01 to investigate the sensitivity of a commercial fringe projection system to vibration. 157

7.2 A plot of increasing the amplitude of vibration in the *x*-axis against the mean cloud-to-cloud measurement error showing a sharp increase in the linear trend between the red and green dashed lines, which is due to the significant measurement errors seen around the edges of the complex features on the artefact. The blue dashed line shows the defined acceptable measurement threshold at the point the trends change. 160

7.3 A plot of increasing the amplitude of vibration in the *x*-axis against the sphere probing error (mean between the positive and negative) of a fitted sphere to the ball of the ball bar fixture on the AM artefact, shows how fringe projection measurements deteriorate on complex features as the vibration levels increase. 161

7.4 Heat map of the cloud-to-cloud error analysis for 0.10 V vibration input of the shaker in the *x*-axis, showing the random distribution of errors across the measurement artefact. 162

7.5 Heat map of the cloud-to-cloud error analysis for 0.25 V vibration input of the shaker in the *x*-axis, showing the large measurement errors around the edges of the complex shapes on the AM artefact, i.e. the large sphere due to the triangulation errors caused by vibration. 163

7.6 A plot of increasing the amplitude of vibration in the *y*-axis against the mean cloud-to-cloud measurement error showing a sharp increase in the linear trend between the red and green dashed lines, which is due to the significant measurement errors seen around the edges of the complex features on the artefact. The blue dashed line shows the defined acceptable measurement threshold at the point the trends change. 165

7.7 A plot of increasing the amplitude of vibration in the *y*-axis against the sphere probing error (mean between the positive and negative) of a fitted sphere to the ball of the ball bar fixture on the AM artefact, shows how fringe projection measurement deteriorate on complex features as the vibration levels increase. 166

7.8 A plot of increasing the amplitude of vibration in the *z*-axis against the mean point-to-point measurement error shows the measurement errors increase but is less sensitive to vibration in this axis compared to the *x* and *y* axes, and does not see the same complex shape measurement errors. The blue dashed line shows the defined acceptable measurement threshold at the point the error trend increases. 168

7.9 A plot of increasing the amplitude of vibration in the *z*-axis against the sphere probing error (mean between the positive and negative) of a fitted sphere to the ball of the ball bar fixture on the AM artefact, shows the trend of the sphere probing errors in the *z* does not match the increasing measurement error trend as it does in the *x* and *y* axes. 169

7.10 Schema of the experimental setup using the developed multi-view fringe projection system, four triaxial accelerometers and a Smart Shaker K2007E01 to benchmark the system and investigate the measurement sensitivity to vibration, as well as demonstrate the use of multi-point condition monitoring. 172

7.11 A plot of increasing the amplitude of vibration in the *x*-axis against the mean cloud-to-cloud measurement error shows a significant rise in measurement errors as the captured images are increasingly blurred. 173

7.12 A plot of increasing the amplitude of vibration in the *x*-axis against the sphere probing error (mean between the positive and negative) of a fitted sphere to the ball of the ball bar fixture on the AM artefact, shows the sphere probing error trend does not match the increasing measurement error. 174
7.13 Heat map of the cloud-to-cloud error analysis for 0 V (baseline) vibration input of the shaker in the *x*-axis, showing the structured modulation errors across the measurement artefact. 175
7.14 Heat map of the cloud-to-cloud error analysis for 0.35 V vibration input of the shaker in the *x*-axis, showing the large measurement errors around the edges of the artefact due to the 'over-smoothing' effect. 176
7.15 A plot of increasing the amplitude of vibration in the *y*-axis against the mean cloud-to-cloud measurement error shows a significant rise in measurement errors as the captured images are increasingly blurred. 178
7.16 A plot of increasing the amplitude of vibration in the *y*-axis against the sphere probing error (mean between the positive and negative) of a fitted sphere to the ball of the ball bar fixture on the AM artefact, shows the sphere probing error trend does not match the increasing measurement error. 179
7.17 A plot of increasing the amplitude of vibration in the *z*-axis against the mean cloud-to-cloud measurement error shows a significant rise in measurement errors as the captured images are increasingly blurred. 180
7.18 A plot of increasing the amplitude of vibration in the *z*-axis against the sphere probing error (mean between the positive and negative) of a fitted sphere to the ball of the ball bar fixture on the AM artefact, shows the sphere probing error trend does not match the increasing measurement error. 181

7.19 Demonstrating the importance of condition monitoring in measurement systems, by showing an example of the different measurement errors (cloud-to-cloud) that could be experienced by each camera-projector pair in the multi-view fringe projection system due to the varying vibrations seen across the measurement frame. 184

List of tables

4.1 Advantages and disdvantages of design concept 1 - individual posts used to evaluate the design for the multi-view fringe projection mechanical frame. . 73

4.2 Advantages and disdvantages of design concept 2 - rectangular item cage used to evaluate the design for the multi-view fringe projection mechanical frame. 75

4.3 Advantages and disdvantages of design concept 3 - one-piece frame used to evaluate the design for the multi-view fringe projection mechanical frame. . 77

4.4 Advantages and disdvantages of design concept 4 - circular arcs frame used to evaluate the design for the multi-view fringe projection mechanical frame. 79

4.5 Advantages and disdvantages of design concept 5 - linkage cage used to evaluate the design for the multi-view fringe projection mechanical frame. . 81

4.6 Design concepts evaluation matrix. 82

4.7 ANSYS aluminium extrusion simulation results investigating the viability of the different profiles to provide the required stability for the proposed multi-view fringe projection system. 84

4.8 ANSYS simulation results for the full frame assembly with the forces applied in the x, y and z axes. 90

5.1 Comparison of the specifications of the available commercial vibration sensors. 103

5.2 Meggitt Endevco 65L-100 accelerometer specifications 105

5.3 Average characterisation response in multiple axes in each of the key identified positions on the designed multi-view fringe projection frame. 122

5.4 Average characterisation results using the laser vibrometer in the x, y and z axes at position 4 on the multi-view frame, in order compare with and verify the accelerometer characterisation results. 127

5.5 Average characterisation response in multiple axes for the direct camera mount, the adjustable camera mount fastened properly, and the pitch mechanism of the adjustable camera mount left loose/unfastened on the designed multi-view fringe projection frame. 128

6.1 CNC lathe settings used in the experimental condition monitoring experiments. 148

7.1 GOM ATOS core 300 fringe projection system specifications 156

7.2 The measurement error results using a commercial fringe projection system with the vibration applied in the x-axis. 159

7.3 The measurement error results using a commercial fringe projection system with the vibration applied in the y-axis. 165

7.4 The measurement error results using a commercial fringe projection system with the vibration applied in the z-axis. 168

7.5 The measurement error results using the multi-view fringe projection system with the vibration applied in the x-axis. 172

7.6 The measurement error results using the multi-view fringe projection system with the vibration applied in the y-axis. 177

7.7 The measurement error results using the multi-view fringe projection system with the vibration applied in the z-axis. 178

7.8 The vibration measured for each axis, with the shaker vibration applied to the same axis of measurement, at multiple positions on the developed multi-view fringe projection frame. 183

Nomenclature

Acronyms

AM	Additive manufacturing
C2C	Cloud-to-cloud
CAD	Computer aided design
CCD	Charged couple device
CMM	Coordinate measuring machine
CNC	Computer numerical control
DoF	Depth of field
DSLR	Digital single-lens reflex
EoM	Ease of manufacture
FEA	Finite element analysis
FFT	Fast Fourier transform
FIFO	First-in-first-out
FPGA	Field programmable gate array

FR	Frequency response
ICP	Iterative closest point
IEPE	Integrated electronics piezo-electric
LED	Light emitting diode
NI	National instruments
NIST	National Institute of Standards and Technology
PSD	Power spectral density
PSF	Point spread function
RAM	Random access memory
SHM	Structural health monitoring
SNR	Signal-to-noise ratio
STL	Standard tessellation language
TDMS	Technical data management streaming
USB	Universal serial bus
VI	Virtual instrument

Symbols

λ	Light wavelength
μ	The mean
ω	Angular velocity

σ	Standard deviation
a	Acceleration
C	Circle of confusion
d	Depth of field
f	Frequency
g	Grey value (0 to 255)
M	Magnification
N	The f-number of the lens
r	Rayleigh criterion
t	Time
v	Velocity
x	displacement

Chapter 1

Introduction

1.1 Background and motivation

Metrology is one of the most fundamental sciences and underpins the work carried out in engineering research and industry, and yet it is a commonly misunderstood and overlooked science. In the simplest terms, metrology is defined as "the science and application of measurement" [2], and is derived from the Greek word for measure. However, metrology goes much further than simply taking a measurement, and covers all of the theoretical and practical aspects of the measurement. Metrology broadly encompasses a range of measurement areas, including: the correctness of any measurement in the accuracy, uncertainty and potential errors; providing the international standards for units and values of scientific constants (i.e. defining the units like length (m), mass (kg), time (s) and constants such as the universal gas constant); developing new methods of measurement as well as validating and improving current methods. In the manufacturing industry length measurement is of particular importance, and has the SI unit of the metre. The metre is defined by taking the fixed numerical value of the speed of light in a vacuum to be (299 792 458 ms^{-1}) when expressed in the unit ms^{-1}, where the second is defined in terms of the caesium frequency Δv_{Cs} [3]. Practically, the metre is realised from the wavelength of radiation from an iodine-

stabilised helium neon laser, which emits at ∼633 nm and has an uncertainty of 2 parts per 10^{11}. For a more extensive overview of the research areas encompassed in the field of metrology but not involved in this thesis, the reader is directed to [4], which gives a more in-depth overview of the field of metrology. For a complete discussion of the other six SI units see [3]. The key concepts and purpose of metrology are briefly discussed here.

Metrology plays a vital role in all scientific work, whether research, academic or industrial, as it provides a number of essential features to modern manufacturing of parts [5–8] including:

- Traceability, is a core concept in metrology and is defined as the property of the result of a measurement whereby it can be related to stated references, usually national or international standards, through a documented unbroken chain of comparisons all having stated uncertainties [2]. The concept of traceability is illustrated in figure 1.1.

- Reliability, repeatability and accuracy. Engineering parts are designed in terms of fit, function and form and so effective application of metrology enables consistent and accurate production of parts within the specified tolerances, thus ensuring the quality of the manufactured parts and minimising scrap parts and/or wastage due to inaccurate parts.

- Process control, ensures that the manufacturing and inspection processes are working properly producing high quality parts, aiding calibration and tolerancing of all the equipment being used, and so uncertainties can be calculated. It is important that all aspects of the process are identified, monitored and controlled if necessary including environmental conditions such as considering temperature, vibration, dust and lot of other potential hostile factors.

- Post-processing troubleshooting, metrology is very useful tool in aiding the detection of manufacturing errors. Repetitive errors in parts can indicate a fault in the manufacturing

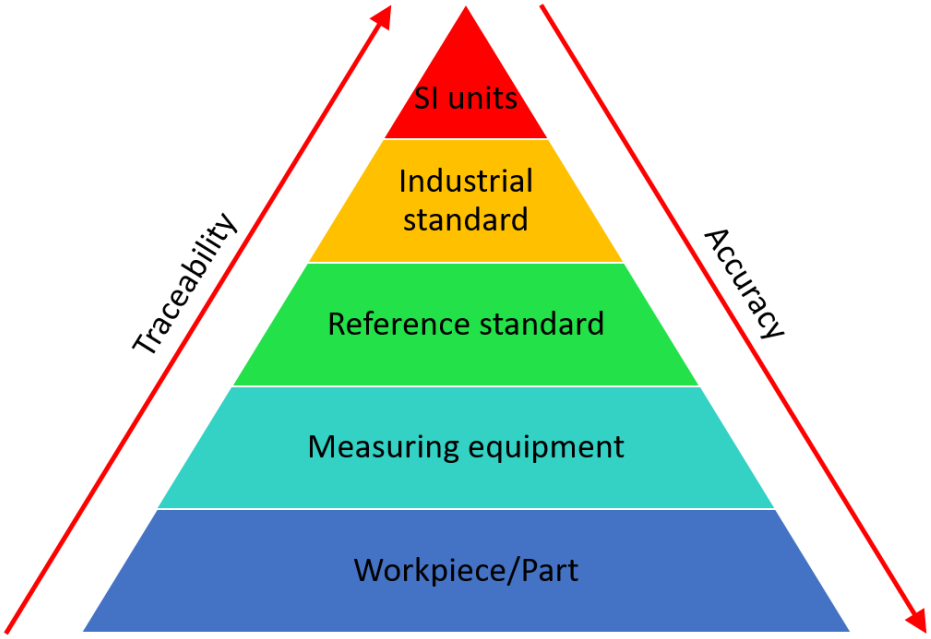


Figure. 1.1 The traceability pyramid. In order to ensure traceability is transferred between each level by calibration, and creates a traceable unbroken chain from the measured part to the definition of the SI unit.

machine, and using effective metrology to further inspect the part, it is possible to identify the source of the fault.

- Reverse engineering, of parts is made increasingly simple with the use of metrology.

Traceability is a fundamental concept of metrology, and an essential step in the manufacturing process to ensure that parts meet their specification and will function as designed. However, measuring the dimensional accuracy of a part goes beyond simply picking up a pair of callipers and measuring the distance between two faces. Each measurement will have an associated measurement uncertainty, which requires a complex procedure to estimate [9], as well as the measurement itself must be 'traceable' back to the definition of the metre. The traceability chain, which illustrates how the measurement is traced back to the definition of the SI unit, has been shown in figure 1.1 [10].

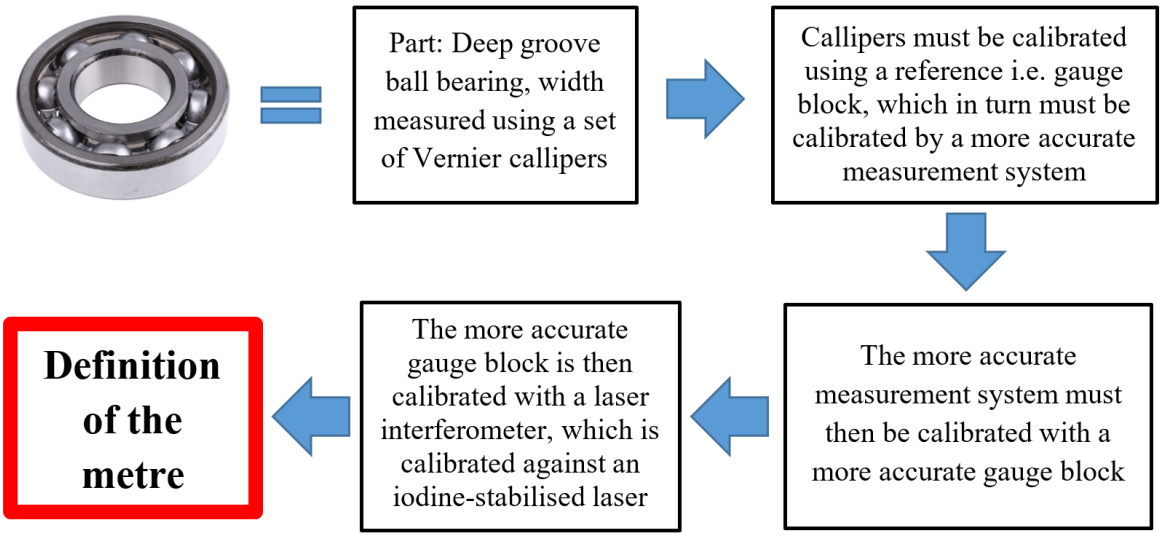


Figure. 1.2 Practical example of the traceability chain applied to a length measurement of the width of a ball bearing part.

A practical example of a length measurement for the width of a deep groove ball bearing has been considered and demonstrated in figure 1.2, and shows how a measurement on the manufacturing shop floor is traced back to the definition of the metre.

In addition to performing the measurement properly, the environment must also be controlled as changes in temperature can cause dimensional variations i.e. steel can change by up to 11.6 $\mu m\,^{\circ}C^{-1}\,m^{-1}$, and so any dimensional measurements taken are only valid at the temperature at which the measurement were taken. This example illustrates the level of metrology application that is required to enable effective and accurate manufacture and shows the process control that is required throughout the development of the part.

Additive manufacturing (AM) is defined as the "process of joining materials to make parts from 3D model data, usually layer upon layer, as opposed to subtractive manufacturing and formative manufacturing methodologies" [11]. AM has gained significant traction in the manufacturing industry in recent years due to the complex geometries and internal features that can be produced. However, it is the concepts of traceability and part checking for repeatability and accuracy that are currently major limitations to the progression and widespread adoption of AM techniques [12]. In order for AM to be more widely embraced

by engineering industries, such as aerospace or aeronautical industries, which have stringent part specifications, AM needs improved measurement systems and process control to provide traceability and increase confidence that AM technologies can produce repeatable parts which meet the tight tolerances required and perform as specified. AM machines have a limited build volume, and are unable to employ traditional assembly-line manufacture/assembly to scale up production. As a result, in order to increase production, multiple machines are used in conjunction with each other on the same manufacturing floor. Each machine can be considered as being an independent manufacturing process or manufacturing line, and so needs process feedback. Therefore, the application and continued advancement of metrology is vital in enabling AM machines to be used in production simultaneously, to allow for comparison of the parts produced, and ensuring the design specifications, tolerances and surface finishes are met.

AM has been widely publicised for its numerous advantages and has been predicted to completely revolutionise the manufacturing industry or bring about the "third industrial revolution" according to a number of publications [13–16]. There is an extensive list of advantages of AM, some of which are not fully supported. The widely accepted advantages of AM [17–23] can be summarised as follows:

- Design freedom: The most publicised advantage of AM is that it offers very few design constraints, and so relatively speaking anything you can design in 3D computer aided design (CAD) software packages, you can create with AM.

- Reduced waste: As AM adds material layer by layer as it builds the part, it only uses the material that is needed so there is very little material wasted, especially when compared to traditional machining which starts with a bigger block than the part desired, and subtracts material to form the designed part.

- Small lead time and no tooling costs: You can create a prototype with AM immediately once the design is finished and converted into an STL file, no specialist tooling or fix-

tures like those in traditional machining are required. So additional costs and excessive lead times are avoided, meaning testing on the part can commence immediately rather than waiting for weeks for the part to come in.

- Complexity reduces costs: It costs less to print an AM part with internal lattice structures than the solid material alternative part that traditional subtractive manufacturing can produce. Lattices and other complex structures can significantly reduce the material required, which means it is faster and cheaper to print it with AM, and so the more complex a part is the more beneficial using AM is.

- No assembly required: Using AM it is possible for moving parts such as hinges and bicycle chains to be printed in metal directly into the product, which can significantly reduce the part numbers and the extra time required to assemble the separate parts.

- Variety and design changes are made quick and simple: Parts which require variations and/or small design changes can be quickly performed on the original CAD file and so the new parts can be made immediately.

- Minimal training and skill required for manufacturing: More complicated parts which require specific parameters and are designed for high-tech applications require professionals to operate and oversee the manufacture. Simpler parts can be made by novice users [24], for example The University of Nottingham have run outreach programmes with local primary schools allowing children to design and build their own figurines using 3D printing processes.

- Multiple materials: Engineers can design parts to have specific materials in different areas of a part in order to tailor the mechanical properties of the part based on the function it provides. This means designers have even more control over the design and can print using different materials as necessary.

As a result, AM has been the focus of numerous studies conducted by a variety of different interested sector including: government agencies [25–27], national measurement institutes [28–30], and commercial industrial groups [19, 31, 32]. The rapid growth and the potential of the AM industry was clearly illustrated in the 2016 Wohler's market report [24], which showed that the AM industry was worth over $5 billion ($5.17 billion) and stated the AM industry continued to show huge scope for growth and has the potential to change the face of the manufacturing industry.

In order for the AM industry to continue to grow, it is vital that the industry addresses the disadvantages that are currently associated with the AM processes/techniques. The current disadvantages of using AM [17–22] are:

- Slow build rates: Some AM techniques have a build rate up to 60 cubic centimetres per hour, and so traditional machining times can be significantly faster. This slower build time not only delays production time, but also increases the costs to manufacture the parts due to increased labour time.

- Limited build volume: AM parts are restricted to the size of the build chamber; currently the largest build volumes for metal parts is 800 mm $\times$ 400 mm $\times$ 500 mm, and for plastics 500 mm $\times$ 330 mm $\times$ 400 mm. In order to increase these volumes, larger machines can be bought but this incurs significant cost increases

- Expert controller/operator required: In order to produce complex, high quality and accurate parts the operator must have extensive knowledge of the chosen AM process, including features such as material design and process parameters

- Discontinuous production: AM parts are printed one at a time and so this prevents optimal economies of scale.

- Poor mechanical properties: The process can cause defects in the parts such as layering, thermal instability and balling.

- Requires post-processing: The surface finish and dimensional accuracy may be lower quality than other manufacturing methods, and so requires additional polishing and surface treatment to bring the surfaces to an acceptable quality.

- Lack of AM applicable metrology: Due to the increased design freedom the measurement systems must be able to cope with the complexities of the design, as well as cope with the different materials and surfaces that AM produces. It is also vital that AM is able to produce accurate, repeatable and traceable parts, so the parts are comparable throughout the industry.

The latter two disadvantages listed are a particular and pressing focus for the AM industry. Development of new measurement systems are vital as they will enable industry wide standards to be produced (both nationally and internationally), to ensure both comparability and traceability for all AM parts, and thus allow production to be scaled up. In conjunction with this, as AM volumes and speeds of production are increased the need to measure quickly and accurately will also increase so as not to delay production times, and so any newly designed system must be capable of meeting these demands. In large scale manufacturing, measuring the outside geometry or form of the part is essential, as it allows the manufacturer to quickly check the parts have been produced correctly. It is the pressing need for development of new measuring systems in both the AM industry and metrology field that motivates this project. This work aims to develop a new system that is capable of coping with all of the new constraints introduced by AM, as well as providing all of the necessary features required for an industry accepted measurement system i.e. high accuracy, consistent measurements and uncertainty values for any and all measurements taken. The work focuses on the development of the mechanical design of the proposed system, which includes an investigation into the mechanical performance and how the changing dynamics of the structure effect the measurement quality. In more vibration sensitive systems, the quality of the measurement is dependent upon the dynamic state of the apparatus, so it is

vital to develop new condition monitoring methods and systems that allow the mechanical performance to be constantly measured. With the aforementioned research and development needs in mind the aims and objectives for the PhD were set and have been discussed below.

1.2 Aims and objectives

1. State-of-the-art review of the literature, regarding the design and development of fringe projection systems focussing on the effects of mechanical error sources such as vibration, and the condition monitoring techniques currently applied in measurement systems.

2. Develop a mechanical design for a multi-view fringe projection system, which is capable of mounting multiple sets of cameras and projectors to enable the multi-view measurement paradigm to be investigated.

3. Enhance the understanding of the effects of mechanical errors on fringe projection measurements, by developing both a simulation and experimental methodology to assess the sensitivity of the measurement technique.

4. Develop a characterisation method to enable the measurement of the dynamic performance of the mechanical system, and provide a method to live condition monitor the mechanical performance throughout the measurement process.

5. Demonstrate the benefit of multiple point live condition monitoring for measurement systems to verify the performance and increase confidence in optical coordinate measurement systems.

1.3 Structure of the thesis

The remainder of this thesis is structured so as to achieve the objectives set out in Section 1.2. As such, the Chapters presented here will flow as follows.

- Chapter 2 presents the state-of-the-art review, which was carried out to identify the key knowledge gaps in the field, and to set the aims and objectives for the PhD to address. The first section of review investigates the different available form measurement techniques in order to identify an appropriate technique for the proposed measurement system. The review then gives a discussion of the potential error sources in the proposed measurement technique, and assesses the mechanical designs of current commercial and laboratory fringe projection systems. Finally, the methodology and benefits of effective condition monitoring are reviewed, in attempt to utilise the principles in measurement system applications.

- Chapter 3 gives an overview of the methodology applied to this thesis, which includes an explanation of the main research steps used, as well as a breakdown of the all of the software and hardware utilised throughout the project.

- Chapter 4 is a complete design history of the development of the multi-view fringe projection frame. The chapter begins by explaining the experimental investigations carried out in order to better define mechanical performance metrics in the statement of requirements for the design. The chapter then systematically details the design process and techniques used to progress from the initial design concepts to the final design stage, and finally how proof of concept was shown before manufacture and assembly of the multi-view fringe projection frame.

- Chapter 5 describes the experimental characterisation work and results that was performed in order to verify the finite element analysis simulation results for the final

multi-view fringe projection design. This chapter also includes a review of available vibration sensors, the development of the accelerometer characterisation method and a comparative study to establish the optimal acceleration to velocity/displacement conversion method.

- Chapter 6 details the development of the live multi-point vibration monitoring setup, this includes a full breakdown of the functions and analysis available in the system, and how the system was designed to be a flexible so that it could be used for a variety of setups. The chapter explains the challenges that were faced to combine multiple triaxial accelerometers, and process large amounts of data simultaneously in real time.

- Chapter 7 details the experimental case studies that were performed to investigate the application of the developed live vibration monitoring system integrated with two different measurement systems. The two measurement systems used were both developed in-house and are a multi-view fringe system and a photogrammetry system. The study detailed in this chapter also investigated the sensitivity to vibration noise of each measurement system.

- Chapter 8 gives a summary of the main findings of the thesis, highlighting the contribution of the PhD to the development of a multi-view fringe projection system and the live structural vibration monitoring system. The chapter then discusses the potential future work to further improve on the system, and how the gaps identified in the literature review could be continued to be addressed.

Chapter 2

State-of-the-art review

2.1 Introduction

In this chapter, a state-of-the-art review is presented which was carried out to identify the key knowledge gaps in the field, and set objectives around these research areas for the PhD to address. The first section of review investigates the different available form measurement techniques in order to identify an appropriate technique for the proposed multi-view system. The ideal measurement technique needed to show potential for measuring AM components and have scope for further research. The review then gives a discussion of the potential error sources in fringe projection measurements, with a focus on the research to understand and eliminate/minimise each error source. To aid the design of the proposed measurement system, the mechanical designs of current commercial and laboratory fringe projection systems are reviewed, to allow the advantages and disadvantages to be evaluated, and to apply the findings to the design of the proposed measurement system design. Finally, the methodology and benefits of effective condition monitoring are reviewed, in attempt to utilise the principles in measurement system applications, in the first instance for the proposed multi-view fringe projection system.

2.2 Measurement techniques

The range of commercially available measurement systems can be grouped into two main categories based on the method they use to perform measurements. The first group are known as contact methods, which are based on systems which measure using touch probe or stylus which contact the surface of the part in order to measure the x, y and z coordinates of each point. The second group of measurement systems are called non-contact methods, which take measurements using optical systems (such as cameras) to capture the surface data and height information, examples include laser scanners, photogrammetry and fringe projection.

2.2.1 Contact form measurement techniques

The first touch probe based measurement system was invented in 1959 by Ferranti [33], and are commonly referred to as coordinate measuring machines (CMMs). Contact methods measure the geometry of a part by touching the probe at several discrete points around the part and use the machines motion to find the x, y and z coordinates of each point to build up a 3D point cloud. The parts geometry can then be reconstructed using the 3D point cloud, so that key features can be measured. The probe can be operated manually by the user or automatically by a robot arm or CMM. More recently, scanning probes have been developed which keep the stylus in contact with the surface and traverse over the geometry to scan a line of points to increase the measurement speed and point cloud density. Scanning probes can be either active, which use control software to stay in contact with the surface, or passive, which follow a predefined path regardless of the detected surface geometry. Traditionally modern CMMs are designed with a gantry or bridge style structure with a 3-axis motion stage and a indexing head which enables CMMs to have 5-axis of motion for flexibility and improved dynamic performance. CMMs are able to measure a wide range of parts reliably and accurately and so are widely used in industry [33]. There are a number of commercial systems available for both large and small-scale measurements. An example of a large-scale



Figure. 2.1 Example of an (a) large-scale CMM from Leitz and (b) a small-scale CMM from Zeiss

measurement system is the Leitz PMM-G (2.1a), which has a measurement volume up to 7 m $\times$ 4 m $\times$ 3 m and a maximum permissible error (MPE) of 3.6 µm [34]. The Zeiss F25 CMM (2.1b) is a small-scale system, which has a measurement volume of 0.1 m $\times$ 0.1 m $\times$ 0.1 m and a MPE of 250 nm [35]. However, whilst CMM speeds have improved in recent years, they still require the stylus to touch every measured point on the surface, and so the technique can take a significant amount of time to measure a sufficiently dense point cloud to reconstruct the complete form of a part. In addition to this, the probe/stylus scratches the surface of the parts as they traverse and measure along the part's surface, which can be highly detrimental in certain applications.

2.2.2 Non-contact measurement systems

The second group of measurement techniques is non-contact methods, which are still relatively new in comparison to contact methods. The focus of the multi-view system was on

fringe projection techniques, however other optical based coordinate measuring techniques were considered, and so the principles and accuracies of each are briefly discussed.

2.2.2.1 Laser scanning

There are two different types of laser scanners with different working principles, which are time-of-flight and triangulation. Time-of-flight measures the elapsed time between a projected pulse of light and its detection after reflection from the target, and uses the measured time to calculate the distance to the target [36]. Time-of-flight techniques are a widely used technique for long-distance and large scale measurements such as surveying [37] and military range finding applications [38]. The accuracy of the measurement is highly dependent on the resolution of the electronics used to measure the time elapsed. Time-of-flight techniques currently offer distance measurement accuracies of the order of 500 μm at a measurement distance of 5 m [39].

Laser triangulation uses the laser light source, the measured point on the object surface, and the reflected laser spot on the receiving sensor to use trigonometry to calculate the height information and reconstruct the surface of the part. The experimental configuration for laser scanning has been shown in figure 2.2. As the laser, sensor positions and angle between them are known, the distance to the surface can be calculated. Laser triangulation is widely used in industry for part inspection and reverse engineering [40]. The measurement range of commercialised laser triangulation systems is 40 mm to 650 mm, with accuracies up to 10 μm [41]. However, a complicated scanning system is required in order to achieve full form measurement and the measurement speed is relatively slow compared with other optical form techniques, as it measures a single point at a time. To increase the measurement speeds, laser line scanners have been developed, but these are still significantly slower than other optical techniques such as photogrammetry and fringe projection.

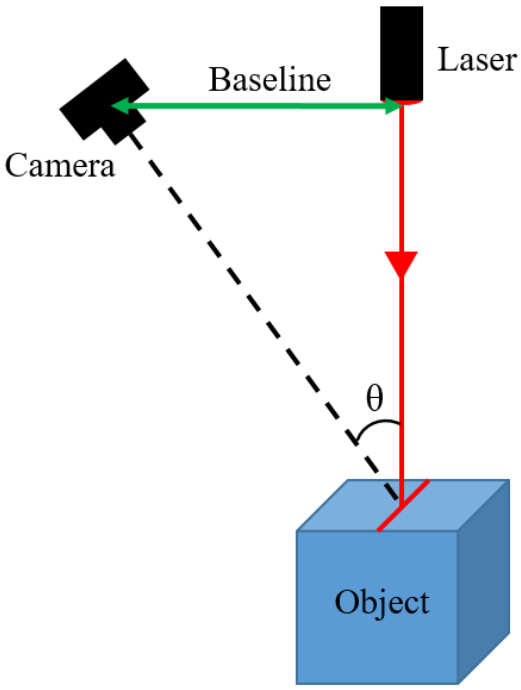


Figure. 2.2 The experimental configuration for laser scanning, which uses a laser and camera, and the principle of triangulation to measure the height of each point on the objects surface.

2.2.2.2 Photogrammetry

Photogrammetry is a measurement technique that uses multiple photographs to measure the form of a part, and is based on the principle of stereovision. Photogrammetry uses a minimum of two cameras to capture multiple images from different views and triangulation between common points to calculate the distance of points on the surface. The baseline is calculated as the distance between the two camera sensors, with common points in the two captured camera images used to triangulate the position of each point. The experimental configuration for photogrammetry has been shown in figure 2.3. Due to its simplicity, photogrammetry has been a popular measurement technique since photography was invented in the 1830's [42]. Photogrammetry relies on the ability to find correspondence between images, and so may require the use of retroreflectors or laser speckle [43] in order to measure optically smooth parts. Photogrammetry can measure millions of points per image and only requires

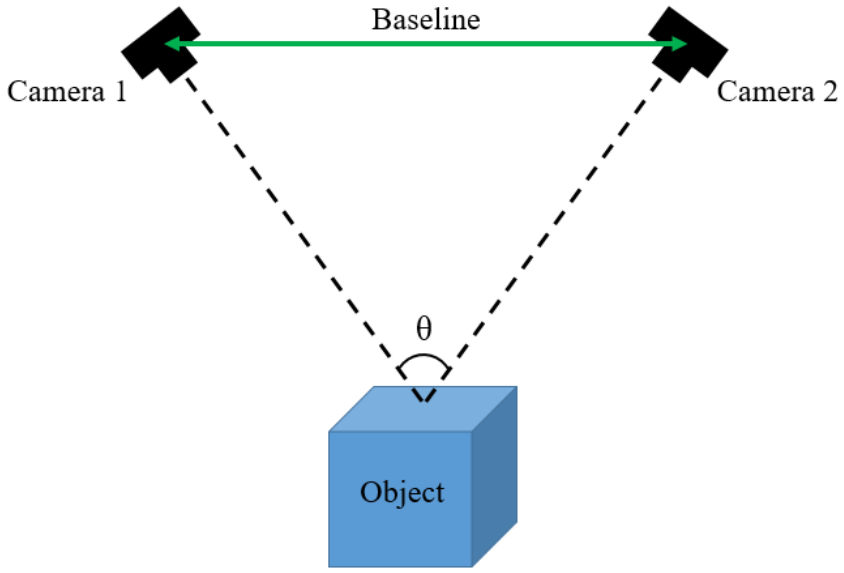


Figure. 2.3 The experimental configuration for photogrammetry, which uses two cameras to measures the form of an object by finding correspondence between the two captured images and triangulation to find the height of each point.

two cameras, and so offers a fast low-cost metrology solution, which is used in industry for high precision inspection [44]. Photogrammetry accuracies are dependent on measurement volume, whilst it has been shown micron accuracy can be achieved for small measurement volumes. Commercial systems such as the Geodetic Systems' V-STARS provide accuracies in the region of 5 μm [44] for a measurement volume of 150 mm × 150 mm × 125 mm.

2.2.2.3 Interferometry

The first interferometer was developed by Albert A. Michelson [45] in 1887, and the working principle of his system is still used in modern interferometry systems. Interferometry works by splitting a coherent laser beam into two separate beams, which are propagated along different paths. The measurement beam reflects of the sample and is superimposed with the reference beam. If there is any difference in the length of path travelled between the measurement and reference beams it will create an interference pattern which is seen by the photodetector. The interference patterns are analysed using phase shifting methods or

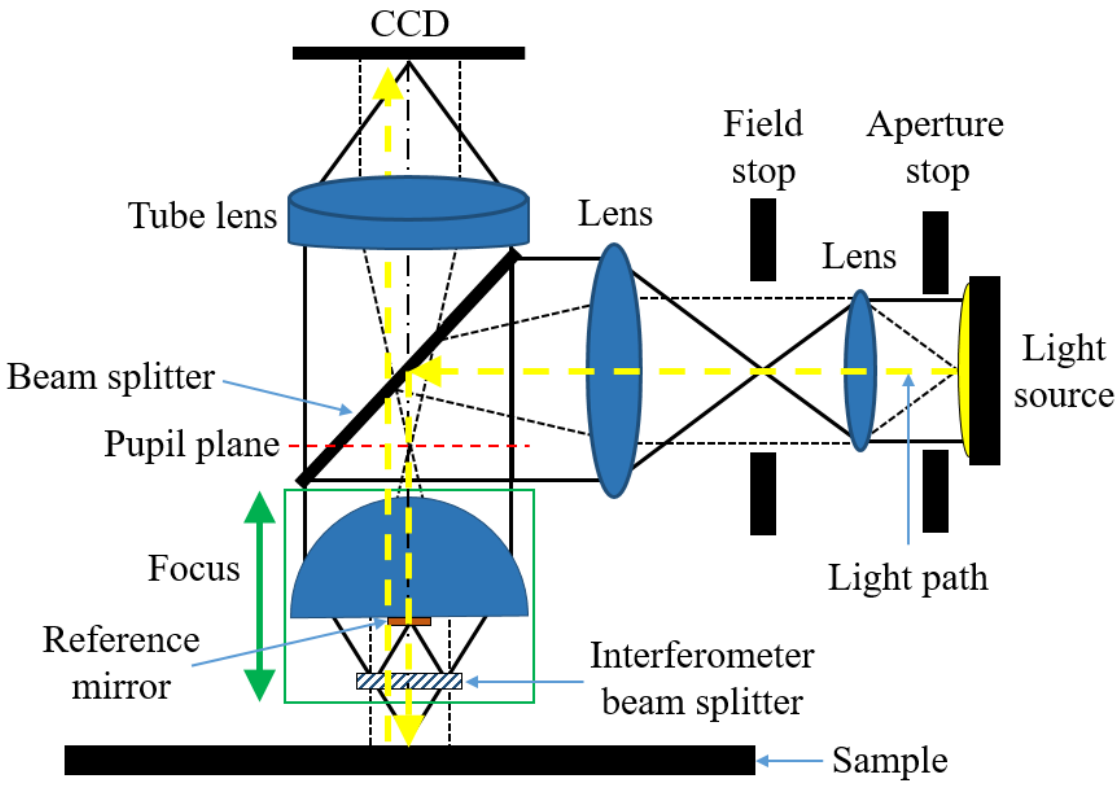


Figure. 2.4 The experimental configuration for interferometry, which reconstructs the object's surface by analysing the interference pattern created when the reference beam and measurement beam are superimposed.

Fourier transform methods to obtain the phase map and from that, the reconstructed surface topography [46]. The experimental configuration for interferometry has been shown in figure 2.4. Interferometers are widely used for very high accuracy small-scale measurements of optical components such as the surfaces of lenses and mirrors. Commercially available systems such as Fizeau interferometer, provide accuracies in the region of 30 nm and a repeatability standard deviation of less than 1 nm [47].

2.2.2.4 Moiré fringes

Moiré techniques are mostly of historical interest but were much more prevalent before the proliferation of digital cameras and computers allowed for fringe analysis techniques to become more straightforward. Moiré fringes acquire the contour of the object surface by

using a moiré interference pattern, which is created by varying the angle between two grating patterns of equal spacing, or two patterns with different periods [48]. The moiré method includes two kinds of techniques, which are shadow moiré and projection moiré. Shadow moiré uses a single grating placed over the object and utilizes the superimposition of a master grating and its own shadow to measure the geometric contours of the part [49]. A single grating is illuminated using a point light source over the object, and viewed through the same grating. The observed fringe spacing on the object is related to the distance between the reference grating and the objects surface, and so the form of the part can be measured from the captured moiré images.

Projection moiré technique projects a grating onto the object surface, and then observes the object through a second grating from a different point of view, which creates a moiré pattern that can be used to extract the surface form of the object [50, 51]. The experimental configuration for Moiré fringe techniques has been shown in figure 2.5. An advantage of projection moiré compared to shadow moiré is that the gratings can be much further away from the objects surface. Both moiré techniques analyse the contours of the fringes produced to obtain the height information of the object. It is also possible to apply phase shifting techniques to extract the heights, but the accuracy and spatial resolution are compromised due to the need to filter out the high frequency carrier. Phase shifting moiré methods have a measurement range of 1 mm to 500 mm, and a $1/10$ to $1/100$ of a fringe, which in the case of Mauvoisin et al. [49] was an accuracy of $\sim$10 µm.

2.2.2.5 Fringe projection

Fringe projection represents an important branch of optical measurement techniques, and shows huge potential for wider application in the manufacturing industry for both subtractive machining as well as AM [52]. Fringe projection techniques are based on projecting a unique coded light pattern onto the object and capturing the projected patterns using a

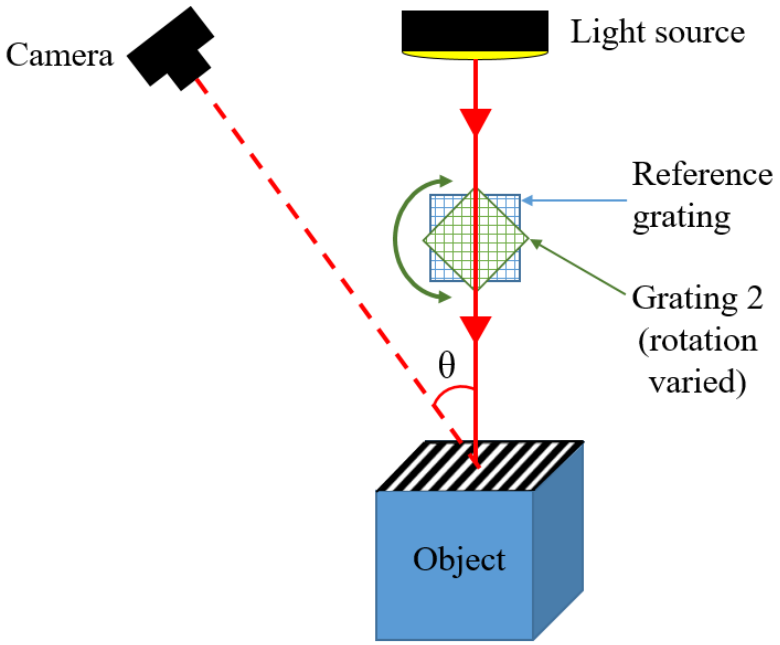


Figure. 2.5 The experimental configuration for Moiré fringe techniques, which uses two gratings to create the fringe patterns, and a camera to capture the pattern, which can be analysed to reconstruct the object's form.

high resolution camera [53]. The projected patterns are commonly referred to as fringes, hence the technique is known as fringe projection. Fringe projection techniques are highly advantageous as they eliminate the correspondence issues which currently limits passive stereovision techniques to 3D surface maps [54, 55], as the projected patterns allow for correspondence to be easily found between captured images. The experimental configuration for fringe projection is similar to that for photogrammetry, where the major difference is the second camera is replaced with a projector to illuminate the object with the coded pattern. The experimental configuration for fringe projection has been shown in figure 2.6, with the baseline (d), angle of projection (α) and the distance between the projector and the object (l) used for triangulation illustrated.

Fringe projection is a widely researched area, with a number of different types of patterns developed to attempt to encode information in different ways [57]. The different fringe projection patterns can be broken down into two main categories of discrete and continuous

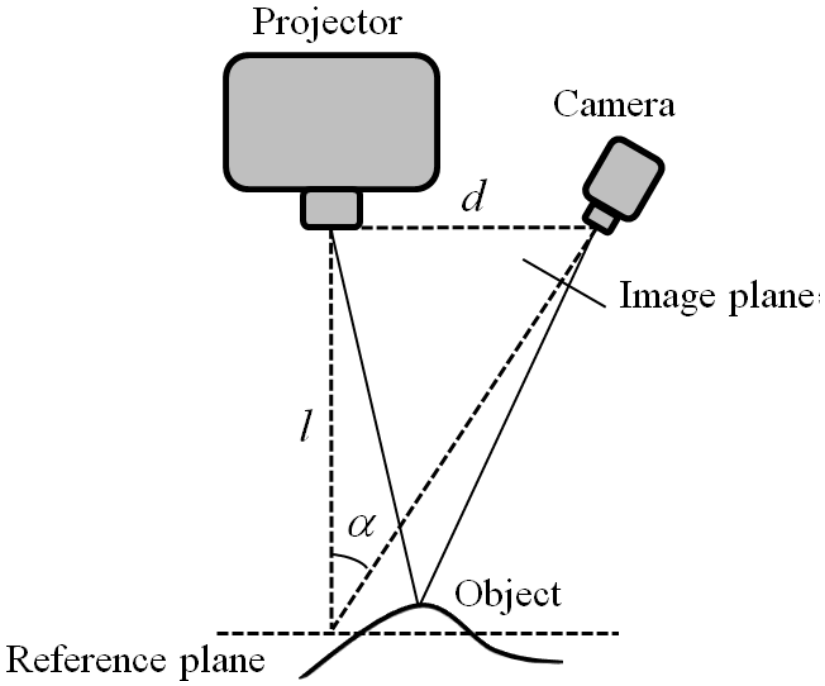


Figure. 2.6 Fringe projection system setup with one projector and one camera, the angles and baseline used for triangulation based fringe projection have also been illustrated [56].

techniques, which are separated based on the method used to reconstruct the part. Discrete fringe projection use triangulation on a pixel-by-pixel basis to reconstruct the parts surface, and uses the known coded patterns to easily find correspondence between images. The most widely used discrete pattern are binary patterns, which vary horizontally with black and white vertical stripes. Continuous fringe projection measures the height of the part by extracting the varying phase intensity of the captured fringe patterns at each pixel. The most commonly researched continuous fringe projection technique is using sinusoidal phase shifting patterns, which projects a number (minimum 3) of sinusoidally varying intensity patterns. Sinusoidal phase shift techniques offer a robust measurement and allow for the phase to be calculated without any *a priori* knowledge of the object being measured. To extract the phase and solve the 2π phase ambiguities, phase unwrapping techniques similar to those used in interferometry are implemented [58–60]. A number of commercial fringe projection systems are available, such as the GOM ATOS core [61] and Zeiss COMET

[35] systems, which can achieve form accuracies in the region of 10 µm, depending on the measurement volume, surface texture and part size [62, 57]. Fringe projection is a suitable measurement technique for our application as it offers a fast (millions of data points in a few seconds), accurate ($\sim$10 µm) and non-destructive method to measure the form of a part.

2.3 Uncertainty and error sources in fringe projection

In order to effectively investigate the different fringe projection methods it is vital that the fundamental limitations and potential error sources of fringe projection are clearly identified. Fringe projection utilises cameras and projectors to project and capture the fringe patterns, a mechanical frame to mount and adjust the positions of the hardware and a computer to process the captured images. The resolution of fringe projection systems are limited by the error sources from the cameras and projectors. The error sources that limit optical equipment include the abbe limit, which is the smallest resolvable distance between two points, speckle noise, particularly when measuring rough surfaces [63], sampling effects and detector size. A number of these attributes are currently important open questions and will present challenges to the design of any new optical based measurement systems. The fundamental limitations are discussed here.

2.3.1 Camera and lens properties

The camera and lens properties play a major role in the accuracy that optical measurement systems can achieve. One of the most fundamental attributes to maximise is the optical resolution of the camera, which describes the ability of an imaging system to resolve detail of the object being imaged. The camera resolution is influenced by several factors but the most important factors in determining the maximum resolution of the system are the diffraction

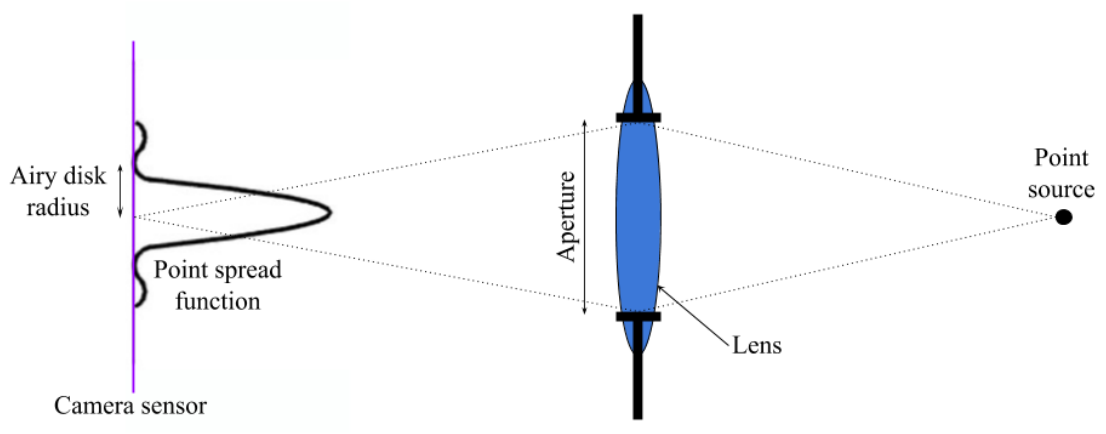


Figure. 2.7 Point spread function produced by a point source passing through a simple optical system consisting of a lens and circular aperture.

limit and/or the pixel size. This section will discuss the effects of the different camera and lens properties on the resolution of the system.

The point spread function (PSF), also commonly called the impulse response, is a function of both the lens focal length and aperture diameter, and describes the response of the imaging system to a point source. It can functionally be considered as the degree of spreading/blurring of the point source, and so in layman's terms is a measure of the image quality. The principle of the PSF is demonstrated in figure 2.7 for a simple lens and aperture imaging system.

If we consider all parts of the imaging system to be perfect then the resolution will only be limited by diffraction of the light. As explained in figure 2.7 and demonstrated in figure 2.8a, instead of capturing a bright spot with sharp edges due to diffraction of light we see a circular spot/disc (also called the Airy disc) with rings of decreasing intensity surrounding it. Figures 2.8b and 2.8c show the effects of two point light sources being closer and closer together, to the point in figure 2.8c where the two separate points are no longer distinguishable and so limits the resolution of the imaging system. As a result of this phenomenon, the minimum distance between two PSFs for which both are still visible and resolvable must be defined by the Rayleigh criterion (measured in radians) and is given by the equation

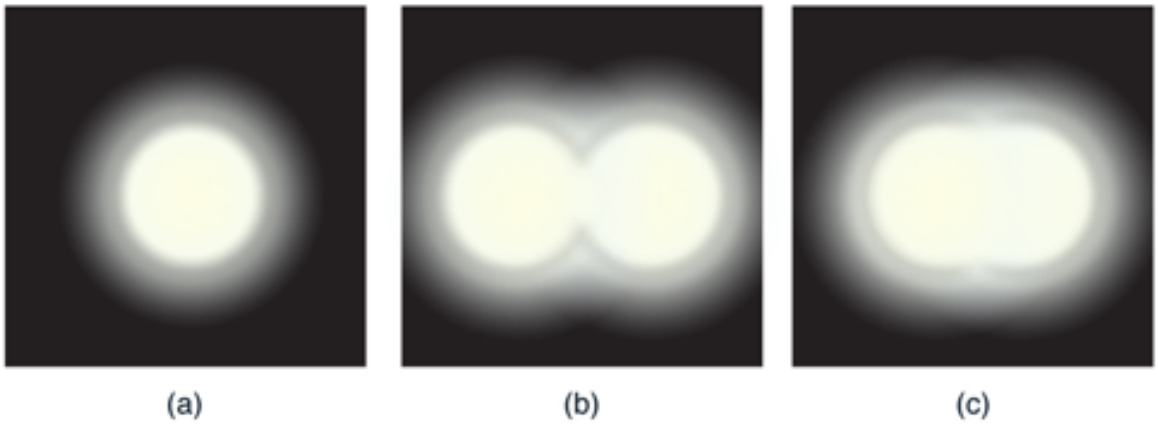


Figure. 2.8 Effects of changing distances between two point spread functions [65]. (a) Easily distinguishable, (b) Only just, but still distinguishable and (c) no longer distinguish the two sources.

$$r = 1.22\lambda N \tag{2.1}$$

where λ is the light wavelength and N is the f-number of the lens, which is the ratio of the focal length to the aperture diameter (f/D) [64].

Therefore, in order to maximise the resolution the Rayleigh criterion, r must be minimised by reducing the f-number, which can be achieved by decreasing the focal length and increasing the aperture diameter. Typical lens arrangements used in optical measurement systems such as fringe projection and photogrammetry have f-numbers of around 1 to 3. For visible light (λ = $\sim$500 nm), a minimum resolvable distance of 610 nm could potentially be obtained with a $f/1$ lens arrangement. However, the solution is a lot more complicated than simply minimising the f-number, as decreasing the f-number has adverse effects on other aspects such as the depth of field and image brightness.

The depth of field (DoF) or focus range describes the range over which the nearest and furthest objects in the image appear in acceptable focus. The DoF is described theoretically as a singular plane in focus but in practice is more analogous to an area of points which are

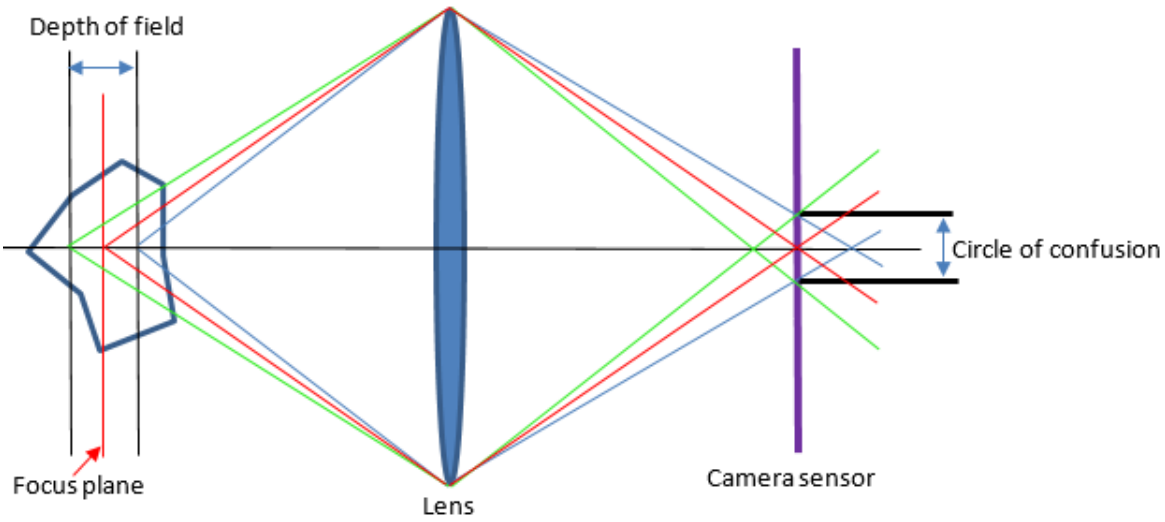


Figure. 2.9 Illustration of the principle behind the circle of confusion.

in focus and gradually begin to decrease in sharpness and blur on each side of the focussed area. Each defocussed point is assumed to produce a blurred circular (same as the aperture) spot which is known as the circle of confusion and is used to define whether each point is considered 'in-focus' or 'out-of-focus'. The 'acceptable circle of confusion' is defined as the maximum permissible diameter at which the circle of confusion is indistinguishable and appears as single point to the human eye [66]. Anything beyond/larger than the acceptable circle of confusion is visible to the human eye and considered to be out of focus. As an example, for a 35 mm aperture the circle of confusion is conventionally set to 0.03 mm [66]. The acceptable circle of confusion changes depending on factors including the visual acuteness, viewing conditions, and the amount by which the image is enlarged.

The circle of confusion is a constant/fixed value for a given f-number, and so the relationship between them can be seen in the DoF equation,

$$d = 2NC\left(1+\frac{1}{M}\right) \tag{2.2}$$

where d is the DoF, C is the circle of confusion and M is the magnification.

As depicted in figure 2.9, if the f-number is increased then the aperture of the lens will be narrower and so as the circle of confusion value is constant, the DoF will have to increase. If the f-number is decreased the opposite effect occurs and the DoF is decreased. This highlights the trade-off challenge between diffraction effects and DoF, as in order to ensure that the diffraction effects do not limit the imaging system, the lowest possible f-number must be used. However, decreasing the f-number leads to a larger aperture, and so decreases the DoF, so the smallest possible f-number would greatly limit the DoF of the system. The trade-off between resolution and diffraction effects is currently one of the major limitations in the field of optics, and does not currently have a complete solution, so a trade-off comparison/decision must be made. Many authors have attempted to find solutions to this trade-off, such as Gallo et al. [67] who proposed an image stacking technique in order to increase the depth of fields when using micro lenses (small aperture). Gallo et al.'s image stacking method was able to measure a maximum depth resolution of 20 µm to an uncertainty of about 10 µm on a volume of diagonal 25 mm. A number of other image stacking methods to increase the DoF have also been researched, including pixel variance algorithms [68], edge detection [69], contrast measurements [70] and multi-resolution approaches [71]. The disadvantage of the image stacking techniques is the significant increase in image acquisition times, due to the need to take several images at different focal lengths, as well as increased processing time to perform the image stacking techniques. This limitation was identified as an area for future work, and could be readily improved with automation and improve processing techniques to decrease the time required significantly.

2.3.2 Sampling

In data collection, the type of sampling used can cause further errors and thus prevent the camera from achieving the best possible resolution previously discussed. In the case of digital cameras, the data is captured in pixels, which are a type of discrete sampling and so will

cause additional effects to the optical system. Sampling is effectively taking an average of the data/signal, which limits optical systems as the local maxima and minima are averaged out. This reduces the contrast achievable in the system from its maximum (100%), as the contrast can be defined as the difference between the maximum and minimum intensity values of the PSF. In addition to the loss in contrast, sampling also does not accurately determine the position of the local maxima and minima. Ambiguity in the position of the maxima and minima is a hugely limiting factor in fringe projection, as the accuracy of the measurement is dependent on the determination of each point within the image captured. As a result, provided the appropriate parameters (i.e. f-number) are chosen, the pixel size will be the main limiting factor to the optical system rather than diffraction limit.

2.3.3 Phase error

It is vital that phase error is understood and minimised as much as possible, as it is widely considered to be the dominant error source in sinusoidal phase shifting fringe projection [72, 73]. In an ideal world the sinusoidal patterns projected would be exactly the same as the perfect sinusoidal waveforms patterns generated, and the measured phase changes would linearly vary with each phase shift in the sinusoidal pattern. However, in reality due to the non-linearity of both the projector and camera detector this is not the case and so leads to significant phase shift errors. Whilst digital video projectors have significantly improved the shift error from previous pattern generation and projection methods, fringe projection systems are still unable to produce a perfect linear response and so phase shift error is an actively ongoing research area for projection based measurement techniques. In addition to the effects of the digital projectors, a number of other factors cause the system to deviate from the ideal sinusoidal waveform including: the camera CCD, ambient light and the parts surface reflectivity [72]. A number of methods to eliminate/minimise the phase shift error have been presented in recent years [73–76]. However, the methods of eliminating the phase

error completely such as increasing the number of shifted patterns used [75] or using the photometric calibration technique [74] have proven to be very slow, and so they limit the speed advantage that fringe projection systems offer, and so neither are considered to be complete solutions to the phase error issues.

2.3.4 Projection errors

Discrete fringe projection uses triangulation of each pixel from the distorted images captured to the original projected pattern in order to calculate the 3D coordinates of each pixel on the object in order to reconstruct the parts surface. However, as a result of this method, projection errors will be caused due to the uncertainty in the projection angle, which causes errors determining the position of each and leads to an area of uncertainty in which each pixel position can be found to be located. Figure 2.10a demonstrates how the divergence caused by the uncertainty in the projected rays leads to the highlighted circled error area, which represents the uncertainty of the 3D coordinate being triangulated. In figure 2.10b with the same projection uncertainty, the effect of changing the length of the baseline (distance between the camera and the projector) on the error area is illustrated by the oval highlighted area of uncertainty. In both figure 2.10a and 2.10b the dashed lines represent the true projection path and show where the real pixel position should be triangulated to. As the uncertainty is in the angle of projection, the errors will be increased as the distance from the projector and camera increases.

2.3.5 Noise

Ideally the only signal received would be that of the light emitted in the each pixel of the fringe patterns projected, however, this is not the case in real applications as the signal is affected by sources of background noise. The level to which the background noise distorts the signal is usually described using the signal-to-noise ratio (SNR), which defines the ratio

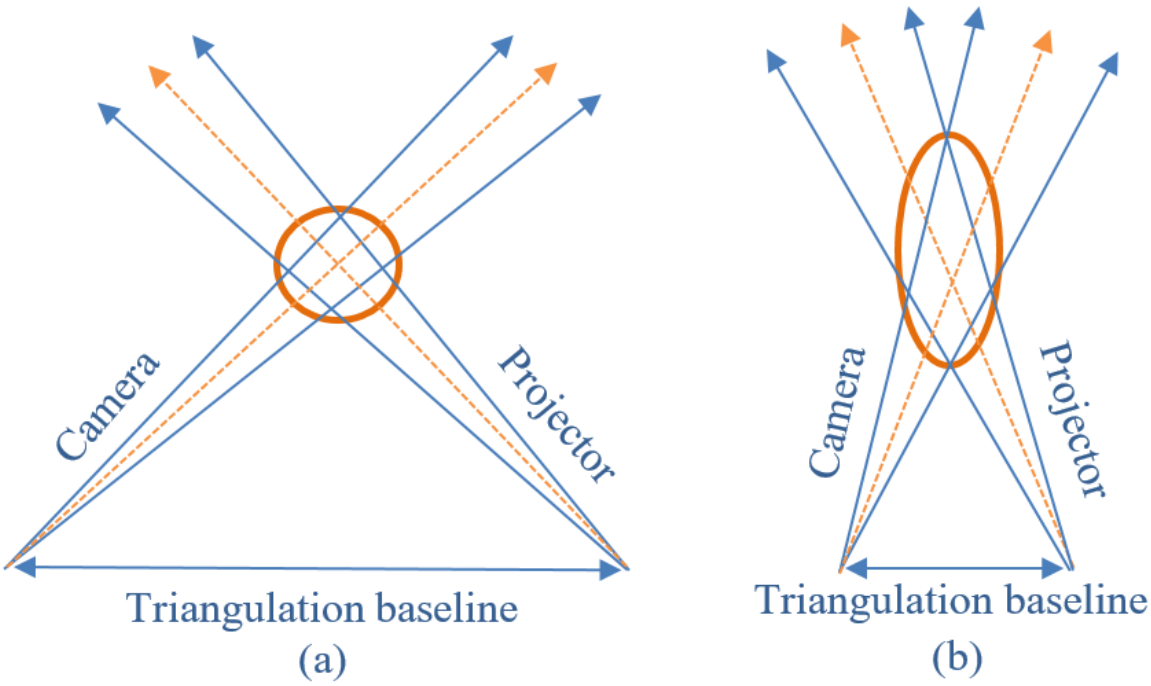


Figure. 2.10 Illustration of the projection errors caused by the uncertainty in the projection angles in both the camera and projector for both (a) wider baseline and (b) narrow baseline.

between the desired signal and the background noise. The effects of noise can be seen in the reduction of the contrast in the image, and subsequent reduction in the contrast-to-noise ratio (CNR), which is similar to SNR, and is used as an indication of image quality. The effect of noise on the PSF is illustrated in figure 2.11. There a number of different sources of noise in digital imaging systems, including Gaussian noise, salt and pepper noise, speckle noise and Poisson noise.

Gaussian noise (also called electronic noise), represents the noises which occur within the camera during the acquisition phase of the image. The camera noise sources include the electrical amplifiers and detectors and thermal emissions [77, 78]. Gaussian noise can be seen to affect the grey values within the digital images captured. It is possible to model the Gaussian noise by

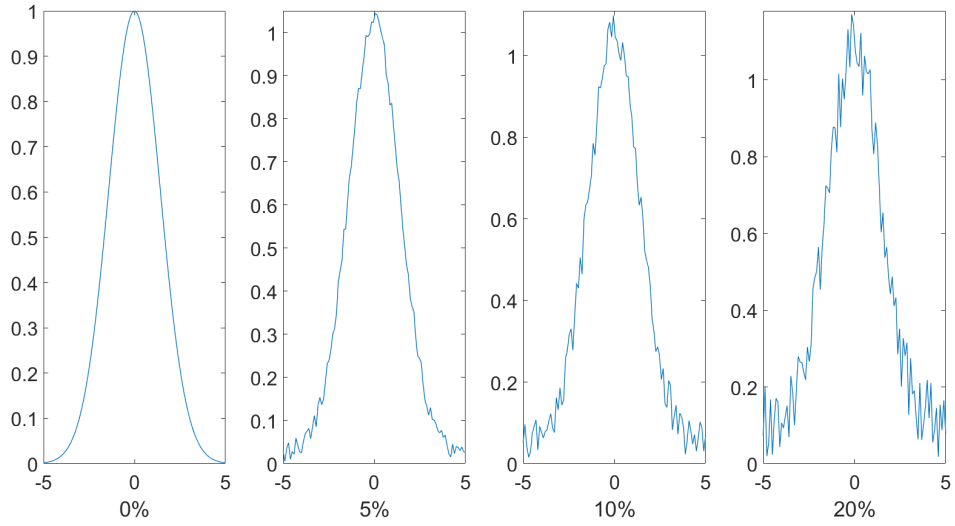


Figure. 2.11 Effect of noise on a point spread function. A noise level of $0\%, 5\%, 10\%$ and 20% are shown.

$$P(g) = \sqrt{\frac{1}{2\pi\sigma^2}} e^{-\frac{(g-\mu)^2}{2\sigma^2}} \tag{2.3}$$

where, g is the grey level value (0 to 255), σ is the standard deviation and μ is the mean. The Gaussian distribution model is generally seen as a good approximation of real world applications.

Another form of noise that arises within the camera, is known as salt and pepper noise or also referred to as impulse valued noise. Salt and pepper noise is caused by pixel corruption during data transmission and errors in analogue to digital conversion. For 8-bit images each pixel will have a grey level value between 0 and 255, varying in integer steps, with 0 and 255 corresponding to black and white respectively. Salt and pepper noise, causes pixel values to corrupt and be replaced with either dark pixel values (255) or light pixel values (0) i.e. cause erroneous 'black' or 'white' pixels in the image hence the name salt and pepper noise. It is possible to remove the salt and pepper noise through the use of a median filter. Inside the camera, periodic noise is also present. This noise is generated by electronic interference

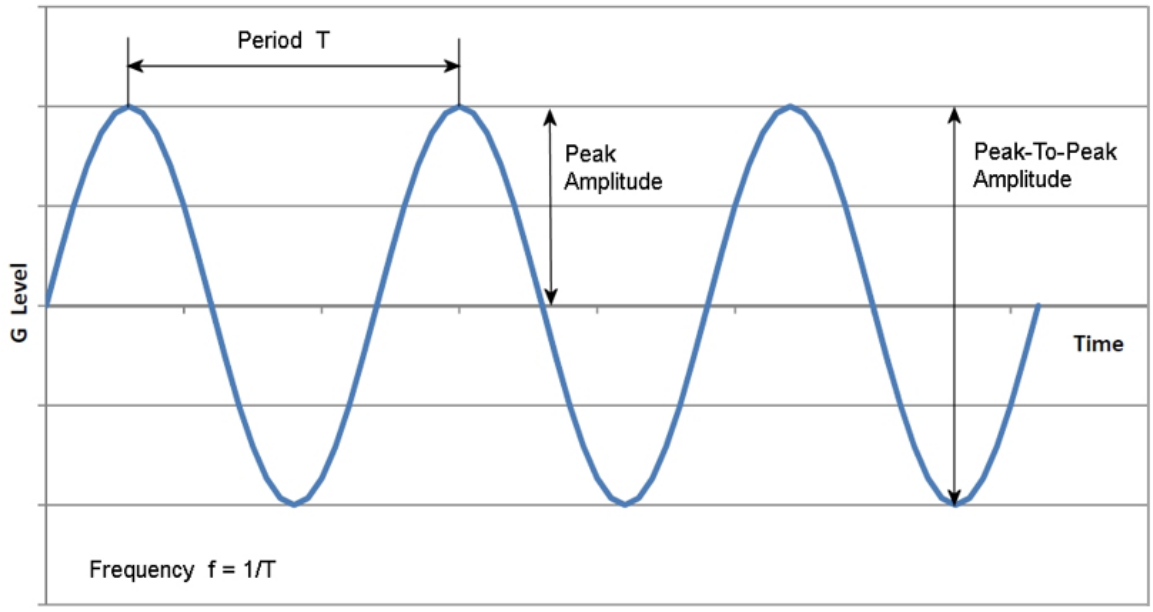


Figure. 2.12 Simple sinusoidal vibration wave with the key characteristics (amplitude, period, frequency and peak-to-peak) used to define the vibration identified.

in the cameras electronic components, but can be removed by using a narrow band filter or notch filter [78].

2.3.6 Mechanical noise

Mechanical and environmental error sources such as vibration and ambient light can cause significant errors in high accuracy metrology systems, and so must be carefully measured, controlled and where possible eliminated. Vibration is the periodic back-and-forth motion of an elastic body or medium, and commonly results when a physical system is displaced from its equilibrium condition and allowed to restore itself back to its equilibrium position. Vibration motion is usually described as oscillating motion and is defined by its amplitude, which is the maximum displacement moved by a point on the vibrating body, and its frequency which is defined as one over the period, where the period is the time that it takes for the body to repeat its motion. A simple sinusoidal vibration wave can be seen in figure 2.12, and illustrate the key characteristics of defining and understanding vibration.

There are a number of different types of vibration, which can be divided into the excitation sources and how the system responds. The different types of vibration include:

- Free vibration occurs when an excitation force is applied to the structure, and then the response to the vibration is solely dependent on the structural properties of the system. An example of free vibration is the pluck of a guitar string which freely responds to excitation, and vibrates at the tuned frequency to produce the desired tone.

- Forced vibration occurs when a repetitive forcing function is applied causing the structure to vibrate at the frequency of the excitation. An example of this is a part of a car such as the rear-view mirror, which will vibrate at the frequency of the engine's revolutions per minute, as the engine is the constant excitation source within the system.

- Sinusoidal vibration occurs when the structure vibrates with pure acceleration and frequency from a single excitation source. Sinusoidal vibration is a special class of vibration and very rarely occurs in practice, but can be a powerful tool in understanding complex vibration signals by breaking the vibration down into the individual components [79].

- Random vibration is the most common type of vibration, and is a result of a complex combination of a number of different vibration excitation sources. Random vibrations are complex to understand and so are usually described with statistical averages and analysed using Fourier techniques to identify the frequencies of the different significant contributors [80].

In practice, the vibrations experienced within a system are generally a combination of several excitation sources, although one input may be dominant and of particular interest. The different vibration sources can be divided into three categories, which are seismic/ground vibrations, acoustic vibrations and forces applied [81, 82]. Seismic or ground vibrations

are transmitted through the ground and caused by very large structures moving. Ground vibrations are elastic waves propagating through the ground and are associated with a number of different sources, which includes artificial sources from railway trains, road traffic and construction, and naturally occurring sources from the shifting of the Earth's tectonic plates and ocean waves. Ground vibrations must be closely monitored as they can cause disturbances and damage to surrounding building structures, as well as affect vibration sensitive equipment within a number of industries [83]. Ground vibrations typically have a frequencies ranging from 1 Hz to 200 Hz. Acoustic vibrations are pressure waves travelling through a medium (gas, liquid or solid), which are commonly referred to as sound, and have a frequency range of 20 Hz to 20000 Hz. The final source of vibration is from forces being applied to the system, which can be from a number of different sources such as moving parts, an external source interacting with the system or wear in a component leading to imbalanced forces. Forced vibrations are common in industrial environments due to the frequent use of rotary machinery, air conditioning units and other mechanical equipment, and commonly range in frequency from 5 Hz to 400 Hz [84].

Vibrations are widely reported as the most significant mechanical error source [74, 85], however, there are currently only limited contributions to fully understand and investigate the magnitude to which vibration affects the accuracy and reliability of fringe projection measurement systems, and how such errors are minimised. Vibrational noise can affect both the pixel intensity of the projected fringe patterns and the perceived pixel intensity in the captured images, which can cause errors when extracting the phase and absolute height information from the pixel intensity values [86, 87].

Many authors have performed error analysis and presented compensation techniques for sources of phase error in fringe projection [72–76, 87–91], such as intensity and gamma correction. However, in their error analysis, some of these authors have omitted vibration entirely [73, 89, 90]. The authors that acknowledge vibration as a significant error source

[72, 74, 75, 87, 88] do not perform any investigation into the scale of the errors caused by vibration, nor do they present any minimisation or elimination methods. One of the few authors to study the effects of vibration was Yao et al. [92], who proposed a technique where 20 fringe images were captured continuously in the same state, in an attempt to average out the effects of vibration. Whilst this averaging technique showed some merit, it significantly decreases the speed of the technique, detracting from one of the major advantages of fringe projection, and so an alternative solution which uses only three phase-shifted images continues to be sought after. Huang et al. [74] and Tao et al. [91] also proposed averaging techniques as a potential method to reduce vibration effects in the measurement calibration. Purcell et al. [93] proposed a method to estimate the effect of vibration and electronic noise on the calibration by repeating the procedure to find an averaged standard deviation at each "patch of pixels" in the image. Whilst the literature showcases some attempts at addressing the effects of vibration in fringe projection measurements, the depths of these investigations are lacking. This research gap in the current state of the art highlights the potential for a better understanding of vibration as an error source in fringe projection measurements by way of a novel methodology that allows the effects to be investigated in greater detail. This is a key focus throughout this PhD.

2.4 Fringe projection frame design

In order to design a simple fringe projection system the basic mechanical considerations that must first be considered includes, choosing the appropriate camera and projector, from which the required angle between the camera and projector can be calculated, as well as the working distance required to achieve a minimum measurement area. The calculated working distance and camera-projector angle specifications guide the geometry requirements of the system, but the mechanical design of fringe projection systems is currently an under researched area. Despite mechanical error sources such as vibration being identified as a

significant error source in precision measuring instruments [74], due to the lack of research into mechanical design for fringe projection systems, there are little to no metrics reported to define the required mechanical performance for an accurate fringe projection system i.e. stability or vibration performance. This identified gap in the research is a key focus of this PhD, and is an area that the work will address.

The majority of the research proposing new fringe projection systems is focussed more on presenting novel fringe patterns, calibration procedures or phase unwrapping algorithms, with the mechanical design kept simple and the effects of design not considered or investigated. Current commercial fringe projection systems offer the two most common design methods where the camera and projector are mounted on either robot arms (figure 2.13) or simple single/tripod beam frames (figure 2.14). Incorporation with robotics has been recently introduced in order to increase measurement automation, flexibility and mobility [94]. This provides an automated method to measure around a part, as well as be able to scan larger part sizes more readily using only a single fringe projection system. As a result, the price of these systems are significantly higher than that of the systems with simpler frame designs. In more affordable commercial fringe projection systems, the frames and mounting are very simplistic and manually manipulated in order to reduce the cost of the overall system. However, the frames offer little to no vibration isolation to ensure the system is stable during the measurements, and so are likely to suffer from much higher levels of noise, which reduces the accuracy and repeatability of the system. Despite the difference in mechanical performance of the aforementioned fringe projection mounting designs, there has been little research to understand the effects of mechanical error sources on the accuracy of fringe projection measurements and so is a gap in the research.



Figure. 2.13 Example of a commercially available fringe projection system mounted on a robot arm.



Figure. 2.14 Example of a commercially available fringe projection system mounted on a tripod.

2.4.1 Condition monitoring

In recent years there has been a marked rise in optical based form metrology solutions [52], however, adoption of optical coordinate measurement systems has slowed due to a lack of confidence, stemming from a lack of performance verification and a calibration framework. One method to increase confidence in a measuring instrument is to more closely monitor the measurement process, in order to provide the user with metrics to show the system is performing as specified by the manufacturer and measurement standards [95, 96].

Condition monitoring [97] is a technique which is particularly prevalent in machine monitoring applications within the automotive [98, 99], aeronautical [100, 101] and machine tool wear [102, 103] industries. Condition monitoring is the process of monitoring a performance parameter of a system to identify a significant change, which is indicative of a fault. Effective condition monitoring promotes a predictive maintenance strategy, rather than operating the traditional run-to-break strategy [104], which can lead to catastrophic failures. Condition monitoring offers a number of benefits over run-to-break strategies such as reducing unplanned failures, decreasing downtime and maintenance costs as fewer failures occur and parts are only replaced when a fault is detected, and eliminating secondary damage to other components in the system [99–101].

There are a number of different techniques used to monitor the condition of a system, which includes:

- Vibration is a common measurand used in structural condition monitoring [105], as it allows for the non-destructive detection of faults within the system before they lead to catastrophic failures. Vibration based conditioning monitoring techniques analyse the systems characteristics in the time, frequency and modal domains and identify changes in dynamic behaviour in the measured signals to detect a fault.

- Lubricant analysis is a measurand commonly used in combustion engine and bearing applications [106]. Monitoring the lubricant in an engine is essential as any deterio-

ration or lack of lubricant can lead to significantly increased wear between moving parts.

- Acoustic emission monitors the transients elastic waves generated in materials under stress, and attempts to detect plastic deformation and crack propagation before catastrophic failure in rotary machinery [107, 108].

- Infrared thermography is a useful condition monitoring tool as changes in temperature are a clear indication that there has been a change in the system and a fault has occurred. Using infrared cameras to monitor temperature changes is widely used in applications such as inspection of electrical equipment, civil structures, weld inspection and evaluation of material fatigue [109].

- Ultrasonic testing is used as a conditioning monitoring method to detect and locate faults such as leaks, cavities, arcing and a lack of lubrication [110]. The method works by propagating ultrasonic waves through the inspected part and measuring the changes in the echo of the signal. Ultrasonic testing is used in a variety of applications such as rail track inspection, bearing inspection and leak detection in pressure and vacuum systems [111].

- Other conditioning monitoring techniques such as motor current signature analysis (MCSA) and model-based voltage and current systems (MBVI) are commonly used for fault detection in electric motors, which is beyond the scope of this review as the focus of the project in on mechanical structure condition monitoring.

A recent branch of condition monitoring to become more prevalent is structural health monitoring (SHM), which involves using sensors to monitor the vibration in the structure to evaluate its ‘health’ through the dynamics of the structure and ultimately predict/prevent failures [112]. SHM is a prominent research area for large-scale structures such as bridges, dams and building, seen in the civil engineering industry, due to the high impact and costs if

catastrophic failures were to occur in such structures. An early SHM system was developed by Beck et al. [113, 114], who developed a method to analyse the ambient vibrations of a structure to determine its health, and demonstrated the application of the system on the Caltech Millikan library (California institute of technology).

More recently, civil SHM systems are moving towards wireless sensor networks, due to the access issues of large-scale structures, and so attempting to reduce the cost of installation and maintenance. Examples of wireless sensor network SHM systems developed include Kim et al. [115] and Bocca et al. [116]. Kim et al. [115] distributed 64 digital accelerometer sensors over the main span and tower of the Golden Gate bridge in San Francisco, in order to measure the ambient vibrations in the structure to detect changes and assess their severity to monitor the health of the bridge. Bocca et al. [116] developed a wireless multi-sensor network, which included a three axis digital accelerometer, temperature and humidity sensors to analyse the mode shapes of a laboratory based wooden bridge structure. SHM has been shown to be a prevalent area of research in the civil engineering industry for monitoring large-scale structures, the measurement and assessment principles are increasingly being applied to new applications.

An application that would benefit from effective structural health condition monitoring is measurement system apparatus. While measurement systems are not prone to catastrophic failures like in civil structure or rotary equipment, they are reliant on reliable mechanical performance to provide accurate measurements, and can be sensitive to vibration [117]. To this end, applying the principles of SHM to monitor the performance of the mechanical structure of a measurement system would be beneficial, as it would allow the dynamic performance of the structure to be continuously measured, and ensure it is performing to the manufacturer's specifications. Despite the importance of the mechanical performance, current measurement systems implement little or no active condition monitoring, and so the performance of the system cannot be verified, and any structural deterioration over time

is not monitored. Therefore, it was identified that condition monitoring for measurement systems was a key research gap, and an area this PhD will address. Development of new condition monitoring systems/methods would allow for the principles and benefits of SHM to be applied to measurement systems, and demonstrate that effective condition monitoring will help to increase confidence in the measurement results and provide quality assurance that the system is performing as specified.

2.5 Chapter summary

The background and motivations in Chapter 1, along with the state-of-the-art review presented have made it clear that AM is gaining significant traction in the manufacturing industry due to the complex geometries and internal features that can be produced. However, a significant limiting factor to the widespread adoption of AM across all engineering industries is a lack of traceability for the manufactured components, and so it was identified that there is a need for new AM specific metrology solutions to enable accurate and traceable measurements. Previous research has highlighted a number of challenges that new measurement systems must overcome in order to effectively measure AM parts, which includes: complex geometries, rough surfaces, material range and internal features. As such, this thesis will aim to address the need for traceability in AM by developing a new measurement system, which can overcome the aforementioned challenges and measure the full form of AM components, with a focus on the design and performance of the mechanical structure for the system.

Through the review of the available form measurement techniques, fringe projection was highlighted as an effective technique to investigate, due to its fast acquisition (potential for one-shot), accuracy ($\sim$10 µm), non-destructive nature and relatively cheap hardware required (only a camera and projector). An extensive discussion of the error sources in fringe projection measurements showed that whilst there have been several contributions, which have proposed methods for minimising the optical error sources, there has been little

published on the effects of mechanical error sources (such as vibration), and so this has been identified as a key research gap, and an area for further research. As such, the project addresses this gap in Chapter 4, by developing a simulation and experimental methodology to investigate the effects of mechanical error sources on fringe projection measurements, to better understand the sensitivity of the measurement technique and our proposed system.

The review of current commercial fringe projection systems showed the mechanical design is often overlooked, with either a robot arm or a tripod used a standard depending on the cost of the system. In addition, the research into developing new and novel fringe projection systems is focussed on software aspects such as calibration and phase unwrapping methods, with no attention to detail applied to the design of the system and understanding the effect the mechanical performance has on the accuracy of the measurements. This research gap is addressed in two chapters; firstly a detailed design has been presented in Chapter 4, with five key design process steps identified, which should be used as standard when developing any new measurement system. Secondly, an experimental characterisation method has been developed and presented in Chapter 5, which provides a methodology to readily evaluate the dynamic performance of the mechanical structure, to enable the effects of changes in the dynamics of the structure on measurement accuracy to be investigated.

This literature review also discussed the benefits of effective condition monitoring, and identified that commercial systems implement little or no condition monitoring, as well as there being a lack of research in this area. This research gap is a key focus of the PhD, and is addressed in Chapters 6 and 7, with a new multiple-point SHM system developed and applied on the multi-view fringe projection system to demonstrate how effective condition monitoring can be a useful tool to increase confidence in measurement instruments, by providing quality assurance that the system is performing as specified by the manufacturer and relevant measurement standards.

Chapter 3

Research methodology

In this chapter, the research methodology used throughout the project is discussed. The methodology is broken down into five core steps.

1. The first step was a detailed literature review, which helped to identify the current state of the art in the field of fringe projection, mechanical frame design and condition monitoring. The review enabled the understanding of the topic, as well as identifying key knowledge gaps within the field.

2. The second step was setting the research objectives to be achieved during the project to address the identified knowledge gaps.

3. The third step of the research methodology was the software development and implementation, which involved any software that was utilised to achieve the research objectives such as performing simulations, computer aided design and data processing.

4. The fourth step was the use of experimental methods to achieve the research objectives, which included the hardware used to collect measurements and technologies used to manufacture artefacts.

5. The final step was the analysis of the results obtained from the work carried out in steps three and four.

In this chapter, each core research step will be discussed in turn, with the application of each method within the work to achieve the research objectives explained.

3.1 Software methodology

The third step of the research methodology was the software packages that were used to aid investigation into the research objectives. The software packages presented here represent a large section of the work presented in Chapters 3 to 7 and so the methodology and application of each software package within the project will be discussed here. The work performed with each software package is described in the respective chapters/sections of the work.

3.1.1 Computer aided design

In order to design an effective solution, PTC Creo and Solidworks computer aided design (CAD) packages were used to create 3D models and 2D detailed drawings for all of the designs required throughout the project. In order to achieve the research objectives, the CAD design packages were used to carry out a number of key design activities, which included:

- Design and manufacture of any new configurations to enable experimental investigations, such as the effects of vibration on fringe projection measurements, as well as the design of the multi-view fringe projection frame. The ability to quickly design and make flexible and varied experimental setups was a useful tool throughout the PhD.
- Concept demonstration and evaluation. An important step in the development of an effective design solution is evaluating a number of potential concept designs in order to identify the ideal solution. To this end, the CAD packages allowed 3D designs to be

developed for a number of different concepts, which aided the visual demonstration of the idea in design discussions, and helped to evaluate the merits of each potential solution.

- Artefact design, for use in laboratory testing work. To aid experimental investigations into multi-view fringe projection measurements, artefacts needed to be designed which highlighted problematic features associated with common AM parts i.e. complex geometries, as well as current limitations of fringe projection measurements i.e. steep surface slopes.

- A number of the parts designed in the CAD software packages were also used in finite element analysis (FEA) simulations and mechanical studies. To achieve this, the designed parts were converted into STL format so they could be imported into simulation software packages, such as ANSYS and POV-Ray.

3.1.2 ANSYS

ANSYS is a software package that supports product design, and allows advanced simulations to be performed to test a design's durability, temperature distribution, fluid movements, structural dynamics and electromagnetic properties. ANSYS was an important tool in the development of the multi-view frame as it supported a number of vital steps of the design process, such as performing mechanical simulations on any potential design solutions in order to verify their performance and prove the design effectively meets any performance requirements detailed in the statement of requirements.

3.1.3 MATLAB

MATLAB is a high-performance numerical based programming language for technical computing, which integrates computation, visualization, and programming in one environment.

To achieve the research objects, MATLAB programming was used throughout the PhD to carry out key processing, control and simulation activities, which included:

- Control of the multi-view fringe projection system (i.e. cameras and projectors), as well as generating and processing the fringe patterns that are projected and captured on the measured part.
- Creating mathematical models to study how the dynamic performance of the system effects the accuracy of fringe projection measurements. An example is the simulation created to investigate the effects of vibrational noise on the phase shifted images, to allow comparison between the theoretical noise with the experimentally measured vibration.
- Performing a variety of processing and analysis techniques for the experimental investigations that were used throughout the PhD, i.e. the characterisation experiments performed on the developed mechanical frame using accelerometers, required processing and analysis of the raw vibration voltage data to obtain usable and reliable displacement results.

3.1.4 LabVIEW

Laboratory Virtual Instrumentation Engineering Workbench (LabVIEW) is a programming language developed by National Instruments (NI), which uses a graphical modular design with an implemented dataflow paradigm, where wires, similar to that of an electrical circuit, connect the different functions of the code. LabVIEW is widely used for systems development as it allows for flexible data acquisition, analysis, and instrument control. To this end, LabVIEW was utilised in the development of the live vibration condition monitoring and characterisation system. The project took advantage of the specialised add-on modules to support the development of the live-monitoring system, such as the field programmable gate

array (FPGA), real-time and MathScript modules, which aided the precise timing, large data rates and rapid processing requirements of the application.

3.2 Hardware methodology

The fourth core step of the research methodology involves development of the hardware that was used to aid the experimental investigations performed to achieve the research objectives. A number of different experimental investigations were performed and constitute a large proportion of the work presented in Chapters 3 to 7, so the methodology of the frequently used hardware will be discussed here to aid understanding and add clarity to the work presented in the relevant chapters.

3.2.1 Additive manufacturing

The measurement artefacts used to investigate the developed multi-view fringe projection system, and in other experiments were all made using AM technologies. The artefacts were designed to highlight problematic features associated with common AM parts i.e. complex geometries, as well as current limitations of fringe projection measurements i.e. steep surface slopes. The artefacts designed were manufactured using two AM technologies, which were both part of the powder bed fusion family [118]. The two AM manufacturing methods allowed artefacts to be created in Nylon 12 and titanium alloy (Ti-6Al-4V) respectively, to investigate the different surface reflectivity and material properties. Both powder bed fusion processes use a laser as an energy source to scan across the powder bed to heat the particles. In the metal based fusion process the particles are heated until they are fully molten, so that they melt together with the neighbouring particles to form a homogenous material [119]. The melting process is repeated on a layer-by-layer basis, to build the three dimensional shape of the part one level at a time. Between each layer, the build platform is lowered and a new

layer of powder is evenly spread across the build plate. The polymer based sintering process uses the same layer-by-layer approach, with the main difference being the particles are not fully melted and are only heated to enable the particles to fuse together [119]. A schematic diagram of the powder bed fusion process setups has been included in figure 3.1.

3.2.2 Piezoelectric accelerometers

Piezoelectric accelerometers were used throughout the PhD in a number of key experimental investigations, and so the working principle is discussed here.

The piezoelectric effect was discovered by Pierre and Jacques Curie in 1880 [120], and is the ability of certain materials (i.e. barium titanate and lead zirconate titanate) to generate a charge in response to an applied mechanical stress. Accelerometers use the piezoelectric effect to produce a charge, which is proportional to the acceleration. A schematic diagram of a piezoelectric accelerometer can be seen in figure 3.2. Accelerometers are mounted on the surface of the structure using either the mounting stud or an adhesive. The vibrations of the structure cause varying inertial forces in the mass, which cause the piezoelectric elements to deform. The change in the strain of the piezoelectric elements due to this deformation is proportional to the acceleration and allows for the mechanical vibration in the structure to be measured. Piezoelectric accelerometers offer a number of advantages including: a good response to a wide range of frequencies ($<$10 Hz to 10000 Hz), triaxial capabilities, have a low mass and are easy to mount [121, 100, 122, 123]. However, it is worth noting that the accelerometer data is unreliable outside of the designed frequency range, and they have a high impedance and so the signal requires amplifying and conditioning, which can lead to errors in the measurements [121, 100, 122, 123].

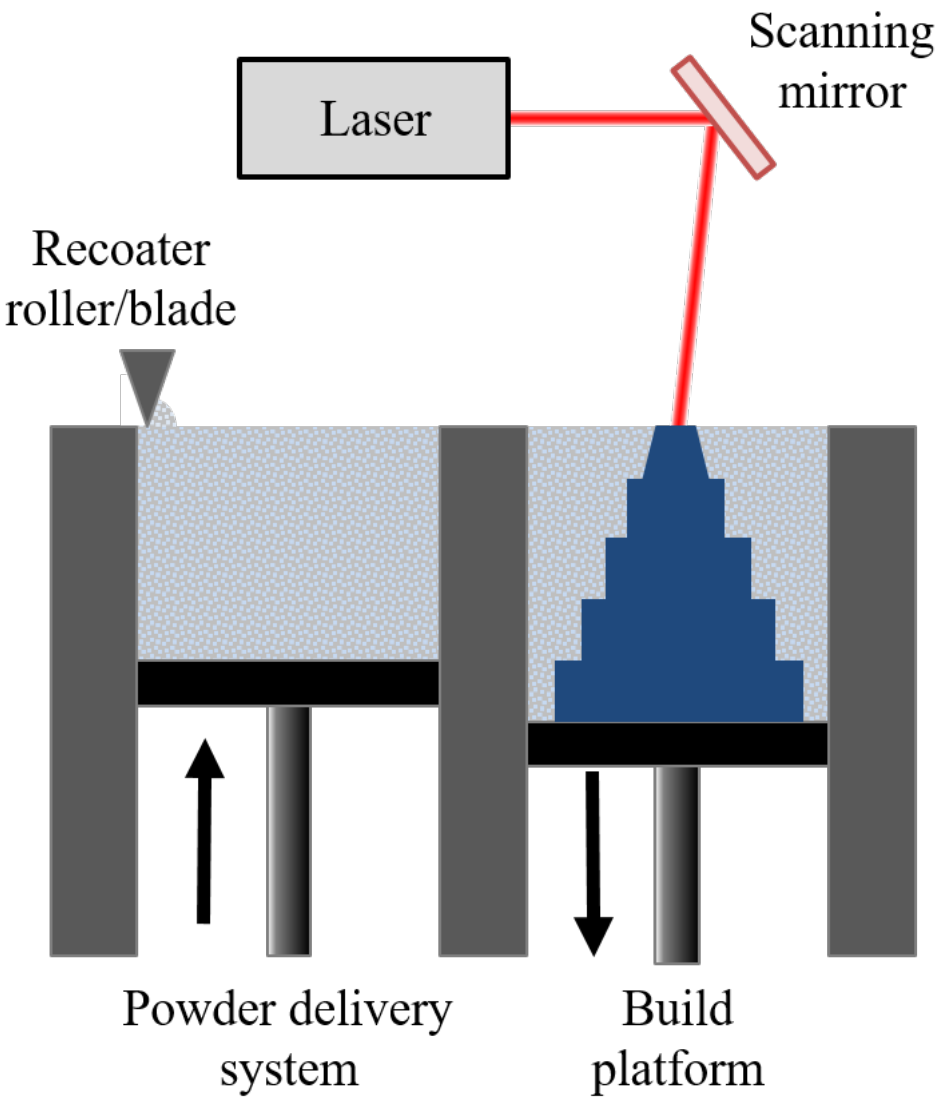


Figure. 3.1 Schematic diagram depicting the process used for additive manufacturing powder bed fusion technologies.

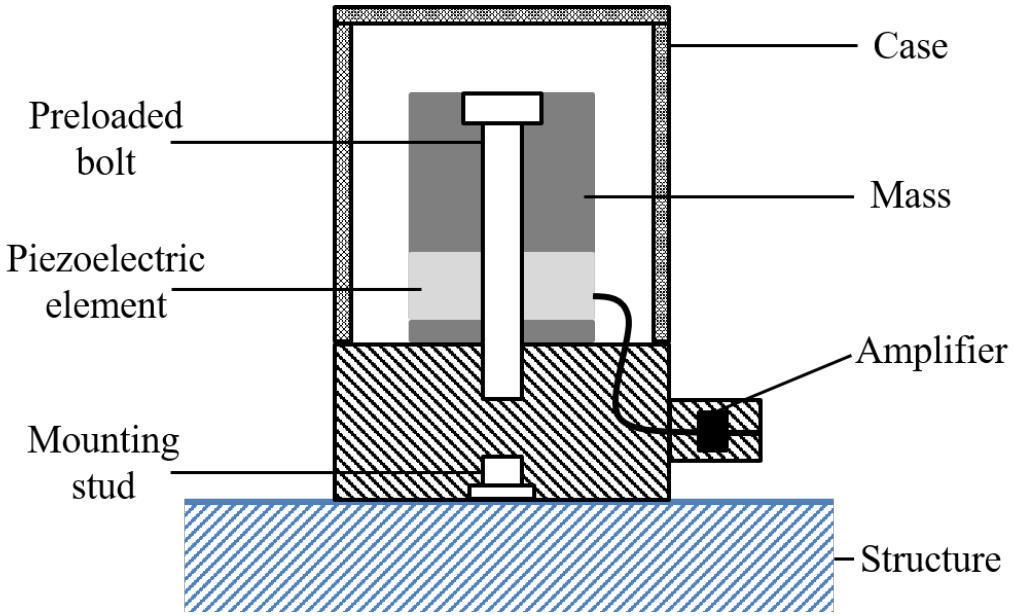


Figure. 3.2 Schematic diagram depicting the key elements of a piezoelectric accelerometer.

3.2.3 Laser vibrometer

A laser vibrometer was used as a secondary vibration measurement technique to verify the results obtained using piezoelectric accelerometers and so the working principle is discussed here.

The laser vibrometer was developed in 1980 by British loudspeaker company, Celestion [124], and uses the same laser Doppler effect principle as a heterodyne interforemeter to measure the vibration on the surface of an object/structure. A coherent laser beam directed at the object's surface is split into two beams of equal frequency, which are called the reference beam and the measurement beam. The reference beam is directed to the photodetector, and the measurement beam towards the vibrating object. As the measurement beam is reflected off a vibrating surface, the back scattered light is changed in frequency and phase, which is related to the velocity of the object. The reflected beam, which contains the characteristics of the motion of the object, is then superimposed with the reference beam to obtain a modulated output signal to detect the Doppler shift in frequency. The vibrational velocity and displacement can be found by analysing the modulated output signal. Laser

vibrometry provides the best displacement (2 pm) and velocity resolution (2 nm/s) of the available vibration transducers, with large frequency ranges (up to several megahertz), and it is non-contact so does not alter the object's surface. However, common laser vibrometers are only single axis, expensive, require line of sight to operate and are limited to materials with sufficient surface reflectance, or require a mirror to be attached.

3.2.4 Smart shaker

A number of experiments were carried out which required the mechanical structure to be excited in order to investigate the effects of vibration on fringe projection measurements. To this end, a smart shaker K2007E01 (from the Modal shop) was used to excite the different structures in each experiment. A picture of the smart shaker can be seen in figure 3.3. The shaker is controlled using a dynamic signal analyzer or function generator, and so allows for any excitation signal to be generated and sent to the shaker. Whilst generating the function/signal, key parameters such as the frequency, amplitude and shape of the waveform, can be defined and readily controlled. The amplitude of the shaker output is modulated by the voltage input of the signal, with a range of 12 VDC to 21 VDC.

3.3 Analysis methods

A number of different analysis methods were used throughout the PhD. The techniques that were only used for a specific part of the work, have been described in the relevant chapters. The analysis techniques which have been used throughout the PhD are discussed here, so as to avoid repetition in describing these methods in each of the sections where they have been used.



Figure. 3.3 The Modal Shop smart shaker K2007E01 [1] that was used to excite the different structures in each vibration experiment

3.3.1 Vibration analysis

Vibration measurement was a key focus throughout the PhD, and so developing appropriate methods to analyse the results was a critical step. The techniques used to analyse the vibration signals were peak-to-peak and frequency response/spectrum, as this allowed the maximum displacement and main frequency components to be monitored [100, 125]. The peak-to-peak represents the amplitude of the positive peak to the negative peak, which in the case of a simple sinusoidal signal would be two times the amplitude as the wave is symmetrical. However, vibration signals are commonly more complex, as shown in the example in figure 3.4, and so calculating a mean peak-to-peak response is a useful assessment to understand the overarching characteristics of the vibration signal over the measurement period. In order to calculate the peak-to-peak amplitude, the signal needs to be separated to isolate the large amplitude vibrations of interest and ignore the low amplitude vibrations. Separating the large and small amplitudes is achieved by obtaining the mean displacement from the zero-

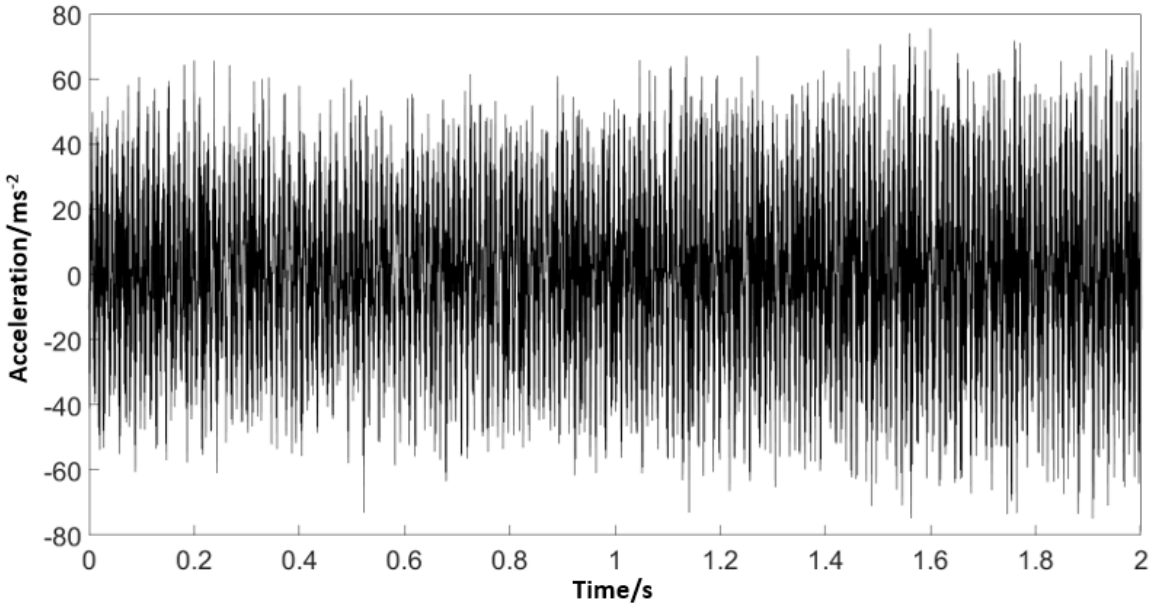


Figure. 3.4 An exemplar vibration dataset collected using an accelerometer mounted on a lathe during the cutting process.

line (operating above and below the zero-line separately), and removing all points that fall below the mean. Then, a further mean operation is performed, on only the high-amplitude components, to obtain the average peak amplitude across the measurement period. The average peak-to-peak displacement of the signal can then be calculated by combining the absolute values of both the positive and negative high-amplitude means.

In the case of shock or impact vibrations, the largest peak-to-peak response is a more appropriate analysis method. The camera shutter and internal mechanism were identified as the largest excitation sources in the developed multi-view fringe projection system, and the impulse would cause shock vibrations in the structure. The largest peak-to-peak response was found using the maximum peaks of both the positive and negative amplitudes in the measured signal.

Frequency spectrum is an effective vibration analysis tool, as it allows the signal to be shown with respect to its vibration amplitude as a function of frequency. The frequency response enables the largest excitation frequencies in the signal to be clearly identified, and

shows key characteristics in the signal such as resonances and harmonics that are hidden in the time history graph. To obtain the frequency spectrum the measured vibration signals were converted into the Fourier domain using a fast Fourier transform (FFT) algorithm. The resolution of the frequency (i.e. the size of each frequency bin) in an FFT is directly proportional to the signal length and sample rate, and so to improve the resolution, the number of samples used in the FFT must be increased. In order to improve the clarity of the Fourier signal and reduce the effects of spectral leakage, window functions, such as Hanning and Blackman, are commonly applied [126]. Windowing reduces the amplitude of the discontinuities at the endpoints by multiplying the time signal by a finite length window function with an amplitude that smoothly reduces to zero at its endpoints, ensuring that the endpoints of the time signal meet and the signal forms a continuous waveform. Window functions are discussed in more detail in Chapter 6.

3.4 Chapter summary

In this chapter, a detailed overview of the research methodology used for this PhD has been presented. The five key research steps were identified as:

1. Detailed literature review, which helped to identify the current state-of-the-art in the field of fringe projection, metrology frame development and condition monitoring.

2. Defining the research objectives based on the research gaps identified in the literature review.

3. Software development and implementation, description of the key software packages and how each was applied throughout the project.

4. Experimental methods, description of the hardware used to perform experimental investigations, collect data and manufacture artefacts.

5. Analysis methods used to investigate the results obtained from the work carried out in steps three and four.

The key software packages, hardware and analysis tools used throughout the PhD have been described, which included a breakdown of their working principles and how each tool was used to aid investigation into the research objectives. This chapter lays the foundation for the work presented in the following chapters, such as the design and simulation software packages, CREO and ANSYS, which were vital tools used in Chapter 4 for the development of the mechanical multi-view fringe projection system.

Chapter 4

Design specification and system design

4.1 Introduction

In order to investigate the challenges of multi-view fringe projection, a mechanical system was required. The purpose of the mechanical system is to facilitate and enable the operation of the developed optical system, so a complex setup must be designed which is able to mount multiple cameras and projectors around the part being measured with effective vibration isolation and kinematic mountings to ensure full-form accurate and repeatable fringe projection measurements can be taken. The design of the frame represented a vital step to the PhD as it was a key focus of the work presented in the following chapters, and provided the ideal platform to further investigate the effects of mechanical noise on fringe projection measurements, test the developed live vibration monitoring system and demonstrate the benefit of condition monitoring for measurement systems.

In this chapter, the complete development of the multi-view fringe projection mechanical design is discussed and followed five key steps: 1) design specification, 2) initial concepts, 3) design evaluation, 4) final design development and 5) proof of concept. Step 1 allowed the requirements of the multi-view mechanical design to be clearly defined, with performance metrics to quantify how each attribute must be met. In order to define the dynamic

performance of the system, an investigation into the effects of vibration on fringe projection measurements needed to be performed. To perform the investigation, a methodology needed to be developed to enable the effects of vibration to be studied in both a computer simulation and experimentally. Step 2 allowed multiple design ideas to be generated, which offered different advantages and disadvantages, in an attempt to approach the challenge from different angles to explore a variety of potential solutions. Step 3 objectively assessed the strengths and weaknesses of each design concept generated in relation to identified key factors, such as dynamic performance and ease of use, to ensure the best design solution is selected. Step 4 developed the concept selected, and improved the design using the insight gained from exploring multiple design solutions. Step 5 was the proof of concept, which involved performing finite element analysis simulations to demonstrate the final design met the requirements detailed in the specification.

A vital step of the design process was writing a statement of requirements to provide a clear description of the functionality and performance metrics for the proposed system. The statement of requirements is an effective tool to guide key design decisions, and enables the design to be readily assessed against the defined performance criteria. However, during the process of defining the statement of requirements, it became apparent that it was not possible to define the required performance metrics without a better understanding of the sensitivity of fringe projection to mechanical noise, such as vibration. To this end, a methodology was developed which allowed the vibrational effects on fringe projection measurements to be investigated and allowed the required performance metrics to be defined.

4.2 The effects of vibration on fringe projection measurements

In order to investigate the sensitivity of fringe projection measurements to vibration, a methodology needed to be developed to allow for a computational simulation, and an experimental study, to verify and compare with the simulated results to be carried out. The methodology and results for each of the theoretical investigation and experimental study are explained in the following sections.

4.2.1 Simulation of vibration in fringe projection

Vibrational noise can affect the values of both the pixel intensity of the projected fringe patterns and the perceived pixel intensity in the captured images, which can cause errors when extracting the phase and absolute height information from the pixel intensity values [86, 87]. To investigate the expected theoretical behaviour, and verify the experimental results, it was first necessary to create a mathematical model which was capable of simulating vibrational effects on a fringe projection measurement.

A simulation was created to generate sinusoidal phase shifting fringe patterns, and determine the measurement errors caused by vibration across a range of amplitudes and frequencies when attempting to measure a flat plane. A flat plane was chosen to investigate the sensitivity to vibration when measuring the simplest surface possible, and reduce the influence of other errors sources which can be caused by more complex geometries. The main steps of the simulation procedure are as follows:

- The three sinusoidal phase shifted patterns are generated with no noise added, and then phase unwrapped to create the baseline ‘ideal’ flat plane fringe projection measurement.

- The effects of vibration are simulated by generating the three sinusoidal phase shifted patterns and combining each generated pattern with a normalised pseudo-random noise signal. This process has been demonstrated in figure 4.1.

- The combined signals were then phase unwrapped to generate the simulated noisy captured measurement of a flat plane. Without noise/errors the measurement would reconstruct a perfectly flat plane, therefore, any distortions from a flat plane seen in the noisy simulated images is a result of the errors present due to the effects of the vibration signal.

- Each simulated 'noisy' fringe projection measurement was compared to the ideal measurement on a pixel-by-pixel basis, from which a mean pixel distortion was calculated across the measurement.

- The simulated process was performed for a range of different amplitudes of vibration, and was repeated 500 times at each amplitude in order to find the mean response at each of the varying levels of vibration.

The results of the simulation can be seen in figure 4.2. The simulation results shows the expected behaviour [127] and it can be seen that there is a clear linear trend between increasing vibration and mean phase error up to 0.52 rad (dashed line in figure 4.2). There is a sharp increase in the mean phase errors at >0.52 rad; this can be attributed to the fact that the vibration amplitude in some instances is larger than the size of the phase shifts between patterns, which affects the phase unwrapping process and so causes significantly larger distortions in the reconstructed surface. The simulation results match well with the expected behaviour, and so confirm the method proposed as an effective way to investigate the theoretical effects of vibration on fringe projection measurements.

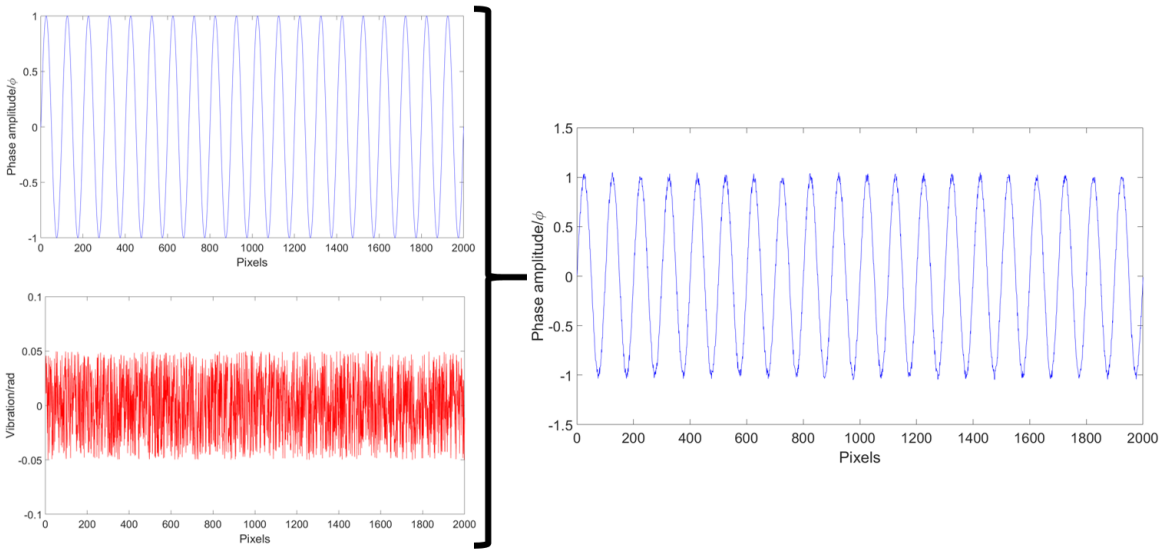


Figure. 4.1 An example dataset created using the simulation method of combining the ideal sinusoidal phase shifting pattern with a normalised pseudo-random noise signal to create simulated noisy fringe projection images.

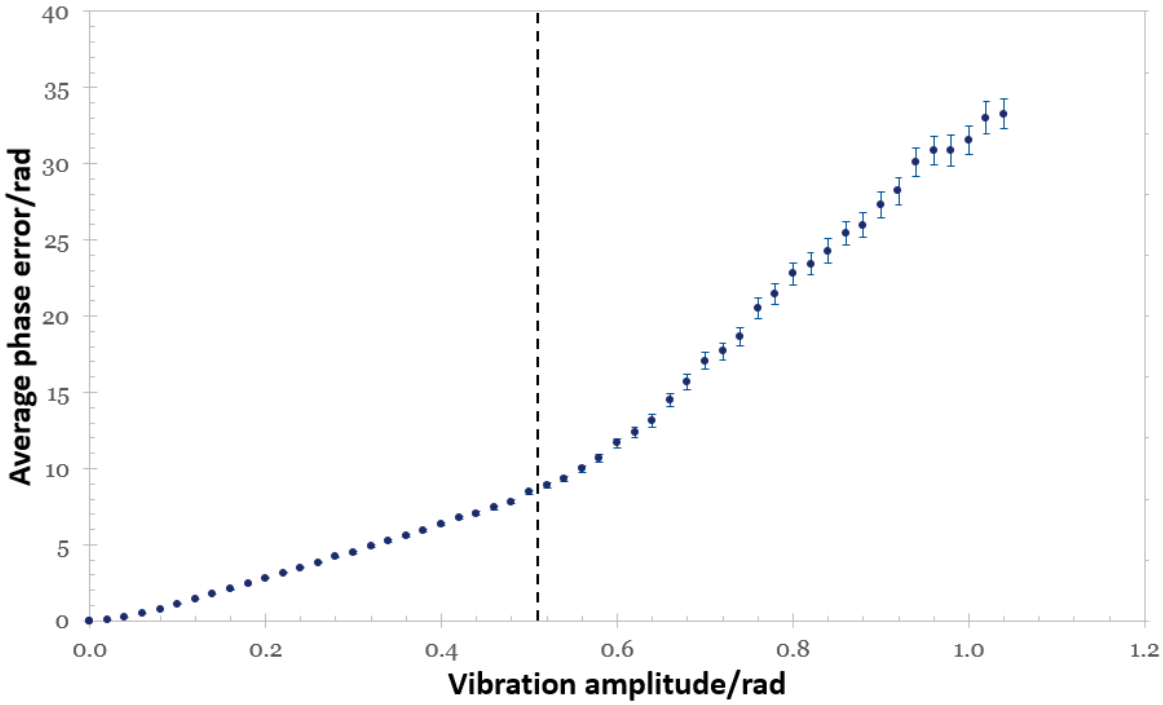


Figure. 4.2 Simulated results for the effects of vibration on fringe projection measurements, which shows increasing the amplitude of vibration causes an increase in the measured phase error, with a sharp increase in error seen when the amplitude exceeds the size of the phase shifts between patterns leading to phase unwrapping errors illustrated by the dashed line.

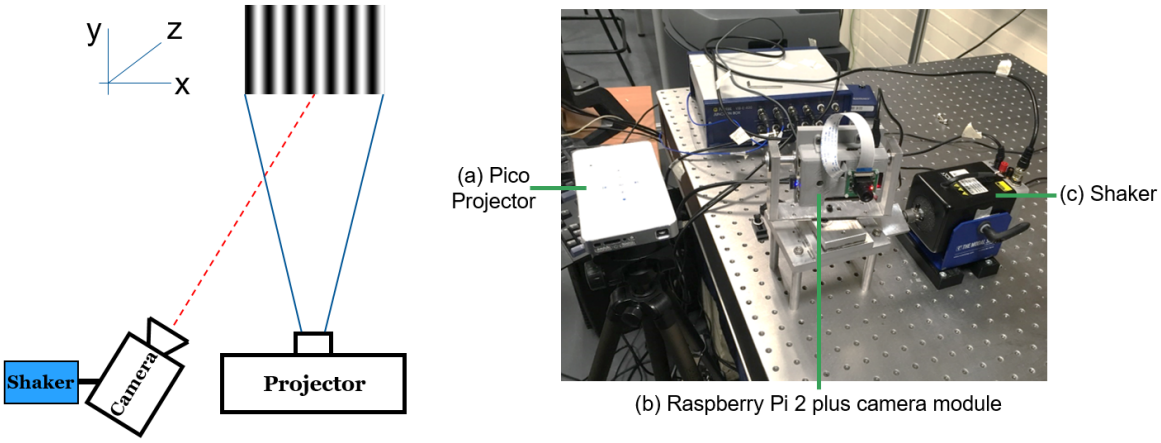


Figure. 4.3 Schema and picture of the camera vibrating isolated experimental setup using an (a) iCODIS G1 pico projector (b) Raspberry Pi 2 with an 8 MP camera module, and (c) Smart Shaker K2007E01 which provides the vibration to the setup

4.2.2 Experimental investigation

A simple experimental configuration was designed to mount a projector and camera, and a shaker was used to apply vibration to the setup. The designed experiments allowed for the vibrational effects on three different fringe projection system configurations to be investigated. The three configurations were: two isolated setups where either only the camera or the projector are vibrating, and one setup with both components vibrating. The equipment used for the experiments was an iCODIS G1 pico projector to project the fringes, a Raspberry Pi 2 with an 8 MP camera module to capture the images, and a Smart Shaker K2007E01 to excite the structure. The three different experimental configurations can be seen in figures 4.3, 4.4 and 4.5. The experimental work also allowed the viability of the low cost equipment being proposed for the final multi-view system to be investigated.

The effects of vibration on fringe projection measurements were then studied using the three designed experimental setups, and a baseline measurement comparison method whereby:

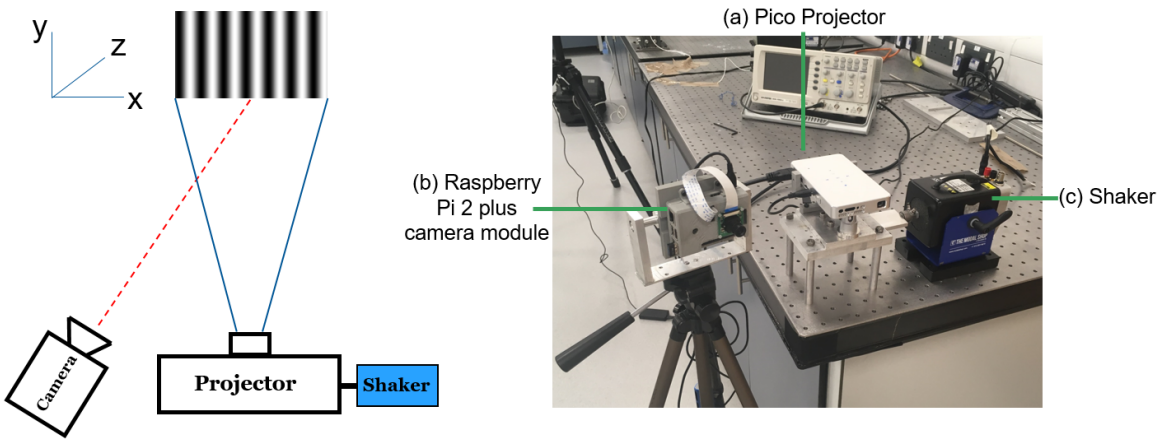


Figure. 4.4 Schema and picture of the projector vibrating isolated experimental setup using an (a) iCODIS G1 pico projector (b) Raspberry Pi 2 with an 8 MP camera module, and (c) Smart Shaker K2007E01 which provides the vibration to the setup

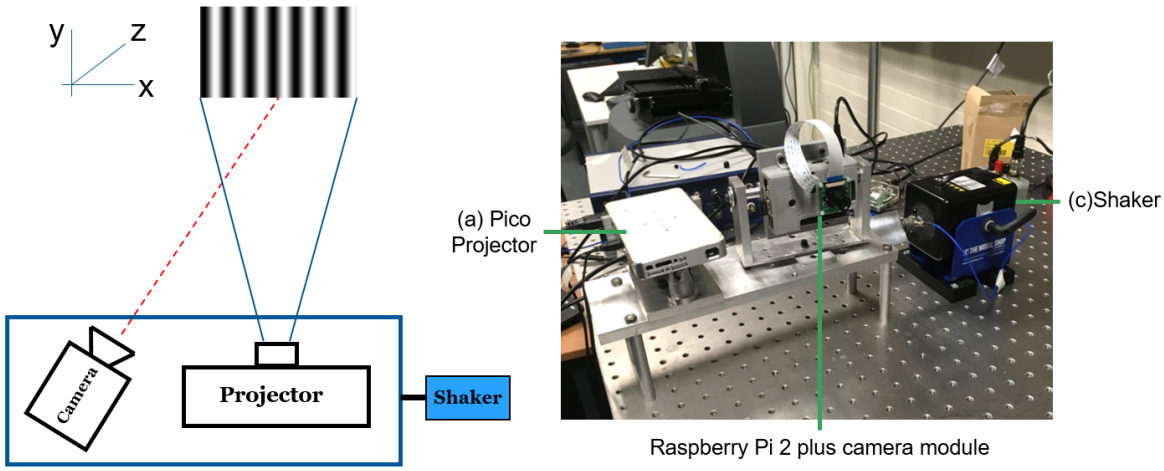


Figure. 4.5 Schema and picture of the combined vibrating experimental setup using an (a) iCODIS G1 pico projector (b) Raspberry Pi 2 with an 8 MP camera module, and (c) Smart Shaker K2007E01 which provides the vibration to the setup

- Ten baseline measurements of a flat 250 mm $\times$ 250 mm plane with no applied vibration excitation were performed, and the mean of the measurements found to give the 'mean baseline measurement'.

- Ten repeat measurements were then taken at each varying level of vibration/excitation applied to the structure. The natural frequencies for the experimental setups was used for the input excitation throughout. The method used to find the natural frequencies is explained below.

- The vibration/excitations present in the structure were measured using a laser vibrometer, as the shaker output excitation could only be controlled by the voltage input and so the responses in the structure needed to be measured.

- A pixel-by-pixel comparison was performed to find the distortion error between each measurement and the mean baseline measurement.

- Using the pixel-by-pixel comparison results, the mean phase error across the measurement was calculated, and the mean response of the repeated measurements found.

In order to investigate the effects of vibration in the 'worst-case' scenario, the experimental investigation was carried out using the natural frequencies of the setups to ensure the largest responses are seen in the system. Much larger amplitude responses are seen at the natural frequency because as the frequency of the forced vibrations approaches the natural frequency, the structure exhibits a resonance and so the excitation is in phase with the natural frequency, which results in vibration with a much larger amplitude. Above the resonant frequency, the driving force of the shaker is out of phase with the oscillation of the structure and so the amplitudes of the responses decrease, where the small peaks present are likely due to harmonics of the natural frequency. To find the natural frequencies a simple frequency analysis experiment was performed, which involved stepping through a range of frequencies with a constant amplitude, and measuring the response on the system to the

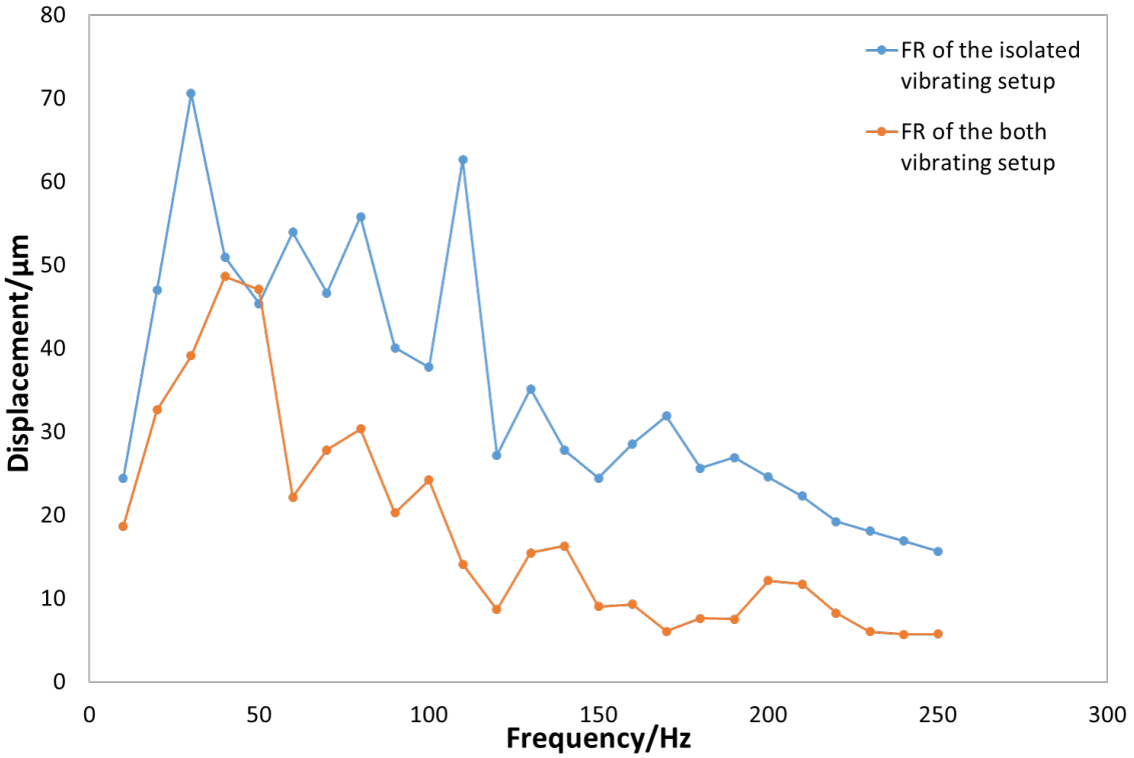


Figure. 4.6 Frequency response of both the isolated configuration and the combined configuration to varying vibration frequencies applied to the system, used to identify the natural frequency of the experimental setups.

different frequency inputs. The frequency response curves in figure 4.6 show the largest responses in both configurations are between 30 Hz to 40 Hz. Based on the frequency analysis results, it was decided that the experimental testing would be performed at 30 Hz to investigate the effects of vibration with the largest responses but also be comparable between the different experimental setups.

The experimental results are shown in figure 4.7, with the increasing vibration excitation input plotted on the horizontal axis against mean phase error in radians and mean measurement error in millimetres. The mean measurement error was calculated by converting the mean phase error to a measurement scale using a phase to step height scaling factor [128]. This conversion allowed the mean measurement error to be related to a physical scale, and compared to the accuracy targets preset for the system. The experimental results

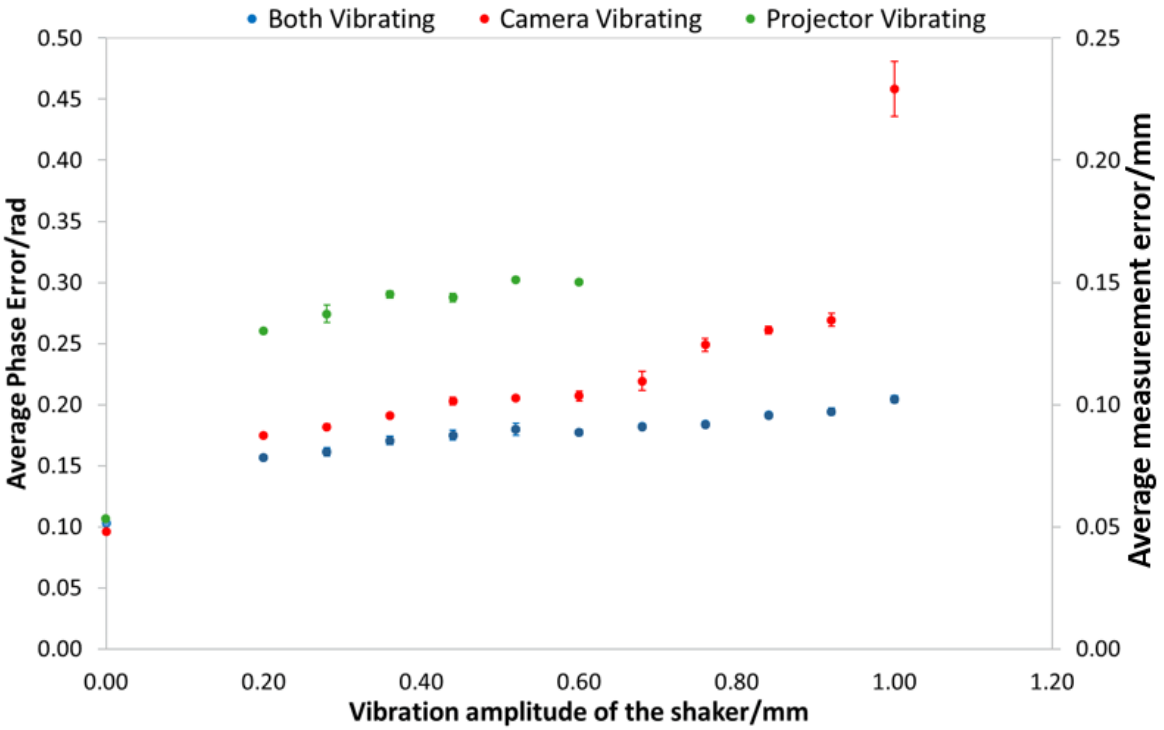


Figure. 4.7 Experimental results showing, increasing the amplitude of vibration on three experimental fringe projection setups causes an increase in mean measurement error.

in figure 4.7 followed a similar trend to the simulated results. The mean error has a near linear response with vibration amplitude, and clearly demonstrates how the fringe projection measurement quality decreases as vibration amplitudes are increased. The results also show that the fringe projection system is more sensitive when the vibration effects are present in only one component in the system, and so any multi-view frame design should mount the camera and projector together to reduce the errors from vibration. The isolated projector vibration experiments were limited to the lower range of vibration amplitudes due to the dropout in operability of the projector at higher vibration amplitudes.

A key finding from the experimental results was that the proposed equipment was too noisy to achieve the 50 µm target set for the system. The mean phase error in the baseline measurements were more than 50 µm when measuring in ideal conditions and a simple surface, so the experimental results showed that the developed multi-view fringe projection system requires new equipment, which is less sensitive to noise. As the noise levels exceeded

the aimed uncertainty, the results could not set the required performance metrics for the mechanical system. In order to set the stability target, a metrology 'rule of thumb' was applied which states that a mechanical system must have an uncertainty no larger than 1/5th of the target accuracy. Following this rule, an uncertainty of $\leq$10 µm of the vibrational movement during the measurement window was set to achieve a target accuracy of 50 µm.

4.3 Statement of requirements for multi-view mechanical design

The statement of requirements were then defined using the findings from the simulation and experimental investigations, and the identified stability performance criteria.

- Provide 180° 3D camera and projector pre-set mounting options in order to enable the ability to project fringes and capture images from the determined optimised views to capture the full form of the component i.e. different heights, angles etc. The system should be capable of mounting multiple sets of cameras and projectors at one time.
- Rigid frame which provides $\leq$10 µm mean stability, which is detectable in the instrumentation throughout the 15 s measurement time, to achieve this control of both physical and thermal properties of the frame, i.e. limits vibrations, deflection, thermal expansion and positional errors, is required. This stability target has been defined so that the measurement system can meet the 50 µm accuracy target, and the pre-measurement calibration is not invalidated, i.e. no movement after calibration or during measurements.
- Minimum camera and projector working distance of 350 mm, to allow for a measurement scan volume size of 250 mm $\times$ 250 mm $\times$ 250 mm to meet the maximum additively manufactured component size using a Renishaw250.

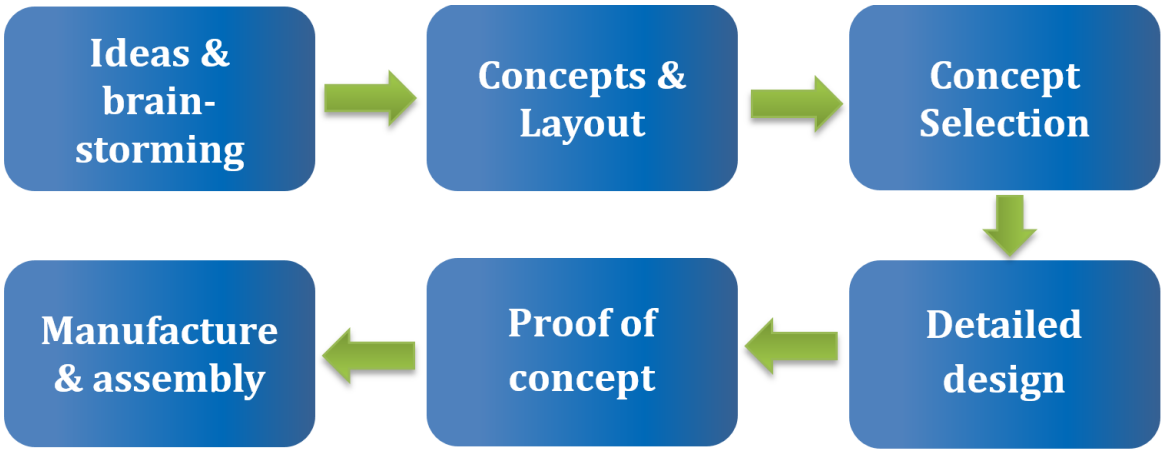


Figure. 4.8 Breakdown of the individual steps used in the design process to produce the multi-view fringe projection mechanical system.

- Modular mounting options to provide the ability to mount a camera or projector in each of the available mounting positions.
- Design simulation studies to be performed and presented for sign-off, before manufacture to demonstrate proof of concept and the design meets the stability target.
- The design should be fully characterised, to analyse the design parameters and system performance.
- Maximise use of AM where possible/feasible. This is important to illustrate AM's ability to be used in complex designs and show AM can be a useful manufacturing method in metrology frame designs moving forward.

4.4 Multi-view fringe projection frame design

In order to design an effective solution, it was vital to follow a systematic and logical design process; the steps have been explained diagrammatically in the flowchart in figure 4.8.

4.4.1 Design concepts

The third step of the design process was generating several different concepts, in order to consider different possible design solutions and find which design was best suited for the proposed measurement system. In order to evaluate each concept generated, a design evaluation matrix was created, which allowed for the merits and flaws of each concept to be objectively assessed. In addition, the design evaluation matrix allowed the key aspects of the design to be identified, so that they could be weighted accordingly to influence the overall design assessment score. The design attributes evaluated in the matrix were:

- Functionality – Assessed each concept based on the design's ability to meet the required applications need. In the case of the multi-view fringe projection system, key functions included: 180° of coverage for camera and projector mounting positions, flexibility of providing multiple mounting positions and adjustment in measurement volume.
- Cost – Assessed each concept based on the predicted cost to manufacture the design, which included considerations of material costs and wastage, machine time and cost of the manufacturing method.
- Performance – Assessed each concept based on the design's ability to meet the required dynamic performance of the system, detailed in the design specification, which included assessing attributes such as the number and type of joints used, mass of the structure and design freedom for the interface between the frame and camera/projector mounts.
- Ease of manufacture - Assessed each concept based on the manufacturing method likely to be used, which involved evaluating the complexity, availability, lead and cost of the method.
- Usability – Assessed each concept based on the ease of use for the end user. Attributes evaluated that contribute to this included: access to the internal features to adjust

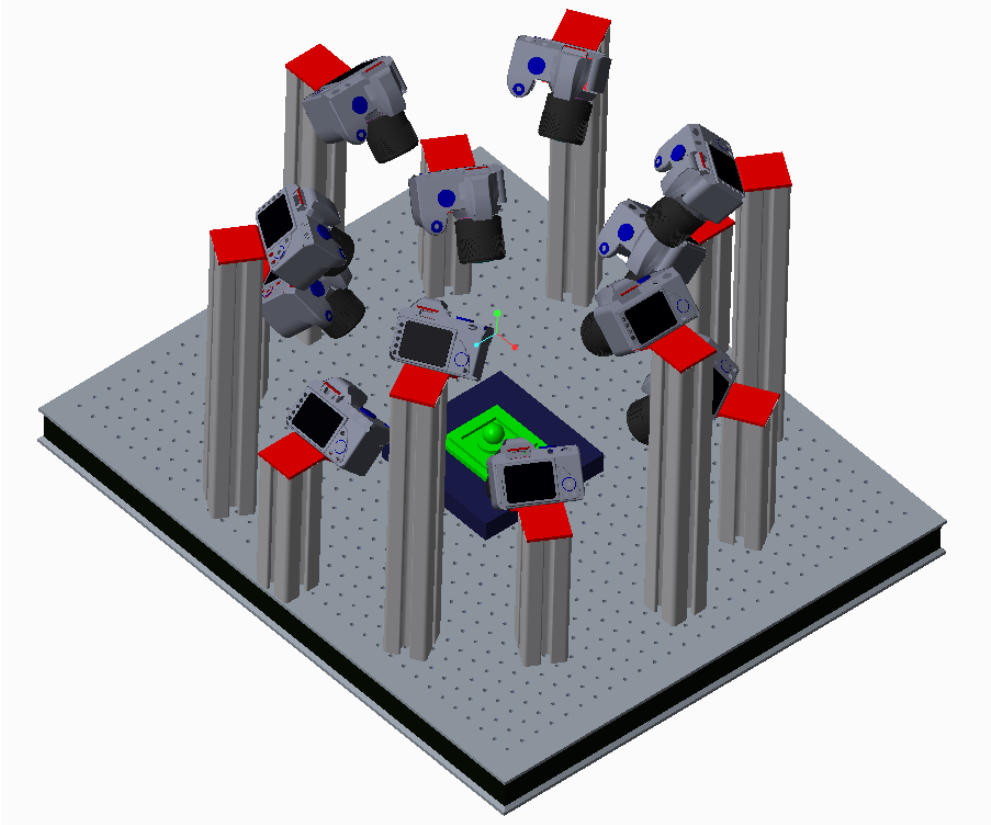


Figure. 4.9 CAD representation of the first concept ('individual posts') proposed as a design solution for the multi-view fringe projection system.

the cameras and projectors, ease of adjusting the frames volume (if possible) and camera/projector mounting positions.

The first concept design generated was the 'individual posts' design shown in figure 4.9. The design concept was generated to provide a simple design for both manufacture and assembly, which is provided as each post could be made using cut to length aluminium extrusion so would require no manufacture and could be easily attach to the optical breadboard. The identified advantages and disadvantages of design concept 1 are discussed in table 4.1.

The second concept design generated was the 'rectangular item cage' design shown in figure 4.10. This design concept is an evolution of concept 1, and also used aluminium extrusion so has the advantages of both being easy to manufacture and assemble, but addressed

Table 4.1 Advantages and disdvantages of design concept 1 - individual posts used to evaluate the design for the multi-view fringe projection mechanical frame.

Advantages	Disadvantages
The camera and projector heights can be readily adjusted, as the aluminium extrusion uses t-slots to mount fixtures so the mounts could slide up and down inside the groove.	The stability of the posts would be limited, as they would only be fixed at the bottom, with the camera/projector mass at the top of the post creating the largest bending moment and instability.
The aluminium extrusion is relatively low cost, and is bought cut to length so would not require machine time.	Does not provide 180° of camera and projector mounting positions, which is a key requirement of the system.
The design is open and so would provide easy access to adjust the cameras, projectors and measured part.	The extrusion profile and t-slot design offer limited design freedom for mounting the camera and projector fixtures.
The measurement volume can be increased or decreased by remounting the individual posts, either closer or further from the measured part as required.	Adjustment of the camera and projectors in the horizontal axis requires remounting of the posts, and is limited by the available space between posts.
Simple design would provide an easy to assemble frame, so would not require an expert engineer to operate/adjust.	Aluminium extrusion profiles have been optimised to be lightweight, which is counter-intuitive for using a larger mass to lower the natural frequency to well below the driving frequency in the system.
Can provide constant working distance for the cameras and projectors.	-

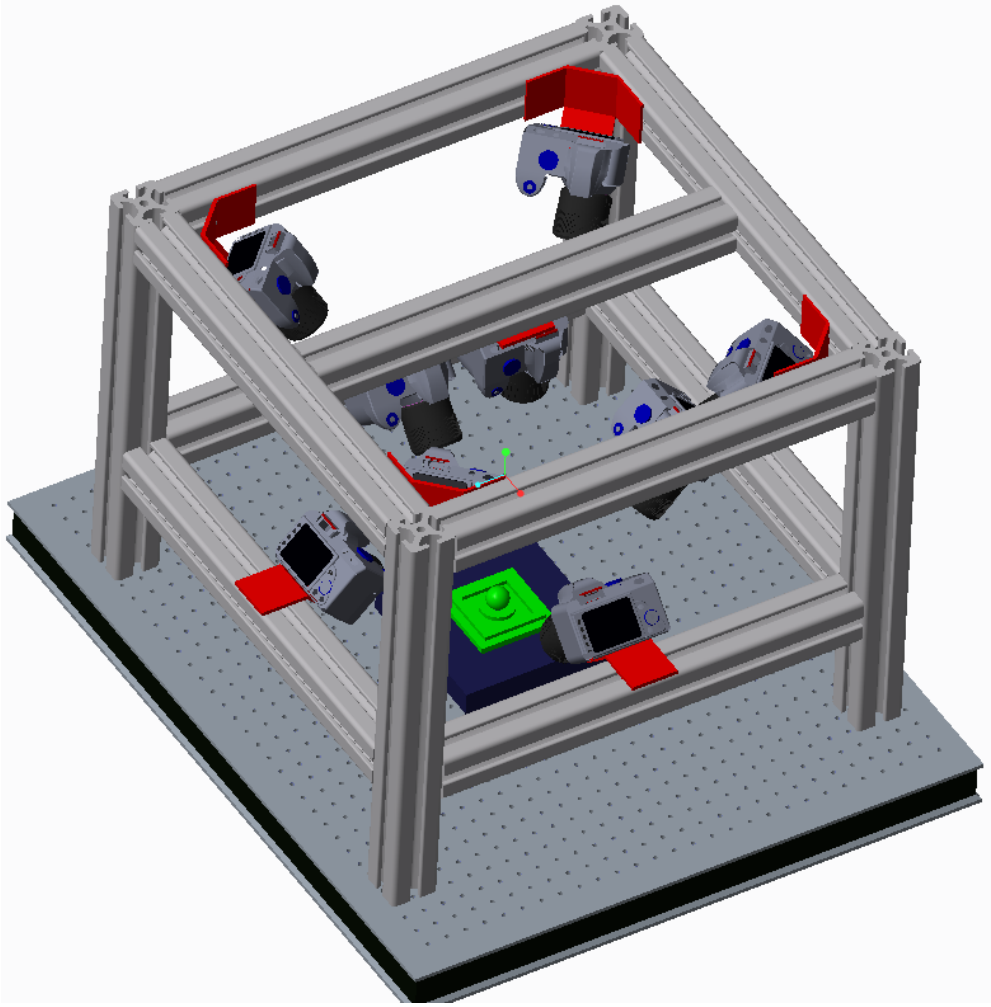


Figure. 4.10 CAD representation of the second concept ('rectangular item cage') proposed as a design solution for the multi-view fringe projection system.

some of the disadvantages identified for design concept 1. The identified advantages and disadvantages of design concept 2 are discussed in table 4.2.

The third concept design generated was the 'one-piece frame' design shown in figure 4.11. An identified disadvantage of design concepts 1 and 2 was the aluminium extrusion has been optimised to have low mass, which is counter-productive, as using increased mass would lower the natural frequency to well below the driving frequency. To this end, a design concept was generated which proposed making the frame as a single piece of material; the frame would have a higher mass and no joints, so would provide improved mechanical

Table 4.2 Advantages and disdvantages of design concept 2 - rectangular item cage used to evaluate the design for the multi-view fringe projection mechanical frame.

Advantages	Disadvantages
The cameras and projectors can be readily adjusted in the horizontal axis, using t-slots fasteners and the extrusion groove to slide the mounts laterally offering more freedom in the available mounting positions.	Aluminium extrusion profiles have been optimised to be lightweight, which is counter-intuitive for minimising the effecrs of vibration as using a larger mass would lower the natural frequency to well below the driving frequency.
The design would provide improved stability. The extrusion beams would be fixed in multiple positions, along with a symmetric design and so would provide more stable mechanical performance.	The method of adjusting the height of the cameras and projectors is inefficient, as the horizontal beam would need to be unfastened and reassembled at the required height.
Would provide 180° of camera and projector mounting positions, which is a key requirement of the system.	The measurement volume is not adjustable through the mechanical frame without manufacturing or buying in new parts.
The aluminium extrusion is relatively low cost, and is bought cut to length so would not require machine time.	Does not provide a constant working distance for the cameras and projectors.
The design is open and so would provide easy access to adjust the cameras, projectors and measured part.	The extrusion profile and t-slot design offer limited design freedom for mounting the camera and projector fixtures.
Simple design would provide an easy to assemble frame, so would not require an expert engineer to operate/adjust.	-

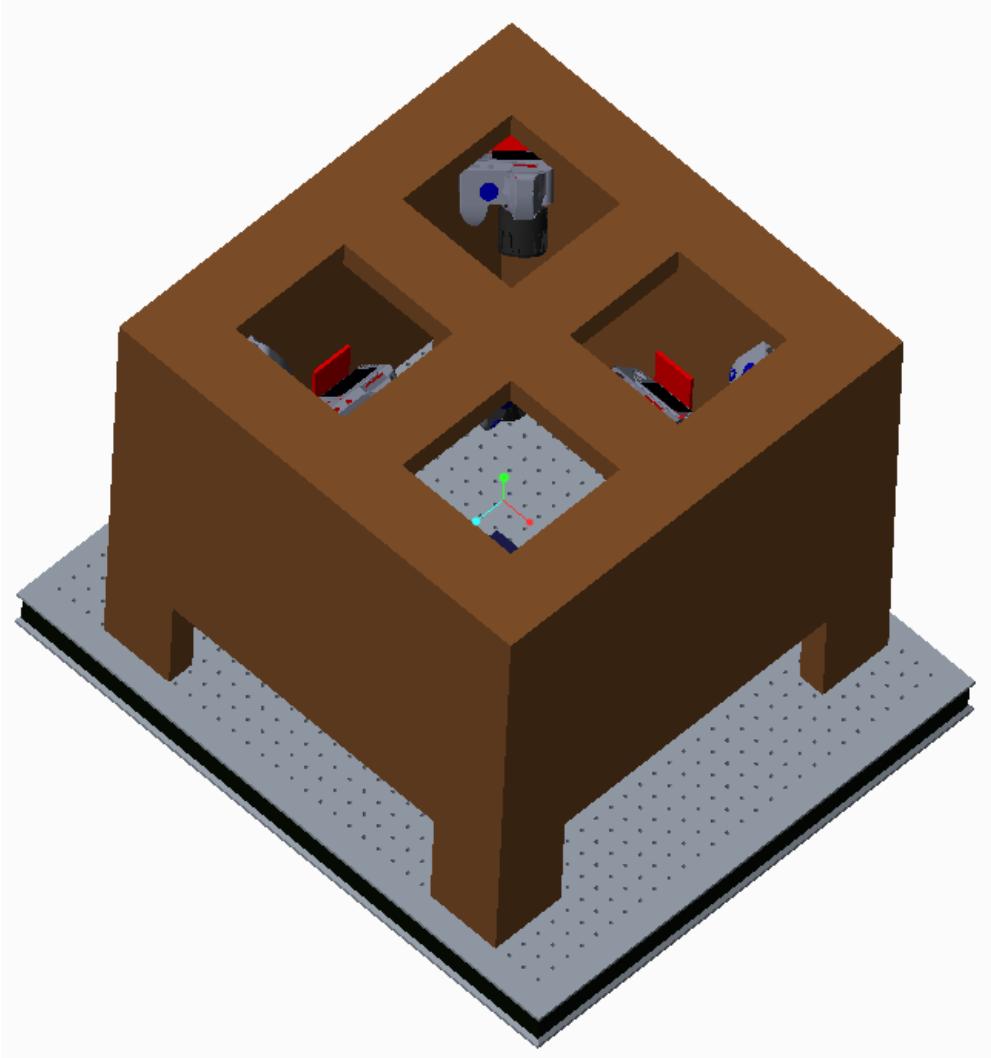


Figure. 4.11 CAD representation of the third concept (’one-piece frame’) proposed as a design solution for the multi-view fringe projection system.

stability. The identified advantages and disadvantages of design concept 3 are discussed in table 4.3.

The fourth concept design generated was the ‘circular arcs frame’ design shown in figure 4.12. The design was generated around the concept of providing a constant working distance for each of the cameras and projectors, which would be useful for fixed focal length cameras or manual adjustment focal length cameras (i.e. the Raspberry pi cameras used previously

Table 4.3 Advantages and disdvantages of design concept 3 - one-piece frame used to evaluate the design for the multi-view fringe projection mechanical frame.

Advantages	Disadvantages
Multiple camera and projector mounting positions could be provided by either designing a rail to adjust the positions in the horizontal axis, or a number of preset mounting positions.	The design is made from one piece so would have accessibility issues when attempting to adjust camera or projector positions, and trying to place measured parts inside the system.
The increased mass, reduced joints and symmetric design would provide good stability and mechanical vibration performance.	Large costs, due to material required and large wastage. The design would also require significant machine time.
Would provide 180° of camera and projector mounting positions, which is a key requirement of the system.	The measurement volume is not adjustable through the mechanical frame without redesigning the system.
More design freedom for the mounting interface between the frame and the camera/projector mounting fixtures.	To allow accessibility, the design would have to remove material to create gaps to access the internal features, however, this would significantly reduce the amount of mounting positions and the
Simple design and minimal assembly so would not require an expert to operate/adjust.	Does not provide a constant working distance for the cameras and projectors.
-	Heavy frame so not easily repositioned.

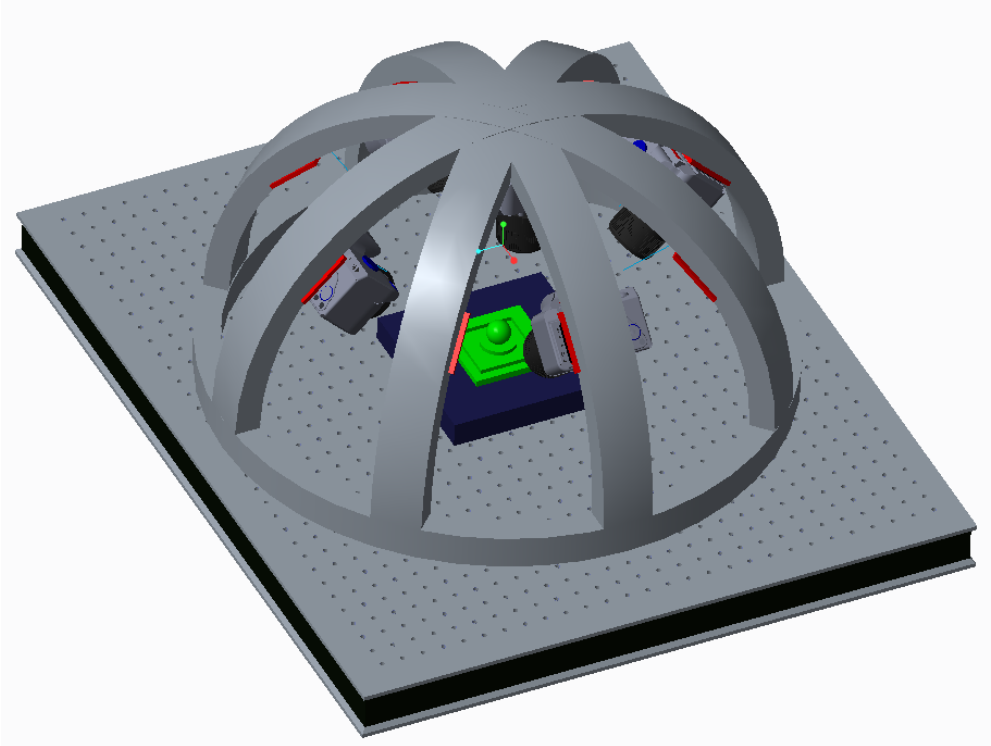


Figure. 4.12 CAD representation of the fourth concept (’circular arcs frame’) proposed as a design solution for the multi-view fringe projection system.

in the fringe projection vibration sensitivity investigation). The identified advantages and disadvantages of design concept 4 are discussed in table 4.4.

The fifth concept design generated was the ‘linkage cage’ design shown in figure 4.13. The design was an evolution from the circular arcs concepts, and attempted to eliminate the machine time and material wastage, by using linkages to create a similar arc. However, the increased number of joints would make the design less stable and so it would be unlikely that the 10 µm target could be met. The identified advantages and disadvantages of design concept 5 are discussed in table 4.5.

The design evaluation matrix created to objectively assess the design concepts generated can be seen in table 4.6. The key factors identified were the performance of the system, the functionality it provided and how easy it would be to manufacture, and so these factors were weighted highly to emphasise their importance.

Table 4.4 Advantages and disdvantages of design concept 4 - circular arcs frame used to evaluate the design for the multi-view fringe projection mechanical frame.

Advantages	Disadvantages
Can provide constant working distance for the cameras and projectors. The arcs of each strut ensure the radius/working distance are the same for all of the mounting positions.	Large costs, due to material required and large wastage. The design would also require significant machine time or need to use an expensive process such as casting to be manufactured.
The arc struts would be made out of solid material, so the frame would have increased mass in comparison to the aluminium extrusion designs. The joining mechanism for each arc to the base ring would also affect the stability, with welding providing the most stability.	Accessibility would be an issue, as increasing the number of arcs for multiple mounting positions would limit the ability to access the internal features. This would particularly be an issue if the joints were welded and so could not be removed to gain access.
Would provide 180° of camera and projector mounting positions, which is a key requirement of the system.	The measurement volume is not adjustable through the mechanical frame without redesigning the system.
Can provide multiple mounting positions, but these would likely be preset, and limited in the horizontal axis.	Welded or fixed position joints for each arc would limit the mounting position adjustability in the horizontal axis.
Ease of assembly of the frame, would be dependent on the mechanism used to join the arc struts to the base ring. Welding the arcs would mean no assembly would be required, other mechanism would increase the assembly complexity.	

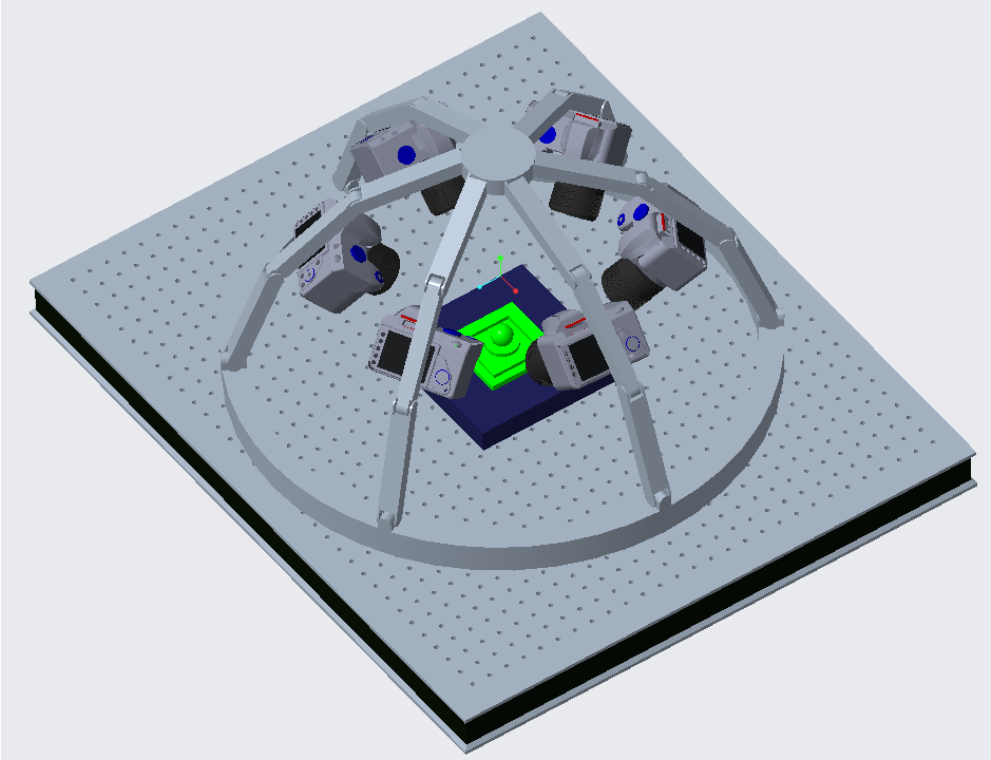


Figure. 4.13 CAD representation of the fifth concept (’linkage cage’) proposed as a design solution for the multi-view fringe projection system.

Table 4.5 Advantages and disdvantages of design concept 5 - linkage cage used to evaluate the design for the multi-view fringe projection mechanical frame.

Advantages	Disadvantages
Accessibility would be improved from the arcs design concept 4, but would also be dependent on the number of linkages included in the system.	Moderate to high costs, due to large number of parts required, and the machine time required manufacturing them.
Would provide 180° of camera and projector mounting positions, which is a key requirement of the system.	The linkages would likely cause instability in the structure due to the increased number of joints and fixing method. In addition, the lightweight frame would increase the natural frequency and so it would be closer to the driving frequency within the system.
Can provide multiple mounting positions, but these would likely be preset, and limited in the horizontal axis.	Complex design and multiple parts would make the system fiddly to assemble, and require an expert to operate/adjust.
The measurement volume can be increased/decreased by adding/removing linkages from the system.	Linkages would provide limited mounting interface between the camera and projector fixture and the structure.
Can provide constant working distance for the cameras and projectors. The arcs of each strut ensure the radius/working distance are the same for all of the mounting positions.	Limited camera and projector mounting options. Increasing number of linkages would decrease the accessibility, so we need a trade-off between these features.

Table 4.6 Design concepts evaluation matrix.

Concept	Functionality	Cost	Performance	EoM	Usability	Overall score
Concept 1 - Individual posts	2	5	2	5	4	60
Concept 2 - Rectangular cage	4	4	4	5	4	76
Concept 3 - One piece frame	3	2	5	4	2	63
Concept 4 - Circular arcs frame	3	2	3	2	3	48
Concept 5 - Linkage cage	3	3	3	3	2	51
Weighting	4	2	5	4	3	-

EoM: Ease of manufacture

From the evaluation matrix in table 4.6, concept 2 – "rectangular item cage" was clearly found to be the most effective solution and scored consistently well in all of the key attributes identified and evaluated. The rectangular item cage concept had key advantages such as low cost and easy to manufacture and assemble, as it utilises bought-in aluminium extrusion components, which are cut to length and straight forward to assemble. In addition, it offers an easy to use solution, as access is readily available around the rig, with a plethora of available mounting positions for cameras and projectors around the rig. Based on the findings of the evaluation matrix, concept 2 was progressed to the next step, to be further developed, before being analysed to demonstrate the design could meet the required performance.

4.4.2 Design development and final design

In order to verify the stability performance of concept 2 – "rectangular item cage", a finite element analysis (FEA) simulation study was performed using ANSYS software, to simulate vibrations on the aluminium extruded beams. The purpose of the study was to quickly assess whether the concept was a viable solution to meet the 10 µm stability target, as well as explore the available extrusion profiles to see how the different sizes affected the frames' performance. The ANSYS FEA simulations were performed with loads of 10 N, 50 N and 100 N applied downwards in the z-axis. Each applied load was stepped through a range of frequencies from 10 Hz to 3000 Hz in 10 Hz steps, and the maximum deformation across the beam calculated. Fixed constraints were applied to the two end faces of the profile, to simulate the aluminium extrusion being welded to a vertical beam on both sides. A heat map showing a visual representation of how the excitation forces propagate around the part can be seen in figure 4.14. The full simulation results for all of the profiles investigated are shown in table 4.7.

From the results of the ANSYS simulations shown in table 4.7 it is clear that the aluminium extrusion can provide the required stability performance. As to be expected the

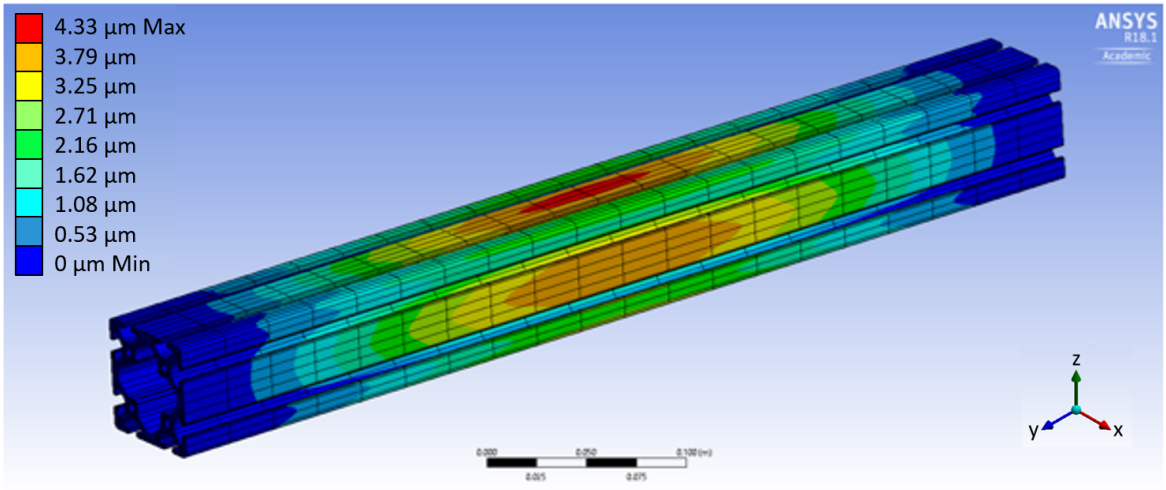


Figure. 4.14 Heat map of the maximum deformation on a 60 mm × 60 mm aluminium extrusion profile showing how the excitation force applied to the middle of the strut propagates around the part.

Table 4.7 ANSYS aluminium extrusion simulation results investigating the viability of the different profiles to provide the required stability for the proposed multi-view fringe projection system.

Item profile/mm	Length/mm	Force applied @ 10 Hz to 3000 Hz		
		10 N	50 N	100 N
		Maximum displacement/µm		
20 × 20	550	12.99	64.97	129.93
40 × 20	550	6.18	30.90	61.79
80 × 20	550	3.09	15.45	30.89
60 × 30	550	1.84	9.20	18.40
60 × 60	550	0.87	4.33	8.65
80 × 40	550	0.53	2.64	5.28
80 × 80	550	0.28	1.42	2.83
100 × 50	550	0.74	3.73	7.46

larger sizes offer better stability, and all of the profile sizes larger than and including 60 mm × 30 mm provide sufficient stability performance up to loads of 50 N. The investigation of different profile sizes yielded the idea of combining different profile sizes in order to add additional stability to the main struts of the frame, and then use thinner profiles for horizontal struts in the frame. The profiles were selected using the 10 μm target as a threshold, which with a force of 50 N can be seen by the dashed line in table 4.7 as between the 60 mm × 30 mm profile and the 80 mm × 20 mm profile. The aim of this was to reduce cost and unnecessary bulk, and so provide a rigid frame that is more user friendly and readily allows access to the all areas of the rig. The final design has been shown in figure 4.15.

The final frame uses 60 mm × 60 mm aluminium profile for the vertical posts, and 60 mm × 30 mm aluminium extrusion for the horizontal beams. The extrusions are connected using the universal right-angled fastening set, which has been designed specifically for resistance to displacement, torsion and deflection. Right-angled brackets have also been used to further stabilise the joints between the struts. Welded feet were designed to connect the vertical extrusion beams to the optical breadboard, the feet use multiple connections to constrain the frame in each axis of motion.

4.4.3 Proof of concept

In order to prove the final design would meet the desired stability performance metric, an ANSYS simulation was setup to test the performance of the complete frame assembly. The DSLR cameras' (chosen as part of the fringe projection software system) shutter and internal mirror mechanisms were identified as the largest excitation source, and so in order to estimate the excitation that the structure would experience an experiment was designed to characterise the forces exerted by the camera excitation.

In the camera characterisation experiments, a triaxial piezoelectric accelerometer was mounted on top of a DSLR camera in order to measure the acceleration caused by the camera

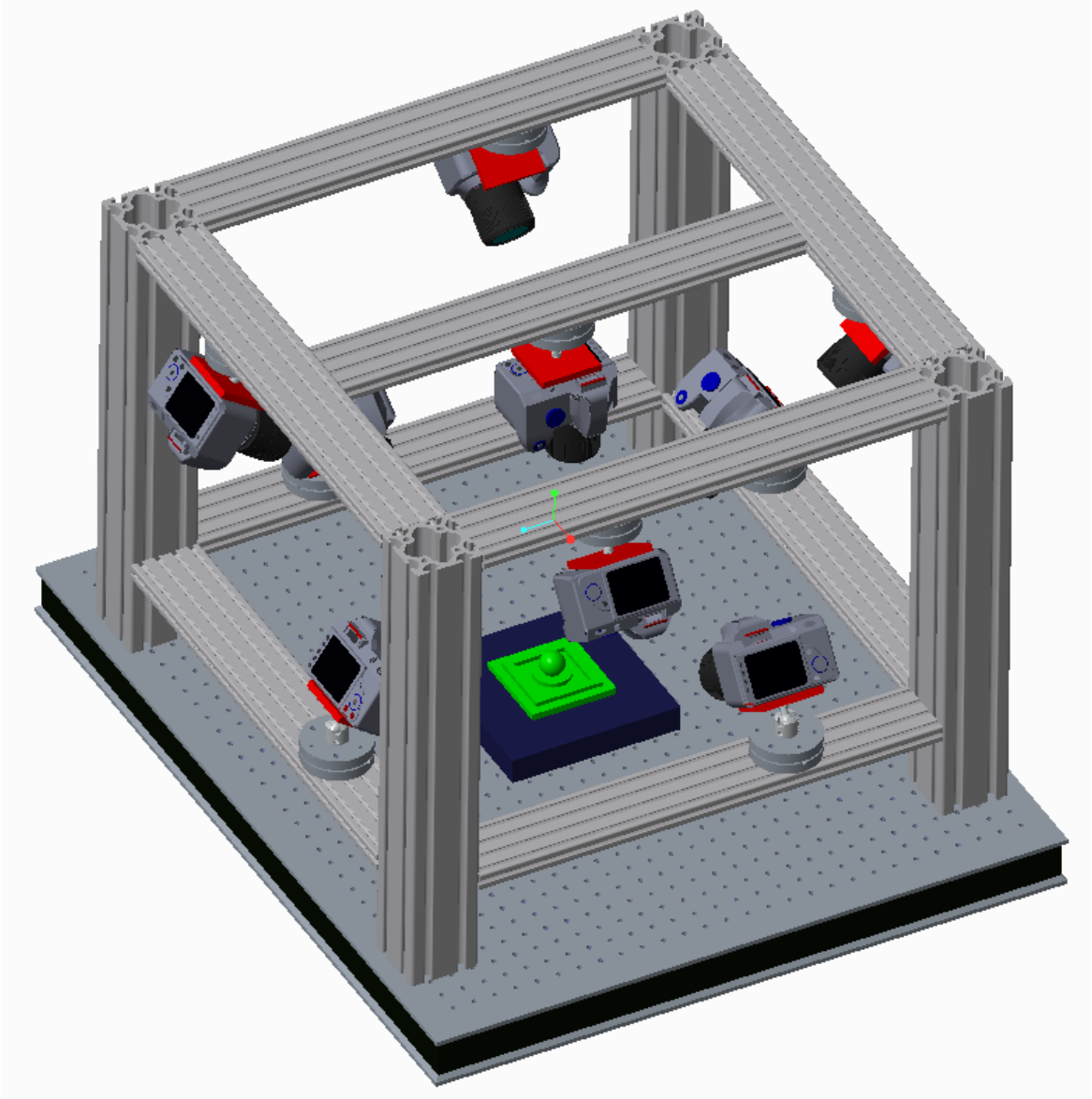


Figure. 4.15 CAD model of the final multi-view frame design, using 60 mm $\times$ 60 mm aluminium profile for the vertical posts, and 60 mm $\times$ 30 mm aluminium extrusion for the horizontal beams, based on the results of the FEA simulations.

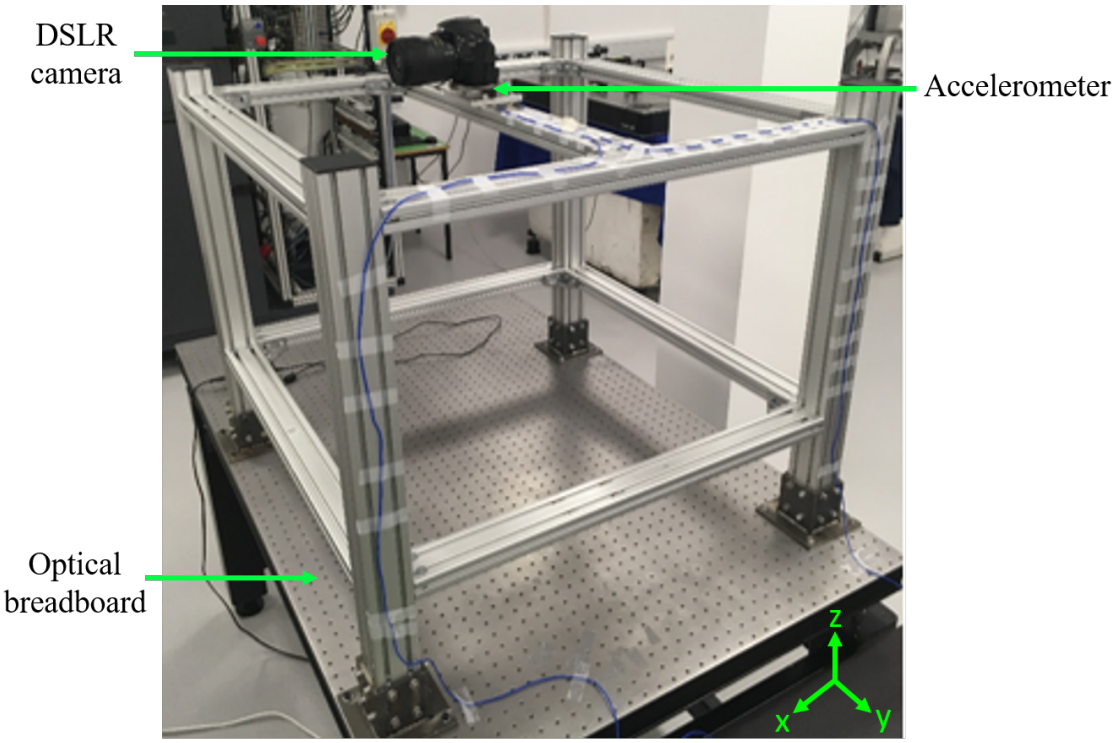


Figure. 4.16 Experimental setup to characterise the excitation that the DSLR camera inputs into the metrology frame, using a triaxial accelerometer to measure the acceleration when capturing images.

shutter and the movement of the internal mirrors. The setup is shown in figure 4.16. This designed experiment was a key step as it allowed for the largest vibration source in the proposed fringe projection system to be measured, and the effect of changing the camera parameters to be investigated.

The triaxial piezoelectric accelerometer measures the change in the strain of the piezoelectric elements and outputs a voltage signal that is proportional to the acceleration. The measured voltage signal was converted into acceleration using the manufacturer's specified sensitivity factor of 102.14 mV/ms^{-2}. The experiment investigated the effect of different camera exposure times by analysing the largest peak-to-peak response when the camera is capturing an image. The experiment was repeated 20 times for each different exposure time to find the mean of the peak responses. The results are shown in figure 4.17, with averaged

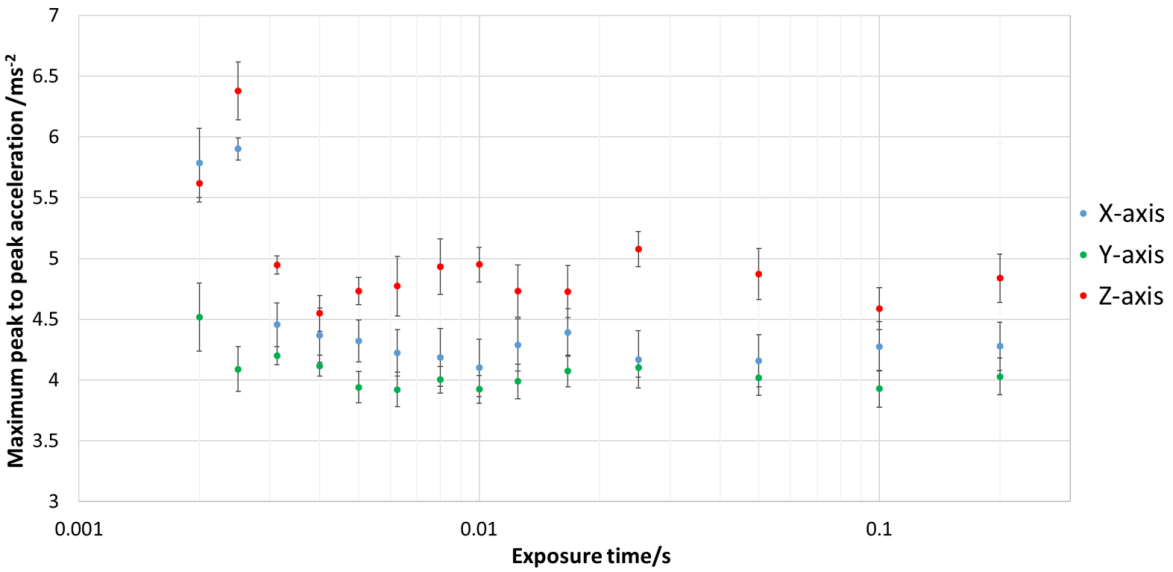
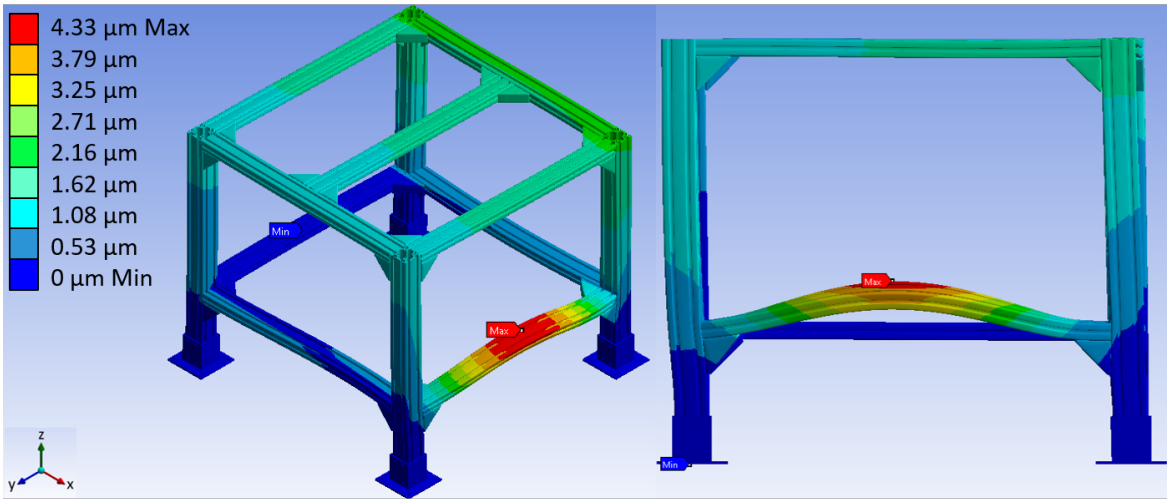


Figure. 4.17 Camera excitation characterisation results, the averaged peak-to-peak response in each of the x, y and z axes, is plotted against log of changing exposure time, and shows that the response of the camera is increased at smaller exposure times but the exposure time negligible effect at the longer exposure times.

peak-to-peak response in each of the x, y and z axes, plotted against logarithm of the exposure time.

From the results in figure 4.17 it can be seen that the exposure time excitation response peaks at 1/400 s, and the largest averaged response of 6.38 ms^{-2} is seen in the z-axis. Using the maximum acceleration result, the camera mass of 0.7 Kg and Newton's second law of motion (force = mass $\times$ acceleration), we find that the peak force exerted on the frame from the camera excitation is 4.47 N. Further ANSYS simulations were performed on the complete frame assembly, using the calculated maximum force to guide the range of forces to investigate and show the design concept can meet the required stability performance. The simulations were performed using fixed constraints on the bottom of the four feet, which would be attached to the optical breadboard and vibration isolation support frame. The joints are designed to be connected using bolts, t-slots and right-angled brackets, however, for simplicity in defining the simulated connections, it was decided to define the joints as welded, which is likely an over-assumption. In order to mitigate this over assumption, the range of



(a) (b)

Figure. 4.18 Heat map results, (a) isometric view and (b) side view, of the maximum deformation on the complete frame assembly with the camera excitation applied to the frame in the z-axis, showing how the camera excitation in the middle of the horizontal strut would propagate around the structure.

forces investigated was the calculated maximum force multiplied by a safety factor of two. The force was applied and stepped through a range of -10 N to 10 N in 2 N steps, with the frequency of the applied force stepped through 10 Hz to 3000 Hz, in steps of 10 Hz. This simulation procedure was performed with the force applied to the horizontal extrusion beam where the camera would be mounted in each of the x, y and z axes individually. An example of the heat map results can be seen in figure 4.18, and the full results have been tabulated in table 4.8.

The results show that the final multi-view frame design can provide the stability performance required with the largest deformation of 0.57 µm found in the z-axis with a 10 N force applied, and so demonstrates proof of concept. The assembled frame is shown in figure 4.24, and the experimental investigation into the performance of the system is discussed in Chapter 5.

Table 4.8 ANSYS simulation results for the full frame assembly with the forces applied in the x, y and z axes.

Force applied/N	Maximum deformation/μm		
	x-axis	y-axis	z-axis
10	0.48	0.23	0.57
8	0.39	0.19	0.45
6	0.29	0.14	0.34
4	0.19	0.09	0.23
2	0.06	0.05	0.10
-2	0.06	0.05	0.09
-4	0.18	0.09	0.20
-6	0.27	0.14	0.31
-8	0.35	0.19	0.42
-10	0.43	0.23	0.54

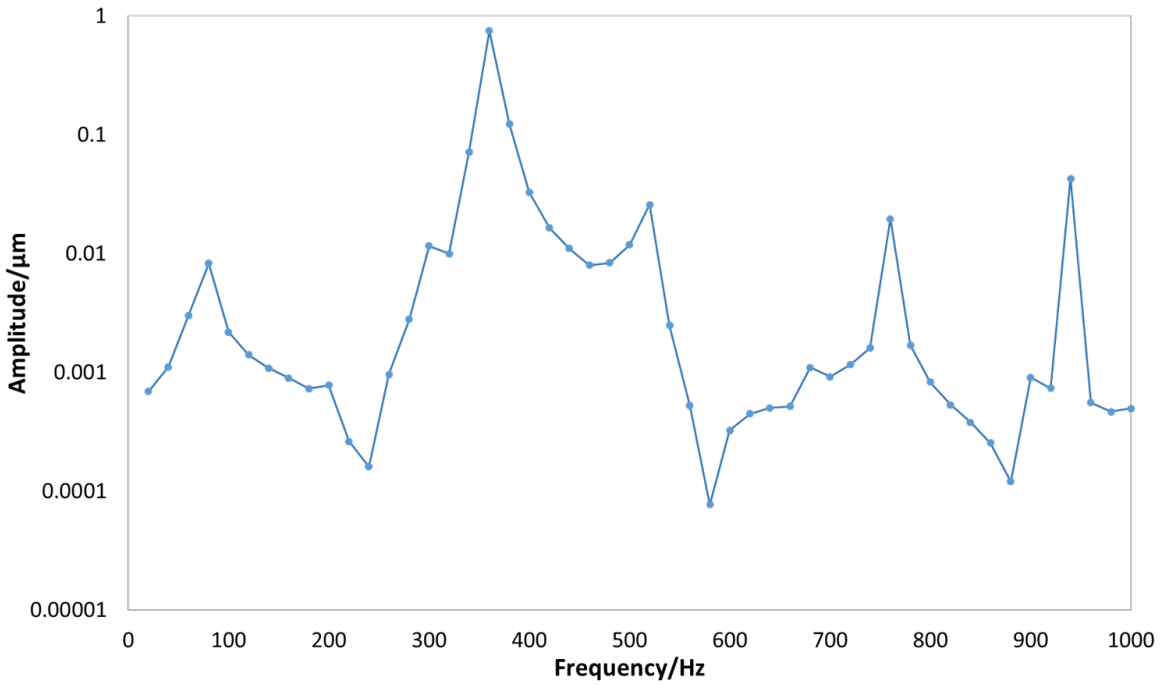


Figure. 4.19 ANSYS simulation results for the frequency response of the full frame assembly, which shows the largest response and natural frequency of the system is at 360 Hz.

4.5 Camera and projector mount design

The multi-view fringe projection system needed Camera (Nikon D3500) and projector (DLPC300 Texas Instruments) mounts to be designed to provide the necessary adjustment and interface with the multi-view frame. In order to design effective mounts, the design requirements for each of the camera and projector were identified:

Camera mount requirements - Based on the results of the vibration study, each camera should be mounted adjacent to a projector and will need to be adjustable, providing both the ability to change the pitch and yaw of the camera. The camera pitch must be adjustable to allow for the angle of the camera to be changed if the height of the horizontal struts are altered. The camera yaw must be able to rotate/swivel to adjust the angle of the camera if the distance between the camera and projector needs to be changed.

Projector mount requirements - Each projector should be mounted adjacent to a camera along each side of the frame. In a standard fringe projection system, the projector is mounted perpendicular to the measured part with the camera offset at an angle, would not require yaw adjustability. However, the multi-view fringe projection system aims to measure complex parts, multiple views may be required from the same side of the frame, and so the yaw angle may need to be adjusted to set the projector perpendicular to the measured part.

To make the projector and camera mounts modular, both designs use the same mechanisms to provide adjustment in the relevant axis. Modular mounts allow for the cameras and projectors to be interchangeable, and enable scope for using multiple measurement techniques (i.e. photogrammetry) for difficult-to-measure parts, such as multi-material parts/assemblies, problematic surface finishes or assemblies. The mounts provide yaw adjustment using a four hole flanged bearing unit, which is mounted to an interface place that attaches to the frame using t-slot connectors. This design provides 360° of yaw adjustment, with the position locked using a grub screw mechanism designed into the interface plate. The mounts provide fine pitch adjustment using a worm gear mechanism, which is driven by a screw threaded

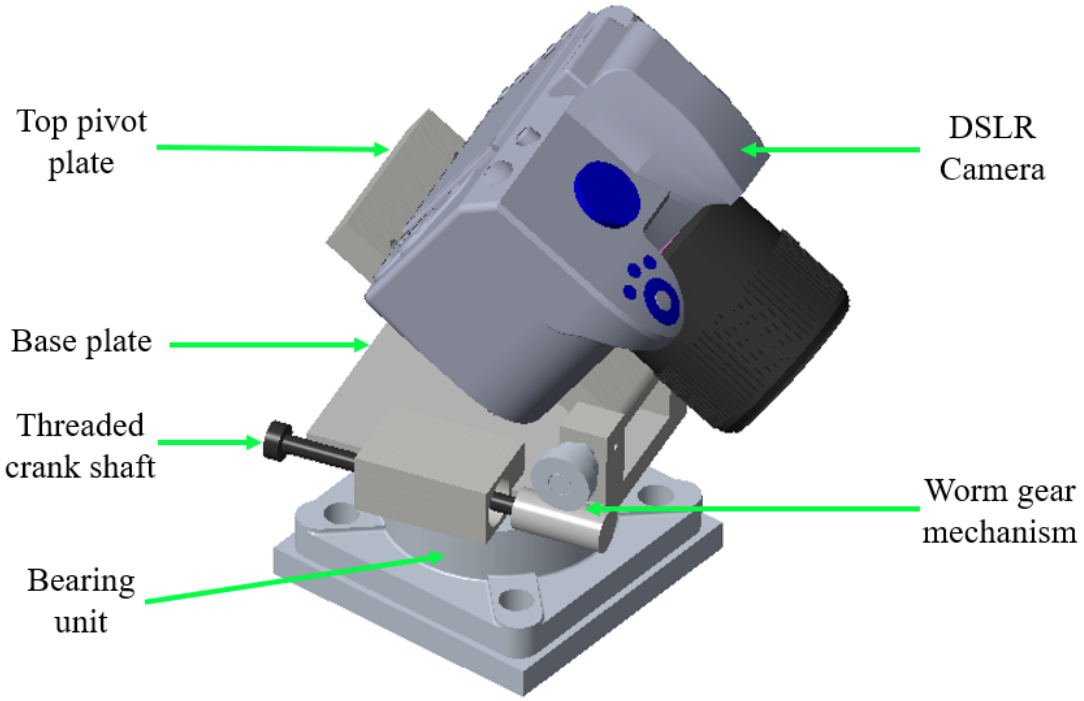


Figure. 4.20 CAD scehmatic of the camera mount design that was used in the multi-view fringe projection system.

crank shaft. This design provides 260° of pitch adjustment, uses two grub screws to lock the mounts pitch angle. The mounts are modular and allow for either a camera or projector to be mounted using three M3 clearance holes for the projector or a 1/4" thread stud for the camera. The final CAD designs and manufactured assemblies for the camera and projector mounts can be seen in figures 4.20 to 4.23.

The final design of the multi-view fringe projection system can be seen in figure 4.24, with four sets of cameras and projectors.

4.6 Chapter summary

The work presented in this Chapter details the full design process used to develop the mechanical setup for the multi-view fringe projection system. A new methodology is presented for assessing the effects of vibration on the measurement accuracy and repeatability

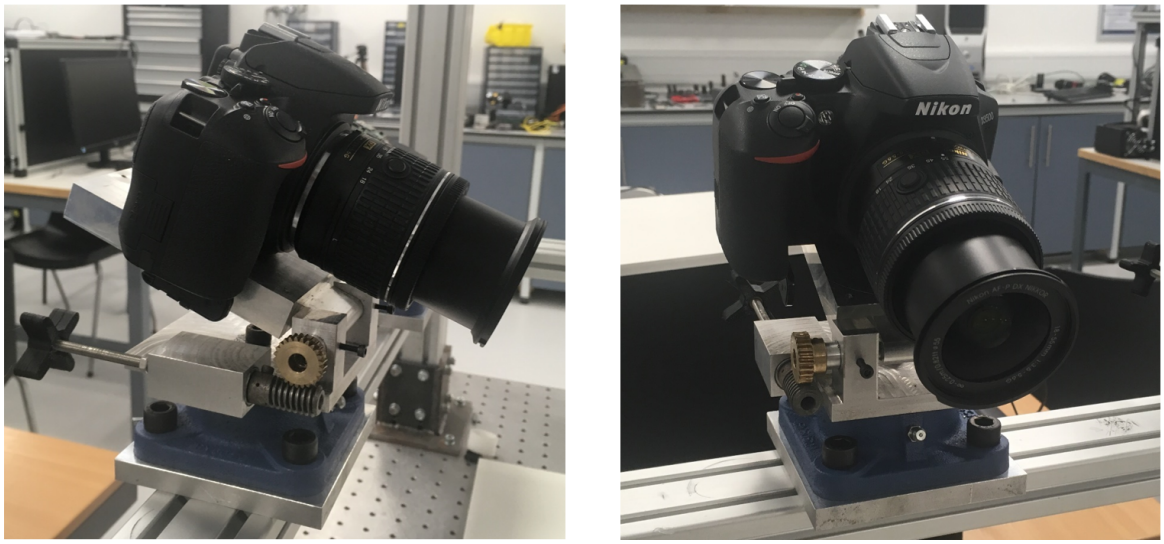


Figure. 4.21 Multi-view fringe projection camera mount, designed to provide adjustability in the pitch and yaw axes of rotation. (a) Side on view and (b) front on view.

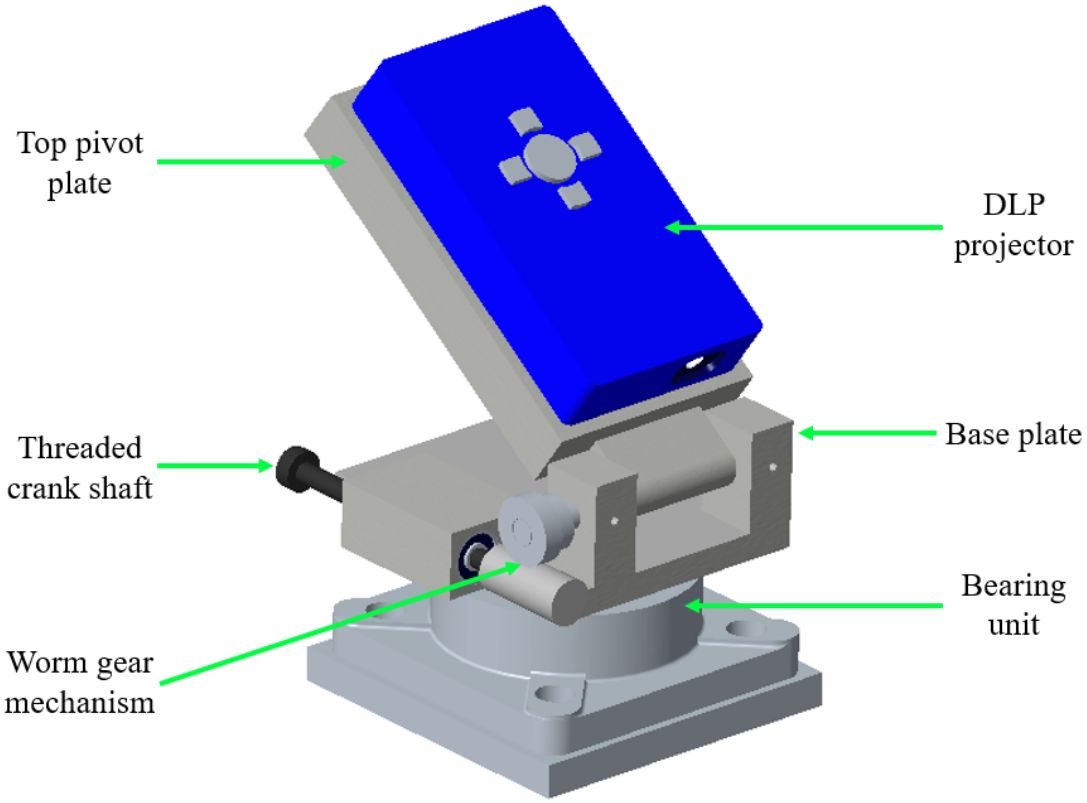
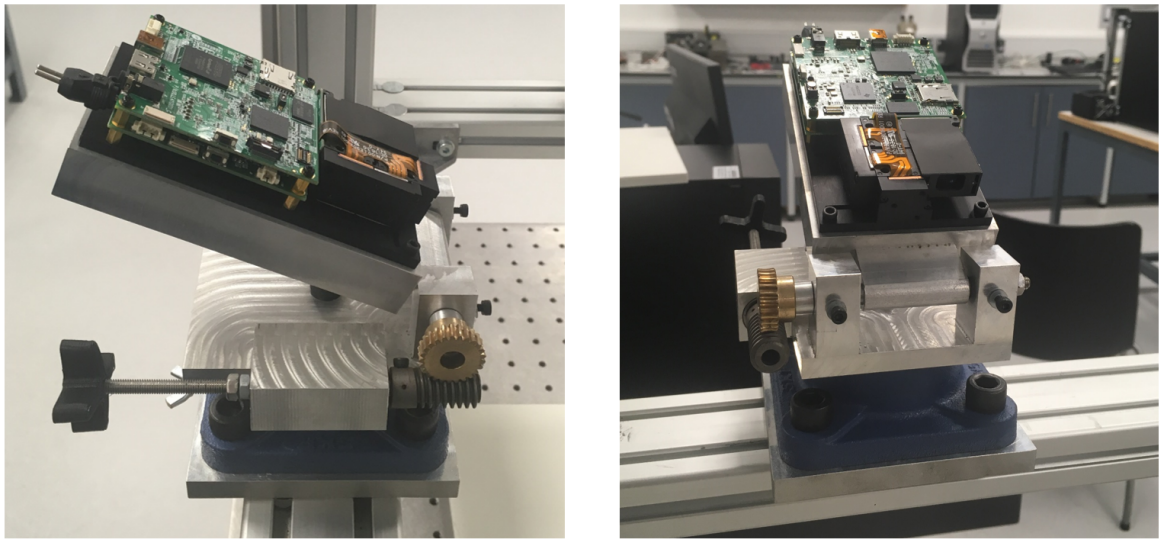


Figure. 4.22 CAD scehmatic of the projector mount design that was used in the multi-view fringe projection system.



(a) (b)

Figure. 4.23 Multi-view fringe projection projector mount, designed to provide adjustability in the pitch and yaw axes of rotation. (a) Side on view and (b) front on view.

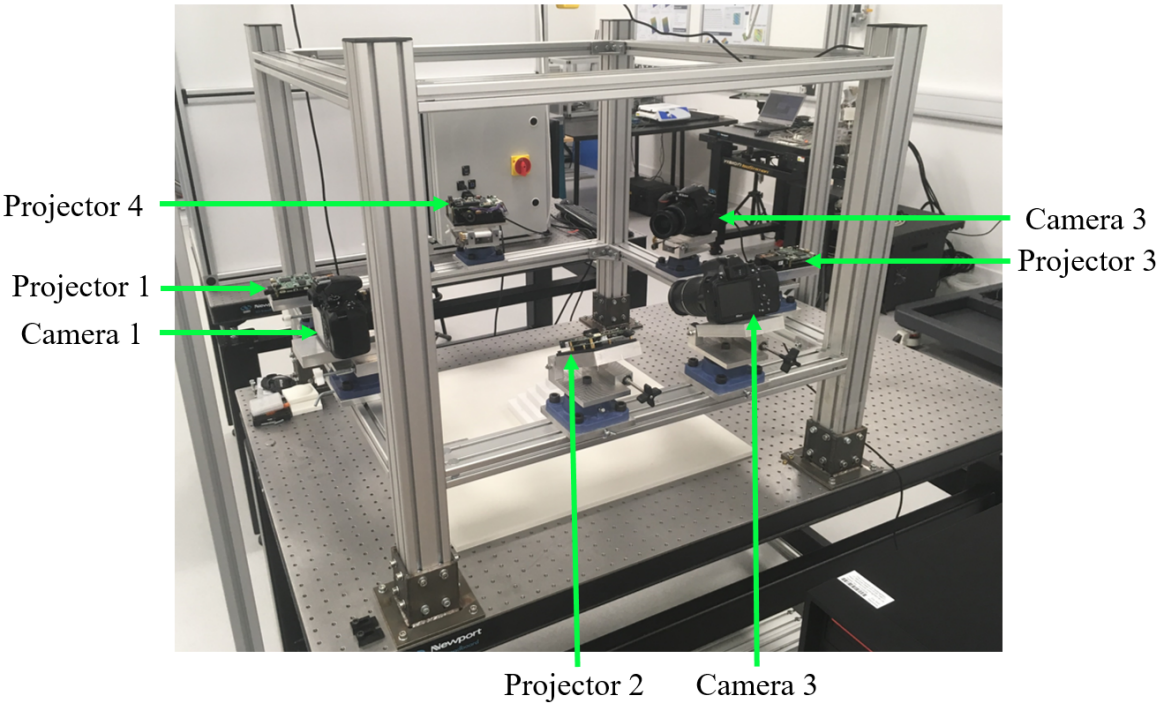


Figure. 4.24 Final design of the multi-view fringe projection frame, mounted on an optical breadboard and vibration isolation support frame, with two sets of cameras and projectors.

of a fringe projection system. The research includes a theoretical investigation of the effects of vibration on FP measurements using a computational simulation technique, as well as an experimental study, which is compared with the simulated results. The investigation represented an important step in understanding the sensitivity of a fringe projection system to vibration, and helped to define the required performance of the mechanical system. The results identified that the cameras and projectors proposed for the final system were too noisy to achieve the 50 μm accuracy target, as the average phase error results in the experimental baseline measurements were more than 50 μm when measuring in ideal conditions and a simple surface.

The design process used to develop the mechanical system followed five key steps: design specification, initial concepts, design evaluation, final design development and proof of concept. The five design stages allowed an effective design solution to be developed, with each decision validated by evaluation metrics and FEA simulations. The development of the multi-view frame was a key step in the project to enable further experimental investigation of the multi-view fringe projection software. In addition, the system developed was a key focus of the work presented in the following chapters, and provided the ideal platform to further investigate the effects of mechanical noise on fringe projection measurements, test the developed live vibration monitoring system and demonstrate the benefit of condition monitoring for measurement systems. The work presented in Chapter 5 details the development of the methodology to characterise the performance of the mechanical system. The experimental characterisation results are compared with and used to verify the FEA full frame simulation results presented in this chapter.

Chapter 5

Design characterisation and results

5.1 Introduction

In this chapter, the methodology developed to fully characterise the mechanical performance of the manufactured multi-view fringe projection frame is presented, with the characterisation results discussed in comparison to the FEA simulations performed and presented in Chapter 4. The process used to develop a metrology frame characterisation method is explained. This includes a discussion of the available sensors and choice of sensor, evaluation of acceleration to velocity and displacement conversion methods, and performance verification of the developed characterisation method. The concept of multi-point characterisation and monitoring is introduced, with the importance demonstrated for the proposed multi-view fringe projection measurement system. The work to develop a vibration characterisation methodology forms the foundation of the developed multi-point live vibration monitoring system, and provides the basis of the investigations that followed throughout the PhD.

5.2 Vibration sensor comparison

Measurement system performance in the closest level of inspection is dependent upon the dynamics of the apparatus, and so a methodology was required, which allowed the performance of the multi-view fringe projection frame to be fully characterised, in order to verify the simulated results and demonstrate proof of design. The first vital step in developing a characterisation method was choosing an appropriate sensor. To this end, a review of the available sensors for vibration measurement was carried out, in order to evaluate them and select the appropriate sensor for the application. The review includes a discussion of the different commercially available sensors, and identifies the advantages and disadvantages of each sensor.

5.2.1 Available sensors

The range of different commercially available sensors, which measure vibrations in the system and could be suitable for condition monitoring, and the advantages and disadvantages of each are discussed here.

Accelerometers use the piezoelectric effect to produce a charge, which is proportional to the acceleration. As vibration of the object causes varying inertial forces in the mass, which cause the piezoelectric elements to deform, the change in the strain of the piezoelectric elements is proportional to the acceleration [121]. A schematic diagram of a piezoelectric accelerometer is shown in Chapter 3, in figure 3.2. Piezoelectric accelerometers are widely used as they offer advantages such as sensitivities up to 100 mV/ms^{-2}, a good response to a wide range of frequencies (1 Hz to 10 kHz), i.e a linear response across a range of frequencies. They also have triaxial capabilities and are small and easy to mount [129–131]. However, the data from accelerometers is unreliable outside of the designed frequency range with increased sensitivity to high frequency noise where they require signal conditioning [121].

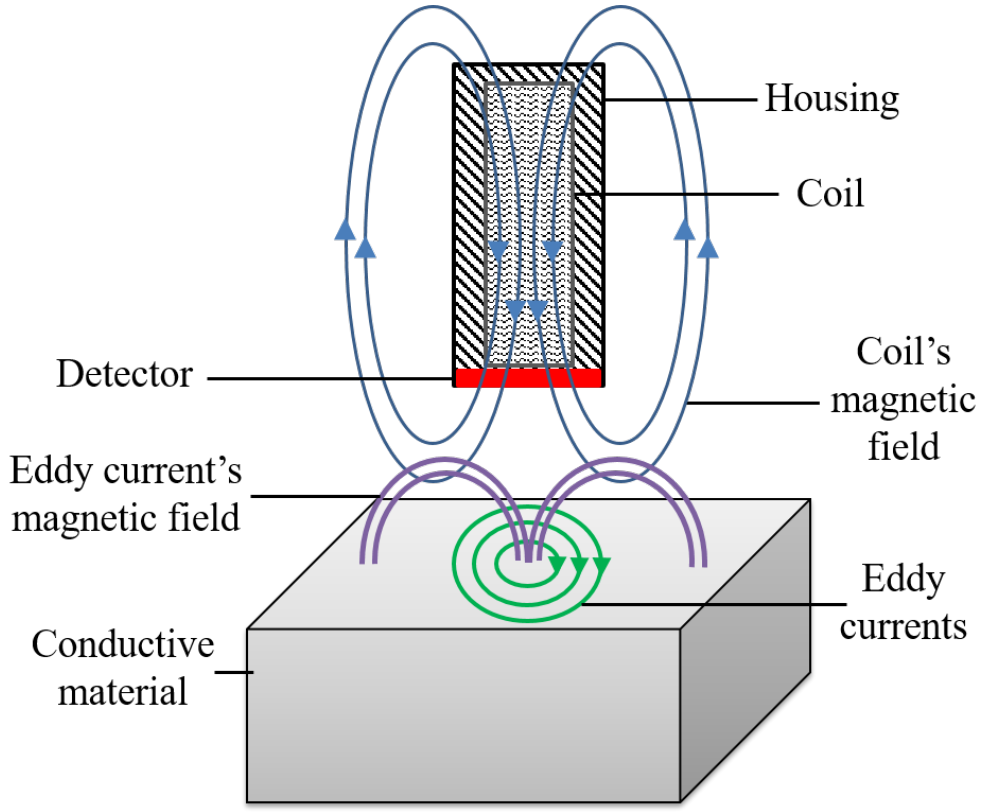


Figure. 5.1 Schematic diagram depicting the key elements of a proximity sensor.

Proximity probes (non-contact displacement sensors), measure the relative distance between the sensor and the part's surface, and are frequently used in bearing measurement applications. Most proximity probes utilise the principle of Eddy currents, measuring the change in electrical inductance of a circuit that is caused by changes in the distance between the coil and the measured surface [132]. The working principle of an Eddy current based proximity probe is illustrated in figure 5.1. Inductive based proximity sensors are generally more accurate, with sensitivities in the order of nanometres [133, 134], and are able to measure static and dynamic displacement in harsh environments, but have a limited operating range, are more difficult to install/design and can only detect metallic materials [135]. Capacitive proximity sensors measure the change in capacitance, and can be used to expand the material range, but are less accurate than inductive based proximity sensors, as they are more sensitive to the environmental conditions.

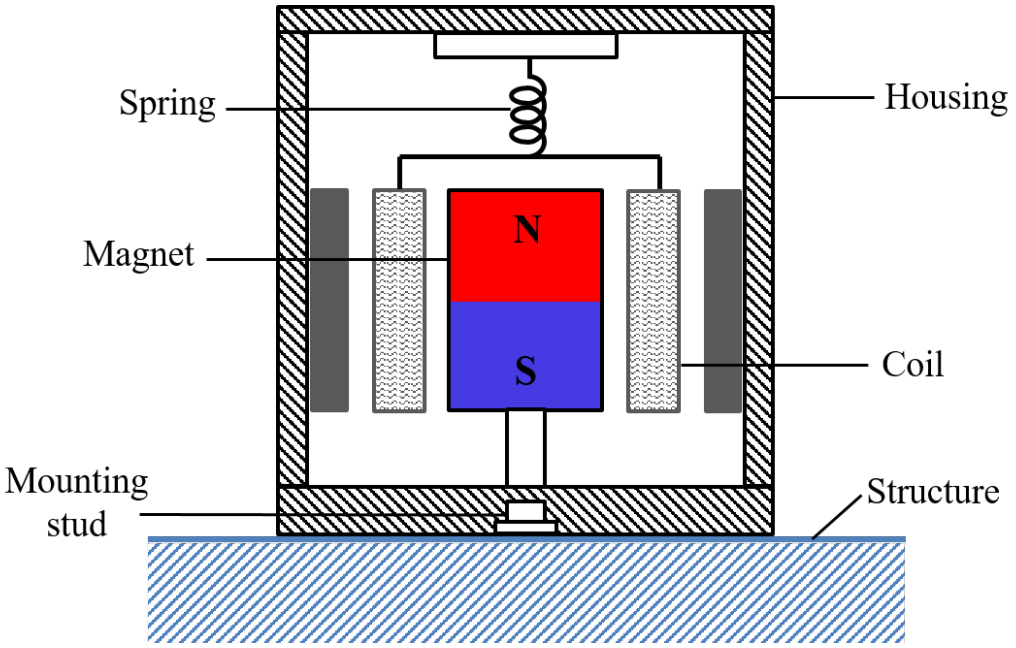


Figure. 5.2 Schematic diagram depicting the key elements of a velocity transducer.

Velocity transducers measure the voltage generated by the movement between a seismically suspended coil and a fixed magnet, where the measured voltage is proportional to the relative velocity of the vibrating object to which the sensor is fixed [136]. The working principle of a velocity transducers is illustrated in figure 5.2. Velocity sensors offer sensitivity of 20 V/ms^{-1} [137], good response at mid-range frequencies, do not need external power, withstand higher temperatures, are easy to install and are relatively low in cost. However, compared with the other sensors discussed they have a lower resonant frequency, are larger in size and mass, suffer from cross noise issues [136] and are susceptible to shocks [138].

The use of laser vibrometers is a technique that has been developed more recently, and uses the laser Doppler effect, where a coherent laser beam is split into two beams of equal frequency. As the measurement beam is reflected off a vibrating surface, the Doppler effect causes a small change in frequency and phase related to the velocity of the surface, which can then be compared to a reference beam to obtain the frequency and phase shifts [139]. The working principle of laser vibrometry is illustrated in figure 5.3. Laser vibrometry provides the highest velocity (2 nm/s) [140] and displacement (2 pm) [141] resolutions of the

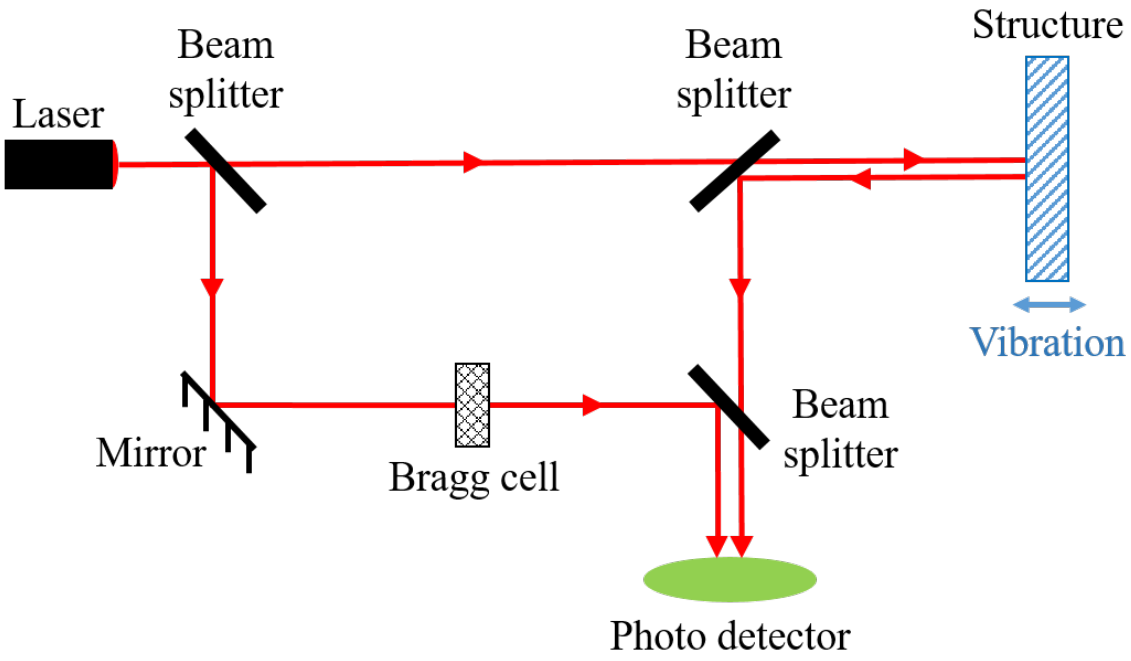


Figure. 5.3 Schematic diagram depicting the key elements of a laser vibrometer.

available sensors, with a very large frequency ranges (up to several megahertz), which is also non-contact and does not alter the part/system surface. However, laser vibrometers are only single axis, requiring line of sight mounting positions and are very expensive considering they are also limited to materials with sufficient surface reflectance.

5.2.2 Choice of sensor

Choosing the appropriate sensor for the application is based on a number of key factors, including the required frequency range, sensor sensitivity, number of axes, mounting options and cost. In order to establish the required frequency range, the frequencies of the expected excitation sources must be identified to inform the choice of a sensor which responds linearly for the required frequency range. Following this, the sensitivity of the sensor will dictate the necessary resolution of the measurements, and so the range of the vibrations amplitudes needs to be gauged (i.e. are the amplitudes being measured in the order of millimetres or

microns). In addition, the number of axes of interest can limit the number of available suitable sensors. The access and mounting availability of the system can also limit the options, for example laser vibrometers require line of sight to access the component being characterised. Overall, each application must undertake a cost-benefit analysis for selecting a certain sensor, given the large variety in cost, resolution and vibration sensitivity - for example, sensors with higher sensitivity will have a larger the cost.

To allow for the different commercially available sensors to be compared and to identify the most appropriate sensor for the application, a comparison table was created and is shown in table 5.1 using the specifications supplied from the leading manufacturers' of each sensor [130, 133, 134, 137, 142].

Table 5.1 Comparison of the specifications of the available commercial vibration sensors.

Sensor	Output signal	Frequency range	Sensitivity	Number of axes	Temperature range	Repeatability	Mounting options	Mass effect	Cost
Accelerometers	acceleration	1 Hz to 10 kHz	>100 mV/ms^{-2}	3	-40 °C to 125 °C	± 5 %	stud/ adhesive	low (few grams)	low/ medium
Proximity probes	displacement	1 Hz to 80 kHz	5 nm	1	-77 °C to 150 °C	± 0.1 %	non-contact - tripod	none	medium
Velocity transducers	velocity	10 Hz to 1 kHz	20 V/ms	1	-29 °C to >300 °C	± 5 %	stud	moderate (0.4 kg)	low/ medium
Laser vibrometers	velocity	0.5 Hz to 22 kHz	0.02 µm/s	1	5 °C to 40 °C	± 1 %	non-contact - tripod	none	high

Using the sensor comparison table 5.1, it was identified that whilst laser vibrometers offer the best resolution, the cost of a multi-point system would not be practical or realistic, so a better value sensor needed to be chosen. The table showed that piezoelectric accelerometers were the best value solution, as they offer a wide frequency range which can effectively measure vibrations from laboratory and industrial sources likely to be seen in metrology systems, i.e. acoustic vibrations (20 Hz to 20000 Hz) and motorized equipment (20 Hz to 500 Hz). Levinzon's work into the fundamental noise limits of piezoelectric accelerometers showed that the measurement range was dependent on the noise floor of the sensor, which has been shown to be as low as a $\sim$2 ng/$\sqrt{Hz}$ at a frequency of 100 Hz in low-noise seismic accelerometers [143]. As such, a sensitivity of 102.5 mV/ms^{-2} was chosen to enable measurements in the micron region and detect faults when they occur in the system, with the sensor noise floor (0.4 μg/$\sqrt{Hz}$) significantly smaller than the measurement range required. The triaxial capabilities were a key advantage of piezoelectric accelerometers, as it would allow the measurement frame dynamics to be condition monitored in three axes simultaneously without the need for remounting, which would be the case if a single axis sensor such as a proximity probe was selected. Piezoelectric accelerometers are easy to install and have a low mass (few grams), and so provide a flexible solution to easily mount the sensors on a variety of different metrology systems without requiring any design changes or effecting the system. The performance specifications of the accelerometers are given in table 5.2. The performance specifications conform to ISA-RP-37.2 (1982) [144] and are typical values, referenced at +24°C and 100 Hz, unless otherwise stated. The accelerometers data provides traceability, as the calibration data and certificate provided are traceable to the National Institute of Standards and Technology (NIST).

Table 5.2 Meggitt Endevco 65L-100 accelerometer specifications [130].

Feature/Attribute	Specification
Model	65L-100
Sensitivity	102.5 mV/ms^{-2}
Number of axes	3
Mass	5 g
Dimensions	(10 $\times$ 10 $\times$ 10) mm
Dynamic range	$\pm$ 50 g
Temperature range	-53 °C to +125 °C
Mounting	Adhesive or M2.5 thread
Frequency response	1 Hz to 6000 Hz
Repeatability	$\pm$ 5 %

5.3 Displacement results

Many applications perform vibration analysis on the velocity and displacement behaviour in the system, therefore a challenge of using sensors, such as the piezoelelectric accelerometer chosen, that measure the acceleration is converting the signal into velocity or displacement. As the maximum displacement of the peak-to-peak response of the signal is of interest, we must find a reliable method to convert our measured to signal to displacement. To choose an appropriate conversion method, an investigation into two methods, which are the 'double integration' method and the 'omega arithmetic' method, has been carried out and is discussed here.

5.3.1 Double integration

The classic method to convert acceleration to velocity and displacement is the double integration method. Acceleration is the rate of change in velocity, and velocity is the rate of change of displacement, therefore the displacement and velocity can be defined in relation to the acceleration as

$$v = \int a \, dt \tag{5.1}$$

$$x = \iint a \, dt \tag{5.2}$$

where, a is the acceleration, v is the velocity and x is the displacement.

The double integration appears theoretically very simple, however, practically this method proves unreliable and achieving usable displacement data is challenging and so an alternative conversion method was required. The challenges of the double integration method are discussed in more detail and compared with the omega arithmetic method in section 5.3.3.

5.3.2 Omega Arithmetic

An alternative method to convert the acceleration signal to velocity and displacement is using a technique called omega arithmetic [145], which performs the conversion in the Fourier domain and attempts to eliminate the errors caused by the integration constants. The time signals of acceleration, velocity and displacement with respect to their Fourier transforms are defined as

Acceleration,

$$\ddot{x}(t) = \int_{-\infty}^{\infty} \ddot{X}(f) e^{i\omega t} \, \mathrm{d}f, \tag{5.3}$$

Velocity,

$$\dot{x}(t) = \int_{-\infty}^{\infty} \dot{X}(f) e^{i\omega t} \, \mathrm{d}f, \tag{5.4}$$

and Displacement,

$$x(t) = \int_{-\infty}^{\infty} X(f) e^{i\omega t} \, \mathrm{d}f, \tag{5.5}$$

where, $\omega = 2\pi f$ and f is the frequency. Using the relationship between acceleration and velocity

$$\ddot{x}(t) = \frac{d}{dt}[\dot{x}(t)],$$

and substituting in equation 5.4 gives

$$\begin{aligned} \ddot{x}(t) &= \frac{d}{dt}\left[\int_{-\infty}^{\infty} \dot{X}(f) e^{i\omega t} \, \mathrm{d}f\right] \\ &= \int_{-\infty}^{\infty} i\omega \, \dot{X}(f) . e^{i\omega t} \, \mathrm{d}f. \end{aligned} \tag{5.6}$$

Comparing this with equation 5.3 it can be seen that

$$\ddot{X}(f) = i\omega \dot{X}(f) = 2\pi f \dot{X}(f). \tag{5.7}$$

This derivation can be extended to displacement using equation 5.5, giving

$$\ddot{X}(f) = -\omega^2 X(f) = -(2\pi f)^2 X(f). \tag{5.8}$$

The omega arithmetic method has a low frequency limit of ∼5 Hz, as the frequency approaches zero the $\dot{X}(f)$ derived from $\ddot{X}(f)$ becomes indeterminate, however, the low frequency components are removed by filtering (filtering method is discussed in a following section) and so this limit does not affect the velocity and displacement results.

5.3.3 Comparison of conversion methods

In order to verify the performance of the piezoelectric accelerometer and investigate the two discussed conversion methods, a simple experimental setup (shown in figure 5.4) was designed using a (GW Instek GDS-1052-U) digital oscilloscope and a SparkFun COM-10975 surface transducer. The digital oscilloscope allowed a known and controllable signal to be generated, in the example discussed a sinusoidal signal was created. A surface transducer acts like a speaker, and allowed the signal to be converted into a physical vibration on the surface/top plate of the transducer. The accelerometer was then mounted on the surface of the transducer to measure the generated signal. A laser vibrometer was also used to verify the behaviour of the surface transducer and the measured accelerometer data. The two conversion methods were then used to convert the signals to displacement data to evaluate the effectiveness of the techniques.

A range of signals were investigated, varying the frequency and amplitude. In the example discussed a sinusoidal signal with a frequency of 200 Hz and amplitude of 0.2 V was used. A discrete sample of the z-axis acceleration data collected using the 65L-100 accelerometer can be seen in figure 5.5. Using the double integration method described previously, the raw

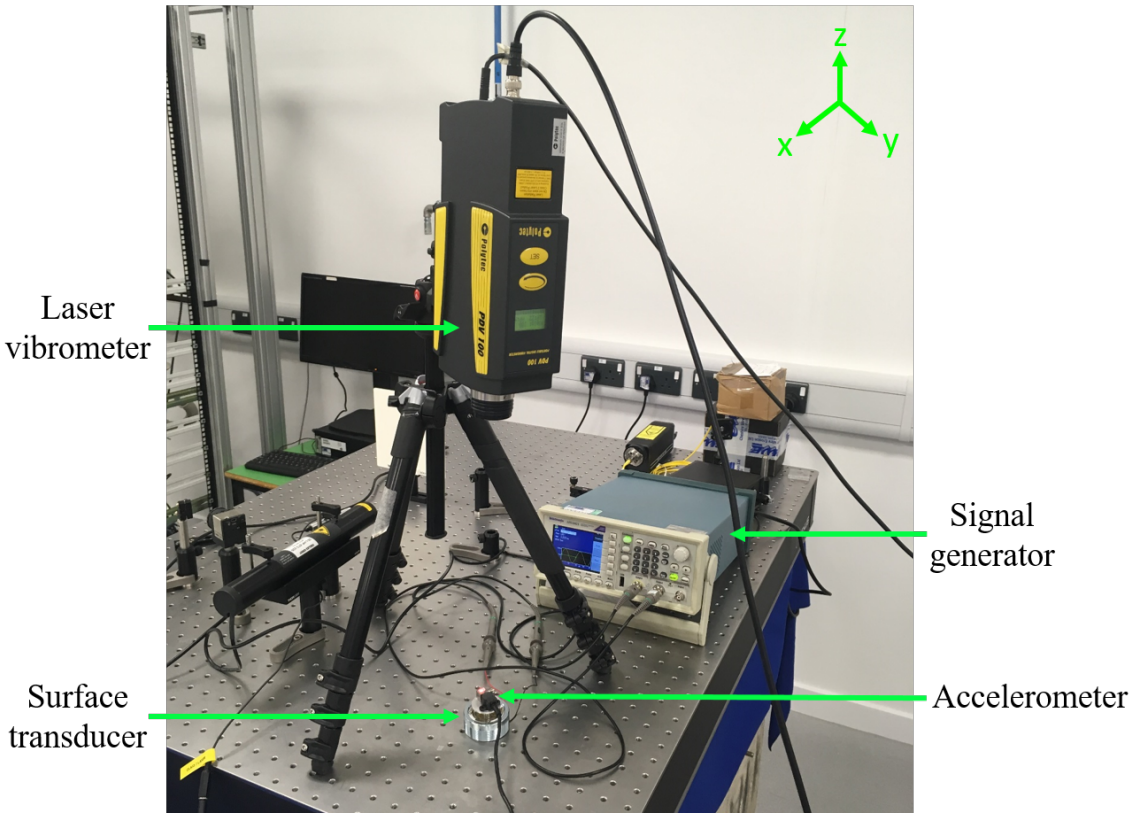


Figure. 5.4 The experimental setup used to investigate the proposed acceleration to velocity/displacement conversion methods, using a piezoelectric accelerometer, digital oscilloscope and surface transducer. A laser vibrometer was used to verify the behaviour of the surface transducer and the measured accelerometer data.

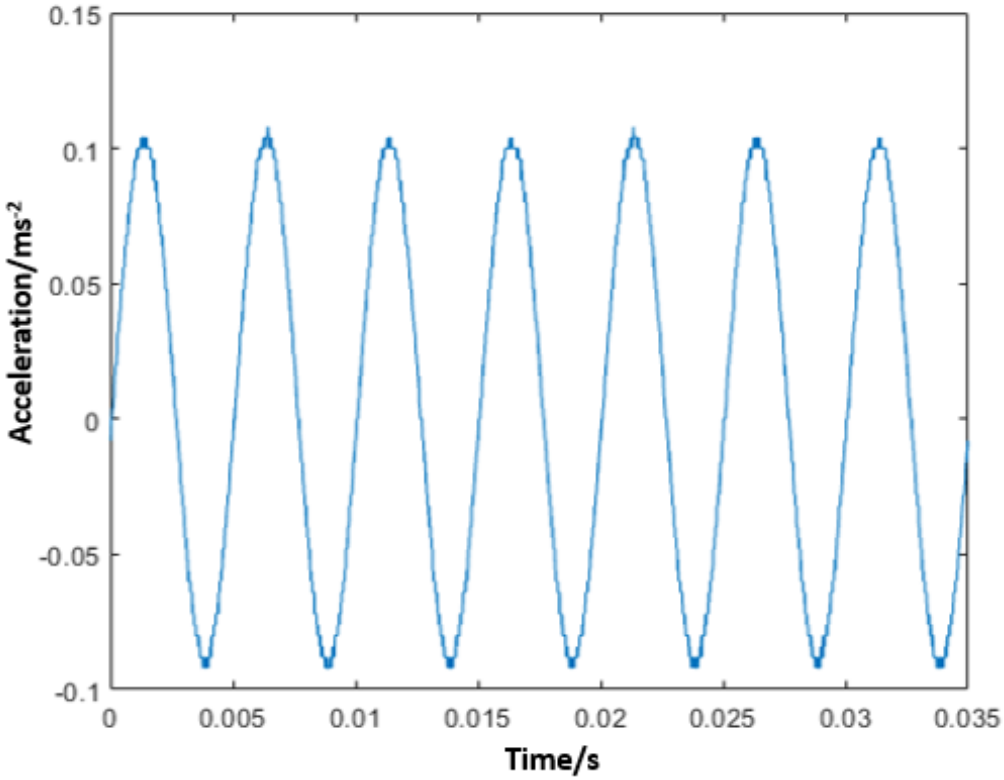


Figure. 5.5 Discrete sample dataset of the raw z-axis acceleration data measured using the piezoelectric accelerometer mounted on the surface transducer generating a 200 Hz sinusoidal signal.

acceleration data was converted to velocity and displacement with the results shown in figure 5.6 and 5.7.

From the results in figure 5.6, it is clear that the positive bias that exists in the raw acceleration data causes large errors in the velocity data, and causes the data to drift from the zero point that the data should oscillate about. This error due to the positive bias can also be clearly seen in the displacement results in figure 5.7, and the data is clearly not an accurate representation of the actual behaviour experienced by the accelerometer. In an attempt to remove this error, the bias was calculated (shown by the red line in figure 5.8) by using the MATLAB 'polyfit' function, which fits a line of best fit of polynomial order one using a least squares method, and then subtracts this line from the raw acceleration data. In

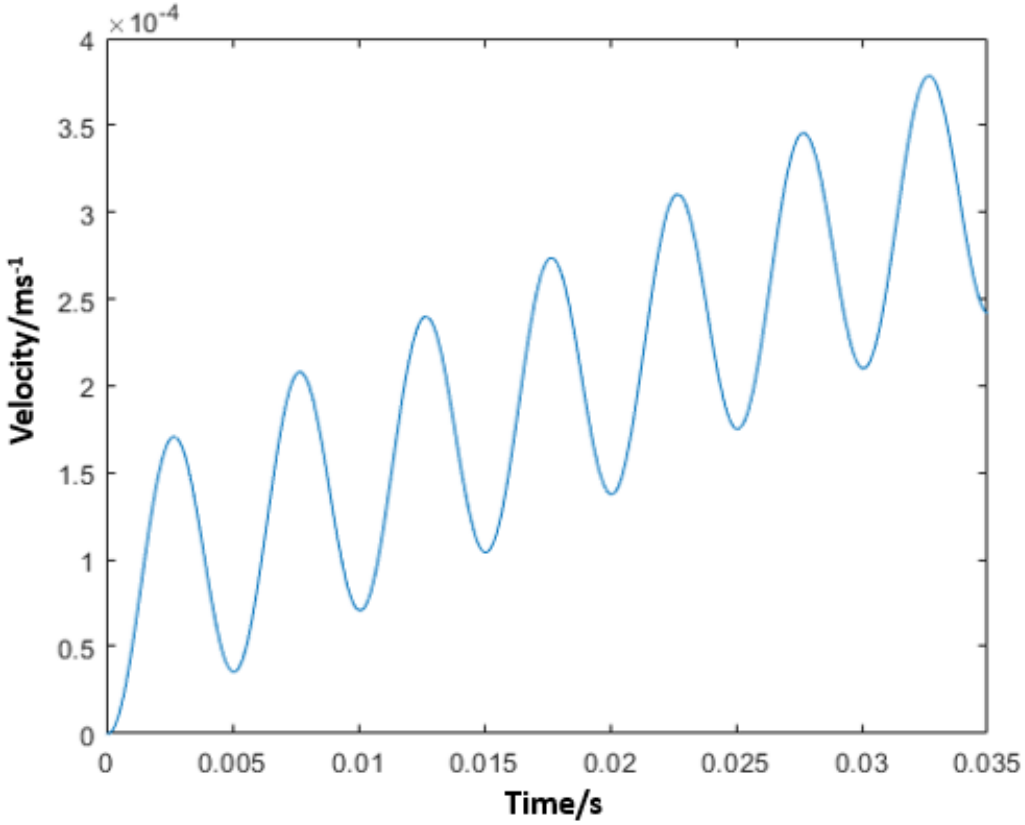


Figure. 5.6 The velocity dataset obtained using the raw measured z-axis acceleration data of a 200 Hz sinusoidal signal and the integration method to convert to velocity.

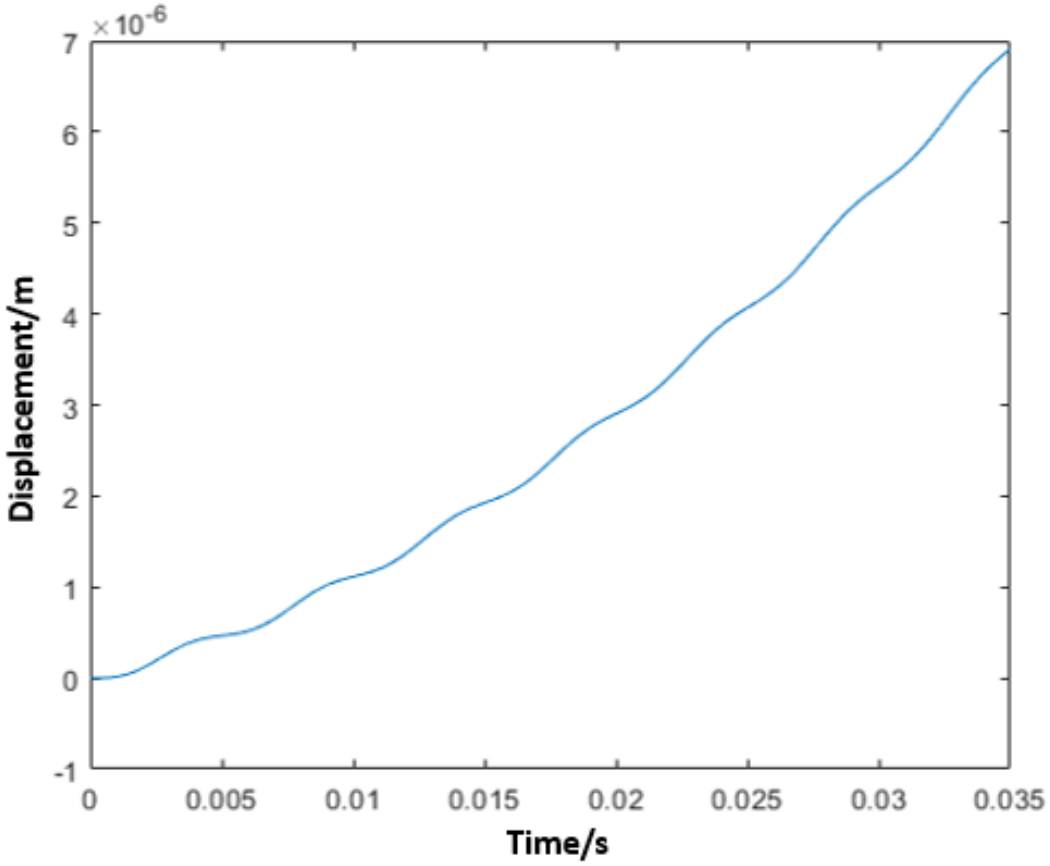


Figure. 5.7 The displacement dataset obtained using the raw measured z-axis acceleration data of a 200 Hz sinusoidal signal and the double integration method to convert to displacement.

addition to the errors caused by the positive bias, there is also high frequency noise and a low frequency component from the drift in the accelerometer which must also be removed. To this end, a Butterworth filter [146] with a pass band of 30 Hz to 1600 Hz was applied to the bias removed acceleration, in an attempt to remove the high frequency noise and the low frequency drift. A Butterworth filter was chosen because compared to other common filter options such as Chebyshev and Bessel, it offered the best compromise between attenuation and phase response [147]. A Butterworth filter has no ripple in the pass band and stop band and so is commonly referred to as the maximally flat filter [148]. The results for the acceleration, velocity and displacement after bias removal and the filter has been applied can be seen in figures 5.8, 5.9 and 5.10 respectively.

It is clear from the results in figure 5.10 that despite bias elimination and over filtering (30 Hz is higher than would ideally be filtered out) using the applied Butterworth filter, the results are still significantly distorted by the propagation of errors caused by the integration constants, and so using the double integration method to obtain reliable velocity and displacement results is not an effective solution.

A more effective conversion method was required and so the 'omega arithmetic' method was evaluated using the same measured accelerometer dataset of the generated 200 Hz sinusoidal signal shown in figure 5.5. The velocity and displacement results found using the omega arithmetic conversion method and applying a Butterworth filter with a pass band of 20 Hz to 1600 Hz are shown in figure 5.11 and 5.12.

It is immediately clear that the results obtained using the omega arithmetic method are significantly improved, and require much less processing to obtain reliable and usable velocity and displacement results. Based on this investigation the omega arithmetic method was identified as the more effective conversion method and so will be used moving forward with the frame characterisation measurements and in the development of the multi-point live vibration monitoring system. As previously noted, the omega arithmetic method has a low

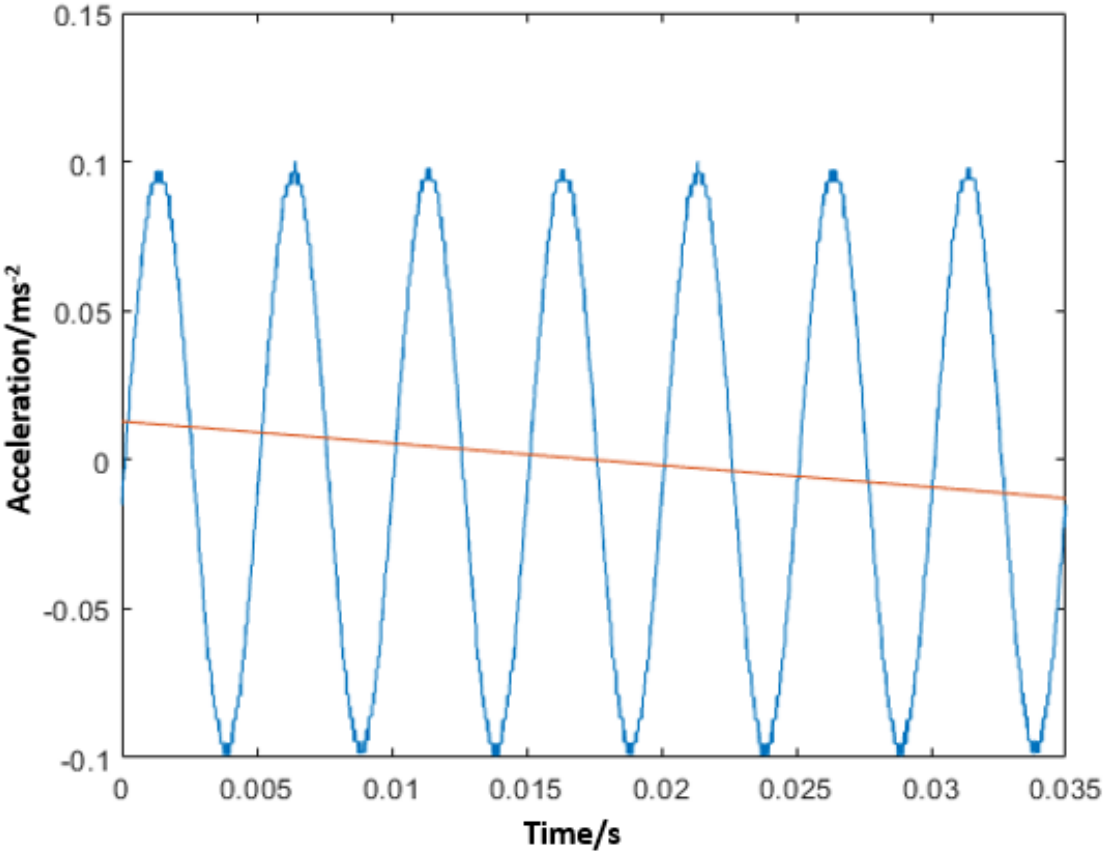


Figure. 5.8 The measured acceleration data after the bias (red line) has been removed and a Butterworth passband filter of 30 Hz to 1600 Hz has been applied to the measured accelerometer z-axis data.

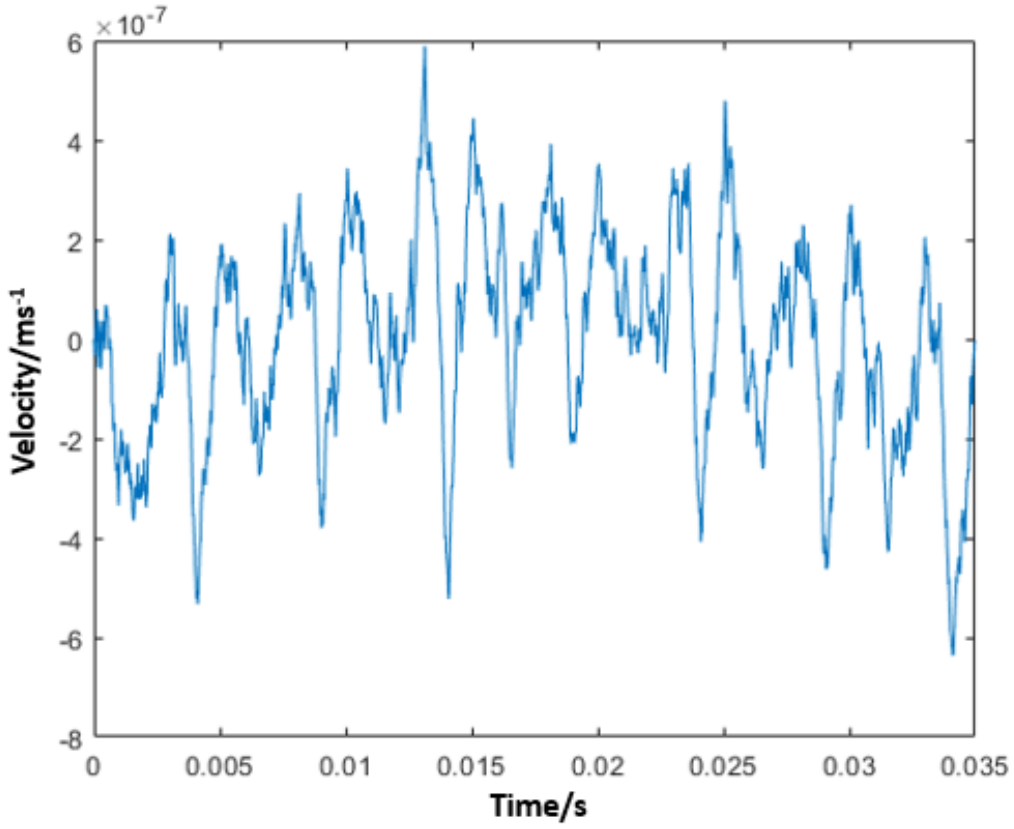


Figure. 5.9 The velocity data obtained using the integration method and the acceleration data with the bias removed and the Butterworth filter applied.

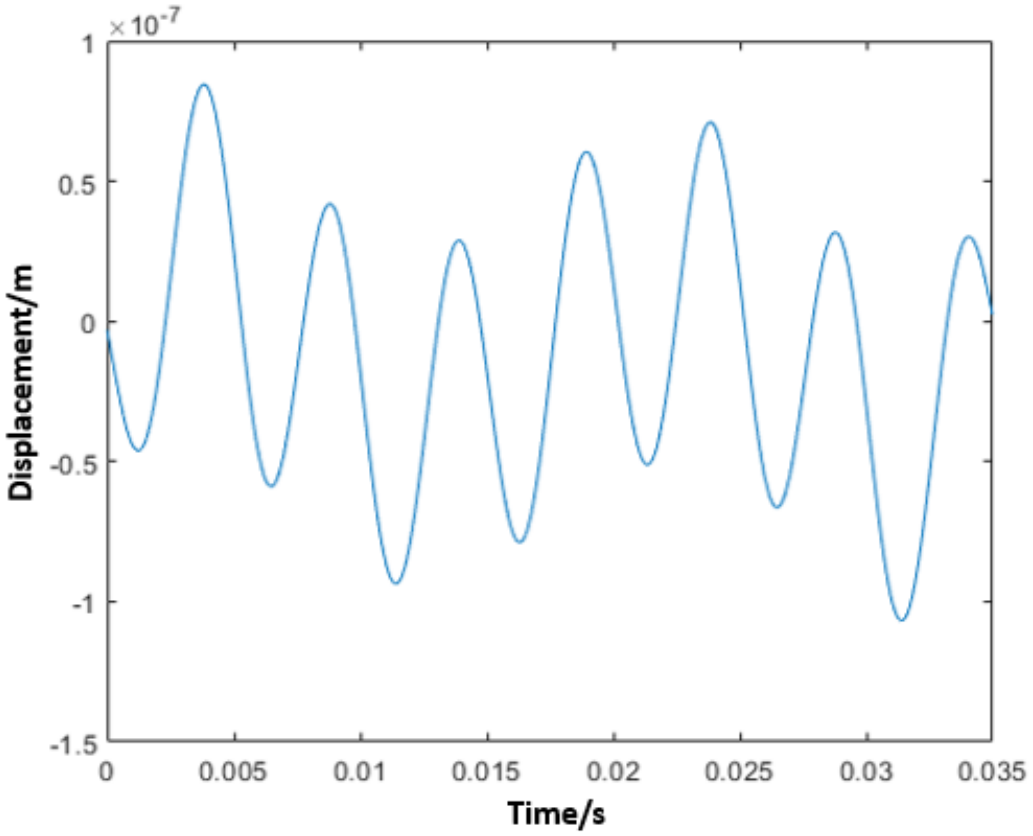


Figure. 5.10 The displacement data obtained using the double integration method and the acceleration data with the bias removed and the Butterworth filter applied.

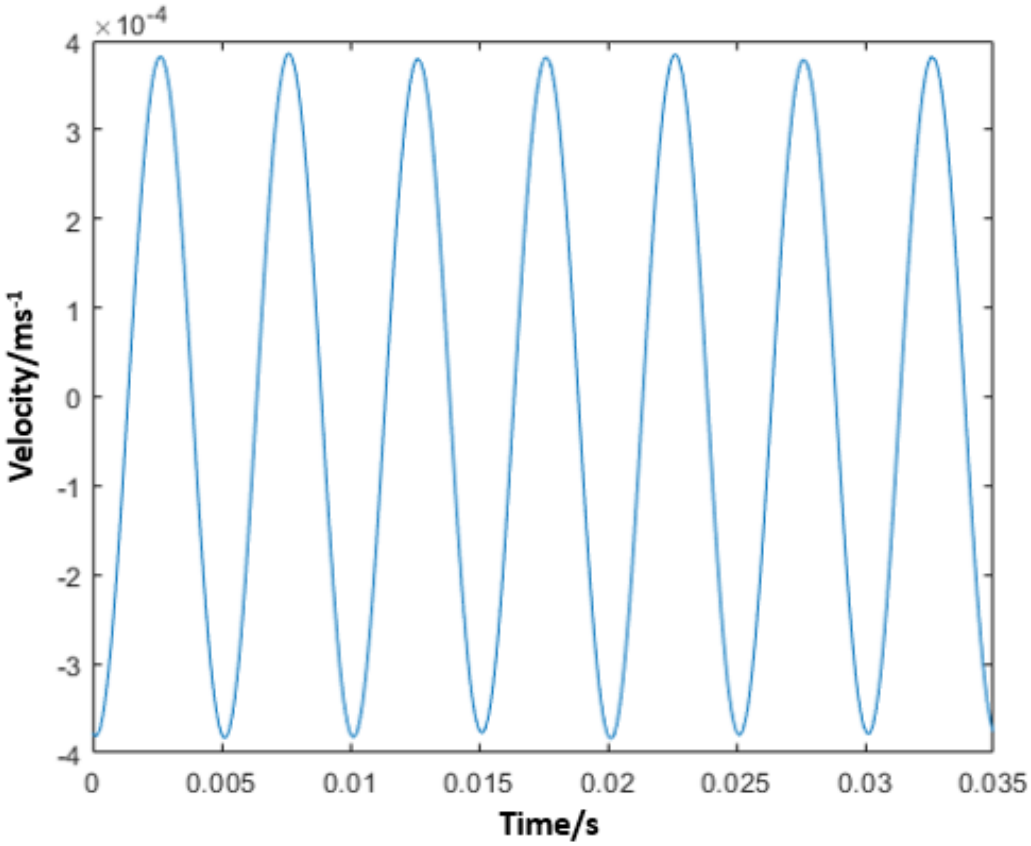


Figure. 5.11 The velocity data obtained using the omega arithmetic method to convert the acceleration data with a Butterworth filter applied.

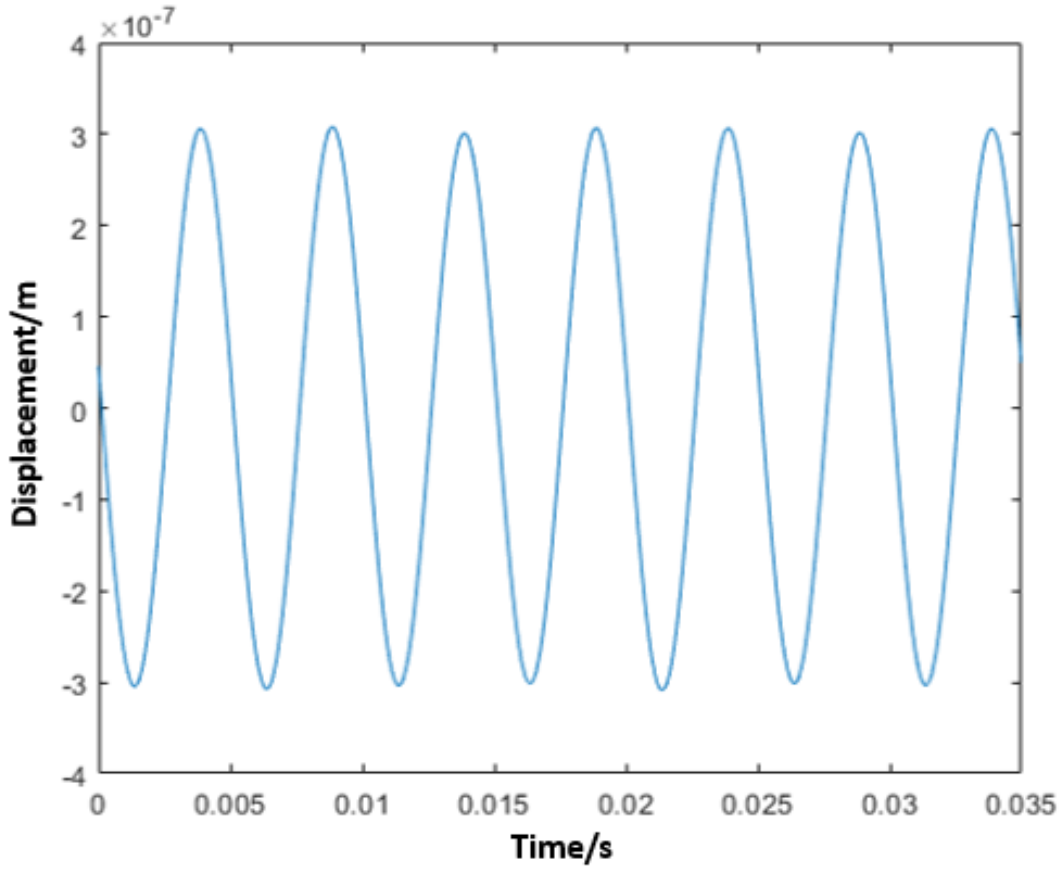


Figure. 5.12 The displacement data obtained using the omega arithmetic method to convert the acceleration data with a Butterworth filter applied.

frequency limit of 10 Hz. In addition to this low frequency limit, piezoelectric accelerometers are unreliable at low frequency ranges (0 Hz to 5 Hz) as they don't respond linearly, so filtering out the lower frequencies is beneficial for both issues, and the effect is negligible for our application as frequencies < 10 Hz are not of interest to our system.

5.4 Multi-point full frame characterisation

After manufacturing and assembling the multi-view frame, using the developed accelerometer characterisation method the experiments to study the mechanical performance of the frame were carried out. The frequency response of the full frame was assessed by mounting a shaker at position one (see figure 5.14) on the designed frame, to apply an excitation in the z-axis with a constant amplitude and vary the frequency from 20 Hz to 700 Hz, in steps of 20 Hz. The results of the frequency response experiment can be seen in figure 5.13, and show the largest peak at 320 Hz, which represents the natural frequency of the frame. The smaller peaks in the frequency response curve are harmonics of the natural frequency, and show that higher frequency vibration will have a larger response on the frame. The natural frequency found at 320 Hz is in line with the simulated frequency response results (natural frequency of 360 Hz) discussed in Chapter 4, with the differences likely due to the increased mass of the structure with the camera and projectors, and the constraints and parameters used in the simulation study.

The frame was then assessed to identify key locations around the frame with the most instability to study the vibrational response of the system in both a non-excited state and excited state. The identified key locations have been shown in figure 5.14. In the case of non-excited the frames response to background vibration sources such as acoustic and seismic, were measured. In the excited case, the fringe projection DSLR camera will be used to excite the structure at the positions shown in figure 5.14, as the camera shutter and internal mirror mechanism have been identified as the largest vibration inputs into the frame

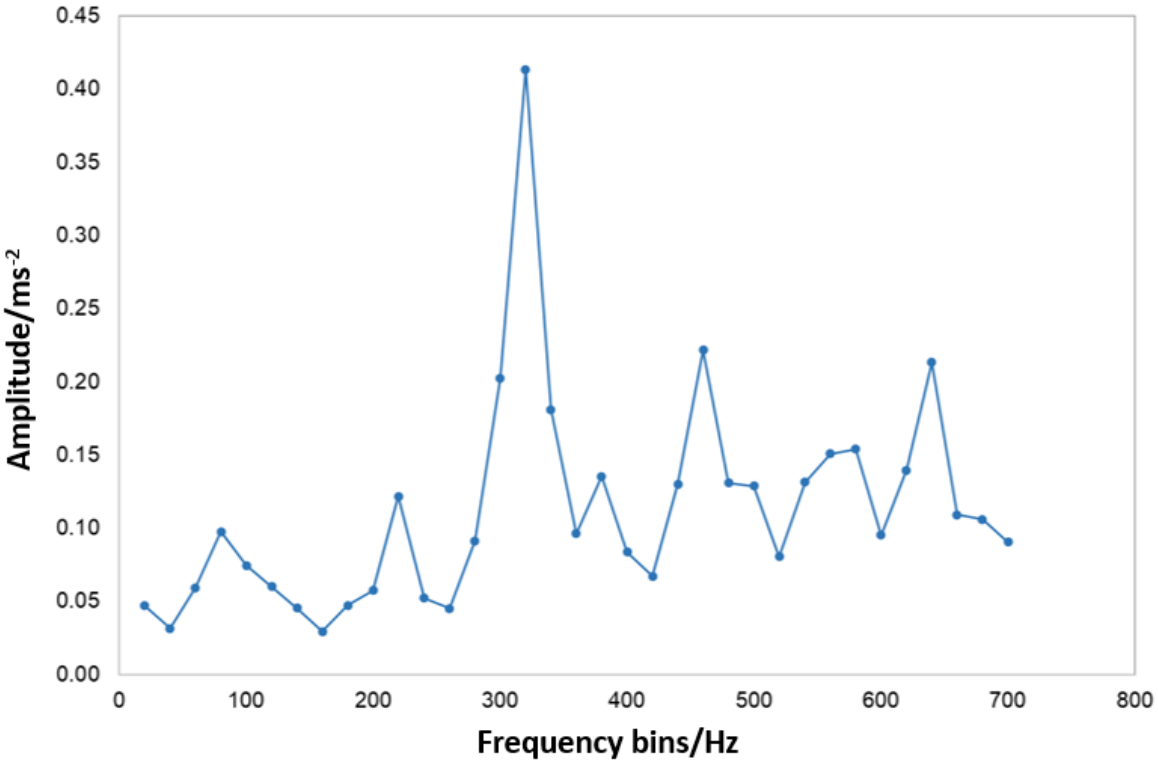


Figure. 5.13 Frequency response experiment on the full frame, applying an excitation in the z-axis with the frequency varied from 20 Hz to 700 Hz, in steps of 20 Hz to study the natural frequency of the frame, which is at $\sim$320 Hz.

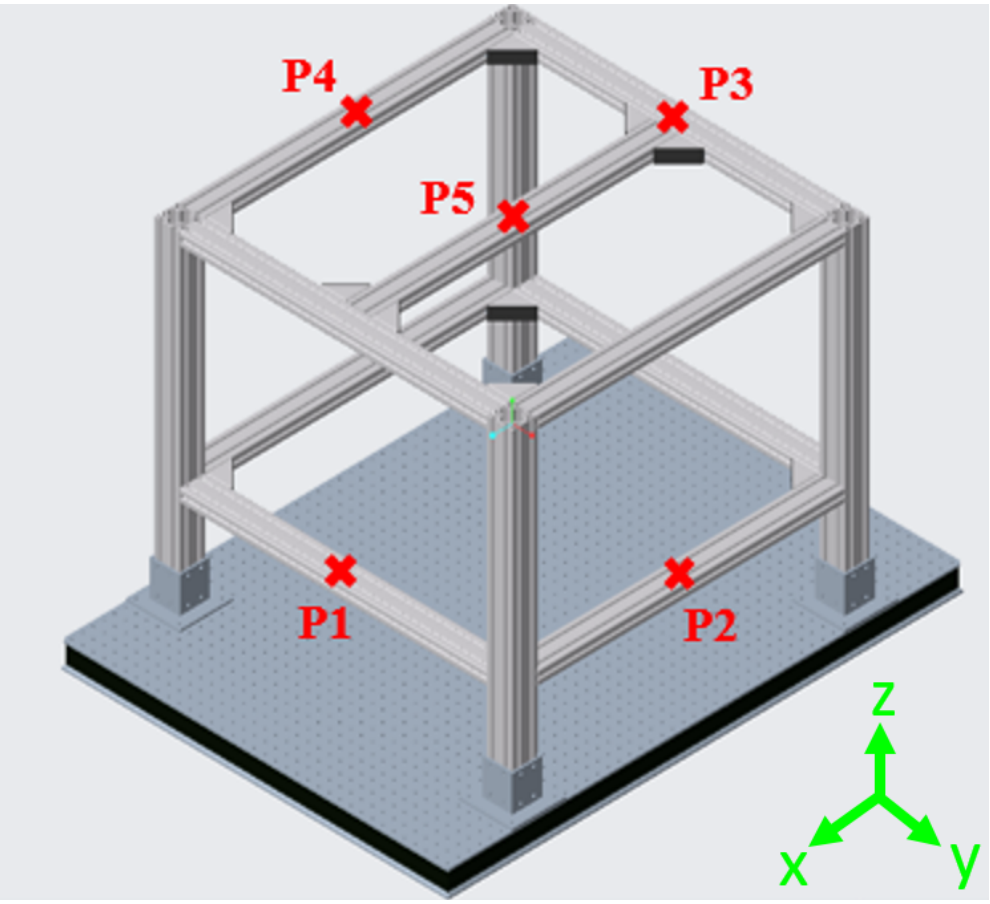


Figure. 5.14 Key locations identified around the multi-view frame to study the vibrational response of the system in both a non-excited and camera excited state.

so characterising the frames mechanical response to this would be an effective representation of the fringe projection measurement process.

The locations around the frame allow for the mechanical performance of the frame to be studied in multiple positions and see how the performance changes around the frame. The experiments were carried out in each position, measuring the peak-to-peak response for each of the x, y and z axes. The measurements were repeated 25 times at each position for both the non-excited and camera excited states, with the mean responses calculated. The mean responses from the characterisation experiments can be seen in table 5.3 and figures 5.15 and 5.16, with an example of the frequency response of the background vibration shown in figure 5.17.

Table 5.3 Average characterisation response in multiple axes in each of the key identified positions on the designed multi-view fringe projection frame.

Axis / Position	Position 1 (μm)	Position 2 (μm)	Position 3 (μm)	Position 4 (μm)	Position 5 (μm)
x-axis static	0.27	0.31	0.26	0.33	0.34
y-axis static	0.32	0.29	0.28	0.30	0.36
z-axis static	0.35	0.32	0.31	0.37	0.40
x-axis camera excitation	2.07	2.08	1.41	1.49	2.09
y-axis camera excitation	2.77	2.61	2.40	2.84	3.15
z-axis camera excitation	3.14	3.75	3.08	3.20	4.23

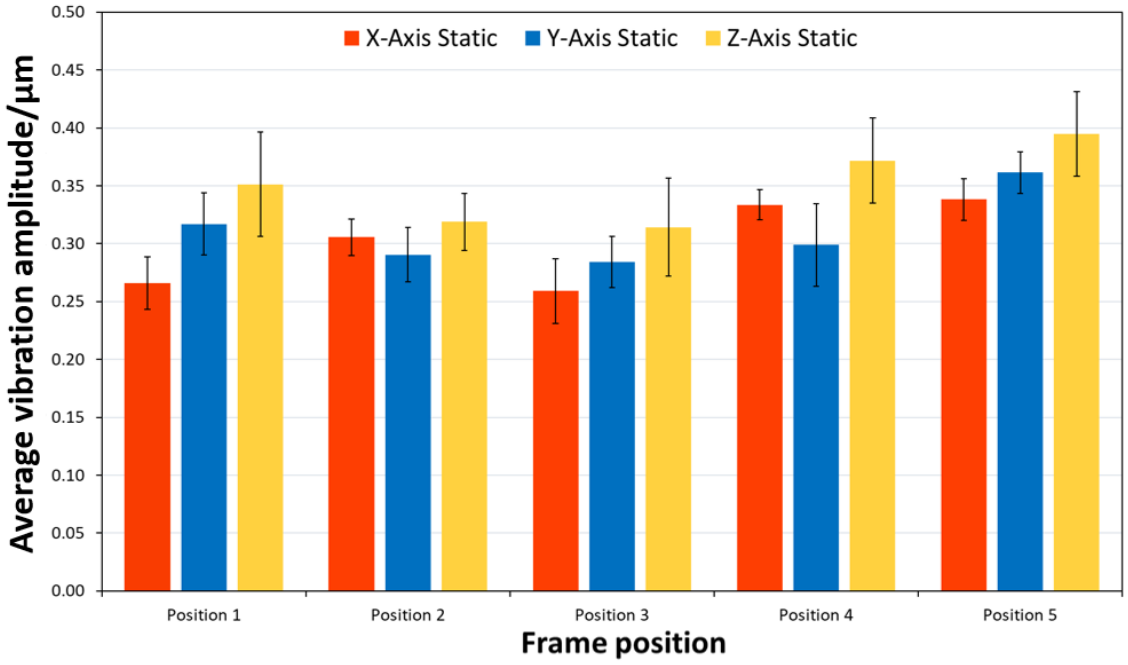


Figure. 5.15 Full frame three axis characterisation results in 5 key positions with no excitation applied to the frame.

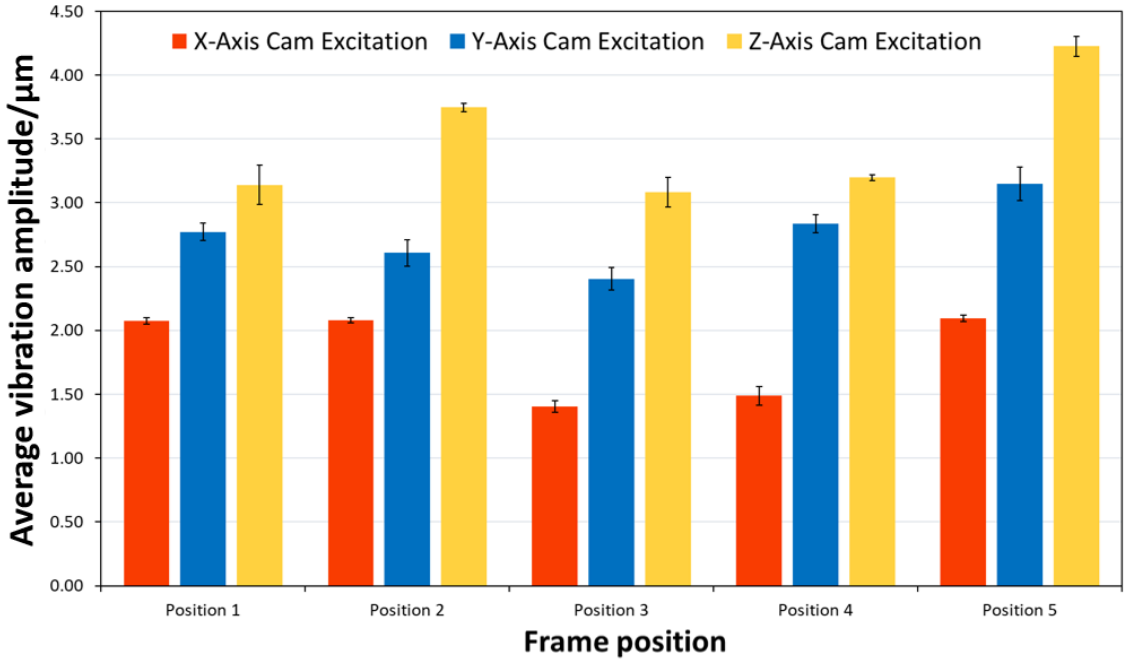


Figure. 5.16 Full frame three axis characterisation results in 5 key positions with the frame excited by a DSLR camera.

From the results in table 5.3, and figures 5.15 and 5.16, it is clear to see that the frame provides mechanical stability performance well below the 10 μm target in both the non-excited and excited cases. The largest response in the background vibration test had a peak displacement of 0.40 μm in the z-axis at position 5, which is $\sim$4% of our maximum allowed displacement target.

The peak responses in all three axes are found to be at position 5, and so highlights this is the area of least stability and should be monitored closely when using this mounting position in the multi-view fringe projection measurements. The results with the DSLR camera excitation show a significant increase in the response of the structure, but it still shows peak displacements lower than our allowable target. The largest response in the background vibration test had a peak displacement of 4.23 μm in the z-axis at position 5, which is $\sim$43% of our maximum allowed displacement target and so the performance of the system is verified and incorporates a performance safety factor of 2. The peak responses in all three axes were

again found to be at position 5, which further highlights this position as the least stable area of the frame. The variance in vibrational responses in both the non-excited and excited states, between each of the positions is clear demonstration of the importance in characterising multiple points around the same system. Multi-point characterisation is particularly vital for our application, as the multi-view fringe projection system will have several sets of cameras and projectors taking separate measurements, so it is critical to understand the difference in structural dynamic performance at each of the different measurement locations. The results further support the development of the live vibration monitoring system (presented in Chapter 6), which is capable of measuring the vibrations at multiple locations in three axes to enable effective condition monitoring to be utilised throughout the measurement process.

The frequency response of the background vibration (figure 5.17 was analysed to identify the different excitation components present. The first two resonance spikes between 0 Hz to 20 Hz corresponds to electrical noises that can be neglected. The spikes seen at 150 Hz, 250 Hz, 350 Hz and 450 Hz, likely are a result of vibrations due to road traffic, machinery and motorized equipment which are common background vibration sources around these frequencies [84]. A common source of background noise is from HVAC (heating, ventilation, and air conditioning) systems, which can cause vibration at several ranging frequencies due to the different components of the system. The laboratory has a large air conditioning unit so it is likely that this is a significant source of the background noise peaks identified and shown in figure 5.17. The main components of HVAC systems and their excitation frequencies [149] are as follows: fan and pump noise 50 Hz to 600 Hz, Reciprocating, centrifugal and screw chillers 250 Hz to 1000 Hz and VAV unit house 125 Hz to 3000 Hz. These are the most likely noise sources of the peaks identified at 250 Hz, 350 Hz and 450 Hz. The peak at 150 Hz, is likely due to the fluorescent lights used in the laboratory, as it is common as they age to hear a buzzing noise at a frequency between 100-200 Hz, as a result of an effect called magnetostriction [150], which causes the iron core within the lights to expand and contract.

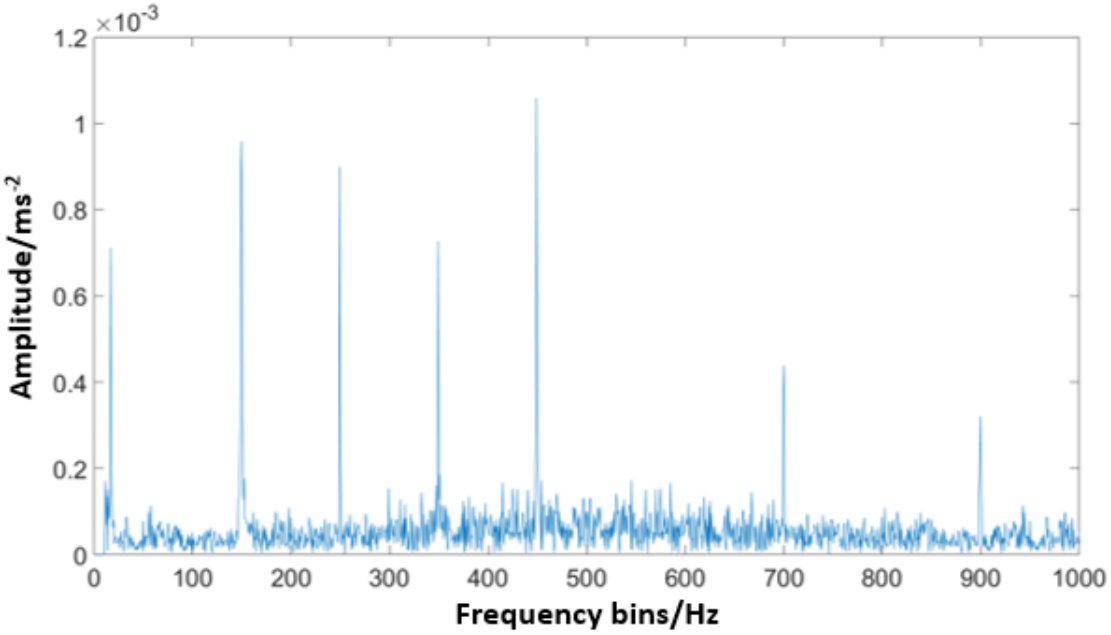


Figure. 5.17 The frequency response of the background vibration used to identify the different components of the signal, such as excitation from motorised equipment, machinery and road traffic.

The smaller spikes seen in figure 5.17 at 700 Hz and 900 Hz are resonant peaks of the floor excitation peaks previously described, or could be vibrations due to acoustics, which can range up to 20000 Hz.

The accelerometer results are traceable as the calibration data and certificate provided are traceable to the National Institute of Standards and Technology (NIST). However, it was still important to verify the characterisation results using a secondary measurement system, and so a laser vibrometer was used to compare with the accelerometer measurements. Using the laser vibrometer ensured further confidence in the accelerometer measured data, as the sensor was identified to have the best resolution in the sensor review presented previously. The basic principles behind laser vibrometer measurements have been explained in Chapter 3 and discussed earlier in this chapter, and so will not be discussed again here. The experimental setup used for the laser vibrometer measurements is shown in figure 5.18.

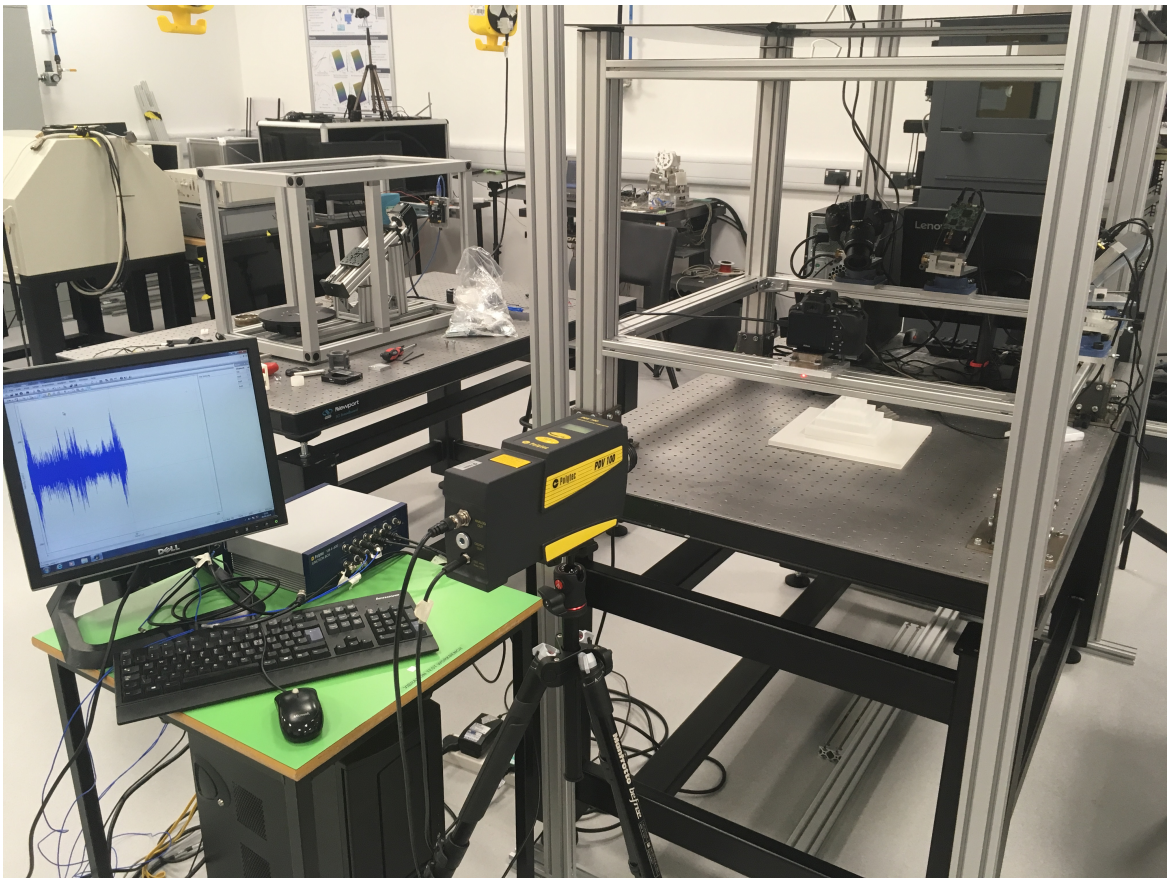


Figure. 5.18 The experimental setup using the Polytec portable digital laser vibrometer (PDV-100) to characterise the multi-view fringe projection mechanical system in order to verify the measured accelerometer results.

Table 5.4 Average characterisation results using the laser vibrometer in the x, y and z axes at position 4 on the multi-view frame, in order compare with and verify the accelerometer characterisation results.

Axis / Measurement	Laser vib (μm)	Confidence interval	Accel (μm)	Confidence interval	P value
x-axis static	0.28	2.24E-08	0.32	4.95E-08	0.07
y-axis static	0.27	2.68E-08	0.31	4.81E-08	0.13
z-axis static	0.33	3.06E-08	0.36	4.72E-08	0.09
x-axis camera excitation	2.51	1.56E-07	2.19	3.38E-07	0.08
y-axis camera excitation	3.34	1.65E-07	3.15	3.15E-07	0.11
z-axis camera excitation	3.88	1.97E-07	3.66	2.64E-07	0.10

Laser vib = Laser vibrometer; Accel = Accelerometer

The Polytec portable digital laser vibrometer (PDV-100) has a frequency range of 0.5 Hz to 22 kHz and a measurement resolution of 0.02 $\frac{\mu m}{s}/\sqrt{Hz}(rms)$. The laser vibrometer experiments were carried out at position 4, measuring the peak-to-peak response for the x, y and z axes. The measurements were repeated 15 times at each position for both the non-excited and camera excited states, with the mean responses calculated. Then using a two sample T-test to check if there is any statistically significant difference between the means of the two measurements, or if they can be considered to be equivalent. The mean responses from the laser vibrometer characterisation experiments and the results of the two sample T-test [151] can be seen in table 5.4.

The results in table 5.4 verify the results using the accelerometer. Both the excited and non-excited results found with the laser vibrometer were of the same magnitude of the accelerometer results. This is supported by the P values calculated using a two sample T-test and shown in table 5.4, which all exceed the recommended alpha value of 0.05 [151], so there is no significant difference between the laser vibrometer and accelerometer results in all three axes. This provides confidence in using accelerometers moving forward to characterise the systems performance and live monitor the vibrations during the measurement process.

Table 5.5 Average characterisation response in multiple axes for the direct camera mount, the adjustable camera mount fastened properly, and the pitch mechanism of the adjustable camera mount left loose/unfastened on the designed multi-view fringe projection frame.

Axis / Configuration	Direct mount (μm)	Adjustable Mount - fastened (μm)	Adjustable Mount - loose (μm)
x-axis	2.09	4.65	4.92
y-axis	3.15	4.79	6.13
z-axis	4.23	7.65	10.12

Using the developed accelerometer characterisation method, an investigation into the performance of the designed camera and projector mounts was carried out. In the investigation, 15 repeats were performed to measure the peak vibration experienced due to the excitation of the DSLR camera shutter and internal mirror mechanism, using two different configurations. The two configurations were the newly designed mounts (shown in figures 4.21 and 4.23) fastened properly and the second was the mounts pitch adjustability mechanism left loose/unfastened. The results allowed a comparison of the dynamic performance between the adjustable mounts and the original direct mount, used in previous frame characterisation experiments with no adjustability. The study also assessed the ability of the characterisation technique developed to identify a fault in the fringe projection setup (I.E mounts not fastened properly) and alert the user there has been a significant change in the dynamic performance of the system, which should be corrected before performing any measurements. The results have been shown in table 5.5 and figure 5.19.

The results show that adding adjustability to the camera and projector mounts has degraded the dynamic performance, with a clear increase in peak excitation in the adjustable compared to the direct mount in all three axes. The increased response was expected as the adjustable mounts have significantly more joints and moving parts than the direct mount (made from one piece), which will decrease the overall stability of the mount. The largest effect was seen in the z-axis with the averaged peak response increased from 4.23 μm to 7.65 μm. This dynamic performance decrease is not ideal, however providing adjustability

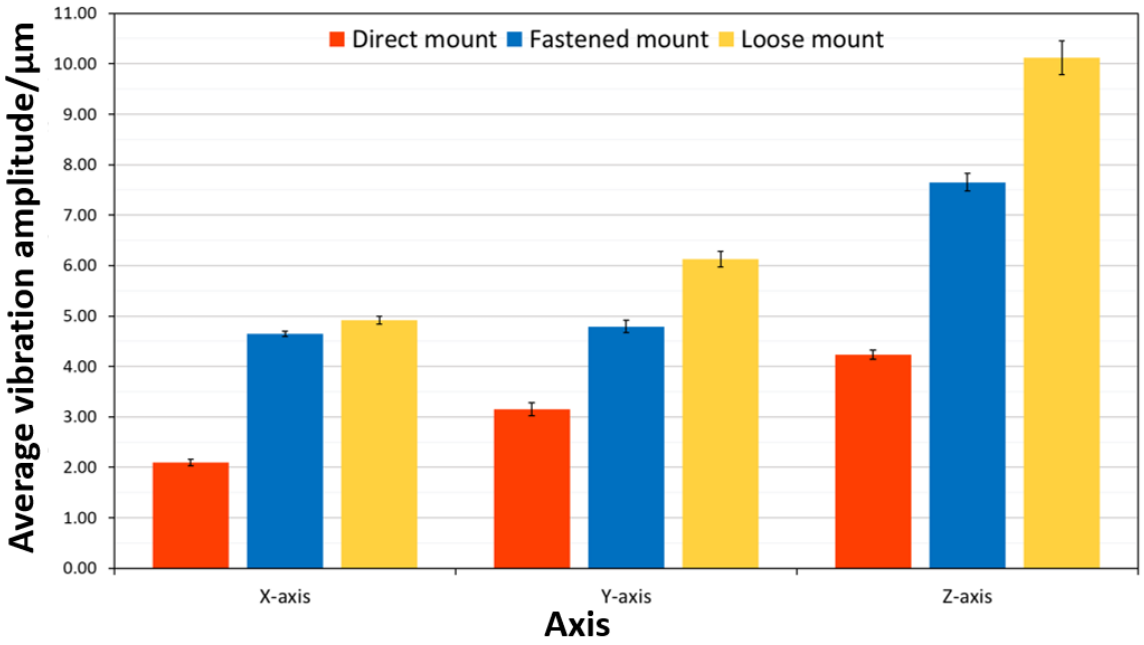


Figure. 5.19 Average characterisation results using a triaxial accelerometer to compare the excitation of the different camera and projector mounts used in the multi-view fringe projection setup, as well as assess the ability of the characterisation method to identify a mechanical fault in the system I.E. the mounts not being fastened properly.

in the pitch angle of the camera and projector mounts is a vital functional requirement. The performance of the adjustable mounts is within the 10 μm tolerance allowance for the mechanical system when the adjustable mounts are fastened properly, so are still suitable to be used in the multi-view fringe projection system. The results for the loose/unfastened mount showed there was little effect in the x-axis, however, the fault was clearly detected in both the y and z-axes, with a significant increase measured in the averaged peak responses in both axes. This comparison demonstrated the effectiveness of using the characterisation technique to identify potential mechanical faults in the system, and highlights the potential for the use of condition monitoring for measurement applications. This concept has been further investigated and its use demonstrated in the following chapters.

5.5 Chapter summary

The work presented in this chapter represents an experimental validation of the designed multi-view fringe projection frame as well as the preliminary work towards developing a live multi-point condition monitoring system. The experiments performed to characterise the mechanical performance of the designed frame, allowed for the stability of the structure to be assessed in both a non-excited state and a camera excited state. A laser vibrometer was used to validate the results, and showed that the accelerometer and software infrastructure offered an effective structural dynamic condition monitoring tool moving forward. The characterisation results for the mechanical system demonstrated the importance of multi-point condition monitoring, as it showed how the structural dynamic performance of a system could vary from position to position, therefore shows condition monitoring is required at each of the different measurement locations used in the developed multi-view fringe projection system. The investigation into the different acceleration to velocity and displacement conversion methods showed the 'omega arithmetic' method to be more effective over the double integration method. This investigation included a demonstration of both conversion methods on a sample dataset generated using a signal generator and surface transducer, which highlighted the problems using the double integration method, and showed the omega arithmetic method could produce reliable results. This study, along with testing on the multi-view fringe projection frame validated using this method in the structural characterisation methodology developed, and has been used in the development of a multi-point live condition monitoring system, which is presented in Chapter 6.

Chapter 6

Development of live multi-point vibration monitoring setup

6.1 Introduction

In this chapter, the development of a novel condition monitoring system is presented along with a case study to demonstrate the utility of the system. The developed condition monitoring system uses commercially available accelerometers (discussed in Chapter 5) in combination with a control-monitoring infrastructure to allow for the live appraisal of the performance of a measurement or manufacturing systems. The system includes two methods of operation, real-time performance monitoring and detailed measurement/manufacturing verification, which will both be detailed with the functionality and purpose of each discussed. A lathe condition monitoring investigation is presented in order to demonstrate the full capabilities of this system and show how the acquired typical machining performance parameters can be used to monitor the 'health' of the system. The development of the system represents a key contribution of the project and allowed for the importance of condition monitoring for measurement systems to be demonstrated in the case studies performed in Chapter 7. The chapter is broken down into four sections; the first section provides a system overview, which

includes the software and hardware used to control the system, capture data and process the results. The second section details the software framework, describing the programming architecture used and an overview of how the different sections of the software execute and transfer the captured data between the hardware and host computer. The third section describes the different available analysis functions of the system, with the two methods of operation discussed. The final section, presents the investigation into monitoring lathe tool wear, in order to demonstrate the functionality of the developed system. The work presented in this chapter has been published in Machines, January 2020, DOI: 10.3390/machines8010003.

6.2 System overview

6.2.1 Software

The system was developed in LabVIEW, which is a graphical programming environment widely used for systems development as it allows for flexible data acquisition, data analysis and instrument control. In addition, the system also utilised LabVIEW's field programmable gate array (FPGA), real-time and MathScript specialised add-on modules to support its infrastructure. The FPGA hardware embedded in the Compact RIO was configured to create an integrated circuit that can interface with the microprocessor of the Compact RIO and the vibration I/O modules installed, to collect and stream data from the accelerometers. Parallel collection and streaming of data on FPGAs can operate at higher speeds than processors that perform tasks sequentially. The real-time module was used to ensure accurate timing within our condition monitoring application, which is vital for a stand-alone multiple channel and high throughput data collection system.

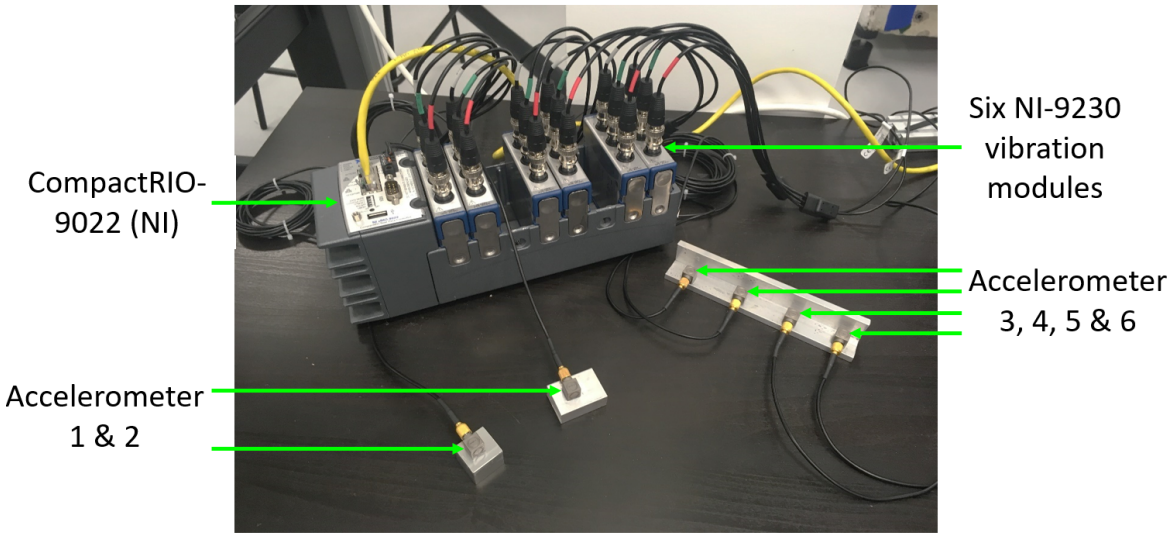


Figure. 6.1 The developed multi-accelerometer live monitoring system, which includes six triaxial IEPE accelereometers, a CompactRIO-9022 controller, with an eight module slot chassis attached and six NI-9230 vibration and sound modules integrated.

6.2.2 Hardware

The system (shown in figure 6.1) was developed using a National Instruments (NI) Compact RIO-9022 (cRIO) real-time embedded controller (533 MHz CPU, 256 MB DRAM, 2 GB storage), which has a variety of connectivity ports, including two ethernet, one USB and one serial port. The cRIO was combined with a compatible cRIO chassis, which allows for up to eight C-series I/O modules to be integrated. Six NI-9230 C series sound and vibration input modules were integrated using a BNC connection, with the cRIO to read and condition the voltage signals from the accelerometers. Each NI 9230 module provided three input channels (used for x, y and z axes of each accelerometer), with sample rates up to 12800 samples per second per channel, and a signal range of $\pm$ 30 V.

Meggitt Endevco 65L-100 triaxial integrated electronics piezoelectric (IEPE) accelerometers were selected for the system as they have a wide frequency range and can effectively measure vibration from laboratory and industrial sources likely to be seen in measurement systems, i.e. acoustic vibrations (100 Hz to 10000 Hz) and motorised equipment (20 Hz to

500 Hz). The sensitivity of 102.5 mV/ms^{-2} is adequate to enable structural measurements in the micrometre amplitude region. Engineering systems may need to be condition monitored in six degrees of freedom, so triaxial accelerometers would only offer a solution to achieve measurement of vibrations in three degrees of freedom. However, the three degrees of freedom that accelerometers measure represent the largest vibration axes of interest in measurement systems, with torsional vibrations more relevant in applications with rotational inputs, such as the crank shaft in a combustion engine [152]. The accelerometers have two mounting options, which are adhesive mounting, where the bottom face is glued onto the frame, or screw mounted, and so offer a flexible solution that can be easily mounted on a variety of different measurement systems without requiring any design changes. The specifications of the accelerometers are given in Chapter 5, table 5.2.

6.3 Software framework

The software has been programmed to use the target and host architecture, which allows for the host computer to interact with the target virtual instrument (VI) compiled on the cRIO, whilst performing different operations in the host computer VI. The target VI is designed to collect data from the accelerometers and stream the data to three FIFOs (First-In-First-Out) buffers for the host VI to read. The host VI on the master computer is designed to read the data from the FIFOs in chunks, based on how much data is available when the read is requested, which will in turn depend on the sample rate and the execution time of the read loop. The host VI then performs the processing and analysis on the collected data, displaying the measurements on the front panel and streaming the data to disk. Utilising the cRIOs FPGA and the host-target architecture allows the system to achieve high sampling rates (up to 12800 samples per second per channel), therefore, ensuring adherence to the Nyquist sampling theorem and measuring across the desired frequency range. High-level function

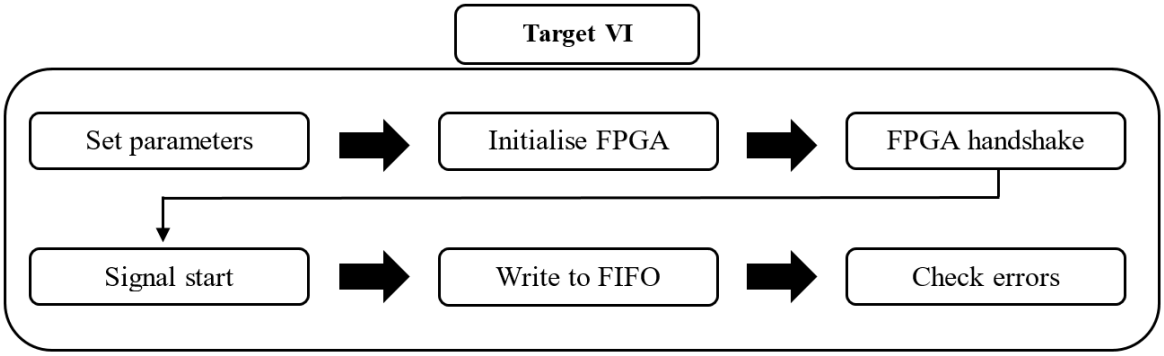


Figure. 6.2 Top-level programme function flowchart of the designed target VI, which is compiled onboard the cRIO, to collect and stream the accelerometer data to the host VI.

breakdown diagrams of the target and host VIs architectures are shown in figures 6.2 and 6.3 respectively.

6.3.1 Establishing parameter set

The settings and parameter section of the front panel allow the user to control key aspects of the device setup, measurement parameters and analysis settings. The cRIO device and input configuration are constants in the current accelerometer system, but could be readily adapted for integration of other accelerometer types. The sample rate can be easily changed to a number of available pre-set sample rates, ranging from 985 samples per second per channel to 12800 samples per second per channel. The user defines the filename and file path for the measurement file so that the data can be streamed to disk. Key analysis settings can be set to specify the analysis time window, peak and valley threshold values, peak separation and type of windowing used. The analysis time window sets the length of time in seconds as decided by the user i.e. the update rate of the results and window time of interest. Threshold values are used to determine the amplitudes above which the magnitudes of the peaks and valleys, used for the peak-to-peak analysis, are found. Peak separation sets the length of the moving window of points, which the peak finding function uses to search for peaks and valleys in the data. The system allows the user to choose the type of windowing applied to the data, to help

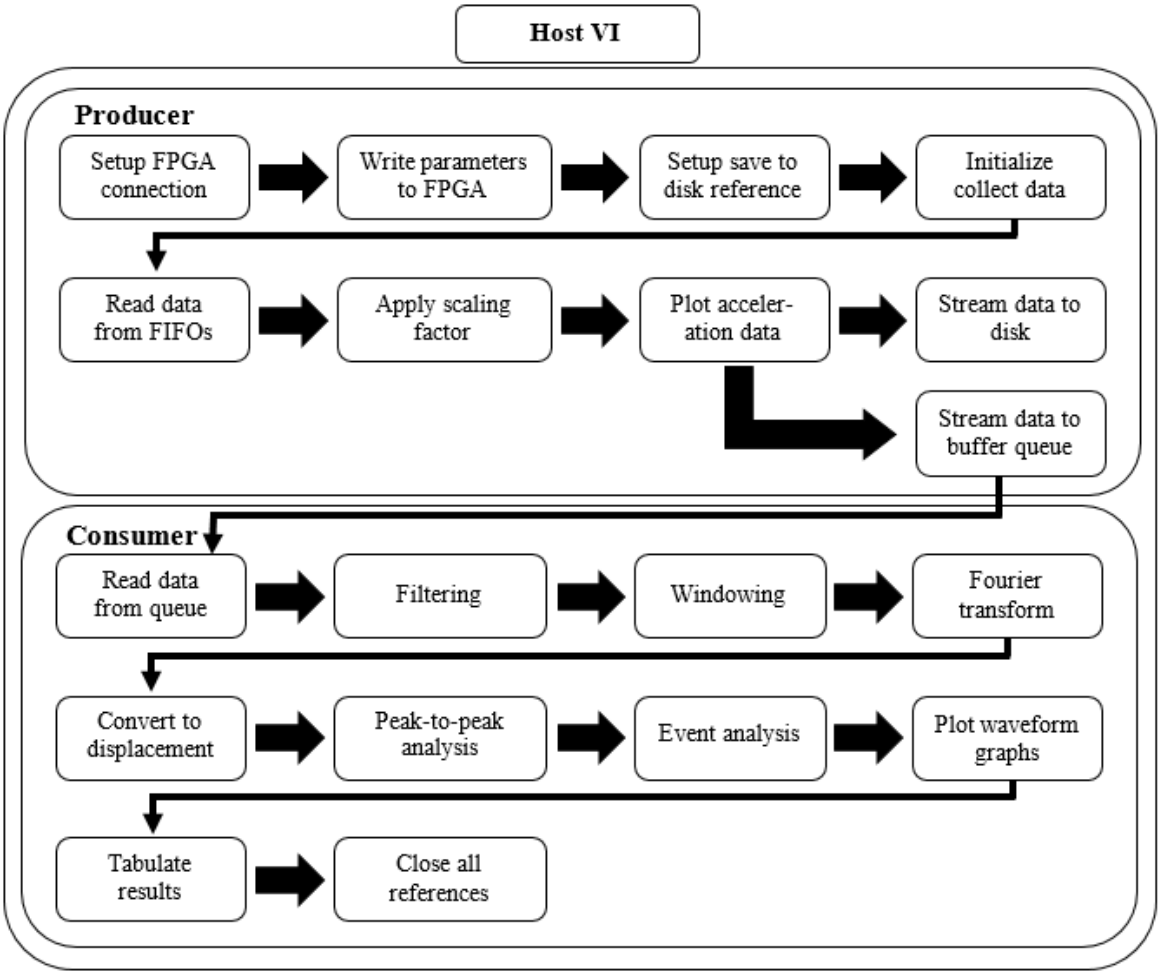


Figure. 6.3 Top-level programme function flowchart of the designed host VI which is executed on the main computer and communicates and reads the accelerometer data from the target VI on the cRIO. The Host VI uses the producer-consumer architecture to read and process data efficiently.

produce clearer results during Fourier analysis of the data by reducing the effects of spectral leakage.

6.3.2 Filtering

As piezoelectric accelerometers are unreliable outside of their designed frequency range [153], it is necessary to filter the acquired signal to remove the unreliable and noisy data outside of the measurement range. A Butterworth filter [146] is applied to remove the unwanted frequencies, where the user defines the upper and lower ranges. A minimum of 5 Hz must be removed from minimum frequency range due to the unreliability of the accelerometer when measuring very low frequencies and as a result of the limits of the conversion method used to obtain velocity and displacement data.

6.3.3 Windowing options

In order to analyse the frequency spectrum of the signal and convert the acceleration data to displacement data, the signal needs to be transformed into the Fourier space. In order to improve the clarity of the Fourier signal and reduce the effects of spectral leakage, window functions are commonly applied. Windowing reduces the amplitude of the discontinuities at the endpoints by multiplying the time signal by a finite length window function with an amplitude that smoothly reduces to zero at its endpoints, ensuring that the endpoints of the time signal meet and the signal forms a continuous waveform. The front panel of the host VI offers the user a choice of windowing function, which include: Hanning, Hamming, Blackman, Blackman-Harris, Blackman exact and no window (often referred to as rectangular or uniform window) [126].

6.3.4 Signal conversion

Many applications perform vibration analysis on the velocity and displacement behaviour in the system. To this end, the acceleration signal is converted to velocity and displacement using the omega arithmetic [145] method described and investigated in Chapter 5. This technique provides significantly improved results in comparison to other available conversion techniques, such as the widely used double integration method, as it eliminates the errors from the integration constants by processing in the Fourier space. The omega arithmetic method has a low frequency limit of $\sim$5 Hz, because as the frequency approaches zero, the $\dot{X}(f)$ derived from $\ddot{X}(f)$ becomes indeterminate, however, as the low frequency components are removed by filtering, this limit should not affect the velocity and displacement results in our measurement frame condition monitoring application.

6.4 Analysis techniques

The type of analysis performed on the acquired signal is dependent on the application and the characteristics of interest in the signal. In the first instance, the system allows the user to choose the type of signal on which to perform the analysis, where the three main vibration signals that are measured are acceleration, velocity or displacement. Vibration analysis techniques can be separated into the different domains in which the analysis is performed, i.e. the time domain or the frequency domain.

The system utilises two main VIs for the processing and analysis of vibration data: one VI for data collection and live processing, and a second VI that performs further analysis on the complete measurement dataset. The live data VI has a limited processing time and RAM ($\sim$3.5 GB). The RAM is limited due to the real-time module, which is needed to develop and embed real-time applications on the cRIO, but currently only operates using a 32-bit processing system. Due to the processing time and RAM limitations, the amount of

analysis and visual outputs in the live data VI is minimised to ensure the code can execute and update at the required rate. A data window strategy is used to provide data updates at regular time windows (every 2 s to 5 s). Displaying multiple graphics for eighteen signals simultaneously is not practical with the current computational limits, and so an automatic peak detection algorithm has been developed to display the data for the three channels with the largest averaged peak-to-peak response over the previous measurement window. Updating the graphs using the peak response method allows the channels (position and axis) with the largest vibrations to be highlighted and displayed on the front panel, whilst ensuring the graph is still legible and the dataset is limited to a size, which can be updated in the processing time available.

In order to limit the amount of processing required in the live data VI, only a subset of the analysis options are available for the user to select on the front panel. The analysis options available in the live data VI are described below.

6.4.1 Peak-to-peak

Peak-to-peak analysis looks at the distance from the positive peak to the negative peak (illustrated in figure 6.4), which in the case of a simple sine wave would be twice the amplitude of the positive peak as the wave is symmetrical. Peak-to-peak analysis is useful when displacement is of interest, and ideal for analysing shock events or assessing clearances in for mechanical assemblies. For measurement system applications, the maximum displacements present during the measurement time are of particular interest, as the system will have a limit for the level of vibration displacement that the system can tolerate and still meet the specified measurement accuracy. The identified peaks and valleys that exceed the user defined threshold values are used to find the average peak-to-peak response of the measurement window.

6.4.2 Frequency spectrum analysis

Frequency spectrum is an effective vibration analysis tool. By converting the signal into the Fourier domain using the fast Fourier transform (FFT) algorithm, the signal can be shown with respect to its vibration amplitude as a function of frequency. Analysing the frequency spectrum allows the different vibration signal contributors to be separated, so that the main excitation sources can be identified. The resolution of the frequency (i.e. the size of each frequency bin) in an FFT is directly proportional to the signal length and sample rate, and so to improve the resolution, the number of samples used in the FFT must be increased.

6.4.3 Power spectral density

The power spectral density (PSD) is a measure of the signal's power content against frequency, and shows how the power of the signal varies with frequency. PSD is a useful analysis technique for comparison of random signals over different sampling lengths because the signals are normalised by the spectral resolution so the signals can be overlaid and compared.

6.4.4 Event analysis

The post-measurement analysis VI is able to run on the 64-bit version of LabVIEW and so does not have the same processing time and memory restrictions as the live data VI. As a result of the increased available RAM, the post-measurement analysis VI is able to perform analysis on much larger datasets, allowing signal analysis of the entire measurement length. In addition, as the processing time is not limited by the data collection loop execution, the post-measurement VI is able to provide additional analysis capabilities and displays such as event analysis and 3D stacked ribbon plots.

In condition monitoring, identification and analysis of vibration 'events' is of particular interest, as sudden and sharp increases in vibration levels can be an indication that there is either a major fault within the system, or that an external source is interacting with the

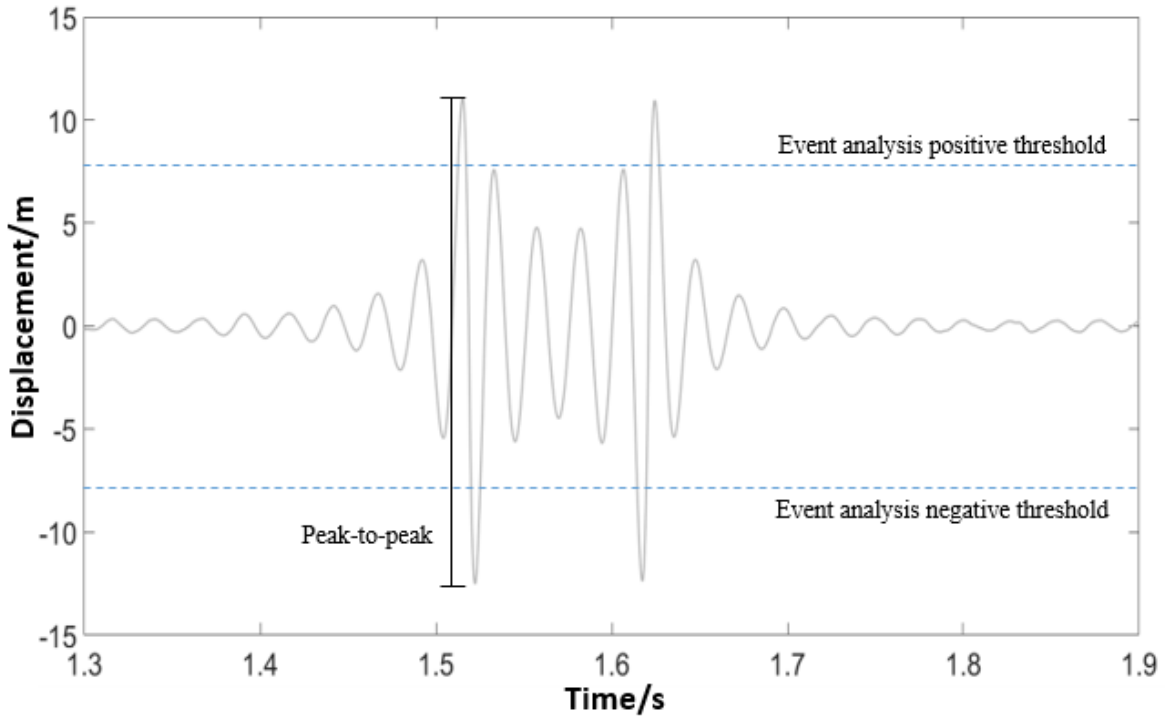


Figure. 6.4 The event analysis plot to investigate the dynamic behaviour around the area of interest, which is identified by the peak above the user defined threshold (dashed line), with the peak-to-peak analysis also illustrated.

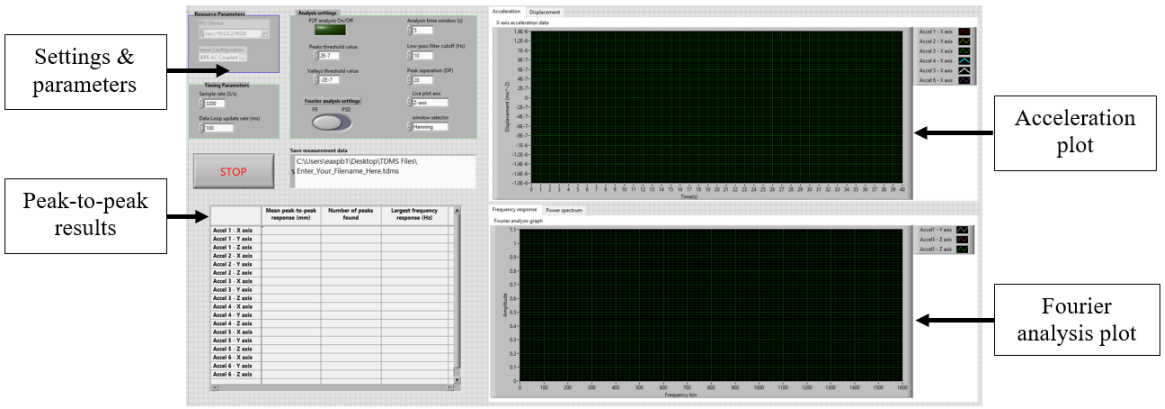


Figure. 6.5 Front panel LabVIEW display of the multi-accelerometer host VI, which allows the user to control the system and view the measurement results.

system. Event analysis identifies any significantly large peaks which are above the peak threshold values set by the user, and are much larger than the usual vibrations present. The 'event' is plotted (figure 6.4) with a much smaller time window to allow further investigation into the dynamic behaviour of the system before and after the vibration spike i.e. to evaluate the dissipation time and check for any reoccurrence.

6.4.5 User interface

The front panel (shown in figure 6.5) was designed for simplicity, so that the user can easily navigate and operate the system. The front panel is comprised of three main sections, which are the settings and parameters, the results and the system properties and errors.

6.4.5.1 Results - Live data VI

The results section shows the raw acceleration data, which is updated live based on the user-chosen axis for all of the accelerometers; an example of acceleration results for the z-axis is shown in figure 6.6. Viewing the live data in the chosen axis for each position allows the user to see an immediate response of the vibration behaviour in the system. The second graph shows the results of the Fourier analysis, and shows a plot of the frequency response

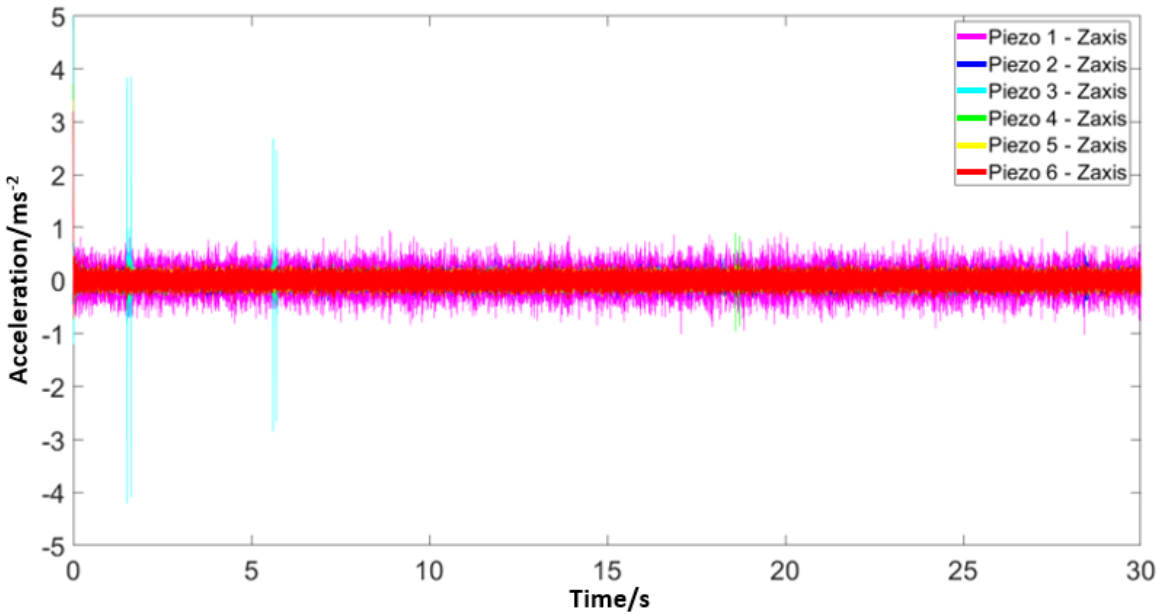


Figure. 6.6 Live acceleration results for the z-axis for each of the six accelerometers allowing the user to immediately see any changes to the dynamics of the system.

or the power spectral density (depending on the choice of the user). The displacement results for the three channels with the largest peak-to-peak responses are displayed on the graph, under the displacement tab on the front panel. The displacement plot updates at the rate of the user defined measurement window, and utilises an automatic peak detection algorithm to identify the channels with the largest responses from the previous measurement window. An example of the displacement results plot and frequency response can be seen in figures 6.7 and 6.8, respectively. The average peak-to-peak response for all eighteen channels and the number of peaks found are tabulated on the front panel.

6.4.5.2 Results – Post-measurement analysis VI

The post-measurement analysis VI displays the displacement and frequency response for all eighteen measurement channels, with the signals separated into the axis of measurement. Given that displaying large datasets in multiple channels is challenging for vibration measurements, a 3D stacked ribbon plot (figure 6.9) was created to show the displacement

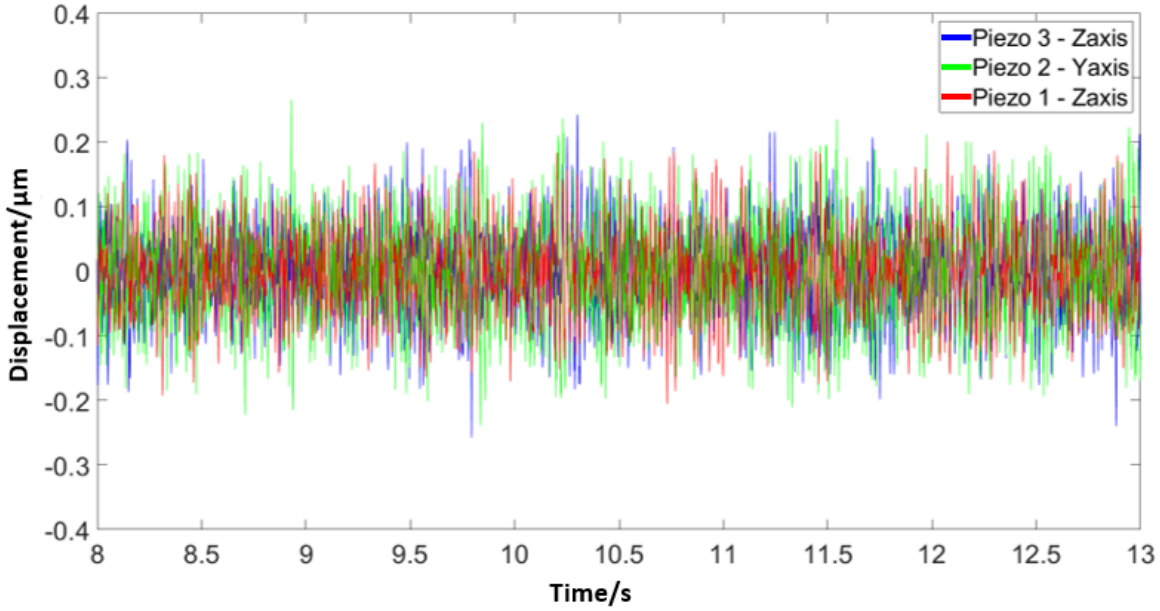


Figure. 6.7 Displacement results for the three channels that have been identified to have the largest average responses in the system within the time window analysed, which was 5 seconds in the example shown.

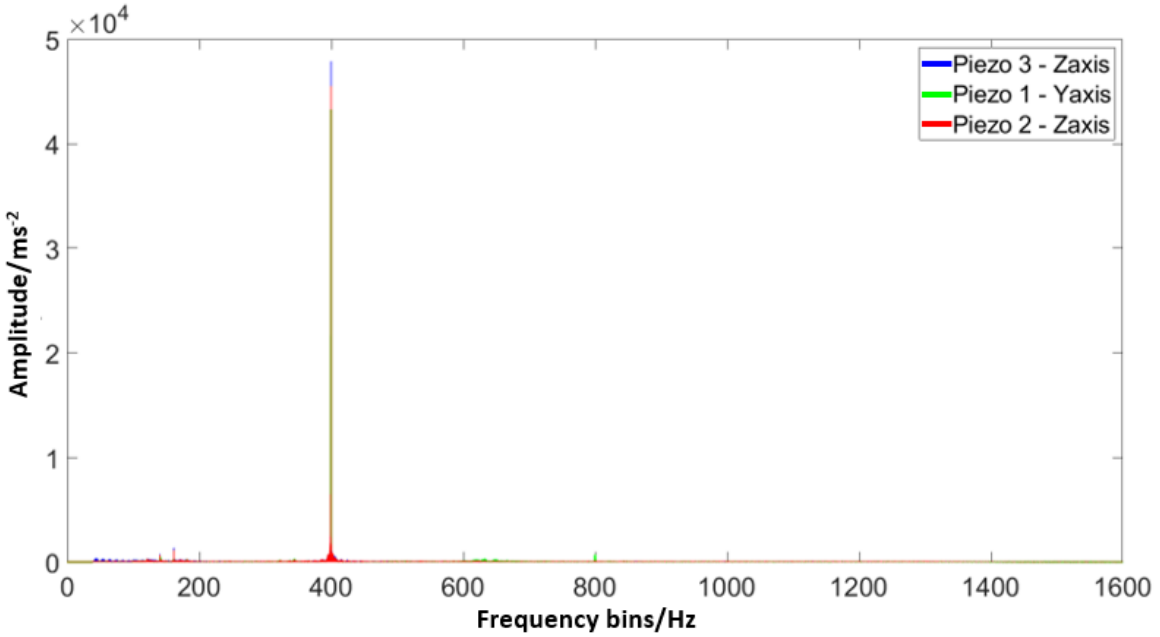


Figure. 6.8 Frequency responses of the three channels identified to have the largest average responses in the system within the time window analysed, which was 5 seconds in the example and shows a dominant excitation input with a frequency of 400 Hz.

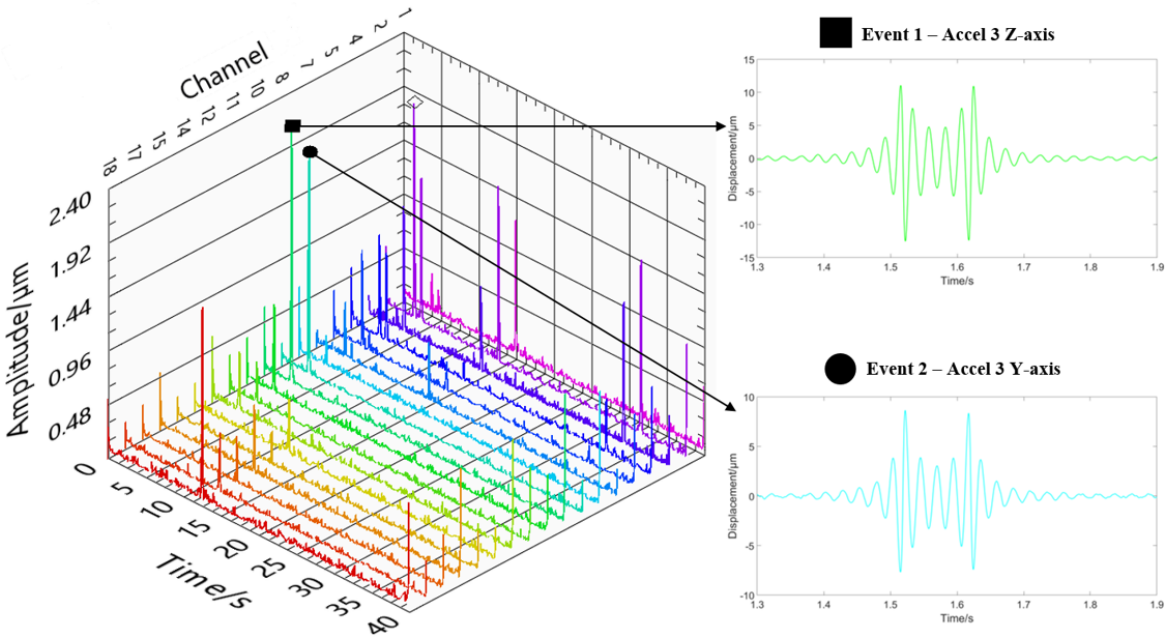


Figure. 6.9 3D stacked ribbon plot of the displacement envelope results for all 18 measurement signals (x, y and z axes for each accelerometer) with the key events that are identified to be of interest and so further analysed.

envelope of all eighteen channels on a singular plot to aid clear comparison. To make the plots distinguishable, the two-dimensional plots for each of the eighteen channels are stacked and evenly spaced along a third dimension and colour coded to help with visual identification. The 3D ribbon plot has also been used to highlight the location of the identified key 'events'. The 3D ribbon plot is currently not possible in the live data VI, due to the limits in RAM and processing time.

6.4.6 System properties and errors section

The system properties and errors section displays key system performance parameters whilst the VIs are executing, including the elements remaining in each of the FIFOs and the buffer queue, so the user can check that they are all being properly emptied. The execution times of both the data collection and processing loops are also displayed, to check they are running at the required rates and to allow the user to identify in which loop the problem is occurring

if either execution time increases. Finally, the LED indicators on the front panel that alert the user if either the FIFO or buffer queue are full. Error handling is an extremely useful tool for identifying and debugging any issues in the system, therefore if the code has any runtime errors, they are displayed in the FPGA error out or the host error out sections at the bottom of the system properties and errors section, depending on which part of the project has experienced the error.

6.4.7 Data handling

In the live data VI the raw accelerometer data is converted from raw voltage data to acceleration data using the sensors sensitivity factor, and then streamed to a TDMS file. This allows for the data to be processed live to monitor the performance/condition of the system, and then allow for post-process analysis to be carried out on the complete measurement dataset.

Another important step is presenting the processed results in a clear and user-friendly manner, so the front panel has been optimised to ensure the user can navigate and follow the information easily, where the quantity of information displayed is limited to ensure simple interpretation for the user. To supplement this, an automatic report generation tool was designed to present all of the data and analysis performed in a clear and easy to read report. As well as including all the key results and data, the report includes details of the parameters and settings used during measurement and an explanation of the methods used for analysis (including filtering and windowing applied during data processing), providing a useful account for reference and interpretation.

6.5 Lathe condition monitoring investigation

In order to demonstrate the flexibility of the system and highlight the analysis tools an experimental investigation into the effects of the depth of cut and tool wear was performed

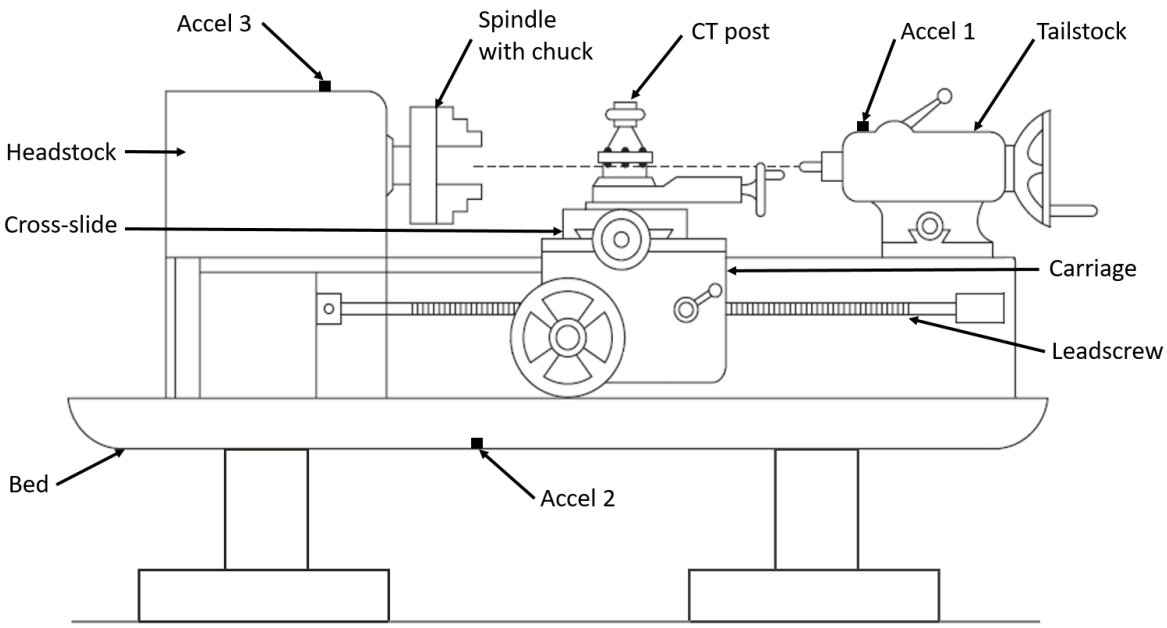


Figure. 6.10 Schema of the experimental configuration showing the key components of a lathe, and the accelerometer mounting positions for the condition monitoring investigation into the effects of the depth of cut and tool wear.

on a typical CNC lathe to show the effectiveness of the developed conditioning monitoring system. Three arbitrary locations were identified to mount the accelerometers on the lathe to allow the different components of the system to be monitored during operation, with the accelerometers readily integrated on the lathe using an adhesive. The locations (shown in figure 6.10) were the tailstock, cutting bed and the headstock.

To investigate the dynamic effects of different cut depths on the condition of the system, the vibrations in three axis were measured for a range of 0.5 mm to 4.0 mm depths of cut with steps of 0.5 mm. A cut of length 100 mm was performed for each depth of cut, with a new piece of stock material used for each test. The experiment was performed once with a new cutting tip, and once using a ‘worn’ cutting tip, which had been used for a number of cutting operations from a previous part, but was deemed in a “usable” condition. A number of parameters were set throughout the experiment and have been shown in table 6.1.

An example of the measured vibration signal for a 2 mm depth of cut using the new cutting tool can be seen in figure 6.11, and the results of the frequency response analysis in

Table 6.1 CNC lathe settings used in the experimental condition monitoring experiments.

Attribute	Setting
Spindle speed	600 RPM
Feed rate	0.15 mm/rev
Cut length	100 mm
Material	EN24 steel
Diameter	38 mm

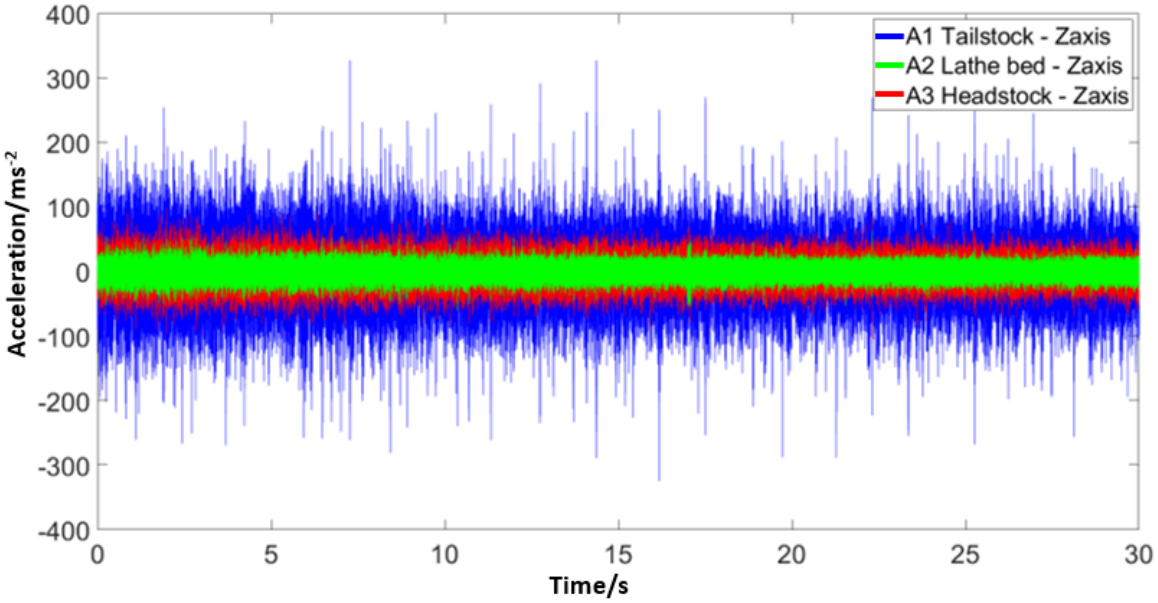


Figure. 6.11 Example measured vibration dataset in the z-axis, collected whilst performing a 2.0 mm depth of cut on a CNC lathe using a new cutting tip.

figure 6.12. The frequency analysis identified the largest frequency components of all three measurement positions to be at ∼10 Hz, which matches well with the vibrations that would be introduced to the system due to the spindle rotating at 600 RPM. The frequency analysis also showed the main frequency components in the lathe system are between 8 Hz to 50 Hz. From each of the measured signals, the average peak-to-peak response was calculated for the cutting process. The results for the x, y and z axes from the investigation using both new and worn cutting tips can be seen in figures 6.13, 6.14 and 6.15 respectively.

It is clear from the results that a larger cutting depth causes an increase in vibration in all three axes, and is consistent in all three positions measured. The largest variation

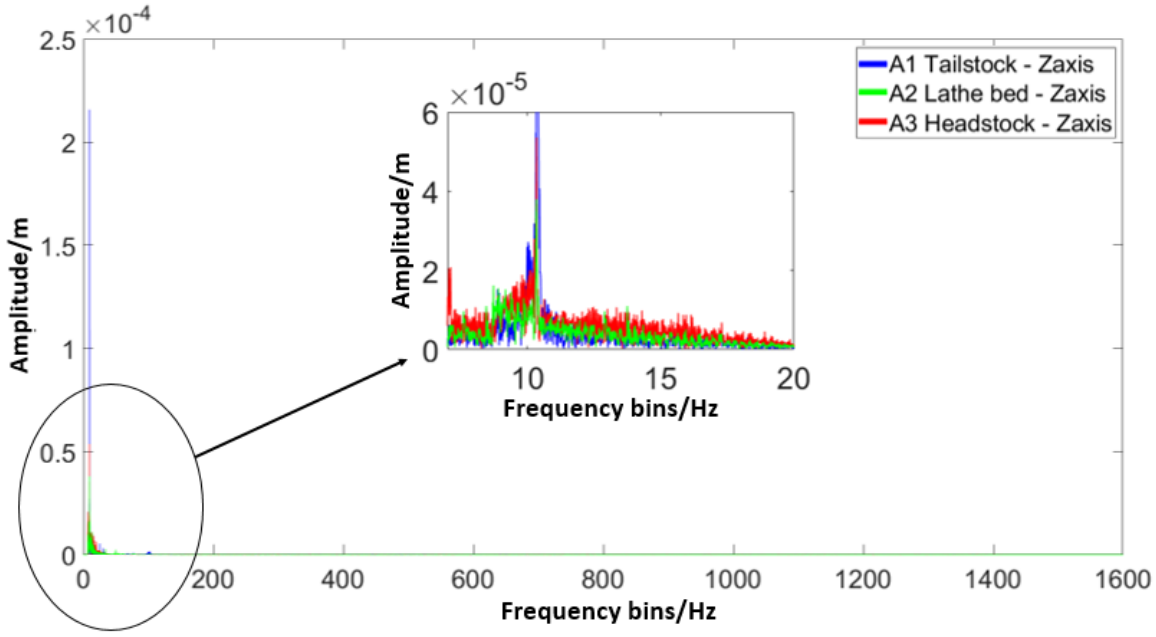


Figure. 6.12 Example frequency response analysis plot of the measured vibration dataset collected whilst performing a 2.0 mm depth of cut on a CNC lathe using a new cutting tip, showing the largest response at 10 Hz, which matches the frequency of the spindle.

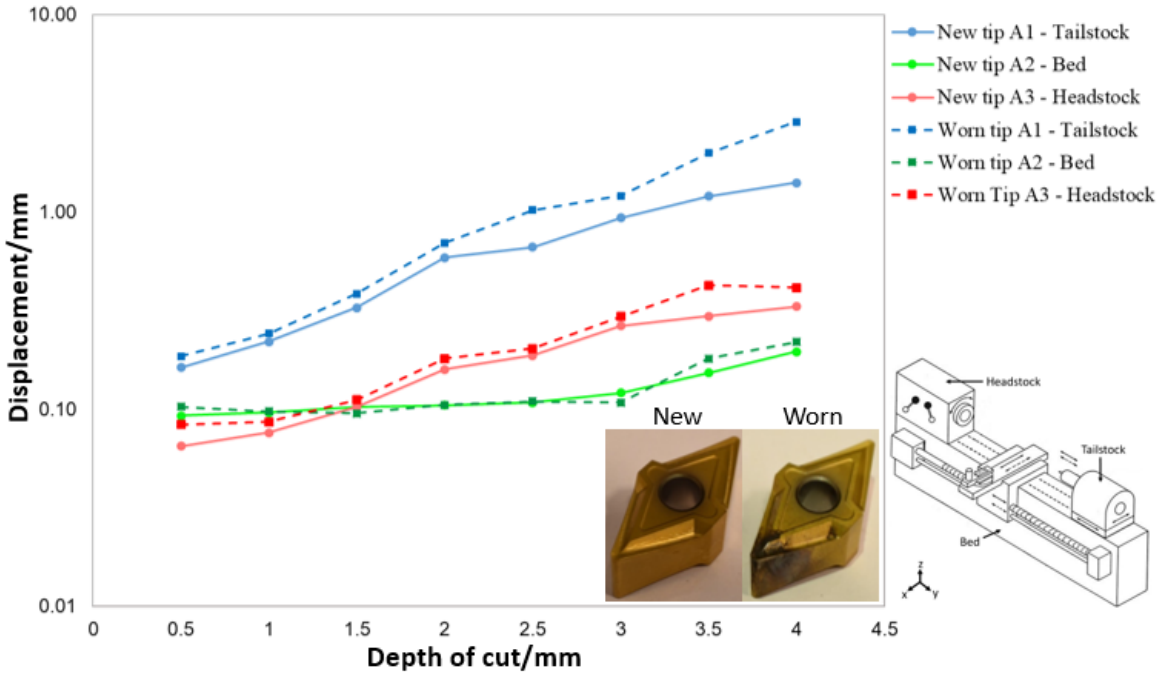


Figure. 6.13 Vibration results in the x-axis for the effect of increasing depth of cut and tool wear, showing the vibration increases that can be measured as the cutting tip progressively wears to predict tool failure.

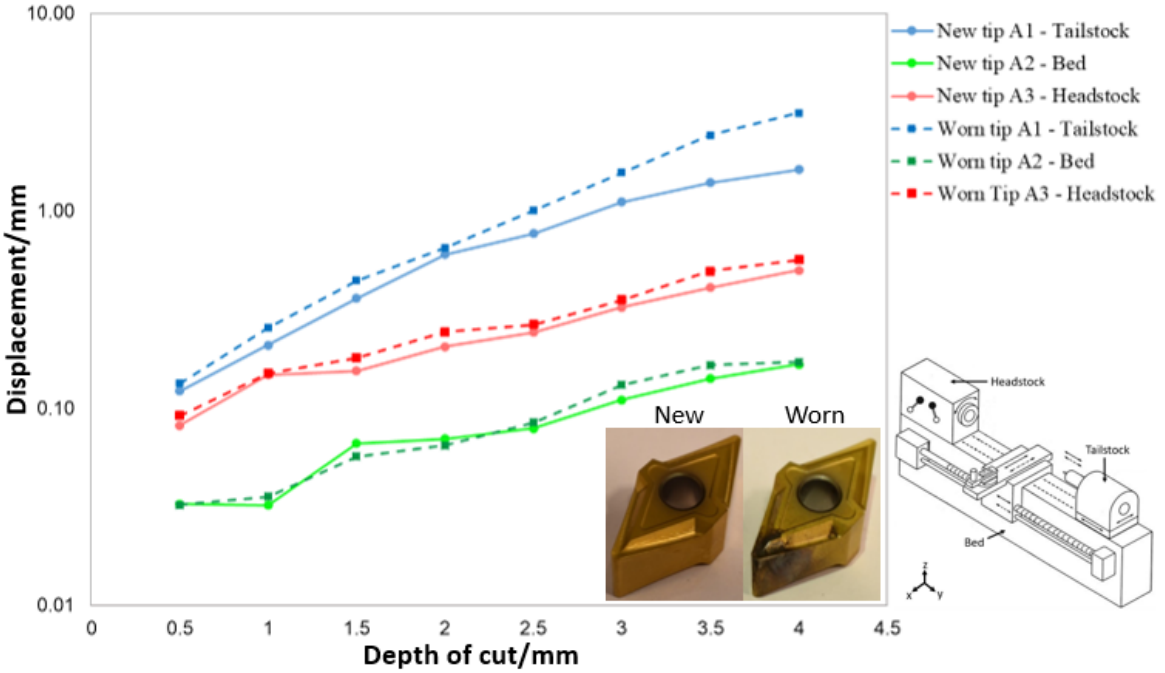


Figure. 6.14 Vibration results in the *y*-axis for the effect of increasing depth of cut and tool wear, showing the vibration increases that can be measured as the cutting tip progressively wears to predict tool failure.

in vibrations was in the tailstock, as it is directly connected to the work piece, and so experiences significantly increased vibration from the cutting process and the spindle rotating. The tailstock results showed there was a marked rise in the average peak-to-peak vibration response when performing cutting operations with a worn tip compared to the new tip in all three measured axes. The trend in both the new and worn cutting tip are similar with increasing the depth of cut, but there is a clear upward shift in the worn cutting tip results; this is a clear indicator of the effects of wear on tip. The clear detection of the increase in vibration due to tool wear in the tailstock demonstrates the effectiveness of the developed condition monitoring system, and shows it offers a flexible method to verify the vibration performance in a variety of applications. In the presented study of lathe cutting, further testing would allow for a vibration performance metric to be defined, which could be used to quantify the threshold of acceptable vibrations in order to monitor the condition of the

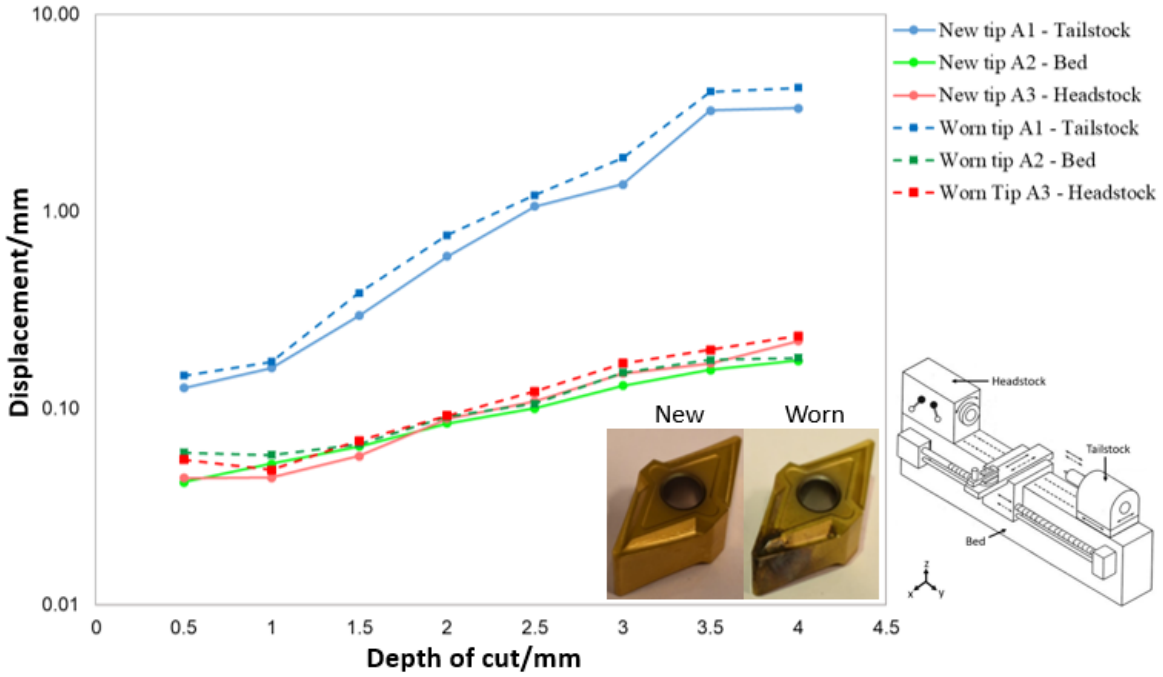


Figure. 6.15 Vibration results in the z-axis for the effect of increasing depth of cut and tool wear, showing the vibration increases that can be measured as the cutting tip progressively wears to predict tool failure.

cutting tip and predict tool tip failures before they occur. An example plot generated based on event analysis function of the developed system has been shown in figure 6.16.

The 'event' identified in figure 6.16 highlights the event analysis function of the developed system, and alerts the user to further investigate the behaviour as an area of interest, due to the higher than 'normal' amplitude of the vibrations measured. In the example shown, after further investigation the event was identified as due to the brake being applied to stop the spindle after the cutting process had finished. The lathe investigation demonstrated the use of the developed multi-point condition monitoring system, and shows how effective condition monitoring can enhance tool wear detection in machine applications, by measuring the increase in vibrations due to the wearing of the cutting tip. The developed system has clearly shown the functionality to readily measure and analysis the vibration changes in the structure to provide this condition monitoring capability.

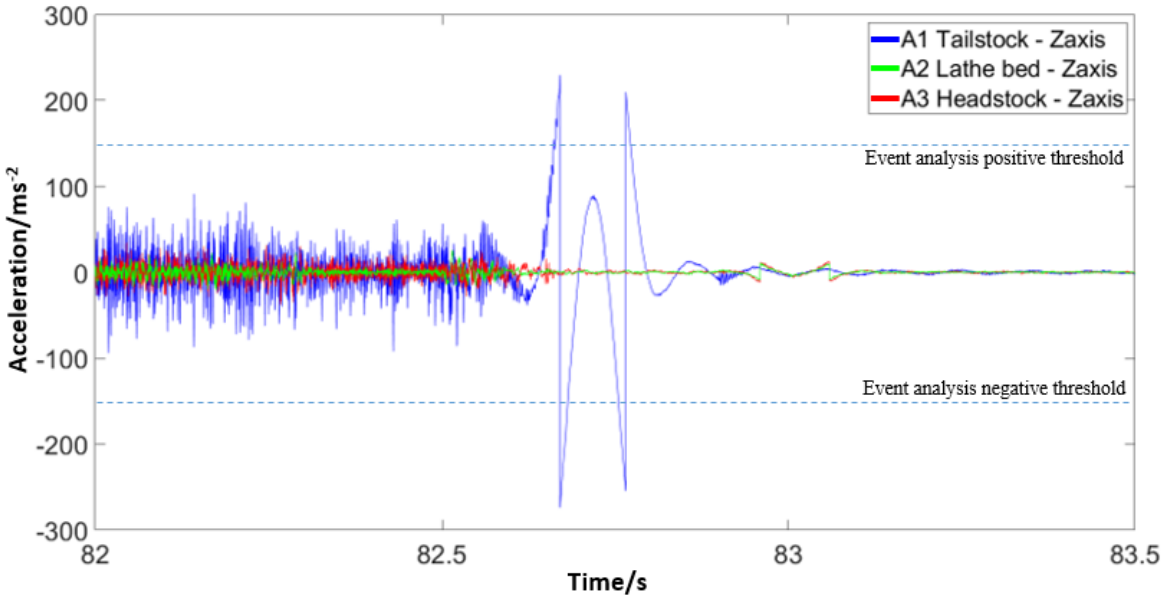


Figure. 6.16 Example of an 'event' identified by the event analysis tool, as the measured signal exceeds the user defined thresholds (dashed lines). In this example, the 'event' is as a result of the brake being applied to stop the spindle after the cutting process has finished.

6.6 Chapter summary

In this chapter, a flexible experimental multi-point vibration analysis performance monitoring and characterisation system has been detailed. The system offers a flexible solution for a variety of applications, and can characterise the dynamics of a structure in x, y and z axes, with a sensitivity of 102.5 mV/ms^{-2}, data acquisition (up to 12800 samples per second per channel) and a frequency range of 5 Hz to 6000 Hz. The developed system can rapidly process the collected dynamic performance data, and offers on-line condition monitoring capabilities to evaluate the structural performance live, with further post-measurement analysis functions also being available. An experimental investigation into the effects of the depth of cut and tool wear was performed on a CNC lathe, in order to demonstrate the capabilities of the developed system and the benefits of effective condition monitoring in a machine application. The system has been developed to be easy to implement to any structure, with a range of analysis functions so has the potential to be used across a wide range of applications.

The development of the system represents a key contribution of the project, and has been used in the case studies performed in Chapter 7, which were carried out to demonstrate the importance of condition monitoring for measurement systems, as well as further investigate the effects of vibration on fringe projection measurements for a commercial system and the in-house multi-view system.

Chapter 7

Live vibration monitoring of fringe projection systems

7.1 Introduction

In this chapter, the multi-point live condition monitoring system (described in Chapter 6) is used to carry out case studies on two fringe projection systems in order to demonstrate the effectiveness of condition monitoring in measurement system applications and to investigate the sensitivity of fringe projection measurements to vibration. The two measurement systems used were a commercial fringe projection system (GOM ATOS Core 300 [154]) and the in-house multi-view fringe projection prototype system [155, 156]. The study of the GOM system allowed for a commercially available fringe projection system to be investigated, in order to understand how sensitive a commercial system is to vibration. In addition, this study assessed how readily the designed mounting tripod for the system vibrated and, therefore, how susceptible the system would be to vibrational induced errors. The second case study into the multi-view fringe projection system allowed the performance of the system to be benchmarked against the commercial system, and a comparison of how sensitive the system is to vibration. The multi-view system also allowed for the importance of multi-point condition

Table 7.1 GOM ATOS core 300 fringe projection system specifications [154].

Feature/Attribute	Specification
Model	ATOS core 300
Measurement volume	(300 × 230 × 230) mm
Measurement point per scan	Up to 2 000 000
Probing Error Form (sigma)	0.003 mm
Probing Error Size	0.004 mm
Sphere Spacing Error	0.015 mm
Length Measurement Error	0.016 mm
Temperature range	+5 °C to +40 °C
System dimensions	(361 × 205 × 64) mm

monitoring to be demonstrated, as the multiple sets of cameras and projectors act as separate measurement systems, and can be affected to varying degrees by the same excitation source due to factors such as position on the frame and distance from the excitation source.

7.2 Case study one – Commercial fringe projection system

The first case study was performed on the ATOS Core 300 [154], which can achieve length measurement errors in the region of $\sim$16 μm. The specifications of the system are shown in table 7.1. The purpose of the case study was to utilise the condition monitoring system described in Chapter 6, and investigate the sensitivity to vibration of a commercially available fringe projection system, which could be then be used as a benchmark to compare with the multi-view fringe projection system. The investigation was carried out using the baseline comparison methodology developed in the earlier study (Chapter 4) into the sensitivity of fringe projection to vibration. An experimental setup was designed to enable a shaker to be mounted on the commercial fringe projection system's tripod, so the system could be excited in the x, y and z axes, and is shown in figure 7.1.

Using the experimental setup, the effects of vibration on the ATOS core 300 system were studied using the baseline measurement comparison method, whereby:

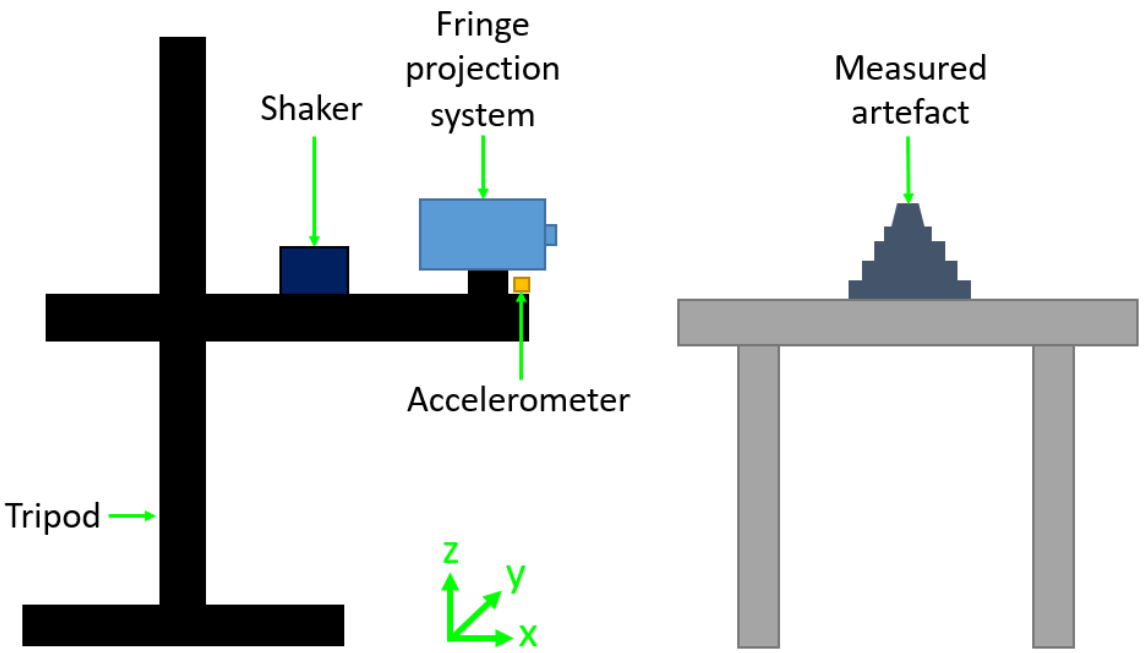


Figure. 7.1 Schema of the experimental setup using the GOM ATOS Core 300, a triaxial accelerometer and a Smart Shaker K2007E01 to investigate the sensitivity of a commercial fringe projection system to vibration.

- Ten baseline measurements of an AM designed artefact, with no applied excitation were performed, and compared to a reference measurement in order to find the mean of the deviations in the cloud-to-cloud analysis. The mean deviations in each measurement were then used to calculated the average baseline measurement error. The AM artefact was chosen as it was designed with multiple features, such as a hemisphere, a ball bar and steep slopes, to assess the system's ability to measure different features and to study how vibration affects the measurement of these features.

- The relative vibration amplitudes for a given frequency input using a fixed shaker voltage is determined by the resonance responses of the mechanical frame, and has been discussed in section 5.4 and shown in figure 5.13. Preliminary tests revealed that the mechanical responses to increasing the shaker voltage are independent of the frequency chosen, i.e. increasing the shaker voltage from 0.15 V to 0.3 V corresponds to an approximately 2$\times$ increase in the mechanical vibration at all tested frequencies.

It was therefore decided that only one frequency was required to showcase the error response of the fringe projection systems.

- For fringe projection systems, it is expected that the maximum frequency of translational vibration that can be perceived by the system is limited by the exposure time of the fringe projection cameras. For frequencies exceeding two times the exposure time, all further movement will be averaged across the range of vibration. Therefore, for an estimated minimum exposure time for the GOM system of 0.05 seconds [157], the system would have a corresponding maximum perceived frequency of 40 Hz, therefore applying a safety factor of two, a frequency of 80 Hz was chosen for the shaker. This frequency was low enough to ensure the shaker was operating well within its capabilities, preventing overheating or performance degradation, yet high enough to exceed the maximum perceived frequency by a factor of two.

- Ten repeat measurements were then taken at each varying level of vibration/excitation applied to the system. This step was repeated for each of the x, y and z axes, to assess the effects of vibration in each axis. The vibration was applied at 80 Hz, with the amplitudes ranged between 0.1 V to 0.45 V with steps of 0.05 V to allow for a range of amplitudes to be studied to better understand the different error effects. The vibration input was then measured using the developed condition monitoring system in order to quantify the amplitudes of the excitations in the structure.

- Two analysis methods were used to analyse the effects of vibration on the measurements. First a cloud-to-cloud comparison of the measured point clouds was performed to find the distortion error between each measurement and the baseline measurement. This was performed using the direct cloud-to-cloud comparison method described by Girardeau-Mountaut et al. [158], who used an iterative closest point (ICP) algorithm

Table 7.2 The measurement error results using a commercial fringe projection system with the vibration applied in the *x*-axis.

Vibration shaker input/V	Measured vibration/μm	Mean C2C error/μm	No. of points measured	Sphere probing error/μm
Baseline	1.76	30.44	756026	121.90
0.10	9.83	31.08	756803	122.20
0.15	12.09	36.38	756901	123.20
0.20	16.15	40.09	756771	141.20
0.25	21.67	47.66	756910	150.60
0.30	26.84	53.64	756958	172.41
0.35	33.35	72.35	757149	399.10
0.40	41.89	119.81	757857	553.00
0.45	52.75	167.67	757871	673.30

C2C: Cloud-to-cloud mean deviation error

[159] to finely align the two point clouds, and then calculated the Euclidean distance on a point-by-point basis between the two point clouds.

- The second analysis method measured the deviation to a fitted sphere, comparing between the baseline and vibration excited measurements. Using the ball bar fixture which had been designed onto the artefact, a least-squares algorithm [160] was applied to fit a sphere to the sphere on the ball bar with more measured points, and then calculate and compare the deviations. The positive and negative deviations were then used to calculate the mean deviation.

The results from both analysis methods for the *x*, *y* and *z* axes are shown in tables 7.2 to 7.4, and figures 7.2 to 7.9.

The results in table 7.2 and figure 7.2 show there is a clear positive trend in the mean error with increasing vibration amplitude in the cloud-to-cloud analysis for the *x*-axis, with significant errors up to $\sim$168 μm found for the higher amplitudes, which is more than five times bigger than the baseline deviations. The mean cloud-to-cloud deviation errors show two sections with different linearly increasing trends. The mean error for the lower vibration

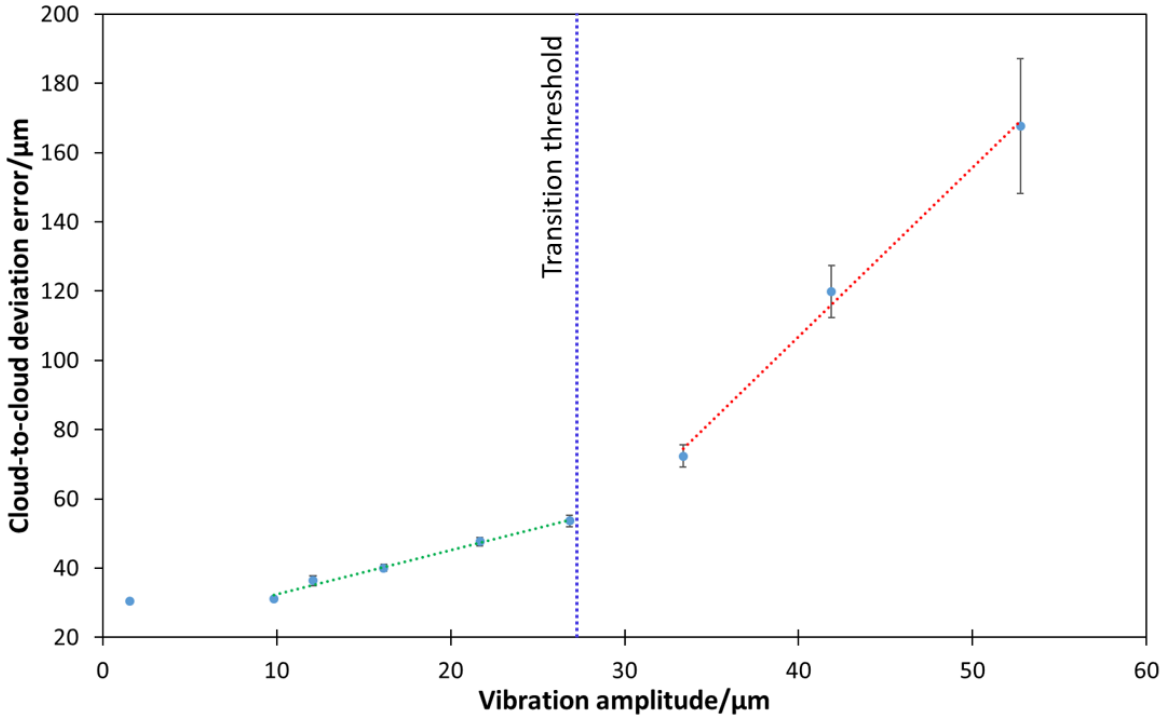


Figure. 7.2 A plot of increasing the amplitude of vibration in the x-axis against the mean cloud-to-cloud measurement error showing a sharp increase in the linear trend between the red and green dashed lines, which is due to the significant measurement errors seen around the edges of the complex features on the artefact. The blue dashed line shows the defined acceptable measurement threshold at the point the trends change.

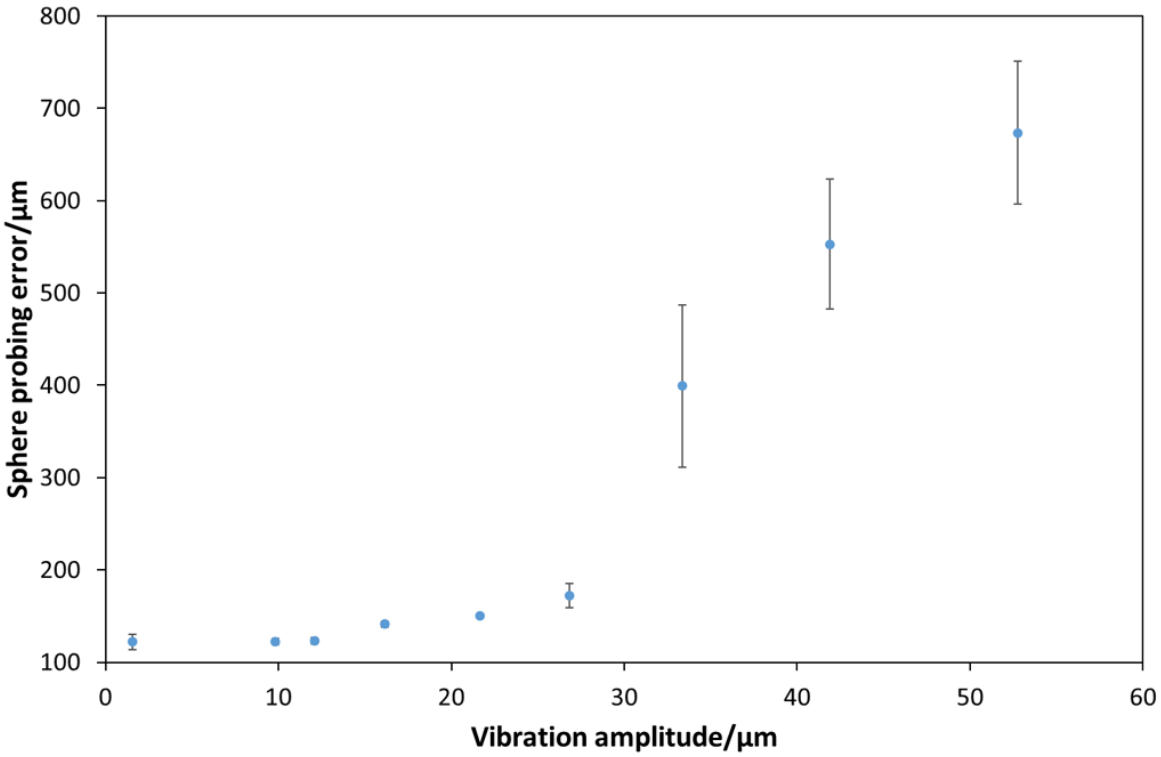


Figure. 7.3 A plot of increasing the amplitude of vibration in the *x*-axis against the sphere probing error (mean between the positive and negative) of a fitted sphere to the ball of the ball bar fixture on the AM artefact, shows how fringe projection measurements deteriorate on complex features as the vibration levels increase.

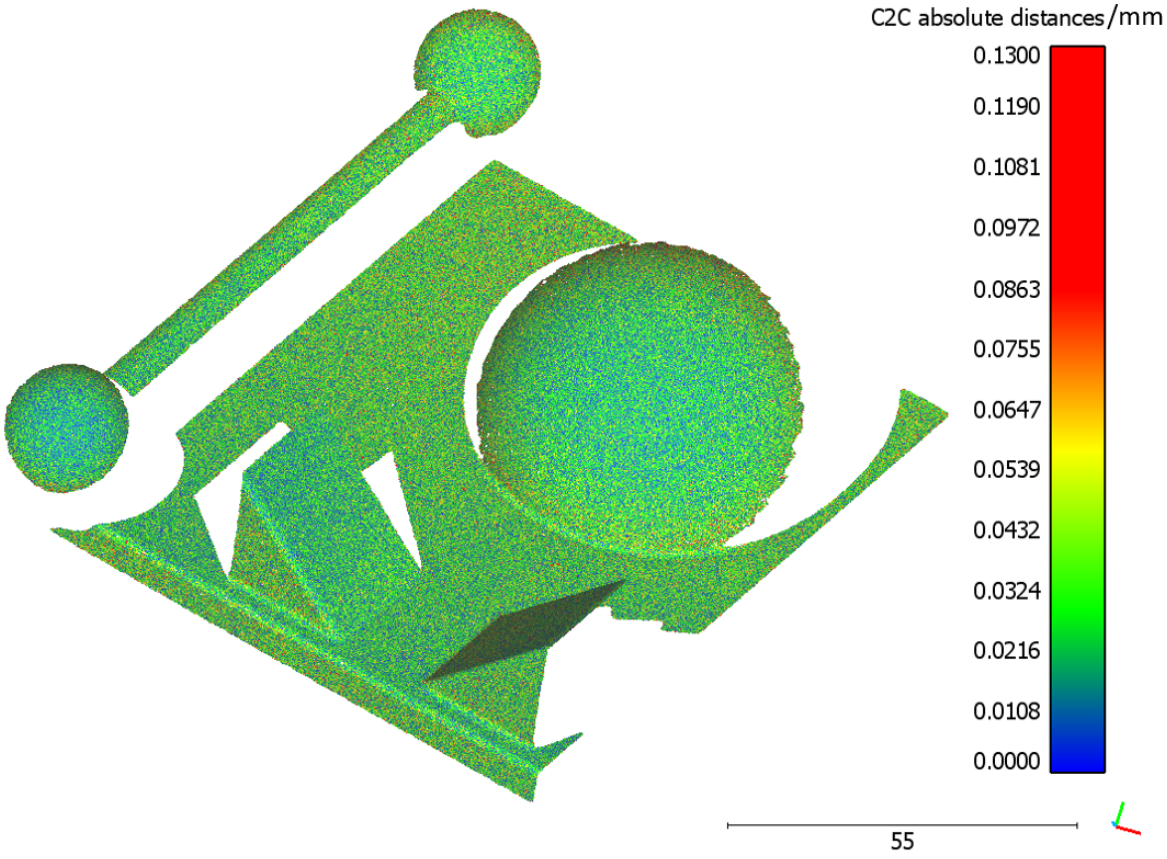


Figure. 7.4 Heat map of the cloud-to-cloud error analysis for 0.10 V vibration input of the shaker in the x-axis, showing the random distribution of errors across the measurement artefact.

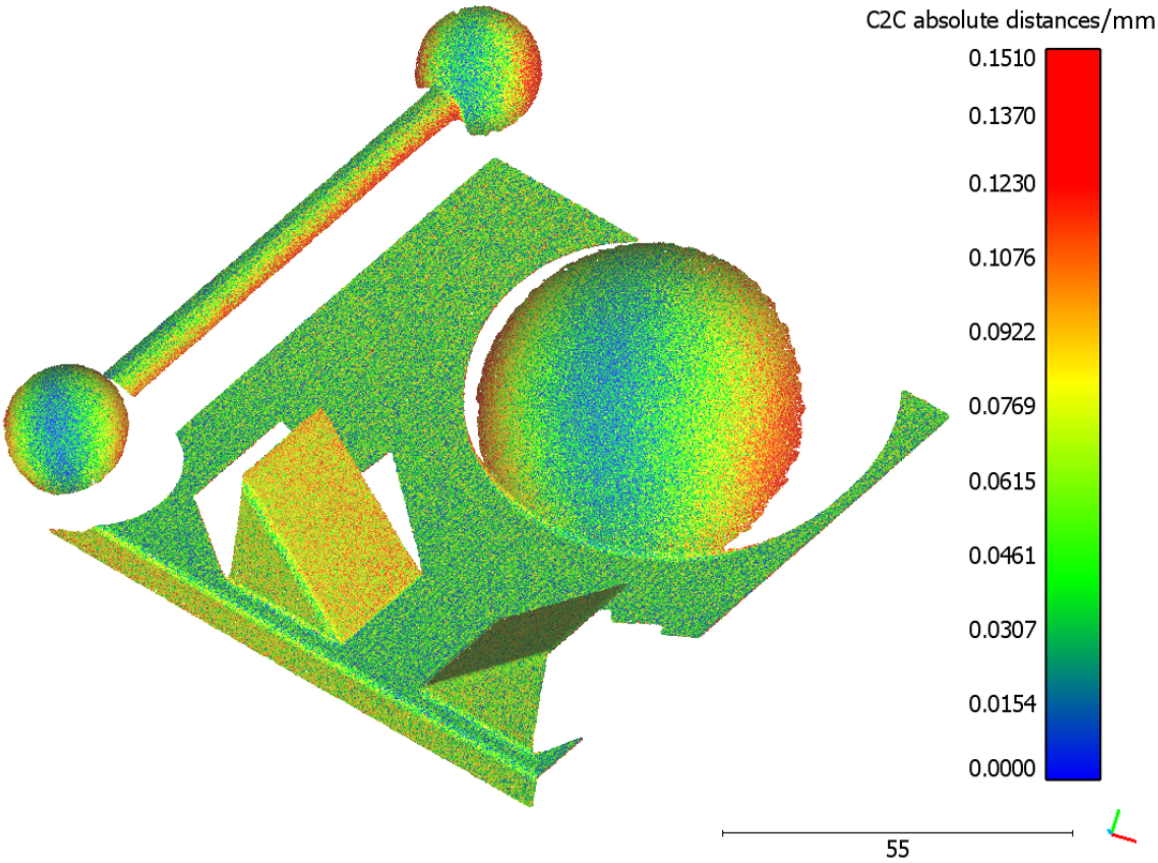


Figure. 7.5 Heat map of the cloud-to-cloud error analysis for 0.25 V vibration input of the shaker in the x-axis, showing the large measurement errors around the edges of the complex shapes on the AM artefact, i.e. the large sphere due to the triangulation errors caused by vibration.

amplitudes (9.83 μm to 26.84 μm) increases more gradually than the errors found for higher vibration amplitudes (33.35 μm to 52.75 μm). Using the results of the maximum sphere deviations shown in figures 7.3 and the cloud compare heat maps in figures 7.4 and 7.5, the two linear trends can be explained. Figure 7.4 shows the random noise that is present in the measurements due to the lower amplitude vibrations, with no identifiable structure to the errors and the range of the errors spread randomly across the measurement area. For the second linear trend (red dashed line), corresponding to larger amplitude vibrations, the errors are clearly structured, and figure 7.5 shows that the vibration is causing significant measurement errors around the more complex shapes on the AM artefact. The largest errors (highlighted in red) are seen around the edges of the spheres and steep slopes on the artefact, with sphere analysis identifying probing errors of $>$0.5 mm at the two largest vibration levels, which are likely due to the errors introduced in the viewing angles of the cameras causing large triangulation errors when calculating the measured points. The double linear trend matches well with the behaviour seen in the results for the simulated effects of vibration on fringe projection measurements (figure 4.2) carried out and presented in Chapter 4. This would suggest that the large measurement errors seen around the spheres are indicators that the measurement technique is breaking down and so cannot be used for reliable measurements with vibrations exceeding this limit. To this end, the measurement error curve has been used to define an acceptable vibration threshold for the *x*-axis by using the change in error trends, and has been illustrated with a blue dashed line in figure 7.2. It is recommended for future fringe projection measurements using the GOM ATOS Core system that the vibration in the *x*-axis does not exceed this threshold value.

The results for vibration in the *y*-axis are shown in table 7.3 and figure 7.6, and show a similar trend to the results for vibration in the *x*-axis, with significantly larger errors seen at higher amplitudes of vibration. The results for the lower vibration level show that the *y*-axis is less sensitive to vibration than the *x*-axis as there is no discernible difference in the errors

Table 7.3 The measurement error results using a commercial fringe projection system with the vibration applied in the *y*-axis.

Vibration shaker input/V	Measured vibration/μm	Mean C2C error/μm	No. of points measured	Sphere probing error/μm
Baseline	1.98	30.18	760558	114.70
0.10	12.05	31.34	760686	121.59
0.15	16.25	32.12	760855	122.70
0.20	21.49	31.90	760879	120.30
0.25	27.62	32.89	761028	122.70
0.30	34.73	34.61	760973	123.70
0.35	42.69	38.51	760995	130.30
0.40	51.63	49.47	761147	141.90
0.45	61.35	65.33	760865	179.60

C2C: Cloud-to-cloud mean deviation error

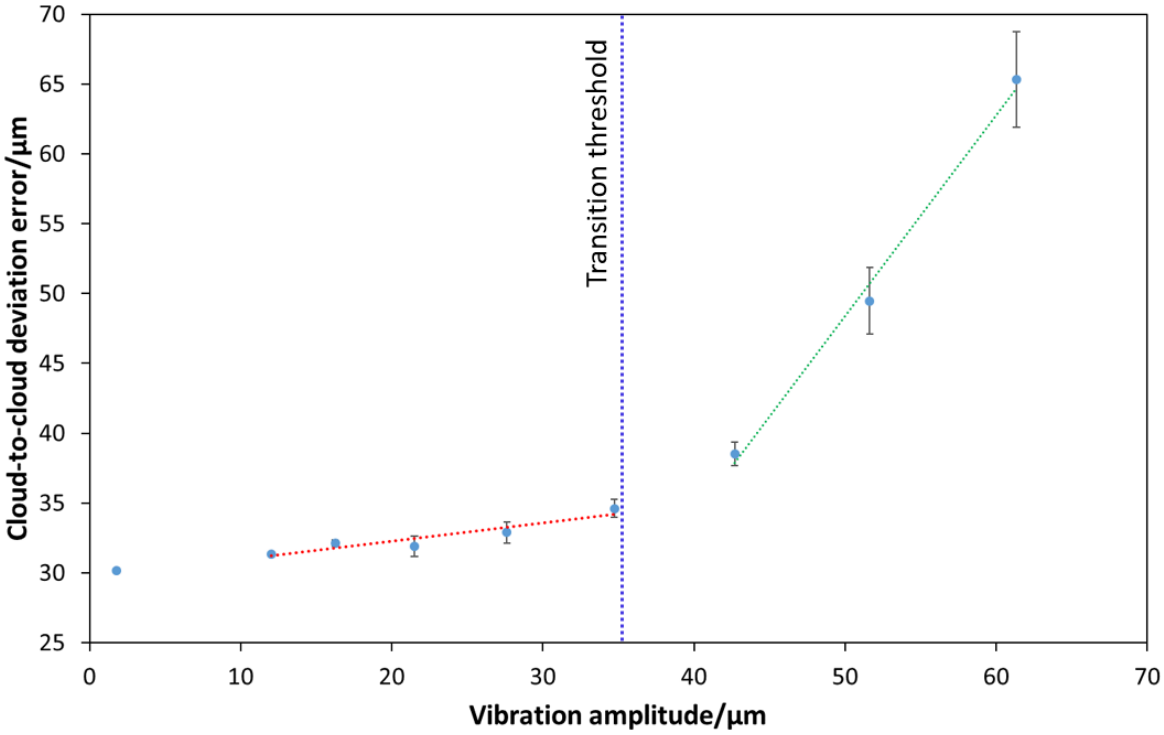


Figure. 7.6 A plot of increasing the amplitude of vibration in the *y*-axis against the mean cloud-to-cloud measurement error showing a sharp increase in the linear trend between the red and green dashed lines, which is due to the significant measurement errors seen around the edges of the complex features on the artefact. The blue dashed line shows the defined acceptable measurement threshold at the point the trends change.

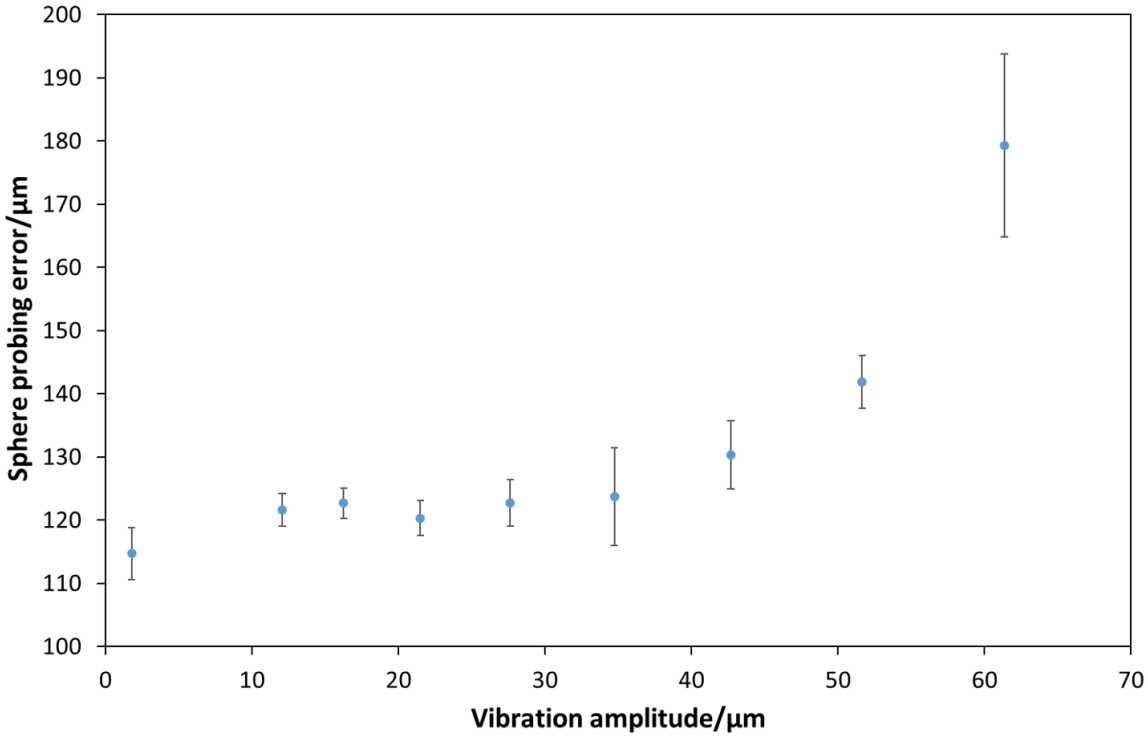


Figure. 7.7 A plot of increasing the amplitude of vibration in the *y*-axis against the sphere probing error (mean between the positive and negative) of a fitted sphere to the ball of the ball bar fixture on the AM artefact, shows how fringe projection measurement deteriorate on complex features as the vibration levels increase.

with vibration amplitudes between 12.05 μm to 27.62 μm. The deviation errors significantly increase for the amplitude vibrations above 27.62 μm, with the maximum error of $\sim$65 μm over two times larger than the baseline deviations. The trends in probing error, shown in figure 7.7, match well with the cloud-to-cloud analysis results, and show the sharp increase in errors that can be attributed to triangulation errors leading to complex shape measurement errors as seen in the *x*-axis results. The probing errors with vibration in the *y*-axis show a notable increase, with the largest probing error found to be $\sim$170 μm, however, the *y*-axis errors are not as large as those with vibration in the *x*-axis. An investigation into the layout of the experimental setup revealed no clear reasons for the difference in errors between *x* and *y*-axis vibrations. The commercial system utilised different sets of fringe patterns aligned perpendicularly, which would account for any setup bias in either the *x* or *y* axes. Therefore, it is expected that the source for this difference is within the closed-source software of the commercial system. Future collaboration with the commercial system manufacturers is required to fully understand the source of these differences. Similar to the *x*-axis, the *y*-axis double linear trend matches well with the behaviour seen in the results for the simulated effects of vibration on fringe projection measurements (figure 4.2) presented in Chapter 4, and so allows the limits of vibration to be set. To this end, the change in trends in the measurement error curve has been used to define an acceptable vibration threshold for the *y*-axis, and has been illustrated in figure 7.6 with a blue dashed line. It is recommended for future fringe projection measurements using the GOM ATOS Core system that the vibration in the *y*-axis does not exceed this threshold value.

The results in table 7.4 and figure 7.8 show there is a clear positive trend in the mean error of the cloud-to-cloud analysis for increasing vibration amplitudes in the *z*-axis. The maximum error of approximately 49 μm is over 1.6 times larger than the baseline deviations, however, the errors seen in the *z*-axis vibrations are significantly smaller than the largest errors in the *x* and *y* axes vibrations, which suggests that the fringe projection measurements

Table 7.4 The measurement error results using a commercial fringe projection system with the vibration applied in the z-axis.

Vibration shaker input/V	Measured vibration/μm	Mean C2C error/μm	No. of points measured	Sphere probing error/μm
Baseline	1.83	29.82	760336	120.20
0.10	8.47	30.76	760332	122.20
0.15	12.18	30.79	760544	121.10
0.20	16.91	31.14	760680	120.50
0.25	22.37	31.84	760733	126.20
0.30	28.41	32.59	760668	126.50
0.35	34.82	33.59	760849	121.20
0.40	41.37	36.89	760826	121.50
0.45	48.76	42.04	760996	129.50

C2C: Cloud-to-cloud mean deviation error

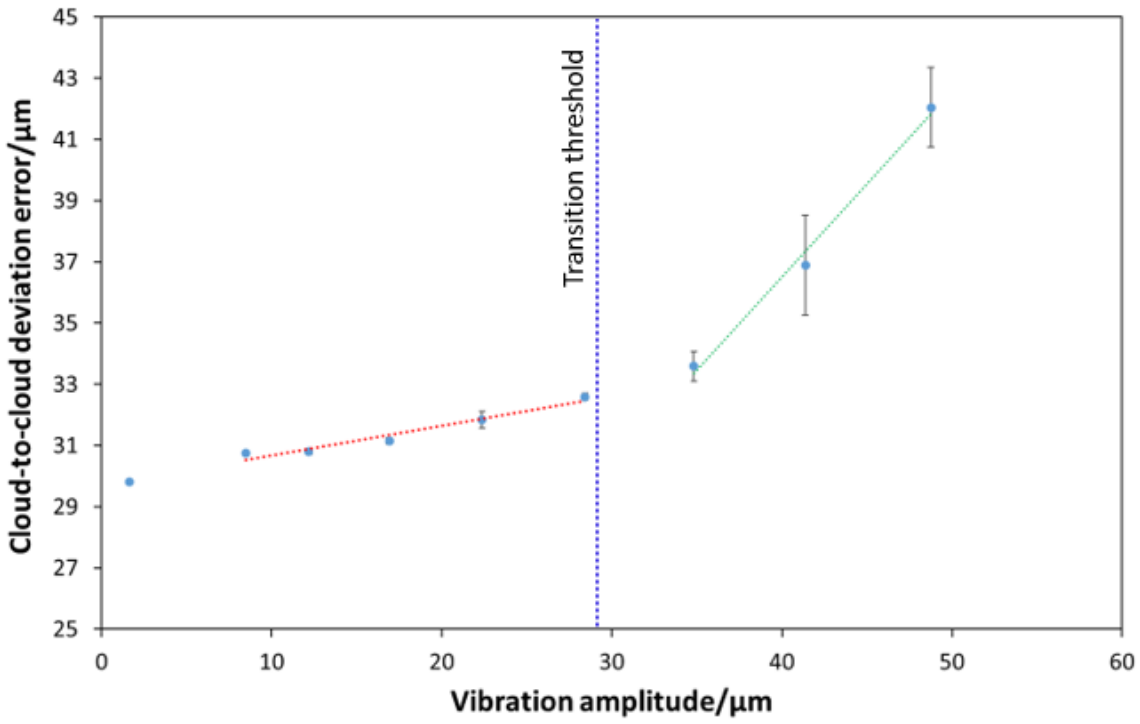


Figure. 7.8 A plot of increasing the amplitude of vibration in the z-axis against the mean point-to-point measurement error shows the measurement errors increase but is less sensitive to vibration in this axis compared to the x and y axes, and does not see the same complex shape measurement errors. The blue dashed line shows the defined acceptable measurement threshold at the point the error trend increases.

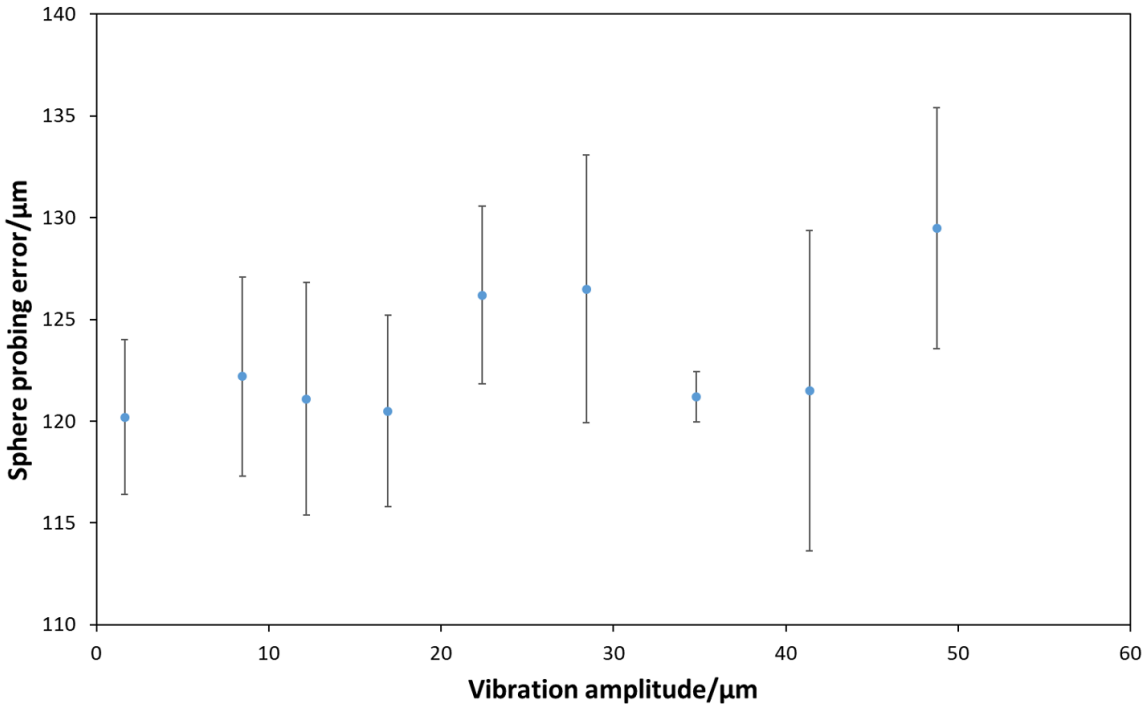


Figure. 7.9 A plot of increasing the amplitude of vibration in the z-axis against the sphere probing error (mean between the positive and negative) of a fitted sphere to the ball of the ball bar fixture on the AM artefact, shows the trend of the sphere probing errors in the z does not match the increasing measurement error trend as it does in the x and y axes.

are less sensitive to vibrations in the z-axis. Further investigation showed that this reduced sensitivity is because the z-axis vibration results do not experience the same complex shape measurement errors at the larger amplitude vibrations. This is confirmed by the sphere probing error results in figure 7.9, which show no discernible trend and vary randomly across the range of vibrations. The cloud-to-cloud errors across all of the z-axis vibration measurements are similar to the random noise seen in the lower amplitude vibrations in the x-axis, and show no identifiable structure to the errors with the range of the errors spread randomly across the measurement area. The trends match well with the simulation results (figure 4.2) presented in Chapter 4, and so suggest the sharp increase in cloud-to-cloud error could be attributed to unwrapping errors caused by the vibration between patterns affecting the phase shifts. To avoid avoid these significantly larger errors, the measurement error curve has been used to define an acceptable vibration threshold for the z-axis by using the change in error trends, and has been illustrated with a blue dashed line in figure 7.8. It is recommended for future fringe projection measurements using the GOM ATOS Core system that the vibration in the z-axis does not exceed this threshold value.

It should be noted that in this work the investigation was limited to showing the differences that exist between the measurement sensitivities to vibration in the different axes, and it is currently not clear as to the cause of these differences. It is likely that these differences are related to the triangulation errors that are caused by the movement in the different positions of the two cameras, leading to erroneous correspondence points being found in the captured images and large measurement errors on the more complex part shapes. However, further investigation into the causes of the differences between axis sensitivity represents a significant research undertaking and is an interesting area for future work.

7.3 Case study two – multi-view fringe projection

The second case study was performed on the in-house developed multi-view fringe projection system. The purpose of the case study was to benchmark the performance of the system in its current state by comparing the system to a commercial system. In addition, the case study was carried out to investigate the systems sensitivity to vibration and demonstrate the usefulness of multi-point condition monitoring using the developed live vibration monitoring system (described in Chapter 6). The investigation was carried out using the baseline comparison methodology developed in the earlier study (Chapter 4) into the sensitivity of fringe projection to vibration and used in the GOM fringe projection system case study (section 7.2). The fringe projection measurement methodology, used in the case study, was developed by a colleague at the university of Nottingham as part of the larger project working towards a multi-view fringe projection system. An experimental setup was designed to enable a shaker to be mounted on the multi-view fringe projection frame, and excite the system in the x, y and z axes, and is shown in figure 7.10.

The results from the cloud-to-cloud analysis for the x, y and z axes are shown in tables 7.5, 7.6 and 7.7, and figures 7.11 to 7.18.

The x-axis results in table 7.5 and figure 7.11 highlight that the multi-view system has a ‘modulation’ issue, which is causing structured waviness errors across the measurement artefact. The modulation errors have been reduced using an increased number of phase shifts to average out the non-linearities in projector intensity, which are assumed to be the primary cause of the observed waviness, however, this is an on-going issue for the system and is yet to be resolved. Interestingly, the errors in the measurement are reduced when low levels of vibration are introduced to the system. The decrease in errors is likely due to the vibration in the system causing a slight blurring in the images, leading to an averaging of the captured pixel intensities which causes a smoothing effect and reduces the waviness modulation seen in the static measurements. The errors are significantly increased with vibrations between

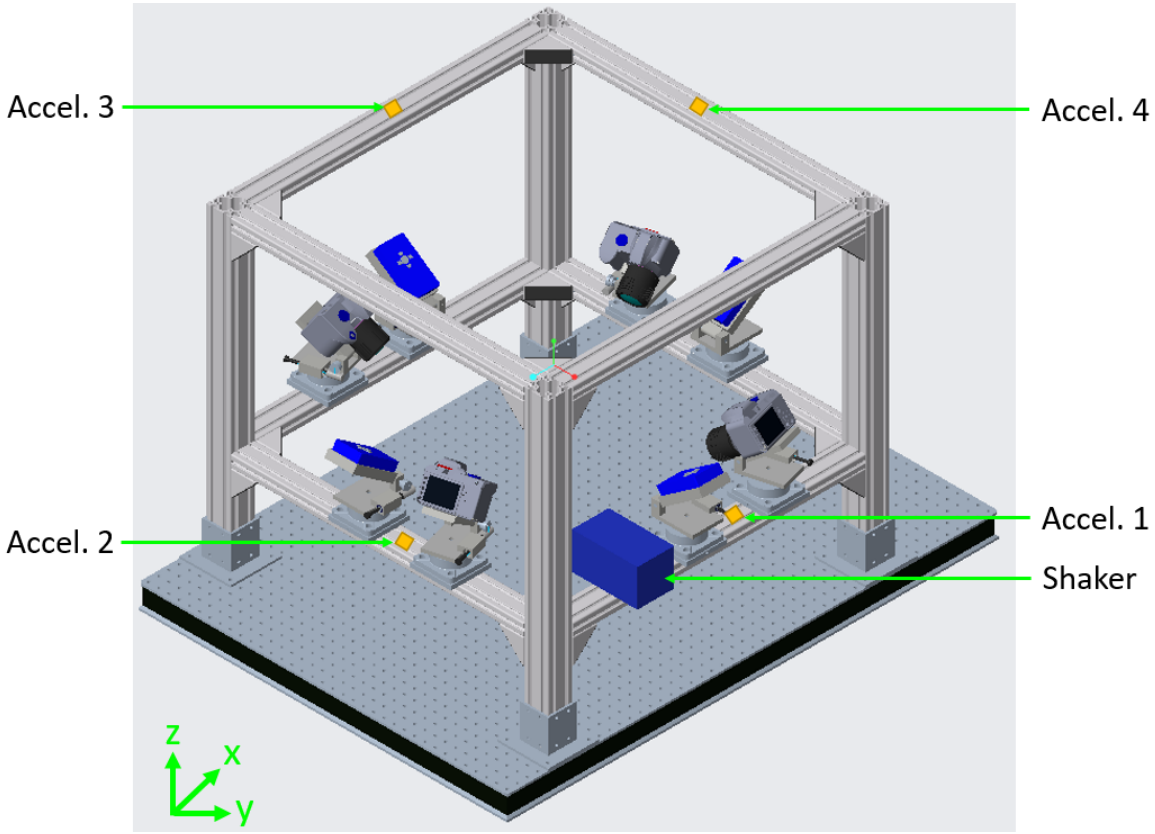


Figure. 7.10 Schema of the experimental setup using the developed multi-view fringe projection system, four triaxial accelerometers and a Smart Shaker K2007E01 to benchmark the system and investigate the measurement sensitivity to vibration, as well as demonstrate the use of multi-point condition monitoring.

Table 7.5 The measurement error results using the multi-view fringe projection system with the vibration applied in the x-axis.

Vibration shaker input/V	Measured vibration/μm	Mean C2C error/μm	No. of points measured
Baseline	0.62	88.42	847775
0.10	8.13	81.14	886479
0.15	11.50	95.96	731368
0.20	14.70	148.36	708485
0.25	18.15	474.48	564490
0.30	21.82	671.14	540285
0.35	25.94	798.98	579196
0.40	30.57	855.24	557955
0.45	35.66	875.74	554983

C2C: Cloud-to-cloud mean deviation error

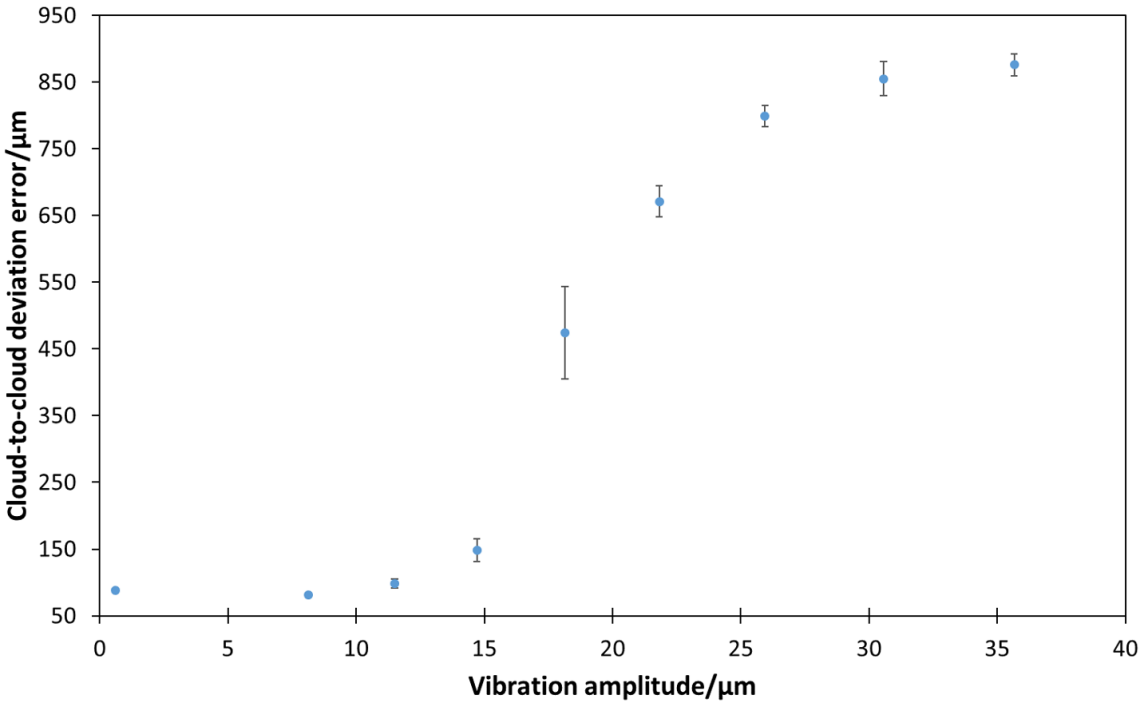


Figure. 7.11 A plot of increasing the amplitude of vibration in the x-axis against the mean cloud-to-cloud measurement error shows a significant rise in measurement errors as the captured images are increasingly blurred.

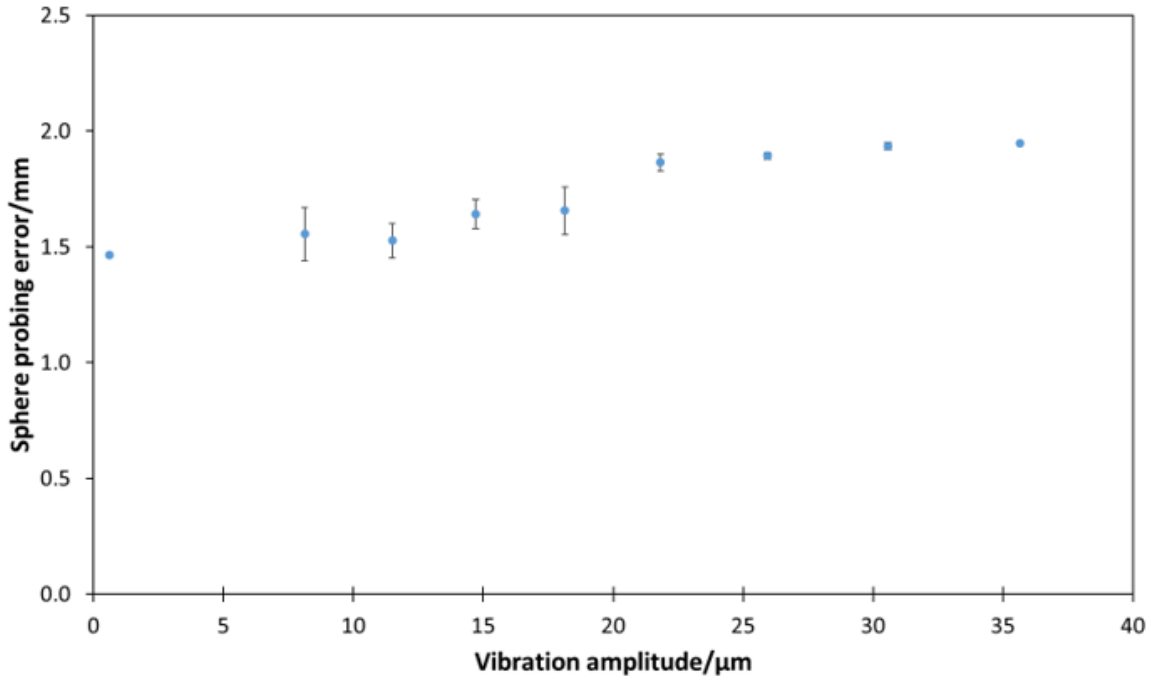


Figure. 7.12 A plot of increasing the amplitude of vibration in the x-axis against the sphere probing error (mean between the positive and negative) of a fitted sphere to the ball of the ball bar fixture on the AM artefact, shows the sphere probing error trend does not match the increasing measurement error.

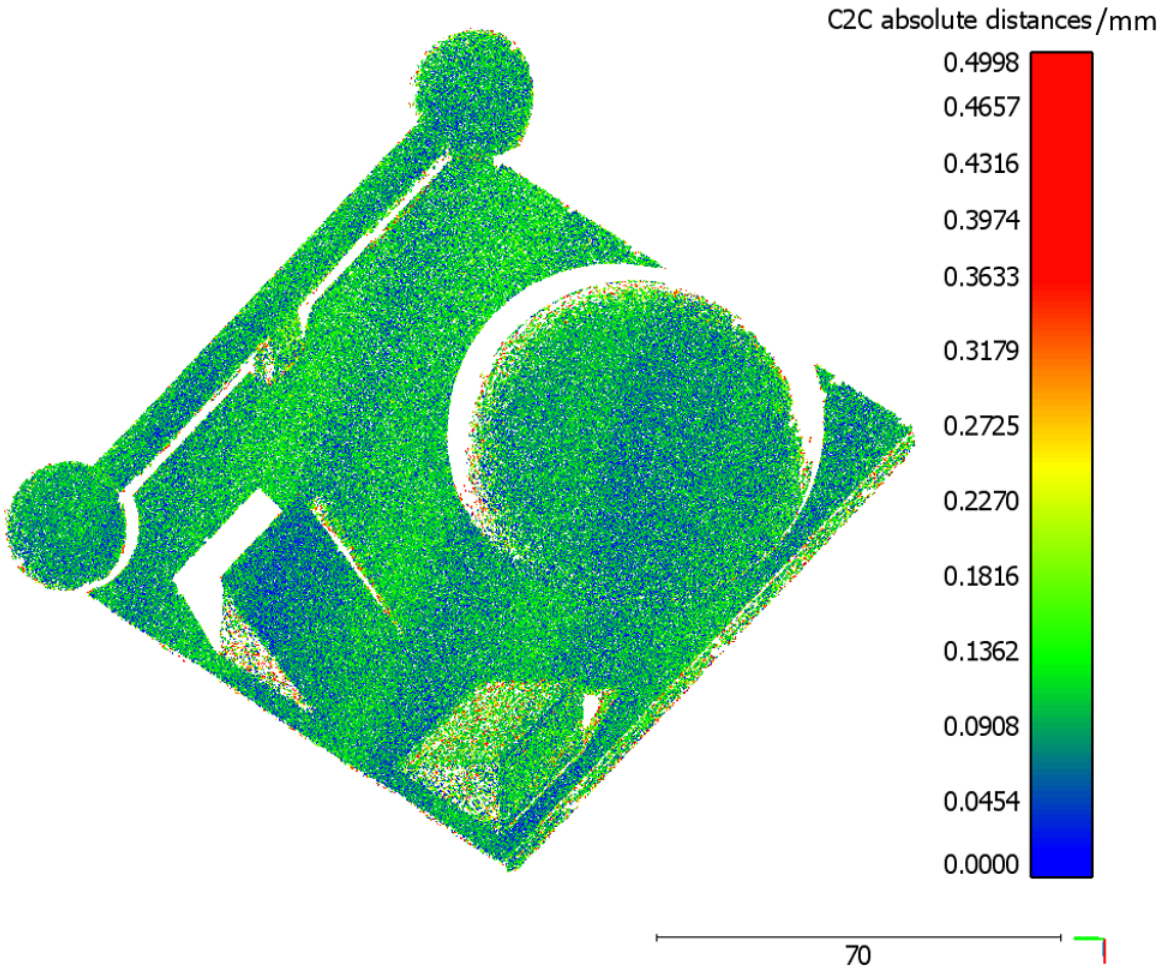


Figure. 7.13 Heat map of the cloud-to-cloud error analysis for 0 V (baseline) vibration input of the shaker in the x-axis, showing the structured modulation errors across the measurement artefact.

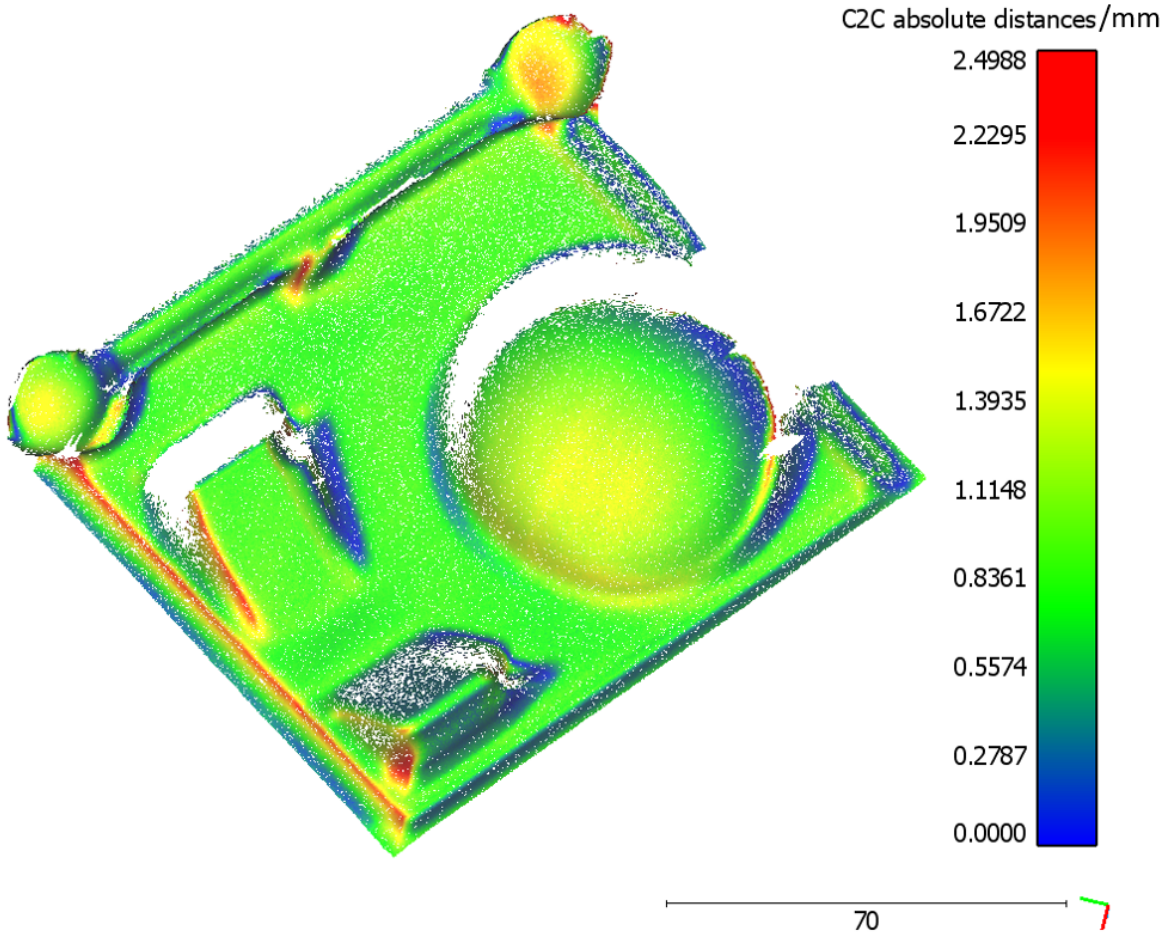


Figure. 7.14 Heat map of the cloud-to-cloud error analysis for 0.35 V vibration input of the shaker in the *x*-axis, showing the large measurement errors around the edges of the artefact due to the 'over-smoothing' effect.

Table 7.6 The measurement error results using the multi-view fringe projection system with the vibration applied in the *y*-axis.

Vibration shaker input/V	Measured vibration/μm	Mean C2C error/μm	No. of points measured
Baseline	0.67	92.80	838423
0.10	9.84	86.30	863055
0.15	14.77	143.30	737803
0.20	19.84	411.94	644386
0.25	25.12	622.40	532736
0.30	29.39	830.56	551052
0.35	33.38	854.24	513594
0.40	37.71	901.06	463560
0.45	42.93	1236.80	438432

C2C: Cloud-to-cloud mean deviation error

14.70 μm (0.20 V shaker input) and 25.94 μm (0.35 V shaker input), which is due to the increase in blurring in the captured images causing an over-smoothing effect that results in edges and sharp changes in geometry being measured as curved slopes. This over-smoothing effect can clearly be seen in figure 7.14 on the edges of the artefact base, as well as in the significant reduction in measured points shown in table 7.5. The results show less significant changes at the most extreme vibration input levels, likely due the effect of blurring sharp edges experiencing diminishing returns as blur is increased. The results of the sphere probing error analysis in figure 7.12, showed the increasing measurement errors were not linked to the complex shape measurement errors that were seen in the previous GOM fringe projection sensitivity case study, and so suggests the behaviour of our multi-view system differs from the commercial system.

The *y*-axis results (table 7.6 and figure 7.15) and *z*-axis results (table 7.7 and figure 7.17) show similar trends to the results in the *x*-axis. These similar trends suggest the same factors as previously described for the *x*-axis cause the same effects to the *y* and *z*-axis measurements. The *z*-axis results are similar to those seen in the *x*-axis, with a significant increase in errors

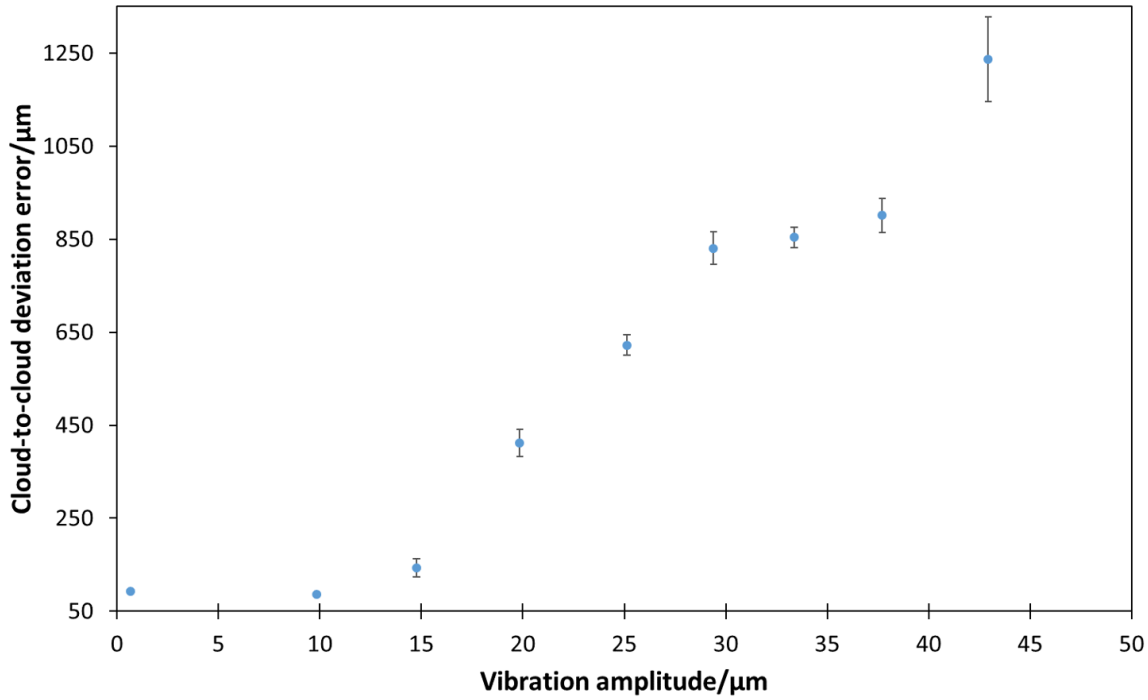


Figure. 7.15 A plot of increasing the amplitude of vibration in the y-axis against the mean cloud-to-cloud measurement error shows a significant rise in measurement errors as the captured images are increasingly blurred.

Table 7.7 The measurement error results using the multi-view fringe projection system with the vibration applied in the z-axis.

Vibration shaker input/V	Measured vibration/μm	Mean C2C error/μm	No. of points measured
Baseline	0.74	93.68	857664
0.10	8.96	90.60	821551
0.15	12.09	106.72	783676
0.20	15.28	149.54	724023
0.25	18.82	469.80	588862
0.30	23.01	693.68	542140
0.35	27.39	806.30	539405
0.40	32.42	793.84	553985
0.45	37.70	827.32	507127

C2C: Cloud-to-cloud mean deviation error

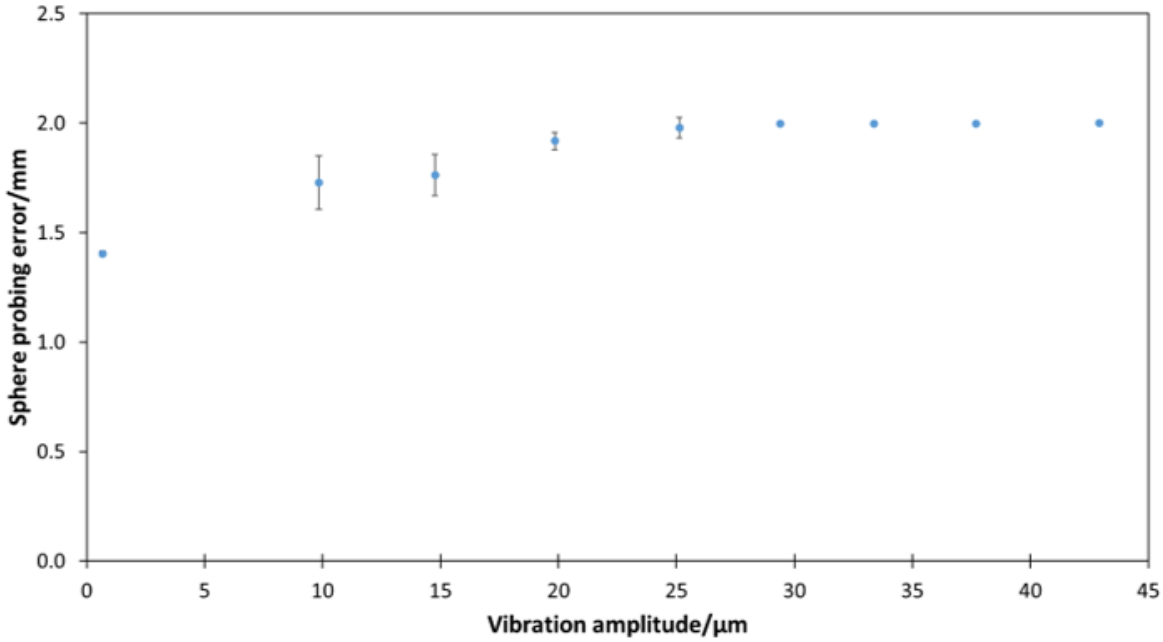


Figure. 7.16 A plot of increasing the amplitude of vibration in the *y*-axis against the sphere probing error (mean between the positive and negative) of a fitted sphere to the ball of the ball bar fixture on the AM artefact, shows the sphere probing error trend does not match the increasing measurement error.

starting at the same shaker vibration input (0.20 V), as well as similar magnitudes of error seen throughout. However, the *y*-axis results differ as they show a significant increase in errors between 14.77 µm (0.15 V shaker input) and 29.39 µm (0.30 V shaker input), which occurs at a lower shaker vibration input than the *x* and *z*-axes. This suggests the system is more sensitive to vibration in the *y*-axis compared to the *x* and *z*-axes. A mean error exceeding 1.2 mm was found in the most extreme vibration case for the *y*-axis, which further suggests that the multi-view fringe projection system is most sensitive to vibration in this axis. The vibration in the *y*-axis acts across the fringe pattern lines, and so, in the extreme cases, could be causing a complete breakdown of the fringe projection measurement technique, with the vibration significant enough to affect the phase shifts between captured images, and so cause additional errors in the phase unwrapping process. The *y* and *z* axis results for the sphere probing error analysis, shown in figures 7.16 and 7.18, were similar to the *x*-axis

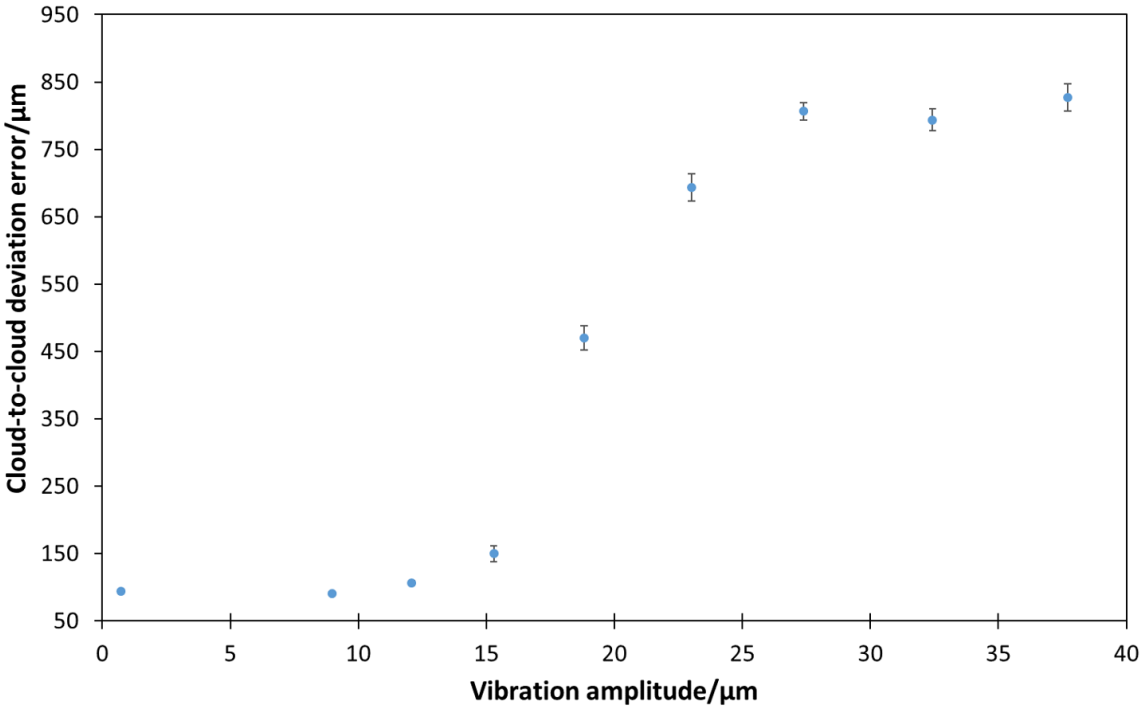


Figure. 7.17 A plot of increasing the amplitude of vibration in the z-axis against the mean cloud-to-cloud measurement error shows a significant rise in measurement errors as the captured images are increasingly blurred.

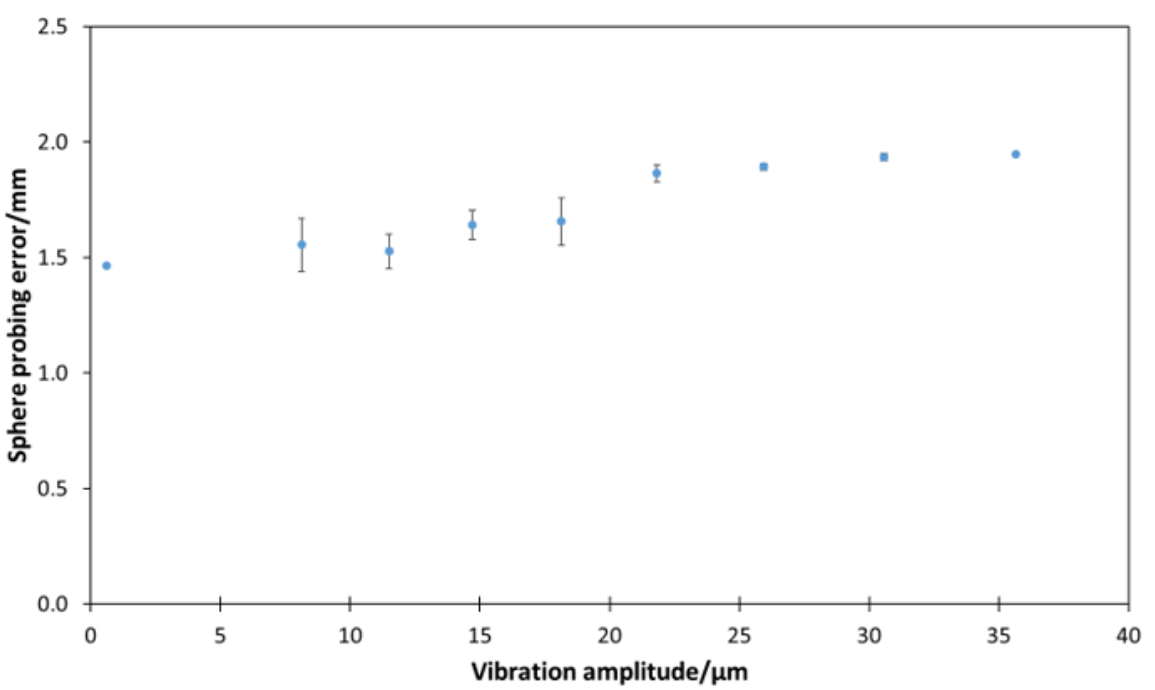


Figure. 7.18 A plot of increasing the amplitude of vibration in the z-axis against the sphere probing error (mean between the positive and negative) of a fitted sphere to the ball of the ball bar fixture on the AM artefact, shows the sphere probing error trend does not match the increasing measurement error.

results, and showed the increasing measurement errors were not linked to the complex shape measurement errors as the trends did not match. This further supports that the behaviour of our multi-view system differs from the commercial system, which is likely due to choice of hardware or the phase unwrapping technique employed. The multi-view fringe projection system produces errors that are over five times larger in all three axes than the commercial system, despite the mechanical frame causing a reduction in vibration amplitudes for the same shaker input. Therefore, the multi-view fringe projection system is considerably more sensitive to vibration than the commercial GOM system. From these results, it is clear that further developments are required to improve the robustness of the system and its software to bring the performance in line with commercial fringe projection systems.

7.3.1 Multi-point condition monitoring demonstration

In order to demonstrate the need for multi-point condition monitoring, an additional experiment was configured which allowed vibration to be measured at four different positions on the frame, using the multi-accelerometer system developed and described in Chapter 6. The purpose of the experiment was to measure the vibration present during the fringe projection sensitivity study, and show how the dynamics around the frame can vary with the same vibration input. The four accelerometer mounting positions have been shown in figure 7.10. The vibrations were measured in each axis, with the shaker vibration (0.20 V) applied to the same axis of measurement on the developed multi-view fringe projection frame, i.e. measurements in the x-axis correspond to shaker vibrations applied to the x-axis. The results of the experiment are shown in table 7.8.

From the results in table 7.8, the vibration measured in each axis around the frame vary despite the same vibration input. The results support the need for multi-point condition monitoring and show how the dynamics of a system can fluctuate and so need to be closely monitored. The multi-point conditioning monitoring concept is particularly important for

Table 7.8 The vibration measured for each axis, with the shaker vibration applied to the same axis of measurement, at multiple positions on the developed multi-view fringe projection frame.

Frame position	Measured vibration with 0.20 V input from the shaker/μm		
	x-axis	y-axis	z-axis
Position 1	14.70	19.84	15.28
Position 2	8.79	32.73	13.74
Position 3	18.16	14.84	10.22
Position 4	10.34	41.27	9.17

a multi-view fringe projection system. In order to achieve full-form reconstruction of the measured part, each camera-projector pair must be mounted at different positions on the frame, each acting as individual measurement systems, with the point clouds merged in post-process after the measurements are carried out. However, if the dynamics around the frame vary, the vibration study shown in section 7.3 suggests that each camera and projector pair will have different levels of error, adding complexity to the task of merging the resulting measurement point clouds. Using the fringe projection x-axis error curve (figure 7.11), and the measured vibration in the x-axis at all four positions (table 7.8), the effect of the varying dynamics around the system on the proposed multi-view fringe projection system can be clearly demonstrated. Figure 7.19 shows the estimated different vibration errors for each camera-projector pair based on the vibration measured at each mounting position for the same excitation.

From the results in figure 7.19 it is clear that if the camera-projector pairs are subject to different magnitudes of vibration depending on their location on the frame, they will experience different levels of measurement error. For example, the camera-projector pair at position 2 is subject to the smallest vibration (8.79 μm, green dashed line in figure 7.19) and so would see mean errors of approximately 75 μm, whereas in the most extreme case (18.16 μm, red dashed line in figure 7.19), the camera-projector pair at position 3 would see mean errors of approximately 490 μm. These large differences in approximated measurement

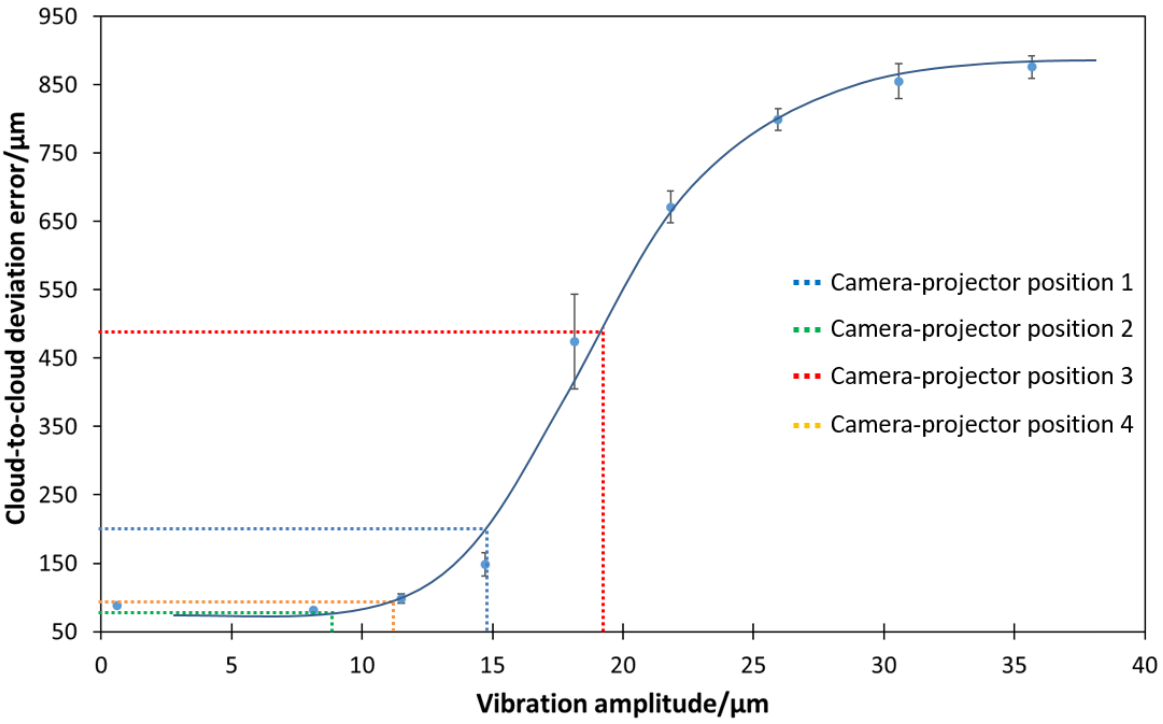


Figure. 7.19 Demonstrating the importance of condition monitoring in measurement systems, by showing an example of the different measurement errors (cloud-to-cloud) that could be experienced by each camera-projector pair in the multi-view fringe projection system due to the varying vibrations seen across the measurement frame.

errors between different positions on the frame would lead to each camera and projector pair being subject to different levels of error, and so add complexity to the task of merging the resulting measurement point clouds [161–163], which further emphasises the need for multi-point condition monitoring for the multi-view fringe projection system.

7.4 Chapter summary

In this chapter, the developed multi-point live condition monitoring system was used to carry out case studies on a commercial fringe projection system and a newly created multi-view fringe projection prototype system, in order to demonstrate the effectiveness of condition monitoring in measurement system applications and to investigate sensitivity of fringe projection measurements to vibration.

The first case study allowed the benchmarking of a commercial fringe projection system, and showed that in all three axes there was a clear positive trend of increasing error with vibration. The study found that the GOM system was most sensitive to vibration in the x-axis, with a mean error exceeding 160 μm found in the most extreme case. The x and y-axis showed significantly increasing measurement errors for the complex shapes on the AM artefact, which was supported by the results of the probing error analysis. The z-axis results showed no clear structure to the errors and highlighted this axis as the least sensitive to vibrational effects to the measurement. The measurement error curves were then used to define an acceptable vibration threshold for fringe projection measurements in each axis. It is recommended that these threshold values should not be exceeded in future fringe projection measurements using the GOM ATOS Core system, in order to avoid the regime in which large measurement errors are present.

The second case study allowed the performance of the system to be benchmarked against the commercial system, and a comparison of how sensitive the system is to vibration. The static results of the study highlighted the system has a 'modulation' issue, which is causing structured waviness errors across the measurement artefact. For the study, these modulation errors were reduced by using a more rigorous calibration and an increased number of phase shifts to average out the non-linearities in projector intensity, however, this is an on-going issue for the system and is yet to be resolved. The results in all three axes showed similar trends, with a significant increase in errors correlating to the blurring effect seen on the captured images. The blurring effect causes the edges on the artefact to be measured as curved transitions rather than sharp edges. The results for the multi-view showed the y-axis to be the most sensitive to vibrational effects with errors in excess of 1.2 mm, however, significantly large errors were seen in all three axes. The large magnitude of the errors in all three axes showed the system is considerably more sensitive to vibration than the commercial GOM

system, and so it is clear that further developments are required to improve the robustness of the system to bring the performance in line with commercial fringe projection systems.

The second case study on the multi-view fringe projection was also used to demonstrate the importance of multi-point condition monitoring in measurement system applications, in particular for the multi-view fringe projection system. In order to achieve a full form reconstruction of the measured part, each camera-projector pair must be mounted at different positions on the frame, each acting as individual measurement systems, with the point clouds merged in post-process after the measurements are carried out. The results of the study showed how the dynamics in four different positions around the frame vary, and as such would lead to each camera and projector pair being subject to different levels of error, and so adding complexity to the task of merging the resulting measurement point clouds.

Chapter 8

Conclusions and future work

Metrology is one of the most fundamental sciences and underpins the work carried out in engineering research and industry, and provides a number of essential features to modern manufacturing of parts, such as traceability, reliability, accuracy, process control, post-processing troubleshooting and reverse engineering (discussed in Chapter 1). To this end, as the manufacturing industry develops the current manufacturing techniques, as well as new methods, the measurements systems must also continue to develop alongside them. A pressing need of the AM industry is for new application specific measurement systems, which are capable of measuring the complex form of the parts produced to ensure accuracy and traceability, and thus increase confidence in AM produced parts across all engineering industries. To address the need for new measurement systems for the AM industry, the review of current form measurement techniques identified fringe projection as an optimal solution, and so the project worked towards developing the mechanical design for a multi-view fringe projection system that was capable of capturing the full-form of the part in a single measurement.

The focus of this thesis was on the mechanical design of the system, which required an investigation into the mechanical performance and how the changing dynamics of the structure affect the measurement quality, as mechanical noise sources such as vibration were

identified as an important and under-researched area in fringe projection measurements. In addition to enhancing the understanding of the effects of mechanical error sources on fringe projection measurements, the review also identified condition monitoring in optical measurement systems as an effective tool, which is currently underutilised and would benefit from the ability to live monitor the performance and health of the system during measurements and over time. With these identified knowledge gaps and needs in mind, the following objectives were set in Chapter 1 and investigated throughout the PhD to address these gaps:

1. Develop a mechanical design for a multi-view fringe projection system, which is capable of mounting multiple sets of cameras and projectors to enable the multi-view measurement paradigm to be investigated.

2. Enhance the understanding of the effects of mechanical error sources on fringe projection measurements, by developing both a simulation and experimental methodology to assess the sensitivity of the measurement technique.

3. Develop a characterisation method to enable the measurement of the dynamic performance of the mechanical system, and provide a method to live condition monitor the mechanical performance throughout the measurement process.

4. Demonstrate the benefit of multiple point live condition monitoring for measurement systems to verify the performance and increase confidence in optical coordinate measurement systems.

8.1 Contributions to the field

Chapter 4 gave a complete design history of the development of the multi-view fringe projection frame, which was used in the final system and throughout the work performed here. In

order to better define the required mechanical performance metrics of the system, a study into the effects of vibration on fringe projection measurements was carried out, which included developing a methodology to investigate the effects in both a theoretical simulation and experimental study. A key finding of the investigation was identifying the double linear trend seen in the theoretical simulation, which showed the significant increase in errors beyond the threshold limit. The limit can be defined by the phase jumps between fringe patterns, with vibration amplitudes exceeding this threshold leading to significant reconstruction errors as the phase unwrapping method breaks down. The systematic description of the design process and techniques used to develop the mechanical system provide a clear and structured methodology, which can be utilised in order to design and develop future measurement frames.

Chapter 5 described the development of the methodology and experimental characterisation work that was performed to verify the FEA simulation results for the frame design. This included a review of available vibration sensors, with piezoelectric accelerometers identified as the most appropriate solution for this application. An investigation into the different acceleration to velocity and displacement conversion methods was presented, which showed the unreliability of the widely used double integration method, and highlighted the advantages of the omega arithmetic method. The development of the characterisation method was a vital step in working towards the multi-point condition monitoring system, as well as characterising the multi-view frame in both a non-excited and camera shutter-excited state to verify the simulation results.

Chapter 6 detailed the development of a novel live multi-point vibration monitoring setup that combined multiple triaxial accelerometers, and processes large amounts of data simultaneously in real-time. This included a full breakdown of the functions and analysis available, and how the system was designed to be flexible for use in a variety of applications. The flexibility was demonstrated through a tool wear investigation on a CNC lathe, which

allowed the importance of structural health monitoring to be demonstrated. The investigation also highlighted the use of key functions on the system, such as event analysis, which can readily identify faults through any significant changes in the dynamics of the system. The development of the live multi-point vibration monitoring setup was a key achievement of the PhD and allowed the potential application of condition monitoring for measurement systems to be explored.

Chapter 7 detailed two experimental case studies that were performed in order to demonstrate the effectiveness of condition monitoring in measurement system applications, and to investigate the sensitivity of commercial and in-house fringe projection measurement systems to vibration. The results revealed new information about the effects of vibration on fringe projection measurements, highlighting regions (i.e. complex shapes or edges) of the measurement that were more susceptible to vibration in particular directions. The established measurement error curves matched well with the trends seen in the previous theoretical simulation, and also showed the double linear trend with significantly increased errors in the higher amplitude vibrations. The measurement error curves were used to define the acceptable vibration thresholds for each axis in order to avoid the regimes in which errors rapidly increase, and set the recommended vibration threshold in future measurements, i.e. for the commercial system vibration should be kept lower than 35 μm to avoid the increased error regimes in all axes. In addition, the vibration-error relationships were used alongside multi-point vibration measurements to estimate the variation in errors for measurement systems at different locations on the multi-view fringe projection frame, highlighting the importance of multi-point condition monitoring.

8.2 Areas for future work

The mechanical system presented in Chapter 4 and used throughout the PhD represents the first iteration of the multi-view fringe projection frame design, and provided all of the required

performance and functionality as laid out in the statement of requirements. However, there is scope further iterations of the design to be developed that would increase the functionality, performance and usability, using the information gained from the design presented here. The second iteration would focus on adding automation to the system by way of controlling the positions of the cameras and projectors on the frame, increasing the flexibility and accuracy of the system. In the initial stages of development of the multi-view fringe projection system, the positions of the cameras and projectors were rarely required to be changed, and the focus was on getting the basic system working by selecting the appropriate hardware and creating effective multi-view calibration and phase unwrapping methods. To this end, manual adjustment of the mounting positions was sufficient for the scope of the work. However, as the system adds functions, such as measurement planning, shadow prediction and pose estimation, the mechanical system must provide more freedom to accurately mount cameras and projectors as required.

A second key addition to future designs would be to provide a method that would allow the full 360° form of a measured object to be reconstructed. The mechanical system in its current form provides 180° of coverage. However, whilst the current system represents a key step in progressing the multi-view system, the manufacturing industry needs to be able to measure the full part, and so to truly capture the part in 'one-shot', the mechanical system must provide a design capable of measuring the full 360° form of the part. A potential solution to achieve full-form reconstruction could be to mount the measurement artefact on a transparent material [164], allowing the underside of the artefact to be seen from below. This approach is dependent on the implications of projecting and capturing the fringes through said material, and so this issue may require a more elaborate mounting/remounting solution.

The investigation into the effects of vibration on fringe projection measurements represents possibly the first in-depth study in the area, and the methodology presented is now readily applicable for use on any fringe projection system. A limitation of the investigation

into the commercial fringe projection system was that the fine details of the system, such as the specific algorithms used, were not available for investigation and so the system had to be treated as a 'black box'. As a result understanding the effects of vibration were limited to assumptions of the working principles and the methods employed. It was theorised that the system combined stereovision with fringe projection [165, 166], in order to increase the robustness of the measurements, hence the decreased effects of vibration in the study. To this end, development of an in-house prototype fringe projection system that incorporates stereovision techniques would allow the investigation to be performed on a fully open system, and so increase the understanding between different hybrid fringe projection techniques and confirm the findings of the original study. An important area of work that must also be performed on the prototype multi-view fringe projection system is to work towards establishing full traceability by developing calibration methods that utilise traceable reference artefacts and standards. With a traceable calibration procedure in place, an uncertainty budget can be calculated that fully accounts for all key sources of error and specifies the performance of the system.

The vibration study performed on the prototype multi-view fringe projection system delivered a benchmarking of the current system compared to the commercial system, as well as an investigation into the traditional fringe projection technique. However, the system was still in the early stages of development, leading to poor repeatability and a significant waviness modulation present in the resulting point cloud data. In the future, the methodology should be reapplied when the system is at a more reliable stage in its development in order to re-benchmark the system and revaluate any future design iterations. This study could be performed in conjunction with the previously mentioned fringe projection and stereovision hybrid system, in order to compare the effects of vibration to the different techniques.

The current scope of the work was focussed on designing a mechanical system to provide the required functionality for understanding the effects of vibration on fringe projection

measurements. However, the work has not focussed on the potential of including any active vibration isolation or damping techniques into the design, and so there is scope for an investigation into including these techniques in any future designs. A current promising research area that could be combined with this application is the use of lattice structures to create vibration band gaps in measurement system structures [167–169]. This technique would allow for a lightweight system to be created, which could eliminate problematic vibration sources of known frequencies and increase the scope for using measurement systems, such as the multi-view, on the factory floor or on-site where mechanical conditions are less ideal.

The final area for future work is to incorporate the live multi-point condition monitoring system with the multi-view fringe projection system. In order to improve measurement quality and effectively condition monitor the fringe projection system, integration with the multi-accelerometer system would allow for the dynamics of the frame to be constantly measured. Using the measured vibration, the system could make informed decisions on when to collect data based on the mechanical conditions e.g. delay the measurement and alert the user if the vibration levels exceed the allowable threshold. This method would increase confidence in the collected data, as measurements would only be performed in acceptable conditions, and the mechanical performance could be reported along with the measurement results.

8.3 Summary

The work performed as part of this thesis was successful in achieving the primary objectives of developing the mechanical design for a prototype multi-view fringe projection system, enhancing the understanding of mechanical error sources (mainly vibration) and developing a live characterisation method to enable the measurement of the dynamic performance of the mechanical system. A number of methodologies were developed throughout this thesis,

which can be readily used for further investigations and design iterations to further increase the understanding of mechanical error sources on optical measurement techniques such as fringe projection. The results of the experimental investigations carried out represent an important step towards a better understanding of mechanical design and performance for optical measurement systems. This work will help to develop new measurement systems that are widely sought after by modern manufacturing industries, such as AM, and will ultimately lead to improved part quality and reduced waste.

References

[1] The Modal Shop smart shaker K2007E01 http://www.modalshop.com/excitation.asp?P=Shop_Talk_-_SmartShaker%99&ID=399 (Date last accessed: 2020-02-14)

[2] BIPM 2012 The international vocabulary of metrology — basic and general concepts and associated terms (vim) *JCGM* **VIM 3rd edition** (Paris, France: Bureau International des Poids et Mesures)

[3] BIPM 2019 The international system of units (si) *JcGM* **9th edition** (Paris, France: Bureau International des Poids et Mesures)

[4] Leach R 2014 Fundamental principles of engineering nanometrology (Elsevier) chapter 1 2nd ed ISBN 9781455777501

[5] Leach R 2016 Metrology for additive manufacturing *Measurement and Control* **49** 132–135

[6] Stavroulakis P I and Leach R K 2016 Review of post-process optical form metrology for industrial-grade metal additive manufactured parts *Review of scientific instruments* **87** 1–33

[7] Sohoni S 2012 Importance of Modern Metrology in the Industries 1–4

[8] Quinn T and Kovalevsky J 2005 The development of modern metrology and its role today *Philosophical transactions. Series A, Mathematical, physical, and engineering sciences* **363** 2307–2327

[9] Kirkup L and Frenkel R B 2006 An introduction to uncertainty in measurement: using the gum (guide to the expression of uncertainty in measurement) (Cambridge University Press)

[10] Leach R and Smith S T 2018 Basics of precision engineering (CRC Press) chapter 1

[11] ISO/ASTM 52900-2015 2015 Additive manufacturing – General principles – terminology (Geneva: International Organisation for Standardisation)

[12] Thomas-Seale L, Kirkman-Brown J, Attallah M, Espino D and Shepherd D 2018 The barriers to the progression of additive manufacture: perspectives from uk industry *International Journal of Production Economics* **198** 104–118

[13] Berman B 2012 3-D printing: The new industrial revolution *Business Horizons* **55** 155–162

[14] Rifkin J 2012 The third industrial revolution - how the internet, green electricity, and 3-D printing are ushering in a sustainable era of distributed capitalism *World Financial Review* 1–8

[15] Economist T 2012 A third industrial revolution *The economist*

[16] Huang Y, Leu M C, Mazumder J and Donmez A 2015 Additive manufacturing - current state, future potential, gaps and needs, and recommendations *Journal of Manufacturing Science and Engineering* **137** 014001

[17] ACMA Staff 2014 Pros and cons of additive manufacturing http://compositesmanufacturingmagazine.com/2014/10/pros-cons-additive-manufacturing/2/ (Date last accessed: 2015-11-15)

[18] Huang S H, Liu P, Mokasdar A and Hou L 2013 Additive manufacturing and its societal impact *The International Journal of Advanced Manufacturing Technology* **67** 1191–1203

[19] Douglas S and Stanley W 2014 Costs and cost effectiveness of additive manufacturing - a literature review and discussion *NIST Special Publication* **1176**

[20] Rosen D W 2007 Computer-aided design for additive manufacturing of cellular structures *Computer-Aided Design and Applications* **4** 585–594

[21] Giannatsis J and Dedoussis V 2009 Additive fabrication technologies applied to medicine and health care: A review *International Journal of Advanced Manufacturing Technology* **40** 116–127

[22] Gibson L, Rosen D and Stucker B 2011 Additive manufacturing technologies *Rapid Manufacturing Association* 1–21

[23] Bandyopadhyay A and Heer B 2018 Additive manufacturing of multi-material structures *Materials Science and Engineering: R: Reports* **129** 1–16

[24] Eisenberg M 2013 3D printing for children: What to build next? *International Journal of Child-Computer Interaction* **1** 7–13

[25] Foresight 2013 The future of manufacturing *A new era of opportunity and challenge for the UK. Summary Report.* 1–20

[26] Wohlers Associates 2014 Additive manufacturing in FP7 and horizon 2020 *Wohlers report* 1–12

[27] European commission workshop on additive manufacturing 2014 Additive manufacturing in FP7 and horizon 2020 1–16

[28] Woolliams P, Halstead J, Morris A and Leach R 2014 NPL Additive manufacturing strategy

[29] Jurrens K and Energetics Incorporated 2013 Measurement science roadmap for metal-based additive manufacturing *Additive Manufacturing* 5–18 (*Preprint* arXiv:1011.1669v3)

[30] Quarshie R, MacLachlan S, Reeves P, Whittaker D and Blake R 2012 Shaping our national competency in additive manufacturing *The Additive Manufacturing Special Interest Group for the Technology Strategy Board*

[31] Ford S L N 2014 Additive manufacturing technology - potential implications for U.S. manufacturing competitiveness *Journal of International Commerce and Economics (USA)* **6** 1–35

[32] Platform A M 2014 Additive manufacturing - strategic research agenda *Allison, A Scudamore, R*

[33] Hocken R J and Pereira P H 2016 Coordinate measuring machines and systems (CRC press) chapter 4

[34] WLeitz PMM-G 3D coordinate measuring machines and gear inspection systems http://www.leitz-metrology.com/3D_measuring_machines_gear_inspection_systems_Leitz_PMM-G.shtml/ (Date last accessed: 2019-06-01)

[35] Carl zeiss industrial metrology systems http://www.zeiss.com/imt/ (Date last accessed: 2019-06-01)

[36] Amann M C, Bosch T M, Lescure M, Myllylae R A and Rioux M 2001 Laser ranging: a critical review of unusual techniques for distance measurement *Optical engineering* **40** 10–20

[37] Fröhlich C and Mettenleiter M 2004 Terrestrial laser scanning - New perspectives in 3D surveying *International Archives of Photogrammetry, Remote Sensing, and Spatial Information Sciences* **36** 7–13

[38] Petrie G and Toth C 2008 Introduction to Laser Ranging, Profiling, and Scanning *Topographic Laser Ranging and Scanning* 1–28

[39] Massa J S, Buller G S, Walker A C, Cova S, Umasuthan M and Wallace A M 1998 Time-of-flight optical ranging system based on time-correlated single-photon counting *Applied optics* **37** 7298–7304

[40] Bogue R 2010 Three-dimensional measurements: a review of technologies and applications *Sensor Review* **30** 102–106

[41] Blais F 2003 Review of 20 years of range sensor development *Videometrics VII* vol 5013 (International Society for Optics and Photonics) pp 62–77

[42] Luhmann T, Robson S, Kyle S and Harley I 2007 Close Range Photogrammetry: Principles, Techniques and Applications (Wiley) 1st ed ISBN 978-0470106334

[43] Sims-Waterhouse D, Piano S and Leach R 2017 Verification of micro-scale photogrammetry for smooth three-dimensional object measurement *Measurement Science and Technology* **28** 055010

[44] Geodetic products http://www.geodetic.com/products/systems/v-stars-n/ (Date last accessed: 2019-06-01)

[45] Michelson A A and Morley E W 1887 On the relative motion of the earth and the luminiferous ether *American Journal of Science* **34** 333–345

[46] Creath K 1985 Phase-shifting speckle interferometry *Applied Optics* **24** 3053–3058

[47] 4d technology: Fizcam fizeau interferometers http://see.4dtechnology.com/clients/4dtechnology/uploads/Data_Sheets/AccuFiz_Data_Sheet.pdf/ (Date last accessed: 2019-06-01)

[48] Creath K and Wyant J 1992 Moiré and fringe projection techniques *Optical shop testing* **2** 653–685

[49] Mauvoisin G, Bremand F and Lagarde A 1994 Three-dimensional shape reconstruction by phase-shifting shadow moiré *Applied optics* **33** 2163–2169

[50] Halioua M, Krishnamurthy R, Liu H and Chiang F 1983 Projection moiré with moving gratings for automated 3-d topography *Applied Optics* **22** 850–855

[51] Choi Y B and Kim S W 1998 Phase-shifting grating projection moiré topography *Optical Engineering* **37** 1005–1011

[52] Zhang S 2018 High-speed 3d shape measurement with structured light methods: A review *Optics and Lasers in Engineering* **106** 119–131

[53] Chen F, Brown G and Song M 2000 Overview of three-dimensional shape measurement using optical methods *Opical Engineering* **39** 10–22

[54] Salvi J, Batlle J and Mouaddib E 1998 A robust-coded pattern projection for dynamic 3D scene measurement *Pattern Recognition Letters* **19** 1055–1065

[55] Batlle J, Mouaddib E and Salvi J 1998 Recent progress in coded structured light as a technique to solve the correspondence problem *Pattern Recognition* **31** 963–982

[56] Barone S, Paoli A and Razionale A 2013 A coded structured light system based on primary color stripe projection and monochrome imaging *Sensors* **13** 13802–13819

[57] Gorthi S S and Rastogi P 2010 Fringe projection techniques: Whither we are? *Optics and Lasers in Engineering* **48** 133–140

[58] Ono N, Shimizu T, Kurihara T and Ando S 2004 Real-Time 3-D Imager Based on Spatio-Temporal Phase Unwrapping 2544–2547

[59] Itoh K 1982 Analysis of the phase unwrapping algorithm. *Applied optics* **21** 2470

[60] Chen W, Bu P, Zheng S and Su X 2007 Study on Fourier transforms profilometry based on bi-color projecting *Optics & Laser Technology* **39** 821–827

[61] Gom atos core specifications http://www.gom.com/fileadmin/user_upload/systems/gom_atos-scanbox_EN.pdf/ (Date last accessed: 2019-06-01)

[62] Pinto T, Kohler C and Albertazzi A 2012 Regular mesh measurement of large free form surfaces using stereo vision and fringe projection *Optics and Lasers in Engineering* **50** 910–916

[63] Leach R 2011 Optical measurement of surface topography vol 14 (Springer) chapter 1, pp 23–48

[64] Coveney T 2014 Good Practice Guide N0.39 *Dimensional Measurement using Vision Systems*

[65] Open Stax Rice University 2013 The Rayleigh Criterion - http://cnx.org/contents/9ANhisjh@5/Limits-of-Resolution-The-Rayle

[66] Percoco G and Sánchez Salmerón A J 2015 Photogrammetric measurement of 3D freeform millimetre-sized objects with micro features: an experimental validation of the close-range camera calibration model for narrow angles of view *Measurement Science and Technology* **26** 095203

[67] Gallo A, Muzzupappa M and Bruno F 2014 3D reconstruction of small sized objects from a sequence of multi-focused images *Journal of Cultural Heritage* **15** 173–182

[68] Eltoukhy H A and Kavusi S 2003 A computationally efficient algorithm for multi-focus image reconstruction *Stanford University*

[69] Xiuqing W, Rong Z and Yunxiang X 2000 A method of wavelet-based edge detection with data fusion for multiple images *Intelligent Control and Automation, Proceedings of the 3rd World Congress 4* pp 2691–2694

[70] Huang W and Jing Z 2007 Evaluation of focus measures in multi-focus image fusion *Pattern Recognition Letters* **28** 493–500

[71] Liu Z, Tsukada K, Hanasaki K, Ho Y K and Dai Y P 2001 Image fusion by using steerable pyramid *Pattern Recognition Letters* **22** 929–939

[72] Pan B, Kemao Q, Huang L and Asundi A 2009 Phase error analysis and compensation for nonsinusoidal waveforms in phase-shifting digital fringe projection profilometry *Optics Letters* **34** 416–418

[73] Zhang S and Yau S t 2007 Generic nonsinusoidal phase error correction for three-dimensional shape measurement using a digital video projector *Applied optics* **46** 36–43

[74] Huang P S, Zhang C, Chiang F p and Brook S 2003 High-speed 3-D shape measurement based on digital fringe projection *Optical Engineering* **42** 163–168

[75] Surrel Y 1996 Design of algorithms for phase measurements by the use of phase stepping *Applied optics* **35** 51–60

[76] Guo H, He H and Chen M 2004 Gamma correction for digital fringe projection profilometry *Applied optics* **43** 2906–2914

[77] Boyat A and Joshi B K 2013 Image denoising using wavelet transform and median filtering *IEEE Nirma University International Conference on Engineering* pp 1–6

[78] Boyat A K and Joshi B K 2015 A Review paper: Noise models in digital image processing *Signal & Image Processing : An International Journal* **6** 63–75

[79] Lalanne C 2014 Mechanical vibration and shock analysis, random vibration vol 3 (John Wiley & Sons) chapter 5

[80] Kelly S G 2012 Mechanical vibrations: theory and applications (Cengage learning) chapter 13

[81] Schiavi A, Rossi L and Ruatta A 2016 The perception of vibration in buildings: A historical literature review and some current progress *Building Acoustics* **23** 59–70

[82] Fahy F and Thompson D 2016 Fundamentals of sound and vibration (CRC Press) chapter 1

[83] 2631-1 I 1997 Evaluation of human exposure to whole-body vibration — part 1: General requirements *Mechanical vibration, shock and condition monitoring* **2nd edition**

[84] Thor labs, sources of vibration http://www.thorlabs.com/newgrouppage9.cfm?objectgroup_id=8275 (Date last accessed: 2019-07-16)

[85] Ibnur R B, Zainal A M, Gerald M L, Mark W, Theresa L, Yu F and Huai M S 2002 A simple laboratory set-up for the fringe-projection method *Proc. SPIE* vol 4588 p 317

[86] Molimard J and Navarro L 2013 Uncertainty on fringe projection technique: A monte-carlo-based approach *Optics and Lasers in Engineering* **51** 840–847

[87] Bräuer-Burchardt C, Kühmstedt P and Notni G 2015 Phase error analysis and compensation in fringe projection profilometry *Modeling Aspects in Optical Metrology V* vol 9526 (International Society for Optics and Photonics) p 952608

[88] Zhang Z 2012 Review of single-shot 3d shape measurement by phase calculation-based fringe projection techniques *Optics and Lasers in Engineering* **50** 1097–1106

[89] Notni G H and Notni G 2003 Digital fringe projection in 3d shape measurement: an error analysis *Optical Measurement Systems for Industrial Inspection III* vol 5144 (International Society for Optics and Photonics) pp 372–380

[90] Sansoni G, Carocci M and Rodella R 1999 Three-dimensional vision based on a combination of gray-code and phase-shift light projection: analysis and compensation of the systematic errors *Applied optics* **38** 6565–6573

[91] Tao J, Juntong X and Junqi Y 2006 An accurate three-dimensional scanning system with a new phase error compensation method *The International Journal of Advanced Manufacturing Technology* **29** 1178–1185

[92] Yao J, Chen X, Zhou Y, Miao H and Chen J 2014 Phase error elimination considering gamma nonlinearity, system vibration, and noise for fringe projection profilometry *Optical Engineering* **53** 094102, 1–7

[93] Purcell D, Davies A and Farahi F 2006 Effective wavelength calibration for moiré fringe projection *Applied optics* **45** 8629–8635

[94] Du H, Chen X, Xi J, Yu C and Zhao B 2017 Development and verification of a novel robot-integrated fringe projection 3d scanning system for large-scale metrology *Sensors* **17** 2886

[95] ISO/ASTM 23165-2006 2006 Geometrical product specification (GPS) - Guidelines for the evaluation of coordinate measuring machine (CMM) test uncertainty (Geneva: International Organisation for Standardisation)

[96] Zygo newview tm 8300 specifications http//www.lambdaphoto.co.uk/pdfs/Zygo/Lambda_NewView8300_Specs_SS0100_3_14.pdf (Date last accessed: 2019-07-10)

[97] Nie M and Wang L 2013 Review of condition monitoring and fault diagnosis technologies for wind turbine gearbox *Procedia CIRP* **11** 287 – 290 2nd International Through-life Engineering Services Conference

[98] Ahirrao N, Bhosle S and Nehete D 2018 Dynamics and vibration measurements in engines *Procedia Manufacturing* **20** 434–439

[99] Lei Y, Lin J, Zuo M J and He Z 2014 Condition monitoring and fault diagnosis of planetary gearboxes: A review *Measurement* **48** 292–305

[100] Randall R B 2011 Vibration-based condition monitoring: industrial, aerospace and automotive applications (John Wiley & Sons)

[101] Duarte D, Pereira P, Gameiro G, Almeida I, Milharadas M, Cordeiro S, Vieira R, Antunes P, Ferreira N, Viana J *et al.* 2019 Development and validation of failure preventive tools for aeronautical applications *Engineering Failure Analysis* **101** 329–341

[102] Ambhore N, Kamble D, Chinchanikar S and Wayal V 2015 Tool condition monitoring system: A review *Materials Today: Proceedings* **2** 3419–3428

[103] Zhou Y and Xue W 2018 Review of tool condition monitoring methods in milling processes *The International Journal of Advanced Manufacturing Technology* **96** 2509–2523

[104] Cawley P 2018 Structural health monitoring: Closing the gap between research and industrial deployment *Structural Health Monitoring* **17** 1225–1244

[105] Bogue R 2013 Sensors for condition monitoring: a review of technologies and applications *Sensor Review* **33** 295–299

[106] Jones N and Li Y H 2000 A review of condition monitoring and fault diagnosis for diesel engines *Tribotest* **6** 267–291

[107] Caesarendra W, Kosasih B, Tieu A K, Zhu H, Moodie C A and Zhu Q 2016 Acoustic emission-based condition monitoring methods: Review and application for low speed slew bearing *Mechanical Systems and Signal Processing* **72** 134–159

[108] Choudhury A and Tandon N 2000 Application of acoustic emission technique for the detection of defects in rolling element bearings *Tribology international* **33** 39–45

[109] Bagavathiappan S, Lahiri B, Saravanan T, Philip J and Jayakumar T 2013 Infrared thermography for condition monitoring–a review *Infrared Physics & Technology* **60** 35–55

[110] Bandes A 2014 Ultrasound condition monitoring (Whitepaper, UE Systems)

[111] Blitz J and Simpson G 1995 Ultrasonic methods of non-destructive testing vol 2 (Springer Science & Business Media)

[112] Huston D 2010 Structural sensing, health monitoring, and performance evaluation (CRC Press) chapter 1

[113] Beck J, May B and Polidori D 1994 Determination of modal parameters from ambient vibration data for structural health monitoring *Proceedings First World Conference on Structural Control* (International Association for Structural Control) pp TA3–3

[114] Beck J L, Vanik M W, Polidori D C and May B S 1998 Structural health monitoring using ambient vibrations *Proceedings Structural Engineers World Congress* (Elsevier) p 294

[115] Kim S, Pakzad S, Culler D, Demmel J, Fenves G, Glaser S and Turon M 2007 Health monitoring of civil infrastructures using wireless sensor networks *Proceedings of the 6th international conference on Information processing in sensor networks* (ACM) pp 254–263

[116] Bocca M, Eriksson L M, Mahmood A, Jäntti R and Kullaa J 2011 A synchronized wireless sensor network for experimental modal analysis in structural health monitoring *Computer-Aided Civil and Infrastructure Engineering* **26** 483–499

[117] El-Basheer T M and Shawky H A 2018 Measurements and limits of vibration affecting the sensitive equipments of some metrological laboratories **102** 2637–2644

[118] ASTM F2792-12a:2012 2012 Standard terminology for additive manufacturing technologies (ASTM International)

[119] Gibson I, Rosen D, Stucker B 2010 Powder Bed Fusion Processes. In: Additive Manufacturing Technologies (Springer, Boston, MA) pp 120–159

[120] Jaffe B 2012 Piezoelectric ceramics vol 3 (Elsevier)

[121] Levinzon, Felix 2015 Piezoelectric accelerometers with integral electronics (Springer, Switzerland) pp 1–41

[122] Meggit endevco piezoelectric accelerometers http://www.meggitt.com/products-services/accelerometers/ (Date last accessed: 2019-08-19)

[123] Serridge M and Licht T R 1987 Piezoelectric accelerometers and vibration preamplifiers: theory and application handbook

[124] Bank G and Hathaway G 1980 A revolutionary 3-d interferometric vibrational mode display *Audio Engineering Society Convention 66* (Audio Engineering Society)

[125] De Silva C W 1999 Vibration: fundamentals and practice (CRC press)

[126] Prabhu K M 2013 Window functions and their applications in signal processing (CRC press) chapter 3

[127] Dotson C L 2015 Fundamentals of dimensional metrology (Nelson Education)

[128] Zhang S 2016 High-speed 3d imaging with digital fringe projection techniques (CRC Press)

[129] Te connectivity accelerometer comparison http://www.te.com/usa-en/industries/sensor-solutions/insights/vibration-sensor-condition-monitoring-white-paper.html#chapter-1-dl (Date last accessed: 2019-07-10)

[130] Meggitt endevco available accelerometers https://buy.endevco.com/accelerometer.html?applications=NaN&range_sensitivity_mv_g=761 (Date last accessed: 2019-07-10)

[131] PCB available accelerometers http://buy.endevco.com/accelerometer.html?applications=NaN&range_sensitivity_mv_g=761 (Date last accessed: 2019-07-10)

[132] Fericean S 2018 Inductive sensors for industrial applications (Artech House)

[133] Micro epsion proximity sensor specifications http://www.keyence.com/products/sensor/proximity/ez/specs/index.jsp (Date last accessed: 2019-07-10)

[134] Keyence proximity sensor specifications http://www.keyence.com/products/sensor/proximity/ez/specs/index.jsp (Date last accessed: 2019-07-10)

[135] Mide sensor comparison http://www.te.com/usa-en/industries/sensor-solutions/insights/vibration-sensor-condition-monitoring-white-paper.html#chapter-1-dl (Date last accessed: 2019-07-10)

[136] Sinha J K 2014 Vibration analysis, instruments, and signal processing (CRC press) chapter 5

[137] Meggitt velocity transducer specifications http://catalogue.meggittsensing.com/vibration-sensors-ca-ce-cv-pv-se-and-ve/cv214.html (Date last accessed: 2019-07-10)

[138] Goyal D and Pabla B S 2016 The vibration monitoring methods and signal processing techniques for structural health monitoring: A review *Archives of Computational Methods in Engineering* **23** 585–594

[139] Fahy F and Walker J 2018 Advanced applications in acoustics, noise and vibration (CRC Press) chapter 4

[140] Johansmann M, Siegmund G and Pineda M 2005 Targeting the limits of laser doppler vibrometry *Proc. IDEMA* 1–12

[141] Halkon B J and Rothberg S 2016 A practical guide to laser doppler vibrometry measurements directly from rotating surfaces

[142] Polytec pdv 100 laser vibrometer specifications http://www.polytec.com/fileadmin/d/Vibrometrie/OM_DS_PDV-100_E_42474.pdf (Date last accessed: 2019-07-10)

[143] Levinzon F A 2004 Fundamental noise limit of piezoelectric accelerometer *IEEE Sensors Journal* **4** 108–111

[144] ISA-RP-372 1995 Guide for Specifications and Tests for Piezoelectric Acceleration Transducers for Aerospace Testing (International Society of Automation (ISA))

[145] Mercer C 2006 Acceleration, velocity and displacement spectra omega arithmetic *Prosig signal processing tutorials*

[146] Brandt A 2011 Noise and vibration analysis: signal analysis and experimental procedures (John Wiley & Sons)

[147] Zumbahlen H 2008 Linear circuit design handbook (Newnes) chapter 8

[148] Mide filter selection for shock and vibration applications http://blog.mide.com/filter-selection-for-shock-and-vibration-applications (Date last accessed: 2019-08-20)

[149] Bujoreanu C and Benchea M 2016 Experimental study on hvac sound parameters *IOP Conference Series: Materials Science and Engineering* vol 147 (IOP Publishing) pp 1–11

[150] Ekreem N, Olabi A G, Prescott T, Rafferty A and Hashmi M 2007 An overview of magnetostriction, its use and methods to measure these properties *Journal of Materials Processing Technology* **191** 96–101

[151] NCSS Statistics - Two sample T-Test http://ncss-wpengine.netdna-ssl.com/wp-content/themes/ncss/pdf/Procedures/NCSS/Two-Sample_T-Test.pdf (Date last accessed: 2020-01-30)

[152] Feese T and Hill C 2009 Prevention of torsional vibration problems in reciprocating machinery *In Proceedings of the 38th turbomachinery symposium* **38** 213–238

[153] Link A, Täubner A, Wabinski W, Bruns T and Elster C 2006 Calibration of accelerometers: determination of amplitude and phase response upon shock excitation *Measurement Science and Technology* **17** 1888

[154] GOM ATOS Core 300 fringe projection system specifications http://www.gom.com/metrology-systems/atos/atos-core.html (Date last accessed: 2019-08-20)

[155] Shaheen A, Sims-Waterhouse D, Bointon P, Piano S and Leach R Automated characterisation of multi-view fringe projection system for three-dimensional measurement of additively manufactured parts *Advancing Precision in Additive Manufacturing, Ecole Centrale de Nantes, France, September 2019*

[156] Shaheen A, Sims-Waterhouse D, Bointon P, Piano S and Leach R A flexible method for the geometric characterisation of a multi-view fringe projection system *3D Metrology Conference, London, United Kingdom, November 2019*

[157] Chen B and Zhang S 2016 High-quality 3d shape measurement using saturated fringe patterns *Optics and Lasers in Engineering* **87** 83–89

[158] Girardeau-Montaut D, Roux M, Marc R and Thibault G 2005 Change detection on points cloud data acquired with a ground laser scanner *International Archives of Photogrammetry, Remote Sensing and Spatial Information Sciences* **36** W19

[159] Besl P J and McKay N D 1992 Method for registration of 3-d shapes *Sensor fusion IV: control paradigms and data structures* vol 1611 (International Society for Optics and Photonics) pp 586–606

[160] Wolfram math world description of least squares fitting algorithm http://mathworld.wolfram.com/LeastSquaresFitting.html (Date last accessed: 2019-07-13)

[161] Petricek T and Svoboda T 2017 Point cloud registration from local feature correspondences—evaluation on challenging datasets *PloS one* **12** e0187943

[162] Mitra N J, Gelfand N, Pottmann H and Guibas L 2004 Registration of point cloud data from a geometric optimization perspective *Proceedings of the 2004 Eurographics/ACM SIGGRAPH symposium on Geometry processing* (ACM) pp 22–31

[163] Li H, Sumner R W and Pauly M 2008 Global correspondence optimization for non-rigid registration of depth scans *Computer graphics forum* vol 27 (Wiley Online Library) pp 1421–1430

[164] Southon N, Stavroulakis P, Goodridge R and Leach R 2018 In-process measurement and monitoring of a polymer laser sintering powder bed with fringe projection *Materials & Design* **157** 227–234

[165] Zhang S 2018 Absolute phase retrieval methods for digital fringe projection profilometry: A review *Optics and Lasers in Engineering* **107** 28–37

[166] Zhang S 2013 *Handbook of 3D machine vision: Optical metrology and imaging* (CRC press)

[167] Elmadih W, Syam W P, Maskery I, Chronopoulos D and Leach R 2019 Mechanical vibration bandgaps in surface-based lattices *Additive Manufacturing* **25** 421–429

[168] Elmadih W, Syam W P, Maskery I, Chronopoulos D and Leach R 2019 Multidimensional phononic bandgaps in three-dimensional lattices for additive manufacturing *Materials* **12** 1878

[169] Elmadih W, Chronopoulos D, Syam W, Maskery I, Meng H and Leach R 2019 Three-dimensional resonating metamaterials for low-frequency vibration attenuation *Scientific reports* **9** 1–8